Chemical Abundances of Local Group Globular Clusters

by

Charli Sakari
B.A., Whitman College, 2009

A Dissertation Submitted in Partial Fulfillment of the
Requirements for the Degree of

DOCTOR OF PHILOSOPHY

in the Department of Physics & Astronomy

Chemical Abundances of Local Group Globular Clusters

by

Charli Sakari
B.A., Whitman College, 2009

Supervisory Committee

Dr. Kim A. Venn, Supervisor
(Department of Physics & Astronomy)

Dr. Don A. VandenBerg, Departmental Member
(Department of Physics & Astronomy)

Dr. Patrick Côté, Departmental Member
(Department of Physics & Astronomy)

Dr. Colin Bradley, Outside Member
(Department of Mechanical Engineering)

Supervisory Committee

Dr. Kim A. Venn, Supervisor
(Department of Physics & Astronomy)

Dr. Don A. VandenBerg, Departmental Member
(Department of Physics & Astronomy)

Dr. Patrick Côté, Departmental Member
(Department of Physics & Astronomy)

Dr. Colin Bradley, Outside Member
(Department of Mechanical Engineering)

ABSTRACT

Detailed chemical abundances of globular clusters in the Milky Way and M31 (the Andromeda Galaxy) are presented based on analyses of high resolution spectra. The unusual Milky Way cluster Palomar 1 (Pal 1) is studied through spectra of individual red giant branch stars; these abundances show that Pal 1 is not a classical globular cluster, and may have been accreted from a dwarf satellite of the Milky Way. The Milky Way globular clusters 47 Tuc, M3, M13, NGC 7006, and M15 are studied through their *integrated light* (i.e. a single spectrum is obtained for each cluster) in order to test high resolution integrated light analyses. The integrated abundances from these clusters reproduce the average abundances from individual stellar analyses *for elements that do not vary within a cluster* (e.g. Fe, Ca, and Ni). For elements that *do* vary within the clusters (e.g. Na and Mg) the integrated abundances fall within the observed ranges from individual stars. Certain abundance ratios are found to be extremely sensitive to uncertainties in the underlying stellar populations, such as input models, empirical relations to determine atmospheric parameters, interloping field

stars, etc., while others (such as [Ca I/Fe I]) are largely *insensitive* to these effects. With these constraints on the accuracy and precision of high resolution integrated light analyses, detailed abundances are obtained for seven clusters in the outer halo of M31 that were recently discovered in the Pan-Andromeda Archaeological Survey (PAndAS) and are likely to have originated in dwarf galaxy satellites. Three clusters are relatively metal rich ([Fe/H] $\gtrsim -1.5$) for their locations in the outer halo; their chemical abundances suggest that they likely originated in one or more fairly massive dwarf satellites. The other four are more metal-poor, and may have originated in less massive dwarf satellites. These results indicate that the Milky Way and M31 have both experienced some amount of accretion from dwarf satellites, though M31 may have had a more active accretion history.

Contents

List of Tables

List of Figures

LIST OF FIRST AUTHOR PUBLICATIONS

Peer-reviewed publications:

- **Detailed chemical abundances of four stars in the unusual globular cluster, Palomar 1**
  Sakari, C., Venn, K., Irwin, M., Aoki, W., Arimoto, N., & Dotter, A. 2011, ApJ, 740, 106

- **Spectrum syntheses of high-resolution integrated light spectra of Galactic globular clusters**
  Sakari, C.M., Shetrone, M., Venn, K., McWilliam, A., & Dotter, A. 2013, MNRAS, 434, 358

- **Optimal Integrated Abundances for Chemical Tagging of Extragalactic Globular Clusters**
  Sakari, C.M., Venn, K., Shetrone, M., Dotter, A. & Mackey, D. 2014, MNRAS, 443, 2285

- **Integrated Light Chemical Tagging Analyses of 7 Outer Halo M31 Globular Clusters from the Pan-Andromeda Archaeological Survey**
  Sakari, C.M., Venn, K.A., Mackey, D., Shetrone, M.D., Dotter, A., et al. 2014, MNRAS, *in prep.*

Conference proceedings:

- **Detailed Chemical Abundances of Four Stars in the Unusual Globular Cluster, Palomar 1**
  Sakari, C.M., Venn, K.A., Irwin, M., Aoki, W., Arimoto, N., & Dotter, A. 2012, in *Galactic Archaeology: Near-Field Cosmology and the Formation of the Milky Way. Proceedings of the conference held 16-20 May 2011 in Shuzenji, Japan.* Edited by W. Aoki, M. Ishigaki, T. Suda, T. Tsujimoto, and N. Arimoto. ASP Conference Proceedings, Vol. 458. San Francisco, CA: Astronomical Society of the Pacific, 2012, 247

- **High Resolution Integrated Light Spectroscopy of Galactic Globular Clusters**
  Sakari, C., Venn, K., McWilliam, A., Shetrone, M., & Dotter, A. 2012, in *Proceedings of the XII International Symposium on Nuclei in the Cosmos (NIC XII)*. August 5-12, 2012. Cairns, Australia

STATEMENT OF COAUTHORSHIP

Astronomy research requires collaborative work. In addition to the many helpful comments, questions, and suggestions, several components of this thesis were completed by my collaborators:

Palomar 1 data: The Palomar 1 data were obtained by Wako Aoki in 2006 and 2007, and were reduced by Kim Venn.

Integrated light spectra: Matthew Shetrone and I obtained all HET spectra taken in 2011-2013. The 47 Tuc spectrum was obtained in 2000 by R. Bernstein & Andrew McWilliam.

Data Reduction Scripts: The original data reduction scripts were provided by Matthew Shetrone; I modified them for the integrated light spectra.

ILABUNDS and other codes: The integrated light equivalent width and spectrum synthesis modifications to `MOOG` were done by Andrew McWilliam. Other scripts, such as the scripts to box up CMDs, to assign atmospheric parameters to resolved boxes, and to populate isochrones were also written by Andy McWilliam. I provided slight modifications to these scripts to update, e.g., molecular data.

PAndAS photometry: The PAndAS *HST* photometry was obtained and reduced by Dougal Mackey.

I thank all my collaborators for their contributions to this thesis work.

ACKNOWLEDGEMENTS

I could not have completed this PhD thesis without the help and support of my family, friends, and collaborators.

First and foremost, I want to thank the people who actively helped me complete this thesis work:

Kim Venn, my PhD supervisor: I have so many things to thank you for... Thanks for all the support and encouragement you've given me over the past 5 years, especially for helping me to build amazing connections in the stellar community. Thank you for always being excited about my research, even when I wasn't, and for helping me to remember that our research really is exciting and useful. Thanks for all the coffee runs, the nights at Big Bad John's, and all the dinners you hosted. Thank you for listening to my problems (both academic and personal) and for helping me to find solutions. In short—thank you for being more than just an academic supervisor.

Andy McWilliam and Matthew Shetrone: Thank you for being such helpful and supportive collaborators! Andy—thank you for developing new codes for me, for debugging things so quickly, for teaching me how to code in Fortran, how to modify MOOG, and how to think about IL analyses; without your guidance the learning curve would have been much steeper. Matthew—thank you for teaching me most of what I know about observing and data reduction and for working through our integrated light confusion together! Both of you—thank you for your patience with all of my questions, for your careful reading of my papers, for your trust in me, and for your support for my post-doc applications. I look forward to continuing to work with you in the future!

Aaron Dotter and Dougal Mackey: Thank you both for all of your help with my photometry, isochrone, and stellar evolution questions. Aaron—thank you for seeding the early ideas for the integrated light projects. Dougal—thank you for getting me involved in PAndAS and for helping me out with the *HST* data.

Caty Pilachowski, my external examiner: Thank you so much for your thesis comments and suggestions, for travelling all the way to Victoria, and for being so supportive throughout the defense process. My dissertation is truly better because of your input.

Don VandenBerg, Patrick Côté, and Colin Bradley: Thank you for serving on my committee, for reading my thesis, and for all your helpful suggestions! Don—your Stellar Populations class was one of the best courses I have ever taken, and I definitely learned a lot!

Hannah Broekhoven-Fiene and Jason Kezwer: Thank you for serving as my Mock PhD Committee! Thank you for reading my thesis, for coming up with excellent questions, and for spending two hours trying to break me. It made the real defense so much easier!

Stephenson Yang: Thank you for all your computing help, particularly during those times when the servers kept crashing and I couldn't run my scripts!

The office staff: Thanks to all of the office staff who have helped me along the way, particularly Susan Gnucci, Amanda Bluck, Joelene Bales, Michelle Shen, Monica Lee, and Megan Cox.

The The Vanier Canada Graduate Scholarships Program: I will always be grateful for the funding I received as a Vanier Scholar. It is so difficult to work on a PhD while worrying about money, and having this scholarship enabled me to focus on my research. Thank you!

Secondly, I want to thank everyone who helped alleviate the stress that comes with being a PhD student. I met a lot of great people in Victoria, and we had a lot of great times! I hope to keep in touch with you.

Hannah Broekhoven-Fiene: Thank you for your friendship and encouragement over the last 5 years. Thank you for helping me with all my extra activities, especially the website and the Astro Grad Forum. You've been my Victoria family for the past 3 years, and I would not be the same without you.

Jillian Scudder: Thanks for being an awesome grumble buddy! Our daily conversations definitely made the stress easier to bear. I will miss having you in the same office building.

Ryan Leaman and Masen Lamb: Thank you for being the best academic brothers a girl could have! Ryan—I learned a lot from you, not just scientifically but also from the Book of Venn; you have always been extremely supportive of me

and you always worked hard to answer all of my questions. Thank you for encouraging me to come to Victoria. Masen—Thanks for just being yourself. I now pass you the official Book of Venn.

Razzi Movassaghi and Jean-Claude Passy: Thank you for all the fun times we had. You guys always helped distract me from my research woes! Razzi—you've both always been so supportive, and just being around you has always made me feel better. JC, my lady—thanks for entertaining me so often, for putting up with our pranks, and for trying to understand.

All the Physics & Astronomy Grads and Postdocs throughout the years: Thanks for all the good times we had! Hopefully there will be many more to come!

The Greater Victoria Concert Band: Music has always been a very important part of my life. Going three years without playing was extremely difficult, and I am so grateful that I could spend my last two years here in the GVCB. Thanks for allowing me to join the senior band; we made some excellent music together!

Finally, I couldn't have gotten this far without all the support and encouragement I received throughout my childhood, high school, and college. I want to thank my family, my friends, my teachers and professors, and everyone who has enriched my life. Thank you for your support! Particular thanks to **Velda Arnaud**, **Carl Sakari**, and **Max Sakari**; you've always been supportive of everything I've done, which has always made me believe I could accomplish anything!

DEDICATION

To my family, both human and feline.

I am an instrument in the shape
of a woman trying to translate pulsations
into images for the relief of the body
and the reconstruction of the mind.
–Adrienne Rich, "Planetarium"

Chapter 1

Introduction

A major goal of modern astronomy is to understand the formation of structure in the early Universe and how this structure has evolved over time. There are several methods for studying the early Universe, such as observations of distant (i.e. high redshift) objects or simulations of structure formation. This thesis utilizes a technique known as *galactic archaeology*, where the properties of current stellar populations are used to infer the assembly history of a galaxy. Observations of nearby galaxies of a range of masses, types, and in a variety of environments can infer possible formation scenarios and determine if all galaxies form in a similar way. In this thesis chemical abundances of globular cluster (GC) systems[1] are used to trace the formation histories of two galaxies: the Milky Way (MW) and the Andromeda Galaxy (M31).

1.1 Globular Clusters

GCs are dense star clusters, containing up to about a million times the mass of the sun in a volume with a radius of a few parsecs.[2] The vast number of stars in such a small region typically makes the cluster look like a circular blob of light (see the image of the Galactic[3] GC M15 in Figure 1.1a). The MW has many GCs (about 157, Harris 1996; 2010 edition)—more massive galaxies can have tens of thousands of GCs (Brodie & Strader, 2006). Many GCs tend to be approximately spherically distributed around their host galaxy and extend to greater distances than the field

[1] See Appendix A for a glossary of acronyms used in this thesis.

[2] 1 parsec (pc) = 3.26 light years = 3.09×10^{16} m.

[3] When the words "Galaxy" or "Galactic" are capitalized, they refer specifically to the MW.

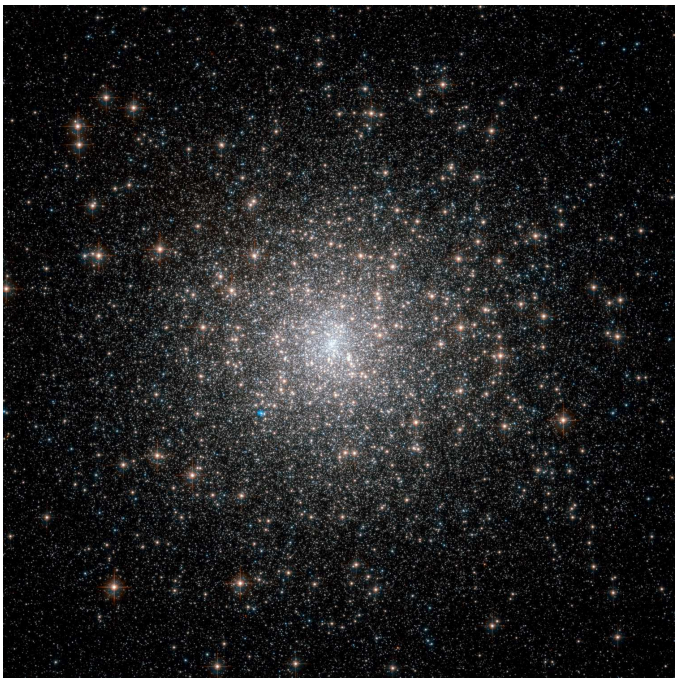

(a) Galactic GC M15

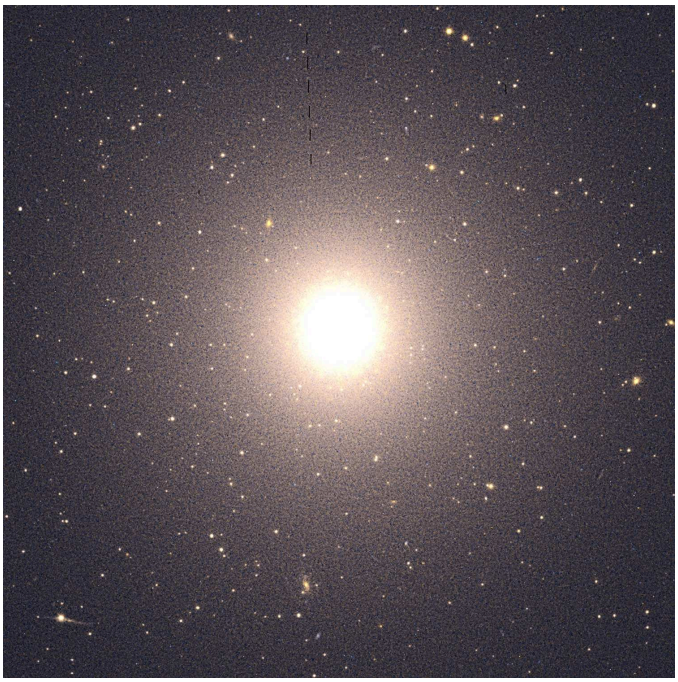

(b) NGC 1407 + GC System

Figure 1.1: Examples of globular clusters. *Top:* A *Hubble Space Telescope* (*HST*) image of the Galactic GC M15, which is one of the targets studied in this thesis. *Bottom:* An *HST* image of the elliptical galaxy NGC 1407, from W.E. Harris. The image has been enhanced to show the star-like GCs around the large galaxy. Note that the field stars in NGC 1407 cannot be resolved, i.e. they cannot be separated from the stars around them.

stars[4] in a galaxy (Harris, 2000). Figure 1.1b shows an image of the distant elliptical galaxy NGC 1407—its GC system can clearly be seen surrounding the galaxy at the centre, with each GC appearing almost like a star, or point source.[5]

GCs are excellent targets to probe the stellar content of distant galaxies, for several reasons:

1. They are ubiquitous in all galaxy types (above a certain mass), suggesting that GC formation must be a natural part of the galaxy formation process.

2. They are plentiful in massive galaxies, which means that there are many of them to observe.

3. They are bright. Since they are compact clusters of stars, they are brighter than individual stars and can be seen at much further distances. In Figure 1.1b the individual GCs can easily be seen, while the galaxy's field stars cannot be resolved.

4. Most (but not all) GCs seem to be old (see Chapter 1.2). The oldest GCs were around at the earliest stages of galaxy formation and should provide information about the earliest stages of star formation in their birth environments. Any young GCs should also offer valuable constraints on the star formation history in a particular galaxy.

5. GCs have a range of metallicities,[6] just like the field stars in a galaxy. Thus, GCs should trace the properties of the various field star subpopulations.

6. They are (approximately) simple stellar populations. Because the stars in the cluster formed out of the same cloud of gas and dust at roughly the same time, all the stars should have similar chemical compositions and ages (although chemically distinct populations *are* found in all GCs; see Chapter 1.2.4). This

[4]Field stars are stars in a galaxy that are not associated with star clusters; the Sun is an example of a field star.

[5]Note that the MW and M31 (the spiral galaxies whose GCs are observed in this thesis) have very different morphologies, star formation histories, stellar populations, and GC systems than the massive elliptical NGC 1407 (see, e.g., Harris et al. 2006).

[6]Astronomers define "metals" as elements heavier than helium. A star's metallicity describes the amount of metals present in the stellar atmospheres. This quantity can be represented in several different ways. This thesis primarily utilizes [Fe/H], a logarithmic ratio of the amount of Fe compared to H, compared to the Sun. A star with [Fe/H] = 0 has the same metallicity as the Sun, while a star with [Fe/H] = −1 has one-tenth the amount of iron that the Sun has.

point will be essential for observations of distant galaxies like NGC 1407, whose GCs must be studied through integrated light (see Chapter 1.4).

The only resource available for studying most distant objects is their light—in the case of GCs, this light comes from the stars. Light can be studied in many different ways; this thesis focuses primarily on spectroscopy, which will be described in Chapter 1.3. However, the work in this thesis also relies heavily on photometry, which is introduced in Chapter 1.2.

1.2 Photometry of GCs

Photometry involves determining how bright stars appear in various filters, e.g. by measuring apparent magnitudes in the Johnson's visual filter, V. GCs are particularly useful for these types of studies—because the stars in a GC are all at the same distance (assuming the depth of a GC is insignificant compared to its distance from the Sun) any apparent brightness differences indicate absolute brightness differences. Furthermore, comparisons of stellar magnitudes in different filters provide an indication of stellar colour (e.g. $V - I$). Since colour is related to temperature, these colour differences indicate intrinsic temperature differences. Figure 1.2 shows Colour-Magnitude Diagrams (CMDs) of the Galactic GCs 47 Tucanae (47 Tuc) and M13, two GCs that are studied in this thesis—note that the apparent magnitudes have been shifted to absolute magnitudes[7] to facilitate comparisons between the two GCs.

1.2.1 Colour-Magnitude Diagrams

Figure 1.2 shows that the stellar distributions in the CMDs are not random. In fact, a star's location in a CMD is related to its location in a Hertzprung-Russell Diagram (HRD, which typically plots stellar luminosity versus temperature) and is based on the physical processes occurring in the stellar interior. The different subpopulations are identified in Figure 1.2 and are described below. Note that the high mass stars in Galactic GCs have already evolved; the descriptions below only apply to low mass stars ($M \lesssim 2$ M$_\odot$)[8], as discussed later.

[7] A star's absolute magnitude is the magnitude the star would have at a distance of 10 pc.

[8] The symbol $\odot$ is the Solar symbol; thus, 1 M$_\odot$ is the mass of the Sun.

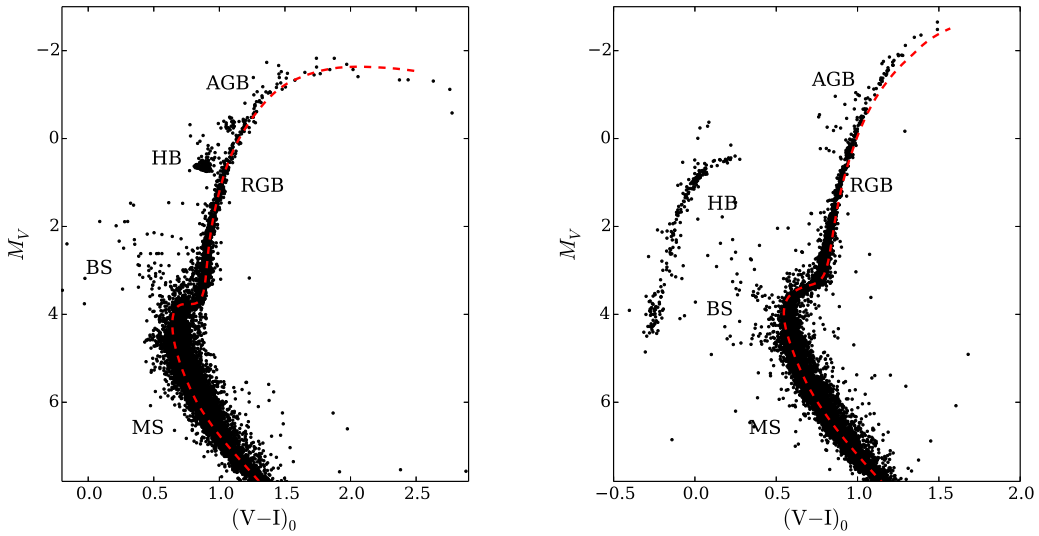

(a) 47 Tuc: A metal-rich GC

(b) M13: A metal-poor GC

Figure 1.2: CMDs of the Galactic GCs 47 Tuc and M13 from the ACS Globular Cluster Treasury (Sarajedini et al., 2007; Anderson et al., 2008). The stellar absolute magnitudes in the Johnson's visual V filter, M_V, are shown on the y-axis; note that a lower magnitude indicates a higher luminosity (or brightness) such that brighter stars appear at the top. The x-axis shows the difference between magnitudes in the V and I filters (where the I filter is redder than the V filter). Redder colours are in the positive x-direction. The main features of a CMD are identified, where MS = Main Sequence, RGB = Red Giant Branch, HB = Horizontal Branch, AGB = Asymptotic Giant Branch, and BS = Blue Stragglers. Overplotted in red are Victoria-Regina Isochrones (VandenBerg et al., 2000, 2006) with the parameters listed in VandenBerg et al. (2013). Note that the slopes of the RGB and the HB morphology differ between the two GCs.

Main Sequence (MS) Stars on the MS are fusing hydrogen into helium in their cores via the proton-proton cycles (and possibly the CNO cycles,[9] where the relative contributions from the two processes depend on the central temperature, which is dictated by stellar mass.) Over its main sequence lifetime the core is converted into a He rich core. The increased mean molecular weight of the core lowers the pressure, and the core collapses slightly as a result—this collapse increases the core temperature, which accelerates the H fusion. The outer layers of a MS star therefore expand slightly as it ages.

The MS is roughly linear in an HRD, where high mass MS stars are hotter and brighter and low mass MS stars are cooler fainter. Higher mass stars burn through their fuel faster and thus have shorter MS lifetimes than low mass stars. A GC younger than 47 Tuc would therefore have MS stars that extend more to the top left. Stars on the MS are dwarf stars.

Subgiant Branch (SGB) and Red Giant Branch (RGB) Eventually a star exhausts all the hydrogen fuel in its core and can no longer produce energy through fusion at its centre—the core of a low mass star then becomes degenerate.[10] The H-rich shell around the core has heated up enough to begin shell H fusion, which produces additional energy and makes the star brighter. The outer layers of the star expand even more, the surface temperature of the star drops, and the star moves off the MS—this point is known as the MS turnoff. The star then moves onto the SGB. The star then moves upward onto the RGB, becoming a *giant*.

The brightest stars in a GC are found at the tip of the RGB. For this reason they are typically the most frequently observed stars for individual stellar spectroscopy (see Chapter 1.3). Note that the precise location/shape of the turnoff, SGB, and RGB depend on stellar chemical composition (see Figure 1.2, Chapter 1.3.4, and, e.g., VandenBerg et al. 2012).

Horizontal Branch (HB): Eventually the core heats up to a temperature where it is possible to fuse helium into carbon (via the triple-α process). This switch to He fusion occurs almost instantaneously throughout the degenerate core in a thermal runaway process and is known as the helium flash. Once the core can

[9]Note that CNO = carbon, nitrogen, and oxygen. In this thesis elements will often be referred to by their chemical symbols.

[10]A degenerate gas obeys quantum mechanical properties; for instance, the gas density is only mildly sensitive to temperature.

again fuse material, the star stabilizes and settles onto the HB.

It is evident from Figure 1.2 that the morphology of the HB can vary between clusters. In a cluster like 47 Tuc the HB is fairly red and close to the RGB, while in M13 the HB stars extend far to the blue and drop down to very faint magnitudes. Many factors can influence HB morphology. The primary driver is metallicity, with more metal-poor GCs having bluer HBs (Arp et al., 1952; Sandage, 1953). However, metallicity alone cannot reproduce the HB morphologies observed in all Galactic GCs; age or helium abundance may also contribute to the shape of the HB (e.g. Sandage & Wallerstein 1960, Sandage & Wildey 1967, Dotter et al. 2010, VandenBerg et al. 2013).

Asymptotic Giant Branch (AGB): When a HB star exhausts the helium in its core it goes through a similar process as when it was a SGB/RGB star. The core contracts and the star moves up the AGB (so named because it approaches the RGB). The stellar evolution becomes much more complicated during this phase. If a star is massive enough it may ignite carbon burning in its core and start another round of fusion; helium and hydrogen shell burning may also occur outside of the core. Regardless of whether or not additional burning can occur, eventually the core cannot fuse any more material, and it contracts and becomes an electron-degenerate white dwarf. When the outer layers are shed in a planetary nebula,[11] the core remains hot but becomes considerably fainter. The white dwarf will slowly cool over time.

If a white dwarf is in a binary system, it can accrete material from a stellar companion. As this accretion proceeds, eventually the electron degenerate white dwarf will reach a critical mass (the Chandrasekhar mass) and will explode as a Type Ia supernova (SN). The type of companion necessary to trigger a Type Ia supernovae (SNe) is still unknown, but leading theories suggest it could be a main sequence star, an RGB star, or another white dwarf.[12]

Blue Stragglers (BSs): Blue stragglers are stars that look like they lie on the MS, blueward of the turnoff. Because MS stars of that temperature should already have evolved to the RGB, these stars are known as blue stragglers. They are

[11]The term "planetary nebula" is a bit of a misnomer, as the process has nothing to do with planets; however, planetary nebula can resemble planets when seen through small telescopes.

[12]However, the precise mechanisms for mass transfers and white dwarf detonation are not yet well understood.

believed to be caused by binary evolution or stellar mergers, which makes them appear brighter and bluer than the individual stars (see, e.g., Leigh et al. 2013).

The above processes only apply to stars with masses $\lesssim 2$ M$_\odot$. Stars with intermediate masses ($2-8$ M$_\odot$) will evolve slightly differently (see Herwig 2005); in particular they will not develop a degenerate core after core H exhaustion, and He will ignite quiescently. Though the basic evolutionary processes are the same for more massive stars, a star more massive than ~ 8 M$_\odot$ will experience more rounds of burning and will have a completely different evolutionary path that will likely culminate in a Type II SN.[13]

1.2.2 The Effects of Chemical Composition

A star's evolutionary path through an HRD varies slightly depending on its chemical composition. For example, MS stars with higher helium have a higher molecular weight at their centres, which drives up the central temperature and the rate of H burning. Thus, a star with higher helium will be hotter and bluer.[14] The most important variations occur because of cluster metallicity. Stars with higher metallicity will be slightly redder, particularly in photometric filters that are sensitive to certain spectral features. Figure 1.2 shows two clusters with different metallicities; the slopes of the RGBs are particularly sensitive to the overall metallicity, with the more metal-poor GC, M13, having a straighter and taller RGB than 47 Tuc. Thus, the stellar abundances strongly affect a star's observed brightness and colour.

1.2.3 Isochrone Fitting

The physical processes that occur during the various evolutionary stages can be modelled reasonably well, enabling stellar evolution tracks to be generated for stars of a given chemical composition. For example, the path of a Sun-like star (i.e. a star of Solar composition with $M \approx 1$ M$_\odot$) through these different evolutionary stages is shown in Figure 1.3. The Sun spends most of its life on the MS. After ~ 10 billion years the Sun exhausts its core hydrogen supply and moves onto the RGB. Eventually

[13]Core collapse SNe are typically referred to as Type II SNe, although Type Ibs and Ics are also core collapse SNe. The I vs. II distinction is based on the presence of certain spectral features rather than the physical mechanisms behind the explosion.

[14]Note that a given star's central He abundance also increases as it ages on the MS, and the star will therefore become bluer as it ages.

it will move onto the HB, then the AGB, and will become a white dwarf. The Sun does not have a stellar companion, and will not explode as a Type Ia SN.

Given its position in an HRD, a star's mass, chemical composition, and (possibly) age can be roughly determined, depending on the type of star; furthermore, given its distance[15] and reddening,[16] a star's position in a CMD can be used to infer its approximate mass, chemical composition, and age (though this process is complicated by uncertain physics, chemical differences, rotation, the presence of binary companions, etc.). GC stars form from (approximately) the same cloud of gas and dust at roughly the same time and at the same distance. Thus, all the stars in a GC should have about the same chemical composition, age, distance, and reddening, and the only differences in stellar brightness and colour will be due to mass differences.[17] An *isochrone* is a model with a single age and chemical composition that predicts the locations of stars of a variety of masses (see the red dashed lines in Figure 1.2). Fitting a model isochrone to an observed CMD therefore gives an indication of the age and metallicity of a GC, assuming an estimate of the distance and reddening can be obtained.[18] This thesis utilizes high quality CMDs of all target GCs to estimate ages and metallicities before chemical abundances are determined.

1.2.4 Multiple Populations

This simple picture of GCs as single stellar populations whose stars have the same age and chemical composition is not entirely accurate. High quality CMDs of many GCs reveal splits in the MS, SGB, and/or RGB populations, implying that there are composition differences between stars in the same GC. The magnitude of the splits depends on the filters used, since different filters are sensitive to certain spectral features. Notable splits are seen in massive clusters like ω Cen, which has multiple MS, SGBs, and RGBs—these splits may be due to variations in He and CNO (e.g. Herwig et al. 2012). Less massive clusters have broadened CMDs, which may be due

[15]The distance of a star is typically expressed as the difference between its apparent and absolute magnitudes. This distance modulus, $(m-M)_V$, is often expressed in the Johnson's visual filter, V.

[16]Reddening is caused by dust in front of the stars; the dust scatters blue light more than red light, and as a result the incoming light appears redder than it should be. This reddening is typically expressed as $E(B-V)$.

[17]Of course, recent observations have shown that this is *not* the case, as many GCs show evidence for multiple populations; see Chapter 1.2.4. However, these chemical differences often only lead to small offsets in an observed CMD.

[18]However, the metallicity is best determined though comparisons with fiducials from well-studied, Galactic GCs.

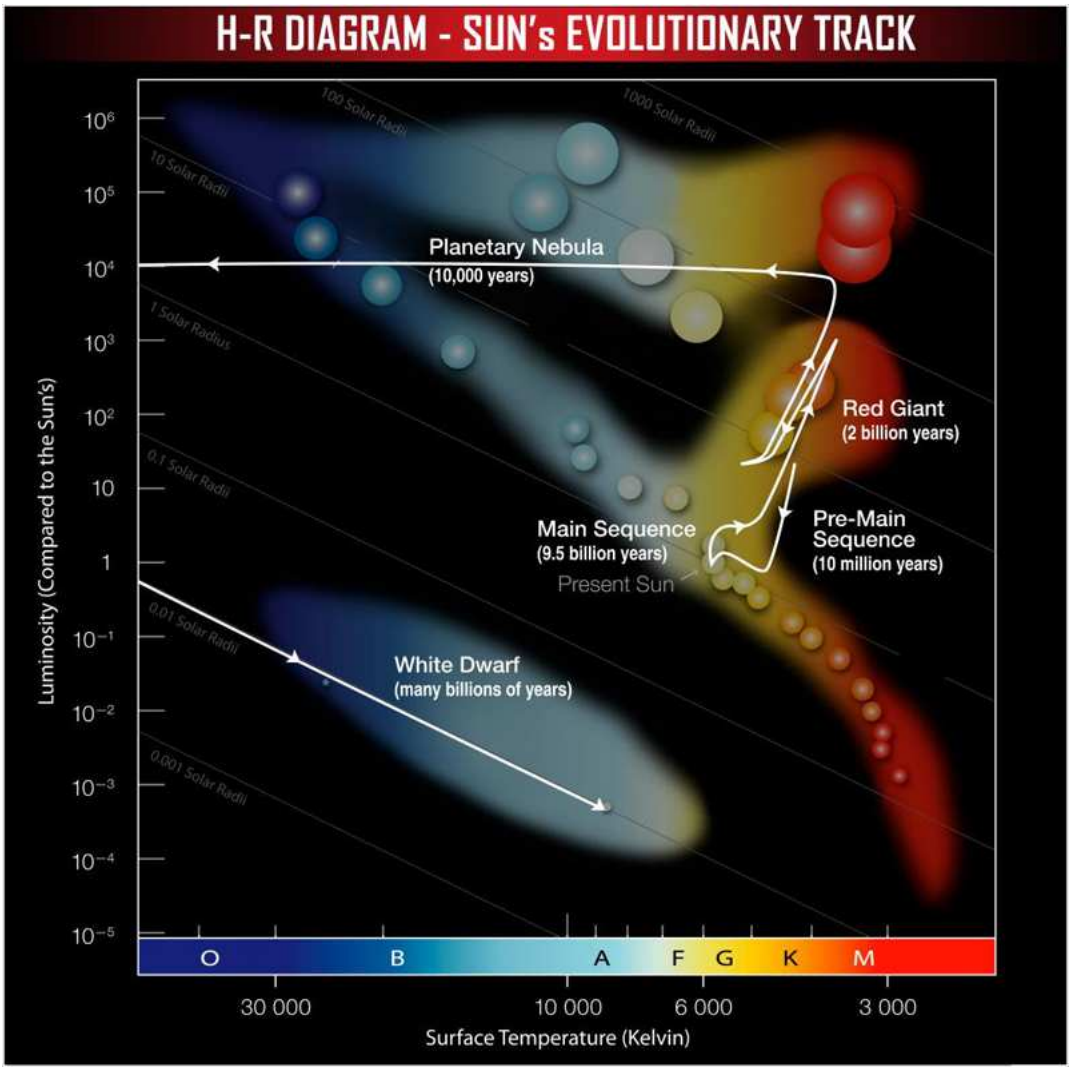

Figure 1.3: The path of a sun-like star across an HRD (image credit: NASA/CXC/SAO). Also shown is a full main sequence, with the highest mass stars at the bright and blue end and the lowest mass stars at the red and faint end.

to CNO variations (e.g. 47 Tuc; Milone et al. 2012; M3 and M13, Zhao & Bailyn 2005). These chemical composition differences have been verified by high resolution stellar spectroscopy (see Chapter 1.3) and indicate that GCs host multiple stellar populations. Furthermore, while these populations may have formed at different times, the age differences between the populations cannot be significant; otherwise, multiple MS turnoffs would be detectable.

1.3 Stellar Spectroscopy

This thesis utilizes high resolution spectroscopy to determine detailed chemical abundances of stars. This section introduces the concepts behind stellar spectroscopy, including the theory of spectral line formation (Chapter 1.3.1), the determination of chemical abundances (Chapter 1.3.2), the nucleosynthetic origins of the elements that create the spectral lines (Chapter 1.3.3), how stellar abundances evolve over time (Chapter 1.3.5), and how chemical abundances can be used to infer the formation history of a galaxy (Chapter 1.3.6).

1.3.1 Spectral Line Formation

The basic purpose of a spectrograph is to take an incoming beam of light and disperse it so that the stellar intensity can be investigated as a function of wavelength. The distribution of starlight at each wavelength is typically approximated by a *blackbody* function, where a "blackbody" is an object that absorbs all incident light and perfectly re-emits it in all directions. The blackbody function, or Planck function, describes the intensity of light at a given wavelength (λ), and is represented by:

$$B(\lambda) = \frac{2hc^2}{\lambda^5} \frac{1}{e^{hc/\lambda kT} - 1} \tag{1.1}$$

where h is Planck's constant, c is the speed of light, k is Boltzmann's constant, and T is the temperature of the blackbody, which in stars is the "surface" temperature, or *effective temperature*, $T_{\rm eff}$. The peak of this function is determined by Wien's Law, which depends only on a star's temperature $T_{\rm eff}$:

$$\lambda_{\rm max} = \frac{2.8978 \times 10^{-3}\ {\rm m/K}}{T_{\rm eff}}. \tag{1.2}$$

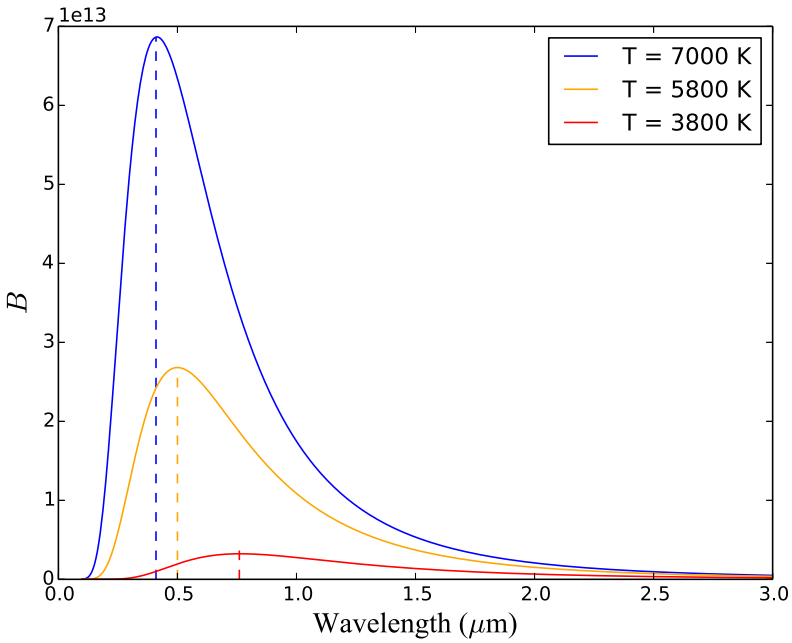

Figure 1.4: Examples of Planck (i.e. blackbody) functions for MS stars of three different effective temperatures. The peaks are shown with dashed lines; note that cooler stars have redder peaks than hotter stars.

The Planck function therefore describes the basic shape of a star's spectral energy distribution (see Figure 1.4).

The light observed from a star is produced through fusion deep in the star, where the temperatures are high.[19] The high temperatures required for fusion are *not* the surface temperatures that produce the observed blackbody function. The photons created during the fusion cannot travel straight through the star's outer layers. Deep in the star the layers are *optically thick*, meaning that the incoming radiation is completely absorbed and/or scattered. The outgoing light can escape the star once the outer layers become *optically thin*, i.e. once most of the light can pass through the outer layers because they no longer behave like perfectly absorbing blackbodies. The light still has to travel through the optically thin stellar atmosphere, which is composed of atoms, each of which has a nucleus (made of one or more protons and possibly neutrons) and electrons (unless the atom is *ionized*).[20] For atoms with

[19]The type and location of this fusion depends on the star that is being observed, as described in Chapter 1.2.

[20]A neutral atom has no net charge, and therefore has the same number of electrons (with negative

electrons, the electrons can only occupy certain energy levels. If a photon encounters the atom and has the precise energy an electron needs to move to another level, the electron will absorb that energy from the photon and change its level. The energy of light corresponds to a specific wavelength, and is given by:

$$E = hc/\lambda. \tag{1.3}$$

Since electrons can only absorb at certain energies, they will remove intensity from the blackbody spectrum at certain wavelengths; these darker parts of the otherwise bright spectrum are the *absorption lines*, which will appear on top of the blackbody function in Figure 1.4. The precise energies differ between elements and between ionization states (e.g. Fe I has different absorption lines from Fe II).

In this idealized picture an absorption line should form at a single wavelength. In practice, however, the shapes of stellar spectral lines are much more complicated. The atmosphere is composed of gas with macroturbulent (i.e. large scale) and microturbulent (i.e. small scale) motions, which leads to velocity dispersions that broaden out the spectral lines, giving each line a Gaussian shape. The star may be rotating, which further broadens the lines. Atomic physics also says that the absorption energies (and therefore the wavelengths of the transitions) are not perfectly constrained because of the Heisenberg Uncertainty Principle:

$$\Delta E \Delta t \geq \hbar/2, \tag{1.4}$$

where E is the energy of the photon, t is the time that the electron remains in the level waiting to be absorbed, and $\hbar$ is $h/2\pi$. This *natural* broadening adds Lorentzian wings to the Gaussian spectral lines. Other effects (e.g. hyperfine structure; see Chapter 3.3.4) also affect the shapes of spectral lines.

1.3.2 Determining Abundances from Spectral Lines

The more atoms present in a stellar atmosphere, the more light that can be absorbed; the more light absorbed, the darker the spectral lines. The strength of an absorption line therefore depends on the *abundance* of an element (as well as the properties of

charge) as protons (with positive charge). A singly ionized atom has lost one of its electrons. These different configurations are denoted with roman numerals, e.g. Fe I is neutral, while Fe II is singly ionized. etc.

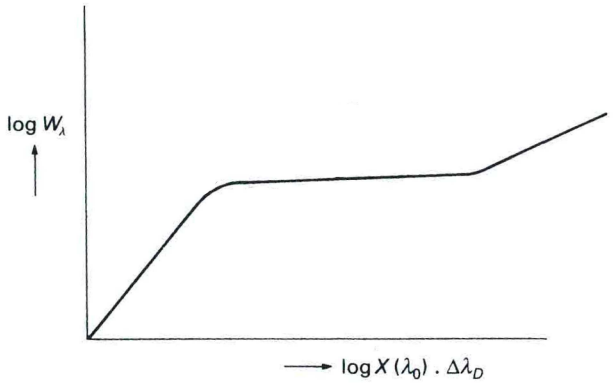

Figure 1.5: The Curve of Growth (modified from Böhm-Vitense 1989), which relates the strength of a spectral line (here expressed as the equivalent width (EW), here denoted as W_λ; see Chapter 3 and Appendix C) to the number of atoms per cm^3 in the stellar atmosphere (here N is included in the quantity $X(\lambda_0)$).

the star, such as temperature). The relation between the strength of a line and the number of absorbing atoms, N, is known as the Curve of Growth (CoG, shown in Figure 1.5). If N is small the amount of absorption is small, and the line strength increases linearly with N. As N increases the line becomes *saturated*, meaning that it reaches its maximum depth. At this stage the CoG flattens considerably, since adding more atoms does not change the strength of a line significantly. As N increases even more, the Lorentzian wings in the outer regions of the spectral line become important, and the CoG again steepens. The precise strength of a spectral feature also depends on other properties. Hidden in the parameter $X(\lambda_0)$ (the x-axis in Figure 1.5) are other parameters, including atomic data about the spectral line itself (e.g. the excitation potential of the line, χ) and atmospheric parameters of the star (such as temperature and surface gravity).

A spectral line comes from a single electronic transition between two specific energy levels in an element with a certain number of electrons (i.e. in a certain ionization state). Strictly speaking, the strength of a single line only provides information about the number of absorbing atoms *in that ionization state* and *with the electrons at the right energy level.* Assuming that the stellar atmosphere is in Local Thermodynamic Equilibrium (LTE) the number of atoms with electrons in a given level a can be

compared to the number with electrons in level b through the Boltzmann Equation:

$$\frac{N_b}{N_a} = \frac{g_b}{g_a} e^{-(E_b - E_a)/kT} \tag{1.5}$$

where g_b and g_a are the statistical weights[21] of levels b and a, E_b and E_a are the energies of those levels, k is the Boltzmann constant, and T is the temperature.

The Saha Equation describes the number of atoms, N, in ionization state $i+1$ compared to those in ionization state i:

$$\frac{N_{i+1}}{N_i} = \frac{Z_{i+1}}{Z_i} \frac{2}{n_e h^3} (2\pi m_e kT)^{3/2} e^{-(E_{i+1} - E_i)/kT} \tag{1.6}$$

where Z_{i+1} and Z_i are the partition functions[22] for ionization stages $i+1$ and i, n_e is the number of electrons in a given layer, m_e is the mass of the electron, k is the Boltzmann constant, and T is the temperature of the layer. Together, Equations 1.5 and 1.6 give the relative numbers of atoms in various electronic configurations. Combined with the CoG and a measurement of a single line from a single transition, the total abundance of a given element can be deduced.[23]

To summarize, the abundance of some element X in a stellar atmosphere can be determined from a spectrum with the following steps:

1. Measure absorption features that are caused by element X.

2. Use the CoG to determine the abundance of element X (in a particular ionization state and with an electron in the necessary level) necessary to reproduce the strength of the observed line.

3. Use the Boltzmann and Saha Equations to determine the total abundance of element X.

The last two steps are typically coded into line analysis codes, such as `MOOG` (Sneden, 1973, see Chapter 3).

[21] A statistical weight describes the number of ways an atom can have electrons in the necessary configuration.

[22] The partition function describes the number of ways an atom can be in the correct ionization state.

[23] Of course, this framework assumes LTE, and does not take radiative processes into account. Occasionally these non-LTE processes are significant, and corrections must be made to the abundances (e.g. Mashonkina et al. 2000, Lind et al. 2011).

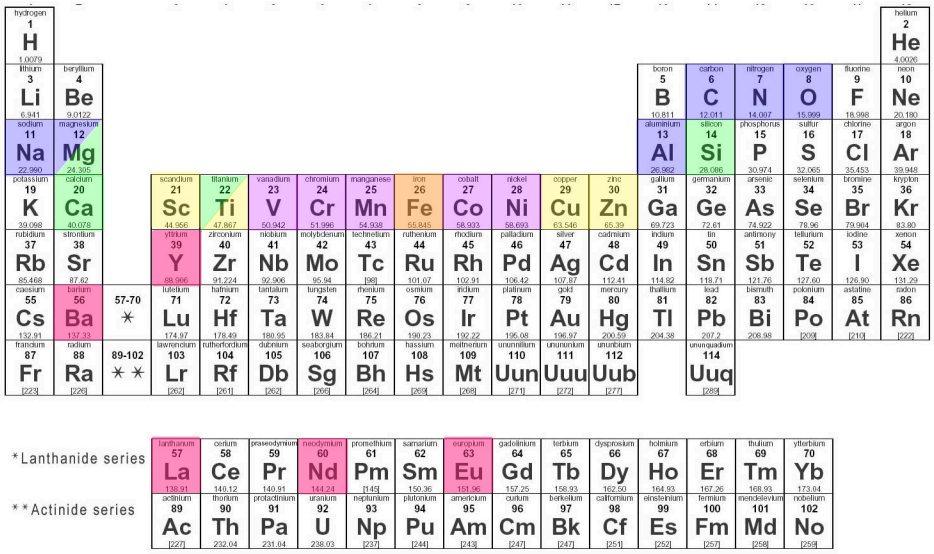

Figure 1.6: A periodic table showing the elements utilized in this thesis' high resolution spectroscopic analyses. The elements have been grouped by element type and/or common nucleosynthetic sites. The metallicity indicator, Fe, is shown in orange. The light elements with multiple formation sites (C, N, O, Na, Al) are shown in blue, α-elements (Mg, Si, Ca, Ti) are in green, iron-peak elements (V, Cr, Mn, Co, Ni) are in purple, neutron capture elements (Y, Ba, La, Nd, Eu) are in pink, and elements with ambiguous or uncertain formation sites (Sc, Cu, Zn) are shown in yellow.

1.3.3 Interpreting Chemical Abundances

The abundances of individual elements provide different clues to the formation and evolution of a cluster. Certain elements are more scientifically useful for spectroscopic studies, depending on their nucleosynthetic origins, their dependence upon galaxy properties, and whether or not they have observable spectral lines. Figure 1.6 shows a periodic table, highlighting the elements investigated in this thesis.

The early universe was composed mostly of hydrogen, with trace amounts of helium, lithium, and beryllium (Coc, 2009). All the elements heavier than this must have been created in stars and distributed into the interstellar medium via supernovae or stellar winds.[24] The formation sites of elements can vary, and the dominant formation sites for each element are not always well constrained (the ambiguous elements are labeled in yellow in Figure 1.6). In order for spectral lines to be visible, the

[24]Although a few elements can form from spallation, such as B.

elements must be present in the stellar atmosphere. The elements that are visible in a spectrum must either *a*) reflect the abundances that the star had when it formed, or *b*) be fusion products that have been mixed (or dredged) up to the surface during the star's evolution.[25]

Light elements: The light elements (C, N, O, Na, and Al) are grouped together as elements which form (and can be destroyed) in various processes. The C, N, and O abundances are altered during H burning via the CNO cycle, which converts H into He using C, N, and O as catalysts. C is created during He burning, where O may also be created. In more massive stars subsequent rounds of C and Ne burning also create the light elements. Many of the light elements can also be created in the envelopes of AGB stars, which have strong winds that blow this enriched material out into the interstellar medium. This processed material might seed primordial variations in a second population of GC stars (Conroy & Spergel, 2011) which would be enhanced in some of these light elements (leading to the multiple populations described in Chapters 4.6.4 and 1.3.4).

α-elements: These elements form via the capture of a ^{4}He nucleus (also known as an α particle). This mainly happens during burning in massive stars, and the α-elements are subsequently released into the interstellar medium by Type II supernovae; however, some of these elements can also be created during Type Ia SNe (e.g. Ca; see Wanajo et al. 2013). Here Mg, Si, Ca, and Ti are identified as α-elements. However, the Mg abundance can also be altered in AGB stars, and may therefore be more similar to the light elements. Ti is another uncertain element which likely has multiple formation sites—however, in many cases it seems to trace the α-elements, and it is therefore frequently used as an α-indicator.

Fe-peak elements: These elements (located in the same general region of the periodic table as Fe) are thought to form in both Type II and Ia supernovae. The relative contributions from each supernova type are not well known, but models suggest that for metal-rich GCs Type Ia supernovae should be the dominant contributor of Fe-peak elements (Iwamoto et al., 1999).

Neutron capture elements: These elements are formed when the nucleus of a

[25]Though note that diffusion (the settling of heavy elements) can remove certain elements from the atmospheres.

lighter atom captures neutrons, increasing the weight of the nucleus. These heavy nuclei are unstable, and will decay. By emitting an electron or positron (i.e. by undergoing β- or β^+-decay, which changes the nucleus' charge) the nucleus can either decrease or increase its atomic number Z, shifting the atom to the left or right in the periodic table. If the charge of a nucleus keeps increasing, new elements are created in this process.

The types of atoms that are created during neutron capture depend on the speed at which the lighter atom is bombarded with neutrons.

rapid (r-) process: The r-process elements are created when the nucleus is bombarded rapidly with neutrons and does not have time to decay between bombardments. Thus, heavier (higher-Z) elements can be created in this process. Rapid bombardment requires a high neutron flux, which is found in energetic events; supernovae are thought to be the source of the r-process.

slow (s-) process: The s-process elements are created as a nucleus is slowly bombarded with neutrons. During each encounter the nucleus has time to decay, meaning that the heaviest (high-Z) elements are not typically created in this process. The main source for the s-process may be AGB stars; the s-process elements are then distributed into the interstellar medium via stellar winds.

Stars create the neutron capture elements via *both* processes, with the relative contributions from the r- and s-processes varying with metallicity (recall that the contributions from AGB stars will increase with age as the stars in a system evolve). At Solar metallicity some elements are dominantly r-process elements (e.g. Eu, which is 97% r-process; Burris et al. 2000), which suggests they should be purely from the r-process at lower metallicities. The other frequently studied neutron capture elements (Y, Ba, La, etc.) form in both r- and s-processes.

1.3.4 Globular Cluster Abundances

Spectroscopic investigations of stars in GCs have confirmed the photometric results described in Chapter 1.2.4, namely that GCs are *not* simple stellar populations with a uniform chemical composition. All bona fide Galactic GCs show star-to-star Na and O variations (e.g. Carretta et al. 2009a, 2010b), while many show Mg and Al

variations (Carretta et al., 2010b). Some GCs also have variations in neutron capture elements as well (such as Ba, La, and Eu; Sneden et al. 1997; Roederer 2011). Several of the most chemically unusual GCs are hypothesized to be the cores of accreted dwarf galaxies, notably ω Cen (though see the discussion in Johnson & Pilachowski 2010) and NGC 2419 (Cohen & Kirby, 2012). However, the vast majority of GCs are thought to be star clusters (not dwarf galaxies) with two chemically distinct populations: one with "primordial" abundance patterns, the other with enhanced He, Na, Al and depleted O and Mg. Furthermore, the spatial distributions of the two populations are different, with the chemically unusual population appearing to be more centrally concentrated (e.g. Kravtsov et al. 2011; Johnson & Pilachowski 2012; Cordero et al. 2014).

The source of the this additional chemical processing is not yet completely understood, though rapidly rotating massive stars (Decressin et al., 2007), AGB stars (Ventura & D'Antona, 2009, 2011), and supermassive ($\sim 10^4$ $M_\odot$) stars (Denissenkov & Hartwick, 2013) have all been proposed. The mechanisms for forming two distinct populations are unclear, though some models suggest that the two populations represent two different generations of stars, with one forming out of the chemically enriched products of the other.

Some elements do not seem to vary between stars in a given GC. Carretta et al. (2010a) find small (< 0.03 dex) Ca variations in their sample of 17 Galactic GCs. Iron seems to be constant in many GCs (e.g. the 19 in the Carretta et al. 2009b sample; M92, Cohen 2011; NGC 2419, Cohen & Kirby 2012). While some GCs do seem to exhibit variations in, e.g., Ca and Fe, these variations are typically lower than the errors in the measured abundances (e.g. NGC 6752, Yong et al. 2013). For those elements that are not expected to vary significantly between the two populations, the GC abundances trace the abundances from the birth environment (Pritzl et al., 2005), suggesting that in spite of the star-to-star variations, GCs can be used to trace the stellar populations in a galaxy.

1.3.5 Chemical Evolution

The earliest stars must have been composed of only hydrogen, helium, lithium, and beryllium (since those were the elements created during Big Bang Nucleosynthesis; Coc 2009). These first stars created the first metals and seeded the second generation stars, which had only trace amounts of heavy elements. Over time as more stars

evolved the heavy metal content of the Universe increased and new stars became more metal-rich. The metallicity ([Fe/H]) of an isolated environment should therefore increase over time.

Furthermore, because various elements have different nucleosynthetic sites (i.e. they form in different types of stars) the relative amounts of the various types of elements change over time. The α-elements, for instance, form primarily in massive stars, which evolve quickly; Fe, on the other hand, forms in SNe from both massive and longer-lived low mass stars. The [α/Fe] ratio (the logarithmic ratio of α-elements to Fe, relative to the Sun) therefore changes with [Fe/H] (see Figure 1.7), as described by Tinsley (1979). When a system is young only core collapse (Type II) SNe occur (since the cores of lower mass stars have not yet evolved to the white dwarf phase and Type Ia SNe cannot yet occur). Both Fe and α-elements are created by massive stars, and in a young, isolated environment [Fe/H] increases while [α/Fe] remains roughly constant (at ~ 0.4 dex). Once lower mass stars have evolved to white dwarfs some will explode as Type Ia SNe, producing Fe but no α-elements. Thus, [Fe/H] continues to increase while the [α/Fe] ratio decreases. This leads to a "knee" in the [α/Fe] vs. [Fe/H] plot (seen at [Fe/H] ~ -1 for the MW stars; see the grey points in Figure 1.7).

Similar changes occur for other element ratios, such as [Ba/Eu]. Because Eu is primarily an r-process element (which is thought to form in Type II SNe from massive stars), it should be produced early on. Ba, however, forms in both the r- and s-processes. Ba will therefore form early on with Eu, leading to a certain [Ba/Eu] ratio that depends on the nucleosynthetic yields in the r-process. Once intermediate and low mass stars evolve to the AGB phase Ba has an additional formation site, and the [Ba/Eu] ratio increases as [Fe/H] increases (see Figure 1.8).

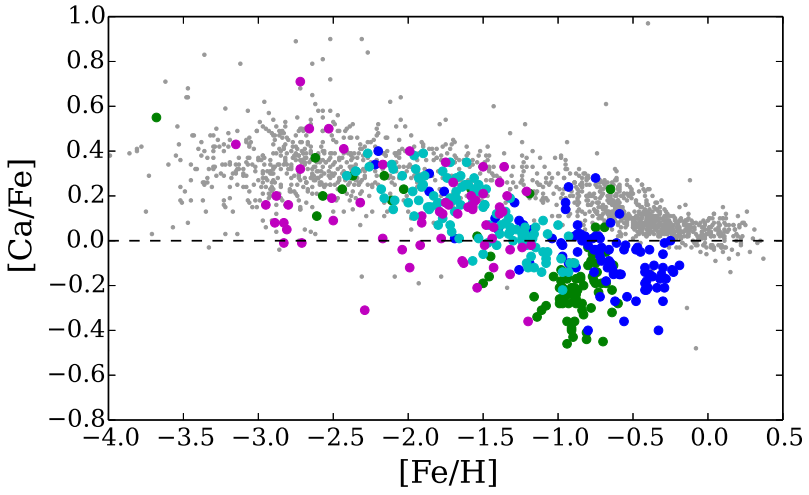

Figure 1.7: [Ca/Fe] vs. [Fe/H] for Milky Way field stars (grey points) versus dwarf galaxy field stars (coloured solid symbols). Ca is an α-element, so that [Ca/Fe] should represent the [α/Fe] ratio. MW stars are from the sources in Venn et al. (2004), with supplements from Reddy et al. (2006). Large Magellanic Cloud (LMC) stars (blue) are from Pompéia et al. (2008); Fornax stars (green) are from Tafelmeyer et al. (2010), Shetrone et al. (2003), and Letarte et al. (2010); Sculptor stars (cyan) are from Tafelmeyer et al. (2010), Geisler et al. (2005), Shetrone et al. (2003), and Frebel et al. (2010); and Carina stars (magenta) are from Venn et al. (2012), Koch et al. (2008), and Shetrone et al. (2003). At low [Fe/H] the [α/Fe] ratios are approximately constant at [α/Fe] ~ 0.4 (albeit with significant dispersion); as [Fe/H] increases the [α/Fe] ratios start to decrease. The location of this "knee" depends on the mass of the galaxy, such that lower mass galaxies have a more metal-poor knee. For instance, the MW knee occurs at [Fe/H] ~ -1, while the Sculptor knee is at [Fe/H] ~ -1.7 (Geisler et al., 2007). At a given metallicity ([Fe/H] $\gtrsim -2$), dwarf galaxy stars clearly have lower [α/Fe] values than MW field stars, which has been interpreted as a signature of slower star formation rates or missing high mass stars.

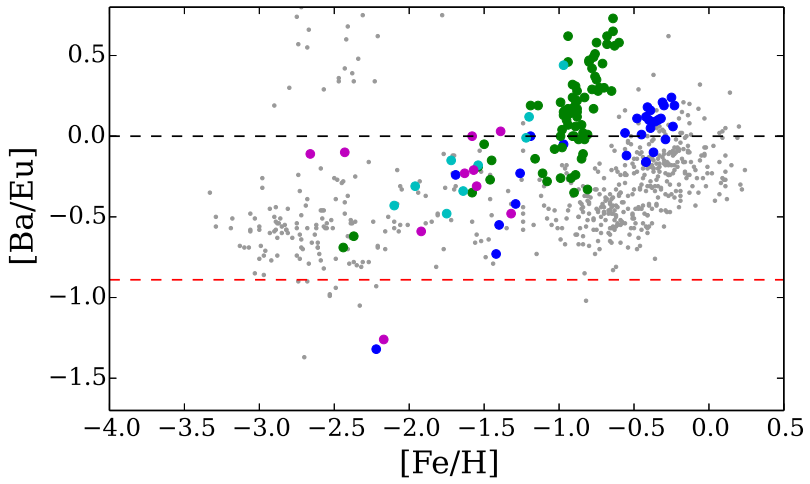

Figure 1.8: [Ba/Eu] vs. [Fe/H] for Milky Way and dwarf galaxy field stars. Points are as in Figure 1.7. The [Ba/Eu] ratio compares the s-process to the r-process; at low [Fe/H] the [Ba/Eu] ratio is low (the precise value is dictated by the r-process yields; the r-process-only [Ba/Eu] value from Burris et al. 2000 is indicated with a red dashed line). Over time Ba also forms from the s-process, and [Ba/Eu] increases with [Fe/H]. As with [α/Fe], the dwarf galaxy stars are clearly separated from MW stars for [Fe/H] $\gtrsim -2$.

1.3.6 Chemical Tagging

The precise chemical evolution of a system depends on its mass. For example, consider two galaxies of different mass. The higher mass galaxy has more stars; therefore, it will become enriched by more heavy metals as those stars evolve and die, and its future stars will be very metal-rich. The less massive galaxy will not have as many stars to enrich the remaining gas, and young stars will not be as metal-rich as stars of the same age in the massive galaxy. Thus, there is some mass-metallicity relation behind a galaxy's chemical evolution.

The [α/Fe] evolution with [Fe/H] also proceeds differently between giant and dwarf galaxies, as is evident in Figure 1.7. A similar separation occurs in [Ba/Eu] versus [Fe/H], as shown in Figure 1.8. There are two main theories for why the chemical evolution of the two systems diverges. The Tinsley (1979) model suggests that dwarf galaxies have slower star formation rates, which leads to lower [α/Fe] at a given [Fe/H]. The timescale for creating Type Ia SNe will be the same in the two environments; however, because the more massive galaxy has been able to build up to a higher [Fe/H] within that time frame, the onset of Type Ia SNe occurs *at different metallicities* in the two environments. Thus, the "knee" in the [α/Fe] plot occurs at a lower metallicity in dwarf galaxies; for instance, the Sculptor knee occurs at [Fe/H] ~ -1.7. This difference is clearly shown in Figure 1.7 and implies that in massive galaxies star formation proceeded quickly, allowing the stars to become enriched in [Fe/H] before Type Ia supernovae exploded. Dwarf galaxies, on the other hand, had a slower star formation rate and could not become as enriched in [Fe/H] before Type Ia supernovae exploded. An alternative explanation is that dwarf galaxies are deficient in the highest mass stars (e.g. McWilliam et al. 2013); in this framework, the dwarf galaxies are deficient in α-elements because they do not have enough massive stars to form the α-elements.

Regardless of the physical mechanism, the dwarf galaxy stars are chemically distinct from MW stars of the same metallicity. For metallicities [Fe/H] $\gtrsim -1.5$ dex, *dwarf galaxy stars have lower [α/Fe] and higher [Ba/Eu] ratios than their MW counterparts at the same metallicity.* These chemical differences between stars that originated in dwarf galaxies versus those from massive galaxies means that *a star's birthplace can potentially be deduced based on its chemical abundances alone.* This process of linking a star to its birth environment has become known as chemical tagging. In the Milky Way, chemical tagging has revealed that some stars and GCs that currently

reside in the MW appear to have been accreted from low mass galaxies (since their chemical abundances agree better with dwarf galaxy field stars than with Milky Way field stars; e.g. Cohen 2004; Sbordone et al. 2005b). Thus, the accretion of dwarf satellites has played some role in the formation of the Milky Way. These types of detailed chemical tagging studies have yet to be performed outside of the MW and its nearest dwarf neighbours.

1.4 Integrated Light Spectroscopy

A generalized picture of galaxy formation requires pushing observations to extragalactic[26] GC systems, particularly those associated with galaxy types (e.g. massive ellipticals) and in environments (e.g. galaxy clusters) that are not found in the Local Group of galaxies. The brightest stars in uncrowded regions can be observed as far away as, e.g., NGC 5128 (which is ~ 3.8 Mpc away), but only for photometric observations (see Rejkuba et al. 2005). Spectroscopic observations of individual stars are currently limited to the Local Group and can only be extended to the M31 systems for low to medium resolution spectroscopy ($R \lesssim 6500$; e.g. Vargas et al. 2014). These restrictions are due to two factors: the faintness of individual stars at large distances (which prohibits high resolution observations of resolvable targets), and the blending together of stellar systems. Because the individual stars in extragalactic systems cannot be *resolved* (i.e. separated from nearby stars), these systems must be studied through their *integrated* light (IL).

IL spectroscopy can be applied to galaxies and star clusters. Galaxies are difficult targets for IL observations—their complex populations with multiple ages and compositions make their integrated abundances difficult to interpret,[27] while their large velocity dispersions broaden out the lines rendering many of them undetectable. However, distant extragalactic GCs appear as bright, point-like sources and can be observed at much greater distances than individual stars (see Figure 1.1b). The flux-weighted average chemistry of a GC can therefore be determined from an IL spectrum of the entire population and these abundances can be used to infer properties of the field star populations. Information on the chemical abundance ratios for a system of GCs can then be used to study the chemical evolution and early assembly history of

[26]Extragalactic means "outside of the MW."

[27]However, massive ellipticals are typically assumed to be purely old and metal-rich, which simplifies IL analyses (e.g. Worthey et al. 2014).

the host galaxy.

1.4.1 Low to Medium Resolution Spectroscopic Observations

Low resolution IL spectroscopy has been used for about a century (e.g. Hertzprung 1915) to determine approximate abundances of stellar populations. Low spectral resolution means that individual spectral lines are blended together into broad features. Early work focused primarily on features that were believed to be sensitive to single elements.

Standard observational and analysis methods were introduced by Faber et al. (1985), who used spectra of Galactic field stars to develop a system of spectral features whose strengths were related to metallicity or age—because the calibration spectra were obtained at Lick Observatory, these features became known as the Lick indices. The Lick indices were refined and expanded by Worthey et al. (1994), who later discovered that age and metallicity can have degenerate effects on the indices (such that a young cluster's Lick indices look similar to those from a metal-poor cluster; Worthey 1994). Subsequent studies have focused on identifying and utilizing indices that break this degeneracy by being sensitive only to age *or* metallicity (such as the Fe 4668 index, which seems to be largely insensitive to age; Worthey 1994). The measured strengths of these features can then be compared to a grid (based on empirical calibrators and/or models) to determine the age and metallicity of a target (see Figure 1.9). Initially this process seemed to work well for early-type (elliptical) galaxies, at least for systems that fell in calibrated regions (e.g. Jones & Worthey 1995).

Surprising results were found when the best Lick age and metallicity indicators were applied to the Galactic GC, 47 Tuc. Gibson et al. (1999) found that Lick indices predicted an unrealistic age of 20 Gyr for 47 Tuc (see Figure 1.9), which disagrees with isochrone fits to the resolved population (Figure 1.2). Furthermore, though age determinations greater than the age of the Universe are not necessarily problematic given the often significant systematic errors, there is no reason why 47 Tuc would be much older than the early-type galaxies. This suggested that the fine details in index calibrations can be extremely important. For example, Vazdekis et al. (2001) showed that including α-enhancement in the input models could bring 47 Tuc's age down to 11 Gyr, which is back in agreement with isochrone fits. The fact that this small level of detail can make such a difference in the derived ages illustrates the difficulty of

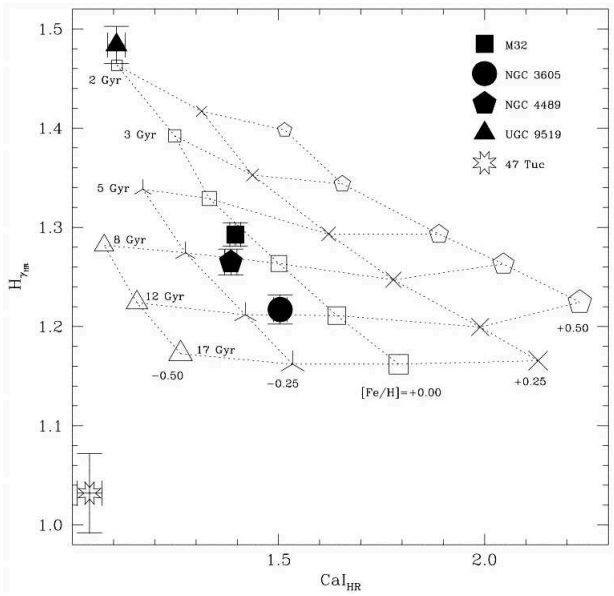

(a)

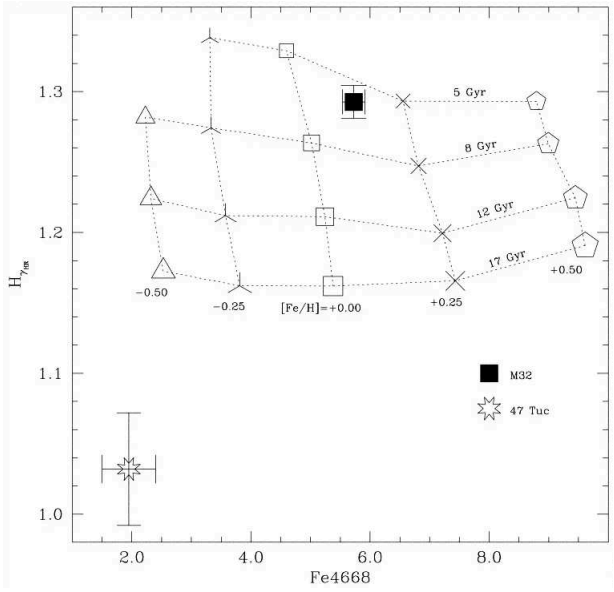

(b)

Figure 1.9: Plots of an age sensitive Lick index ($H\gamma_{HR}$) versus two different metallicity sensitive Lick indices (Ca_{HR} on the top and Fe4668 on the bottom), from Gibson et al. (1999). The black symbols are different galaxies, while the open symbols represent intersecting grid points from the different models. The open star (which lies off the grid) represents the globular cluster 47 Tuc. Note that the predicted age for 47 Tuc is at least 20 Gyr, which is much older than the early-type (elliptical) galaxies.

applying such complicated techniques to unresolved systems with little or no *a priori* constraints.

Since then, a significant number of studies have attempted to investigate, quantify, or avoid the effects of complicated details. These tests have been performed on well-studied Galactic GCs, nearby extragalactic GCs, early-type galaxies, and synthetic populations. Some particularly notable details include:

Abundance sensitivities: Because Lick indices are blends of multiple features, indices can be sensitive to multiple elements, even if an index is dominated by one element. For example, C and Mg abundances can affect certain Fe-dominant indices (Tripicco & Bell, 1995; Korn, Maraston, & Thomas, 2005; Lee et al., 2009). This means that multiple abundances must be determined at once, or that other features have to be examined.

Missing stellar subpopulations: Stellar models cannot yet perfectly reproduce all the stars in a simple stellar population. The most difficult stars to model are evolved AGB and HB stars and anomalous stars like BSs (since the underlying physics is complicated and cannot yet be perfectly modelled). Though there are few of these stars in a GC population (compared to the MS and RGB stars), they can have a significant effect on IL spectra. For example, if blue HB stars are not properly accounted for, spectroscopic ages will be skewed to younger ages to compensate for the absence of the hot stars (e.g. Lee et al. 2000; Ocvirk 2010).

Multiple Populations: Galaxies are complex stellar populations, meaning that they have stars of varying ages *and* chemical compositions. It is therefore unclear exactly what an integrated age or [Fe/H] means, or if they are weighted in the same way.

GCs are expected to be simpler populations, with much smaller abundance variations. As described in Chapter 1.3.4, however, it is now well-established that all bona fide GCs have significant star-to-star Na and O variations (Carretta et al., 2009a). Furthermore, large dispersions in C and N abundances are also prevalent in GCs (e.g. 47 Tuc; Briley et al. 2004). Massive GCs can even show dispersion in heavy, neutron capture elements such as La and Eu (Roederer, 2011). Thus, it is not straightforward to interpret integrated abundances, even in GCs.

Despite these (potentially) large uncertainties, low to medium resolution IL spectroscopy has proven effective at determining ages, metallicities, C, N, O, and α-abundances for GC systems (e.g. Schiavon et al. 2002; Lee & Worthey 2005; Graves & Schiavon 2008) with precisions $\sim 0.1 - 0.2$ dex.

1.4.2 High Resolution IL Spectroscopy

The first high resolution IL spectral analysis of a GC was presented by McWilliam & Bernstein (2008, hereafter MB08). Their methodology was based on the same principles as for individual stellar spectroscopy and was meant to be largely calibration-independent. Their analysis of the Galactic GC 47 Tuc showed that detailed literature abundances (from individual stars) could be reproduced by a high resolution IL analysis, *provided that the underlying stellar populations are well modelled.* Cameron (2009) applied these techniques to additional Galactic GCs, again showing that literature abundances could be recovered from a GC's IL spectrum. The high resolution techniques were then applied to more distant GCs, such as those associated with M31 (Colucci et al., 2009), the Large Magellanic Cloud (Colucci et al., 2011a, 2012), and NGC 5128 (Colucci et al., 2013)—these studies have shown that GC integrated abundances seem to agree with the expected values for field stars.

Of course, high resolution techniques are not free from uncertainties or assumptions. Galactic GCs can be well modelled because the individual stars can be resolved in high quality CMDs—however, studies of distant extragalactic GCs do not have this luxury, and any uncertainties in the unresolved populations will affect the integrated abundances. Furthermore, the fact that the IL abundances from unresolved targets *seem* reasonable does not mean that they are correct, particularly given the presence of multiple populations in GCs. Detailed integrated abundances need to be obtained for more GCs, and then compared to other independent analyses of the GC properties. Despite these current shortcomings, high resolution IL spectroscopy will become an invaluable tool for studying the detailed abundances of distant GCs.

1.5 Models of Galaxy Formation from Field Star and Globular Cluster Observations

Despite the limitations in IL techniques, previous photometric and spectroscopic observations (of individual stars and entire GCs) have provided substantial evidence for how various galaxies have formed and evolved.

1.5.1 The Milky Way

"Classical" Theories of MW Formation

The Eggen, Lynden-Bell, & Sandage (1962, ELS) model of galaxy formation is often referred to as the "monolithic collapse" model. Their photometric observations of Galactic field stars in the Solar neighborhood investigated how stellar metallicity (as determined from a star's ultraviolet excess) varies as a function of orbital properties (i.e. eccentricity, angular momentum, 3D space velocities, and maximum distance above the MW plane). Their results showed that metal-rich stars are primarily confined to the disk, have low eccentricity (mostly circular) orbits, and are rotating with the disk. Metal-poor stars, on the other hand, have a huge scatter in their kinematic properties, and it is uncertain if there is any significant correlation of metallicity with kinematics or location. If metallicity is used as a rough proxy for age, then the metal-poor stars will be older than the metal-rich stars. The ELS results therefore imply that the Galaxy must have initially formed quickly, creating metal-poor stars in the collapse of the proto-Galactic gas cloud; the metal-rich stars then formed from the remaining, enriched gas, which had sufficient time to come to dynamical equilibrium before star formation commenced (creating a rotating metal-rich population with circular orbits). Though ELS never explicitly say that the collapse must be monolithic (i.e. from a single giant cloud of gas), their model does assume that the stars formed *in situ* (in the galaxy that they will eventually be observed in).

Later observations of outer halo[28] (> 8 kpc) Galactic globular clusters (GCs) showed results that led to a different interpretation. Searle & Zinn (1978, SZ) examined *very* low resolution spectra of Galactic GC red giants in the outer regions of the GCs, and used the strength of a Ca, CH, and CN[29] blend to determine the GC metallicities. They then examined the trends in metallicity with various parameters

[28]The halo is the population of stars that are spherically distributed around the MW.

[29]Note that CH and CN are molecules.

including Galactocentric distance, $R_{\rm GC}$ (i.e. the distance from the centre of the MW). SZ found no signs of an abundance gradient in the GCs, which would have indicated formation through slow, pressure-supported collapse (because the gas slowly becomes increasingly enriched with supernovae products as it collapses towards the centre). They argued that while the ELS interpretation could still apply, a better explanation is that the outer halo stars and GCs were accreted from satellite galaxies. This theory was supported by observations of the HB morphologies in the clusters: assuming that the second parameter governing HB morphology is age (the first being metallicity; see Chapter 1.2.1), the lack of a correlation between HB morphology and [Fe/H] in the outer halo implies that the outer halo GCs must have a spread of ages, and therefore had to have formed over a longer timescale than the quick collapse required by the ELS model.[30]

Recent Simulations and Observations

The SZ formation scenario agrees with the current Cold Dark Matter (ΛCDM) model of hierarchical formation (e.g. Springel et al. 2005), where small dark matter subhaloes form early on and merge together to create larger haloes. Côté et al. (2000) demonstrate with Monte Carlo techniques that the MW and its GC system could have been build up by accretion. Cosmological simulations show that accreted stars could represent as much as 30-85% of the observed MW halo stars, depending on the merger history (Zolotov et al., 2009). The accreted stars exhibit significant, coherent substructure soon after the accretion (i.e. they will grouped into stellar streams), while *in situ* stars have little to no substructure (Bell et al., 2008). Over time this accreted substructure will be erased, and any visible structure should be only from recent accretions (Helmi & White, 1999; Johnston et al., 2008). Zolotov et al. (2009) argue that accretion should be more important in the outer halo, in agreement with the SZ observations.

Signs of accretion and substructure *have* been observed (e.g. the MW is currently accreting the Sagittarius dwarf galaxy; Da Costa & Armandroff 1995). Perfectly smooth models with no substructure are incompatible with the observed MW, suggesting that some amount of recent accretion has taken place (Bell et al., 2008). Furthermore, investigations of the Galactic GC Age Metallicity Relation (AMR) argues for the accretion of dwarf satellites and their GCs: Forbes & Bridges (2010)

[30]Recall that chemical variations are also viable candidates for the second parameter governing HB morphology; see Chapter 1.2.1.

illustrated that many GCs (including Pal 1; see Chapter 3) are younger than they should be given their [Fe/H], suggesting that they were accreted from dwarf satellites. Thus, accretion must have played some role in the assembly of the MW.

However, the vast majority of MW stars are dissimilar from the stars in current dwarf satellites. Firstly, the stellar ages in the two populations do not match: only $\sim 10\%$ of the halo could have come from modern dwarfs because there are not enough intermediate age stars in the halo (Geisler et al., 2007). Secondly, the chemical abundances between the two environments are also distinct (see Figures 1.7 and 1.8, Chapter 1.3.6, and the observations and analyses of Shetrone et al. 2001, Venn et al. 2004, Pritzl et al. 2005, and Tolstoy et al. 2009); there *are* several chemically anomalous stars in the halo (e.g. Fulbright et al. 2002; Nissen & Schuster 2011), but the vast majority of MW halo stars are *not* chemically similar to the dwarfs. Thus, it seems that MW halo stars could have originated in classical dwarfs only if they were accreted very early on, before the chemistries had time to diverge. It is also unclear how the accretion of modern dwarfs can be the dominant process for the formation of the outer halo, given the vastly different RR Lyrae periods in the two environments (Clementini, 2010). These results seem to suggest that the MW must have formed *early on* from fairly *massive* progenitors, in agreement with ΛCDM predictions.

Finally, some signatures of the monolithic collapse model have also been observed in the MW and M31, such as abundance gradients (Harris, 2000; Brodie & Strader, 2006). Based on stellar kinematics and metallicities, Hartwick (1987) and Carollo et al. (2007) have suggested that the MW may have two separate halos, a dissipative ELS-type one, and an accreted SZ-type one.

Whatever the final scenario, it appears that some aspects of both the ELS and SZ formation scenarios are necessary to create the current MW. However, a universal picture of galaxy formation requires observations of other galaxy types (e.g. massive ellipticals) and of galaxies in very different environments than the Local Group (e.g. large galaxy clusters). Thus, observations of other galaxies are necessary for truly understanding galaxy formation.

1.5.2 Other Galaxies

Observations

Observations of distant GC systems have hitherto been conducted primarily through integrated photometry and low resolution IL spectroscopy. Several key observational

findings include:

Colour/metallicity bimodality: The GC systems of most galaxies show a distinct colour bimodality, with clearly separated red and blue peaks. A wide variety of galaxies show this GC colour bimodality, including the MW (Harris, 2000), though not all galaxies have significant bimodalities. The presence of a blue population of GCs seems to be ubiquitous in all galaxies, while the fraction of red GCs in a system decreases with decreasing galaxy luminosity (such that the red peak is more difficult to detect in low mass systems; Peng et al. 2006).

The general interpretation is that the GC colour bimodality corresponds to a metallicity bimodality, where the red GCs are metal-rich and the blue GCs are metal-poor. Of course, this assumption requires that all GCs are old;[31] this is not necessarily an unreasonable assumption given the GCs in the MW, which *are* mostly old (Dotter et al., 2010) and *do* show a bimodal [Fe/H] distribution (Harris, 2000). Red and blue GCs seem to have distinct kinematics in several galaxies (e.g. in the large elliptical galaxy NGC 1399; Schuberth et al. 2010), suggesting that the red and blue GCs are from populations that had different formations histories/mechanisms. Furthermore, integrated Ca II triplet (CaT)[32] observations show a CaT-strength bimodality in the bright elliptical NGC 1407 (Foster et al. 2010; though note that no CaT bimodality was detected in another elliptical, NGC 4494; Foster et al. 2011), which implies that there is a metallicity bimodality. Finally, low-resolution IL spectra show bimodalities in Lick indices such as MgFe, a metallicity indicator (e.g. in the elliptical galaxy NGC 5128; Woodley et al. 2010).

A counter-argument for metallicity bimodalities suggests that nonlinear colour to metallicity conversions can transform a unimodal metallicity distribution into a bimodal colour distribution (Yoon et al., 2006). The colour to [Fe/H] conversion *is* suspected to be nonlinear; however, it is uncertain if this effect is enough to create the observed bimodalities, nor does this theory explain CaT, MgFe, or kinematic differences between the two populations.

Thus, observations of extragalactic GC systems imply that the colour bimodality *is* due to an intrinsic metallicity bimodality in the GC system and that

[31] Recall that young GCs have bluer MS stars—the integrated colour of a young ($\sim$ 2 Gyr) GC will therefore be bluer than an old ($\sim$ 12 Gyr) GC of the same metallicity.

[32] The CaT is a group of three strong Ca II lines (at $\sim$ 8498, 8542, and 8662 Å) that are primarily sensitive to metallicity. These features can be detected and measured at low spectral resolution.

many galaxies have two chemically and kinematically distinct populations of GCs. The ubiquitousness of the blue population suggests that every galaxy (of a sufficient mass) experienced a metal-poor SF and GC formation burst. The presence of red GCs is dependent on galaxy mass, suggesting that only massive galaxies can create a significant number of metal-rich GCs.

Galaxy mass/GC metallicity relation: Large samples of GCs across a wide variety of galaxy types show that the colours (and therefore metallicities) of the red and blue peaks in the bimodal colour distributions depend on the properties of the host galaxy. Peng et al. (2006) find that blue peak has a weak dependence on galaxy luminosity (which is related to galaxy mass), while the red peak has a strong dependence on galaxy luminosity and colour. Thus, at least for the metal-rich GCs there appears to be a Mass Metallicity Relationship (MMR) between GC metallicity and the host galaxy's stellar mass, which implies that the formation of the metal-rich GC population is strongly linked to the formation of the galaxy's field stars. The lack of a significant MMR for the metal-poor GCs implies that their formation is similar across galaxies of a variety of masses (though there may be intrinsic differences between giant and dwarf galaxies; Forte et al. 2009).

Specific frequency: The *specific frequency* of a galaxy (Harris & van den Bergh, 1981) is the number of its GCs normalized by the host galaxy's brightness (or its stellar mass). Ultimately, the specific frequency measures two things: how efficiently a galaxy forms GCs relative to field stars and how effectively it prevents its GCs from being destroyed (Georgiev et al., 2010). Observations of extragalactic GCs show that the specific frequency is higher in dwarfs and giants and lower in intermediate-mass galaxies. Both red and blue GCs have high specific frequencies at the high mass end (where the specific frequency for blue GCs is higher than for red ones, i.e. there are more metal-poor GCs than metal-rich ones); for some reason, massive galaxies overproduce metal-poor GCs. At the low mass end the specific frequency of blue (metal-poor) GCs also increases. Thus, the relative number of blue GCs changes between galaxies of different masses. Giants and dwarfs have considerably more blue GCs (normalized to stellar mass) than intermediate mass galaxies, while for intermediate and high mass galaxies the specific frequency of the red population seems to increase with mass.

These results suggest that dwarf galaxies are either more efficient at producing metal-poor GCs than intermediate mass galaxies or are better at keeping them. The most massive galaxies are efficient at creating both types of GCs.

Colour/metallicity gradients: Many galaxies show evidence for colour gradients, where integrated GC colours change with distance from the centre of the host galaxy. This is primarily due to the different locations of the red and blue subpopulations. The red (metal-rich) subpopulation is more centrally concentrated than the blue (metal-poor) population, leading to a net colour gradient. The total colour gradient may also be slightly affected by metallicity gradients in each of the GC subpopulations.

Detections of metallicity gradients can be controversial, since the gradients are often quite shallow (Liu et al., 2011). However, significant (albeit shallow) gradients *have* been observed in high, intermediate, and low mass elliptical galaxies in a variety of environments (e.g. Harris 2009a,b; Forbes et al. 2011). The gradients of the red population tend to be steeper than the blue population (Liu et al., 2011). Again, whether or not this indicates a stronger *metallicity* gradient depends on the colour to metallicity conversion. The slopes of both subpopulations seem to depend on galaxy mass, where low mass galaxies can have positive, negative, or zero slopes, but higher mass galaxies have increasingly shallower slopes (Liu et al., 2011). This suggests that low mass galaxies show galaxy-to-galaxy variations as a result of their different formation histories, while high mass galaxies have distinct formation histories from low mass galaxies. The gradients seem to disappear in the outer regions of massive galaxies (e.g. Forbes et al. 2011).

GC ages: Determining ages of unresolved GCs requires IL spectroscopy. At low resolution, ages can be obtained using individual spectral features (e.g. the Balmer lines[33]) or full spectrum fitting. As in the MW, most metal poor GCs seem to be old. There may be signs of increasing age with galaxy mass, such that the most massive galaxies have the oldest GCs (Chies-Santos et al., 2011)—this is consistent with the concept of "downsizing," which says that massive galaxies

[33]The Balmer lines are a series of H lines. Young GCs have bluer/hotter stars with strong Balmer lines. Thus, young GCs can be distinguished from old GCs because strong Balmer lines indicate the presence of hot MS stars. However, the Balmer lines can also be affected by blue HB stars (see Chapter 5.2.3).

should form before lower mass systems. Certain galaxies (e.g. NGC 5128; Woodley et al. 2010) also have metal rich GCs that appear to have a large dispersion ($\sim$ 10 Gyr) in age.

[α/Fe]: In extragalactic studies [α/Fe] is often used as an indicator for star formation rates. The [α/Fe] abundance can be determined from low resolution IL spectra through observation of Mg- and Ca-dominant features. Puzia et al. (2008) showed that GCs associated with dwarf galaxies have lower [α/Fe] ratios than the GCs at the same [Fe/H] that are associated with more massive galaxies. This result agrees with the MW GCs, suggesting that chemical evolution proceeds in a similar way in extragalactic systems. In the most massive galaxies, Puzia et al. (2006) find extremely α-enhanced GCs (with [α/Fe]$>$ 0.5), which may be a unique signature of very fast star formation. However, these results imply that extragalactic GCs can be different from Galactic GCs, which takes the observed index strengths outside of the calibrated regions and could indicate a problem with the adopted calibration. The [α/Fe] distributions and Age-α relations in galaxies (e.g. NGC 5128; Woodley et al. 2010) may also prove useful for determining star formation rates in different galaxy types.

Stellar streams: Stellar streams from accreted satellites have also been detected in the outer halo of the nearby spiral M31 by the Pan-Andromeda Archaeological Survey (PAndAS; McConnachie et al. 2009). These streams illustrate that M31's outer halo is currently being built up by the accretion of satellite dwarf galaxies. Furthermore, GCs have been discovered that appear to lie on these streams: using Monte Carlo techniques, (Mackey et al., 2010) find a $<$ 1% chance that the coincident locations of the streams and the GCs are random. This suggests that these GCs formed in the dwarf galaxies (or formed during the accretion), and are currently being accreted along with the dwarf galaxy field stars.

Formation Theories

These observations of extragalactic GC systems have discovered some important clues for the formation of their host galaxies:

1. Most galaxies have two distinct populations of GCs; these populations appear to be kinematically *and* chemically distinct, suggesting that they formed in

different environments and/or on different timescales.

2. The properties of these GC populations (metallicity, specific frequency, age) vary with galaxy mass; all galaxies (of a sufficient mass) have blue (metal-poor) GCs, suggesting that metal-poor GC formation is ubiquitous. The red (metal-rich) GCs form only in the more massive galaxies and are more metal-rich in the most massive galaxies.

3. Accretion of dwarf satellites is currently happening in M31, and may be happening in more distant galaxies as well.

There are three popular theories to explain the presence of these disparate GC populations:

The *in situ* Model: This model (also known as the Multiphase Dissipational Collapse model) was developed by Forbes et al. (1997). It proposes two phases of ELS-type star formation, with GCs forming in each starburst. The first round of metal-poor star formation happens in all (sufficiently massive) low mass subhaloes, which will merge to form larger halos. This explains how every sufficiently massive galaxy will have a population of metal-poor GCs whose metallicity is not dependent on galaxy mass. The most massive galaxies can retain some gas for a second round of star formation, which creates the metal-rich population of GCs.

The Accretion Model: The accretion model from Côté et al. (1998) suggests that a single population of GCs forms in each galaxy, with the metallicity of the GC population depending on the galaxy mass (such that the most massive galaxies create the most metal-rich GCs, while dwarfs create metal-poor GCs). Over time the most massive galaxies accrete their closest dwarf companions, bringing in metal-poor field stars *and* GCs (as is observed in the MW and M31).

The Major Merger Model: The major merger model of Ashman & Zepf (1992) is based on the assumption that giant elliptical galaxies are formed via major mergers of spirals. This model suggests that lower mass galaxies form populations of metal-poor GCs, which are then brought into the new massive halo as spirals merge. The merging process induces star formation in the (enriched) gas from the spirals, forming a new generation of metal-rich GCs that are now associated with the new elliptical galaxy. This model therefore predicts a universal

population of metal-poor GCs in all low mass galaxies, and that metal-rich GCs will only exist in galaxies that have experienced a major, gas-rich merger. Furthermore, the properties of the metal-rich GCs will depend upon the properties of the new elliptical galaxy.

These scenarios can all explain the presence of two kinematically and chemically distinct populations of GCs in massive galaxies. They can also explain the ubiquitousness of metal-poor GCs in all galaxies and why the properties of the metal-rich GCs depend on galaxy mass. However, each model cannot explain all of the observed properties of galaxies and their GC systems. In reality, some components of all three models are probably necessary for galaxy formation, and the dominant formation mechanisms likely differ between galaxies (e.g. a galaxy at the centre of a crowded galaxy cluster is likely to experience more major mergers than the MW).

1.5.3 The Future Role of High Resolution Spectroscopy

As discussed in Chapters 1.3.5, 1.3.6, and 1.4.2, high resolution spectroscopy can provide detailed chemical abundances, which will be useful in inferring the formation histories of specific galaxies. High resolution spectroscopy offers two main benefits over lower resolution spectroscopy:

1. Blends can be better resolved at high resolution, removing (or lessening) index dependencies on multiple elements. Similarly, more lines for a given element can be detected, enabling more independent measurements to constrain the abundances. Thus, high resolution spectroscopy should offer increased *precision* and *accuracy* over lower resolution spectroscopy.

2. Weaker features can be detected (e.g. the Eu II 6645 Å line). High resolution spectroscopy therefore provides detailed abundances for more elements.

Future high resolution observations can therefore fill in some of the gaps in the existing theories of galaxy formation by providing more elements and by placing tighter constraints on abundances.

Resolved Spectroscopy in the Milky Way

High resolution spectroscopy has been used extensively in the MW to identify streams from dwarf galaxies and to tag field stars and GCs to those streams. New streams are

being discovered, and there are many field stars and clusters left to observe. Combined with detailed kinematic information, these observations should help characterize the nature of the progenitors that built up the current MW halo.

IL Spectroscopy

Because high resolution proves more abundances and better precision, high resolution IL spectroscopy will allow individual GCs to be chemically associated with dwarf galaxies or massive galaxies, as in the MW (provided that they are in the right metallicity regime). The signs of accretion could therefore be directly detected in distant systems, assuming that abundances can be obtained with sufficient accuracy and precision. This kind of detailed chemical tagging has not yet been possible outside of the MW and its dwarf satellites.

1.6 The Goals of This Thesis

The ultimate goal of this thesis is to determine the detailed chemical abundances of GC stars and to use these abundances to learn about the formation and evolution of their host galaxies. Three different types of targets have been observed and analyzed:

1. *Individual stars in the unusual Galactic GC, Palomar 1.* Pal 1 is an ideal target for chemical tagging because it is an unusual cluster. In particular it resembles neither a GC nor an open cluster, and may have been accreted from a dwarf galaxy. Chapter 3 demonstrates that Pal 1 *is* chemically more similar to a dwarf galaxy, though it remains an unusual object. This standard chemical analysis of RGB stars serves as an excellent introduction to high resolution spectroscopic techniques.

2. *Integrated light of standard Galactic GCs.* As discussed in Chapter 1.4.2, high resolution integrated light analysis techniques have not yet been tested on a wide variety of objects. In order to verify the accuracy and precision of high resolution IL analysis techniques, IL spectra of standard (i.e. old and α-enhanced) Galactic GCs have been obtained. The target clusters (47 Tuc, M3, M13, NGC 7006, and M15) span a range of metallicities and HB morphologies and have detailed literature abundances for large samples of individual stars.

3. *Integrated light of newly discovered, outer halo M31 GCs.* With the knowledge gained from the tests on the Galactic GCs, IL analysis techniques are then applied to extragalactic GCs that are located in the outer halo of M31. Two of the clusters were discovered by Huxor et al. (2008); the other five were discovered in the Pan-Andromeda Archaeological Survey (PAndAS; McConnachie et al. 2009). These GCs may be in the process of being accreted from satellite galaxies and therefore serve as excellent candidates for *IL chemical tagging.* Their proximity enables partially resolved photometry for the upper RGB and HB, enabling constraints to be placed on age and [Fe/H].

1.7 Thesis Outline

The thesis is organized as follows.

Chapter 2: This chapter outlines the details of target selection, the specifications for the observations, and the data reduction techniques. Sample spectra are also shown for all targets.

Chapter 3: The analysis of the individual RGB stars in Palomar 1 is presented in this chapter. Standard abundance analysis techniques are described and are used to determine the detailed chemical properties of Pal 1. The implications for its formation are then discussed.

Chapter 4: The analysis then turns to IL spectroscopy of the Galactic GCs. The analysis techniques are based on the standard procedures outlined in Chapter 3 but are extended to entire populations. The measurement techniques are investigated in detail, and the derived abundances are compared to literature values for individual stars.

Chapter 5: This chapter investigates the systematic errors that can occur in a standard IL analysis. Uncertainties in the underlying stellar population are considered, both for resolved and unresolved populations. The most stable abundance ratios are identified and are suggested for future unresolved analyses.

Chapter 6: The IL analysis techniques are then extended to new systems. Integrated abundances are determined for the PAndAS clusters, and are used to determine the formation history of M31's outer halo.

Chapter 7: Finally, the results of the thesis are summarized, and suggestions for future work are proposed.

Appendix A: A list of the acronyms is provided in this appendix.

Appendix B: A list of all other PAndAS targets is given, along with justifications for why they were not observed.

Appendix C: Extra information on the techniques to measure equivalent widths of spectral lines and the final values for all targets are given in this appendix.

Chapter 2

Observations and Data Reduction

The spectra presented in this thesis were observed with two separate *echelle* spectrographs: the High Dispersion Spectrograph (HDS; Noguchi et al. 2002) on the Subaru Telescope (for the individual stellar spectra analyzed in Chapter 3) and the High Resolution Spectrograph (HRS; Tull 1998) on the Hobby-Eberly Telescope (HET) at McDonald Observatory in Fort Davis, TX (for the IL spectra studied in Chapters 4, 5, and 6). This chapter outlines the observations and data reduction of these high resolution spectra. First the target selection is discussed in Chapter 2.1. The basic design of an echelle spectrograph is then outlined in Chapter 2.2, and the specific configurations for each set of targets are detailed in Chapter 2.3. The data reduction procedures (to convert the images to analyzable spectra) are discussed in Chapter 2.4, and samples of the final spectra are shown in Chapter 2.5.

2.1 Target Selection

2.1.1 Palomar 1

As discussed in Chapter 1.6, Pal 1 was selected as a target for high resolution spectroscopy because it is an unusual cluster that does not conform to the characteristics of traditional Galactic GCs; this suggests either that Pal 1 is not a GC or that it is not Galactic. Furthermore, Pal 1's similarities to the sparse GCs associated with the Sagittarius dwarf spheroidal and to the Large Magellanic Cloud (LMC) intermediate-age GCs hint at an extragalactic origin. Pal 1's brightest stars were therefore targeted for high resolution spectroscopic observations to test these theories.

Pal 1 is a distant, faint cluster, and only the brightest stars can easily be observed

at high resolution. It is also a sparsely populated GC, with only a handful of bright stars to observe. This sparse cluster can be contaminated by Galactic field stars; to avoid observing non-members, it is preferable to observe stars that have already been confirmed as cluster members (e.g. with radial velocity determinations from lower resolution spectra). Four of the target stars were previously observed by Rosenberg et al. (1998b) in their Ca II triplet analysis and have radial velocities that make them likely cluster members. As in Rosenberg et al., these stars are identified as Pal 1-I, -II, -III, and -IV. The bright object located at the centre of the cluster, Pal 1-C, was also included as a target even though it had not been observed by Rosenberg et al. The locations of these stars in an image of the cluster and in a CMD (from the ACS GC Treasury, see Sarajedini et al. 2007, Anderson et al. 2008) are shown in Figure 2.1.

A similar analysis of a well-studied star (and a comparison with literature results) provides an excellent verification of the observation, data reduction, and analysis methods. Therefore, in addition to the Pal 1 stars, an analysis of a "standard" star, M67-141 (as identified by Fagerholm 1906), is included. This star resides in the metal-rich, Galactic open cluster M67 and has previous detailed, high resolution chemical abundances from Yong et al. (2005) and Pancino et al. (2010).

Table 2.1 shows the positions and magnitudes of the target stars. The Pal 1 positions and V and I magnitudes (in the Johnson system) are from Sarajedini et al. (2007), while M67-141's position and V and I magnitudes (in the Kron-Cousins system) are from Høg et al. (2000), Sanders (1977), and Janes & Smith (1984), respectively. All of the K magnitudes are from the Two Micron All-Sky Survey (2MASS) Point Source Catalog.[1]

2.1.2 Galactic GCs

The second part of this thesis focuses on high resolution IL spectroscopy, which is a relatively new type of analysis. Testing the precision, accuracy, and limits of high resolution IL spectroscopy requires observations of nearby, well-studied GCs. For the Galactic IL tests, standard (i.e. old and α-enhanced) Galactic GCs that span a range of metallicities (from [Fe/H] = -0.7 to -2.4) and HB morphologies (from red to very blue) were selected as targets. In particular, M3, M13, and NGC 7006 form a "second

[1] `http://tdc-www.harvard.edu/catalogs/tmpsc.html`

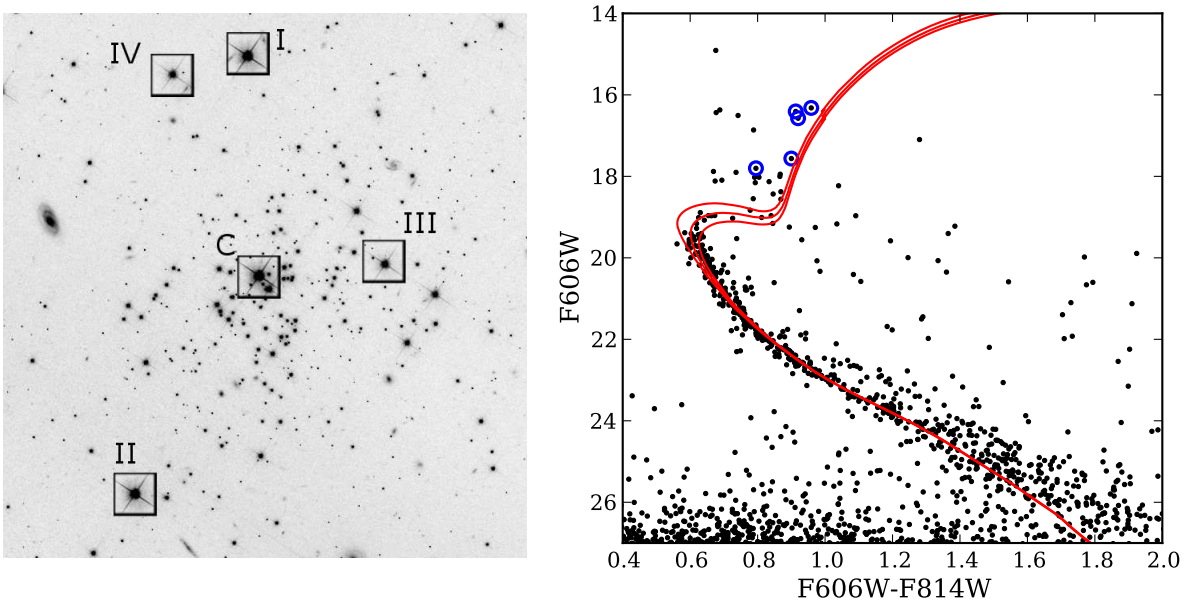

(a) Pal1 *HST* Image

(b) Pal1 *HST* CMD

Figure 2.1: An *HST* F814W image (left) and CMD (right, roughly V, V-I) for the central field of Pal 1, from Sarajedini et al. (2007). The observed targets are indicated. The field of view in the image (left) is approximately $1.'7 \times 1.'7$; north is up, and west is to the left. Also shown on the CMD (right) are fitted isochrones from the Dartmouth Stellar Evolution Database (Dotter et al., 2008) for ages of 4, 5, and 6 Gyr. Values of $[\mathrm{Fe/H}] = -0.6$, $[\alpha/\mathrm{Fe}] = 0.0$, $(m-M)_V = 16.27$, and $E(B-V) = 0.20$ are adopted, as discussed in Chapter 3. Pal 1 is a young and faint cluster, and has a sparse RGB and a barely detectable HB.

Table 2.1: Properties of the target stars for the Palomar 1 study.

Star	RA (J2000)	Dec (J2000)	V[a]	I[a]	K[b]	References
M67-141	$8^h51^m22.8^s$	$+11°48'1.''7$	10.480	9.400	7.942	1, 2, 3
Pal 1-I	$3^h33^m21.8^s$	$+79°35'16.''2$	16.675	15.459	13.832	4
Pal 1-II	$3^h33^m29.6^s$	$+79°34'16.''2$	16.843	15.618	13.983	4
Pal 1-III	$3^h33^m12.3^s$	$+79°34'59.''2$	17.827	16.628	15.281	4
Pal 1-IV	$3^h33^m27.0^s$	$+79°35'34.''9$	18.032	16.969	15.779	4
Pal 1-C	$3^h33^m21.0^s$	$+79°34'57.''1$	16.603	15.328	13.715	4

References. (1) Høg et al. (2000); (2) Sanders (1977); (3) Janes & Smith (1984); (4) Sarajedini et al. (2007)

[a] M67-141 V and I magnitudes are in the Kron-Cousins system, while the Pal 1 V and I magnitudes have been transformed from the HST system to the Johnson system.

[b] All K magnitudes are from the 2MASS Point Source Catalog.

Table 2.2: Properties of the target Galactic GCs.

Cluster	RA (J2000)	Dec (J2000)	$V_{\rm int}$	[Fe/H]	HB index
47 Tuc (NGC 104)	$00^{\rm h}24^{\rm m}05^{\rm s}.67$	$-72°04'52''.6$	3.95	-0.70	-0.99
M3 (NGC 5272)	$13^{\rm h}42^{\rm m}11^{\rm s}.62$	$+28°22'38''.2$	6.19	-1.60	0.08
M13 (NGC 6205)	$16^{\rm h}41^{\rm m}41^{\rm s}.24$	$+36°27'35''.5$	5.78	-1.60	0.97
NGC 7006	$21^{\rm h}01^{\rm m}29^{\rm s}.38$	$+16°11'14''.4$	10.56	-1.50	-0.28
M15 (NGC 7078)	$21^{\rm h}29^{\rm m}58^{\rm s}.33$	$+12°10'01''.2$	6.20	-2.40	0.67

References: Positions and integrated magnitudes are from Harris (1996; 2010 edition). The [Fe/H] estimates are from isochrone fitting (Dotter et al., 2010, 2011). The HB index, $(B\ -\ R)\ /\ (B\ +\ V\ +\ R)$, comes from Mackey & van den Bergh (2005).

parameter" triad, i.e. the three GCs have similar ages and metallicities, yet different HB morphologies.

Basic information about the target clusters is provided in Table 2.2. Positions and integrated V magnitudes are from Harris (1996; 2010 edition); the [Fe/H], [α/Fe], and age estimates come from isochrone fits by Dotter et al. (2010, 2011); and the horizontal branch (HB) index, $(B\ -\ R)\ /\ (B\ +\ V\ +\ R)$, (where B, R, and V are the number of stars blueward, redward, and inside of the instability strip) comes from Mackey & van den Bergh (2005).

2.1.3 PAndAS GCs

This thesis also presents new integrated abundances of GCs in the outer halo of M31 that were discovered in the Pan-Andromeda Archaeological Survey (PAndAS; McConnachie et al. 2009; Huxor et al. 2014). The primary goal of this high resolution spectroscopic investigation of M31 GCs is to identify GCs that may have originated in dwarf galaxies. The targets were therefore restricted to outer halo GCs (i.e. with projected distances from the centre of M31 that are $R_{\rm proj} \gtrsim 30$ kpc; see Figure 2.2); particular emphasis was placed on the GCs with the largest projected radii. Observational constraints required that the targets were sufficiently bright (with total magnitudes $M_V \lesssim -7.3$) and centrally concentrated. These selection criteria were best met by seven outer halo GC targets, whose properties are summarized in Table 2.3; for comparison, the properties of the other PAndAS GCs are given in Appendix B. Two of these target clusters (H10 and H23) were presented by Huxor et al. (2008);

Table 2.3: Properties of the target PAndAS clusters.

Cluster	RA (J2000)	Dec (J2000)	$V_{\rm int}$	$R^a_{\rm proj}$ (kpc)	[Fe/H]	Spatial Association
H10	$00^{\rm h}35^{\rm m}59.7^{\rm s}$	$+35°41'03''.6$	15.7	78.5	-1.84	–
H23	$00^{\rm h}54^{\rm m}25.0^{\rm s}$	$+39°42'55''.5$	16.8	37.1	-1.54	Stream D?
PA06	$00^{\rm h}06^{\rm m}12.0^{\rm s}$	$+41°41'21''.0$	16.5	93.7	MP	–
PA17	$00^{\rm h}26^{\rm m}52.2^{\rm s}$	$+38°44'58''.1$	16.3	53.9	?[b]	–
PA53	$01^{\rm h}17^{\rm m}58.4^{\rm s}$	$+39°14'53''.2$	15.4	95.9	MP	–
PA54	$01^{\rm h}18^{\rm m}00.1^{\rm s}$	$+39°16'59''.9$	15.9	95.8	MP	–
PA56	$01^{\rm h}23^{\rm m}03.5^{\rm s}$	$+41°55'11''.0$	16.8	103.3	MP	–

References: Positions, integrated magnitudes, and projected distances from M31 are from Mackey et al. (2007) and Huxor et al. (2014). Metallicity estimates for H10 and H23 are from Mackey et al. (2007), and were determined with Galactic GC fiducial fits. Based on their CMDs, PA06, PA53, PA54, and PA56 all appear to be metal-poor (Mackey et al., *in prep.*). Possible stream associations based on spatial information are listed in Veljanoski et al. (2014).
[a] Projected distances are from the centre of M31.
[b] PA17 does not have an *HST* CMD, and there is therefore no *a priori* information about its age and metallicity.

the other five were discovered in the PAndAS programme (Huxor et al., 2014). Note that only one of these clusters is spatially associated with a stream—based on its location H23 appears to lie along "Stream D," though its kinematics are uncertain (Veljanoski et al., 2014).

The tests on Galactic GCs (presented in Chapter 5) show that systematic errors in integrated abundances can be quite high if there is no *a priori* information on GC metallicity, age, HB morphology, etc. Thus, observing priority was given to those targets with partially resolved photometry. Six of the seven target PAndAS GCs have *Hubble Space Telescope* (HST) photometry down to the horizontal branch (Mackey et al, *in prep.*).

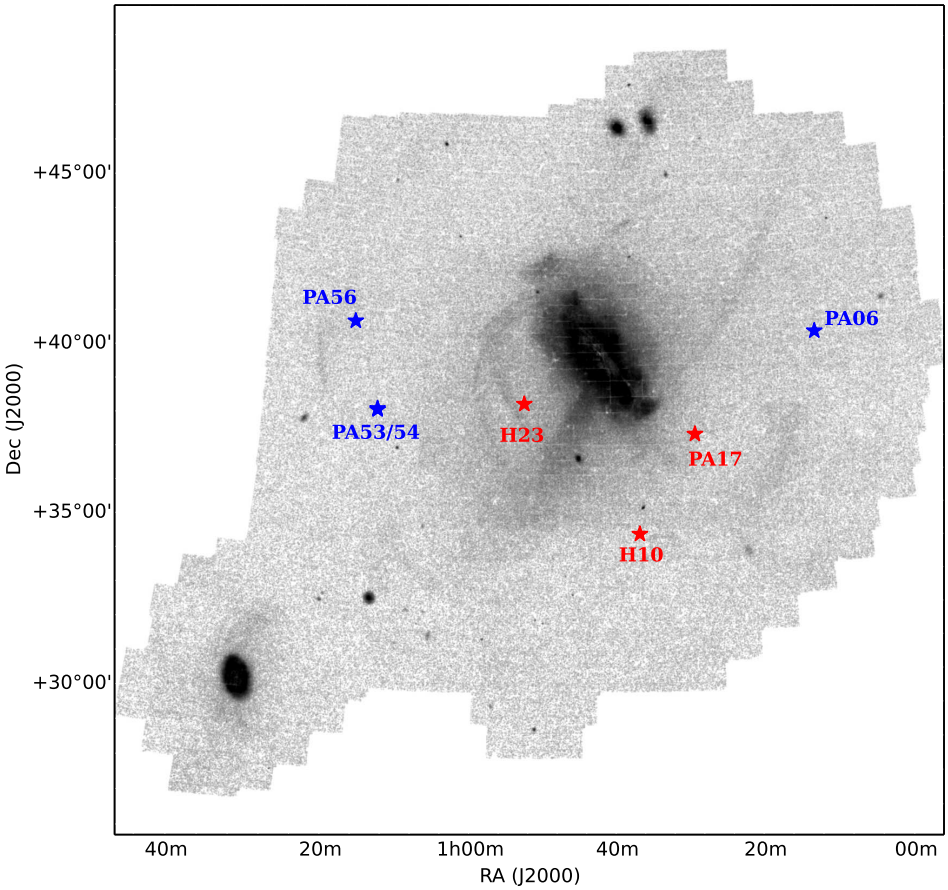

Figure 2.2: Locations of the target PAndAS clusters on a metal-poor density map of the full PAndAS footprint. The locations of stellar streams and satellite galaxies are obvious as dark regions. The red stars show the metal-rich PAndAS clusters observed in this thesis, while the blue stars show the metal-poor GCs (see Chapter 6). PA53 and PA54 are very close together and share a single point in the plot.

2.2 A Description of Echelle Spectrographs

The thesis targets were all observed with echelle spectrographs. An echelle spectrograph provides high spectral resolution, so that individual lines can be separated (or *resolved*) from nearby lines. Though HDS and HRS have slightly different designs, the basic components are the same. A schematic of HRS is shown in Figure 2.3—the design of HDS is very similar. The principal components are outlined and described in detail below in the order in which light encounters them:

Slit: When the light enters the spectrograph it first travels through a narrow slit, which isolates the object of interest and allows light only from a small region to enter the instrument. The presence of a slit creates a single slit diffraction pattern, where the width of the slit dictates the width of the spectral lines. Thus, the slit defines the instrumental line broadening and the spectral resolution ($R = \lambda/\Delta\lambda$), where λ is the wavelength of the transition.

Echelle Grating: The echelle grating is the dispersive element of a high resolution spectrograph. Diffraction gratings have many closely spaced lines or grooves, which lead to multi-slit diffraction. Echelle gratings are *reflection* gratings, where the incident light is reflected off the surface (this is different from transmission gratings, where the light travels through the grating). The basic design of an echelle can be understood by examining the standard grating equation:

$$m\lambda = \sigma(\sin\beta + \sin\alpha) \tag{2.1}$$

where m is the spectral order, σ is the distance between the rulings, and α and β are the angles of incidence and reflection. A spectrograph is designed to spread out the incoming light, separating it by wavelength as much as possible—this is equivalent to maximizing the angular dispersion, $A = \partial\beta/\partial\lambda$. Differentiating Equation 2.1 with respect to β leads to the angular dispersing equation:

$$A = \frac{\partial\beta}{\partial\lambda} = \frac{m}{\sigma\cos\beta}. \tag{2.2}$$

Equation 2.2 illustrates that there are two ways to maximize A: high spectral orders can be observed (i.e. large values of m can be selected), or a small distance between grating grooves can be selected (i.e. σ can be minimized).

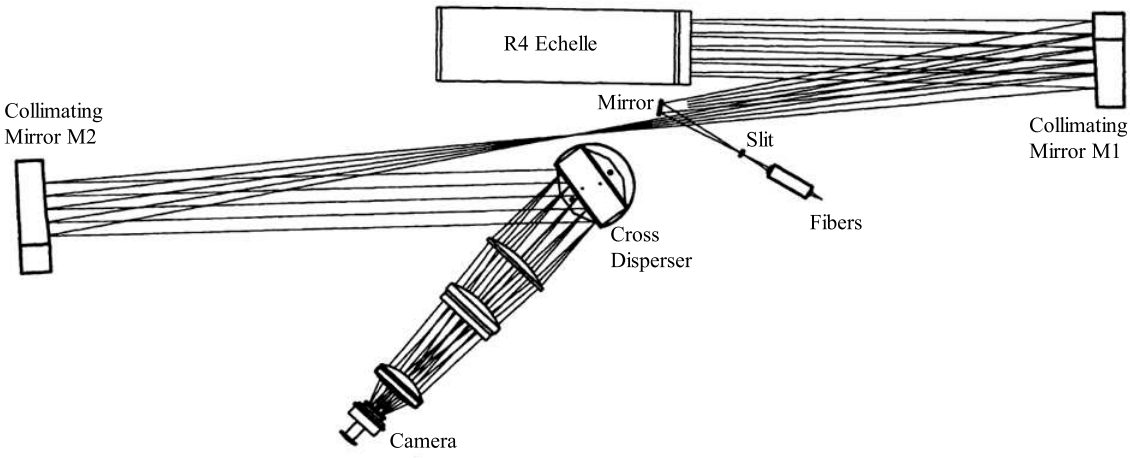

Figure 2.3: A schematic of the HRS on the HET, adapted from Tull (1998). Light from the telescope enters the spectrograph through fibres. The light then travels through the spectrograph slit, reflects off the collimating mirror M1, is dispersed (i.e. is separated by wavelength) by the echelle, is again reflected by M1, travels to the second collimating mirror M2, is separated into different orders at the cross disperser, and finally travels to the camera. The individual components are described in more detail in Chapter 2.2.

Standard diffraction gratings are designed to meet the latter criterion, and therefore have finely spaced rulings. Echelles are designed with much coarser rulings than standard diffraction gratings and with high spectral orders selected. For example, the HRS and HDS echelles have 31.6 grooves/mm with spectral orders $m \gtrsim 50$, while a standard diffraction grating might have $m = 1$ and 1200 gr/mm (Schroeder, 1987).

After encountering the echelle, the light follows the well-known pattern for single slit diffraction (the "blaze function") modified by the multi-sit interference pattern from the grating—these patterns are shown in Figure 2.4, where it is clear that most of the incoming flux is in the zeroth order, with very little flux left in the higher spectral orders where the angular dispersion is largest. To increase the efficiency of the spectrograph the blaze function is moved until its peak overlaps with the desired order(s). This process is called "blazing," and is accomplished by tilting the echelle by some blaze angle δ.

Cross Disperser: After the echelle disperses the light, the various orders overlap, particularly at high orders. To isolate the orders, a standard, finely spaced diffraction grating is inserted into the spectrograph to disperse each order in the opposite direction from the echelle—this grating is therefore known as a cross disperser. Because the order dispersion occurs perpendicular to the wavelength dispersion, the final image has a two-dimensional shape (see Figure 2.5). The groove spacing of the cross disperser dictates the spacing between the orders. The tilt of the cross disperser can also be modified, so that the desired orders (and therefore the desired spectral regions) fall on the CCD.

Camera: The dispersed and cross-dispersed light then travels through the optics of the camera before landing on the charge-coupled device (CCD) which records the number of photons hitting each pixel. The final data from the camera must then be reduced (i.e. converted into a usable format), taking into account several important calibrations (Chapter 2.4).

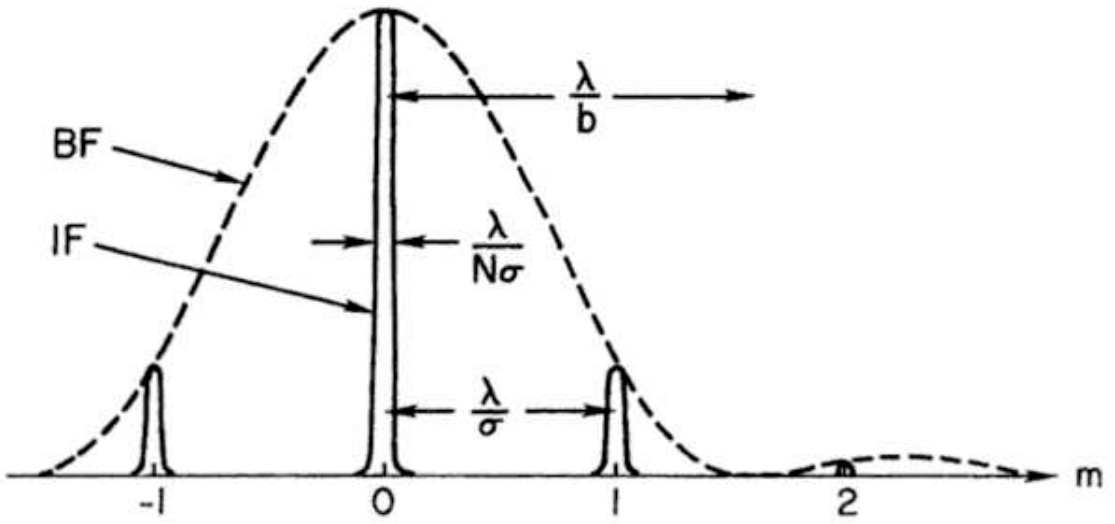

Figure 2.4: An example of how the blaze function (BF) and the interference factor (IF) work together to create the final profile of light traveling through a spectrograph (from Schroeder 1987). The blaze function modulates the interference pattern; as a result, most of the light is located in the zeroth order of the dispersed light. Because high orders are used with echelle spectrographs, the echelle is "blazed," meaning that the echelle is tilted so that the BF peak moves, funneling most of the light into the higher orders.

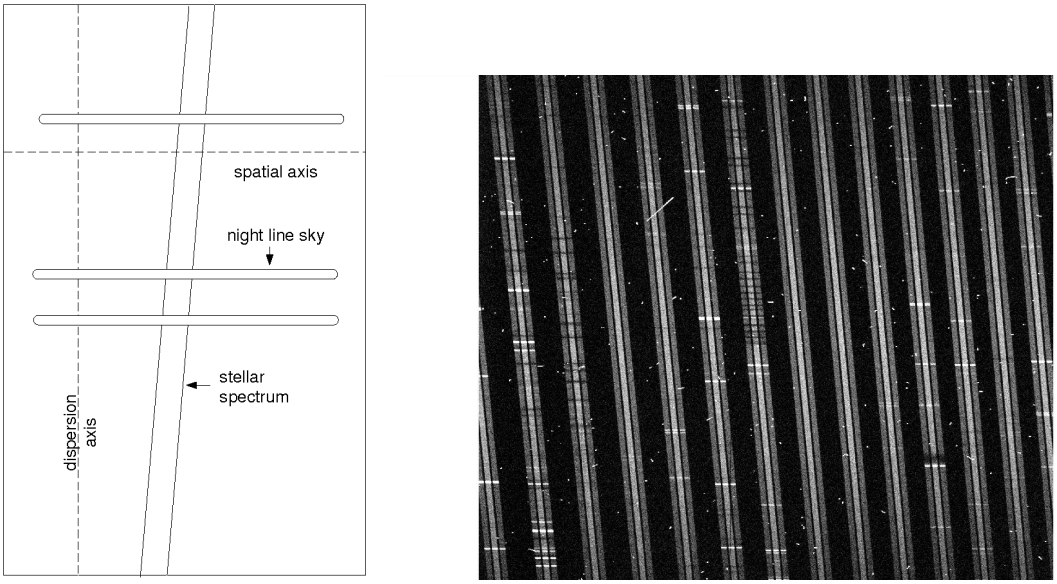

(a) An ideal spectrum

(b) An observed spectrum

Figure 2.5: Examples of echelle spectra. *Left*: an illustration of an idealized column, from Massey et al. 1992. The dispersion and spatial axes are labelled; note that in this illustration the labelled dispersion axis does not align with the spectrum's real dispersion axis. *Right:* a red ($\sim 6350 - 7300$ Å) spectrum of the Galactic cluster NGC 7006; the axes are as in the left image. The two-dimensional nature of the spectrum is obvious: the echelle grating has dispersed the light along the dispersion axis, while the cross disperser has separated the orders along the spatial axis. The thirteen red orders are shown as columns, with spectral lines running horizontally across each order. Dark absorption and bright emission lines are evident in the columns; many of the darkest absorption lines are telluric (sky absorption) lines, though Hα is very clear in the tenth order. The two sky fibres border the central sky fibre (see Chapter 2.3.2); in this observation the sky fibres are also on the target, though normally these fibres would be on the sky, and would have significantly less flux. Cosmic ray hits have also left their mark on the detector; they are the bright spots on the image.

2.3 Description of Observations

Each observation requires specific configurations of the echelle, based on the science goals. In particular, some of the important factors that must be specified are listed below.

- Slit width, which determines the instrumental resolution, R. Small slit widths increase resolution but also increase the exposure times necessary to reach a given signal-to-noise (S/N) ratio.
- Slit length or fibre size, which dictates how much of the object to observe.
- Cross disperser coarseness, which determines the spacing between spectral orders. This choice will affect, e.g., wavelength coverage and whether calibration sky fibres can be included.
- Cross disperser tilt, which selects the observed wavelength ranges.
- Exposure times, which dictate the S/N ratios of the final spectra. Telescope size, instrumental R, instrument optics, and observing conditions (such as sky brightness and seeing) dictate the amount of time necessary to accumulate enough source photons to achieve the desired S/N ratios.

This section outlines the parameters that were chosen for the observations of the targets.

2.3.1 Palomar 1

Observations

The Pal 1 targets were observed during several runs in 2006 January and 2007 January using HDS on the Subaru Telescope. A slit length of 5.6 arcsec was adopted for all stars, allowing for sky observations at the ends of the slit. The adopted slit widths were 1 arcsec for the Pal 1 stars and 0.6 arcsec for M67-141, leading to spectral resolutions of $R = 36000$ and $R = 60000$, respectively. The default grating was centred at 5500 Å, providing spectral coverage from $\sim$ 4380 to 7120 Å. Table 2.4 shows a list of the dates, total exposure times, and S/N ratios for these observations.

The position of the Moon was not ideal for observations of the Pal 1 stars, as the primary target of this observing run was the Sextans dwarf galaxy (Aoki et al., 2009),

Table 2.4: Observations for the Pal 1 targets.

Star	Observation Dates	Exposure Time (s)	S/N[a] (5300 Å)	S/N[a] (6600 Å)
M67-141	2006 Jan 21	5985	100	150
Pal 1-I	2006 Jan 20, 21	9000	15	30
Pal 1-II	2006 Jan 20	9000	15	30
Pal 1-III	2007 Jan 25, 26	12600	31	45
Pal 1-IV[b]	2007 Jan 27, 28, 29	21600	–[b]	–
Pal 1-C	2007 Jan 6, 27	5400	35	55

[a] S/N ratios are per pixel and were determined in IRAF.
[b] Pal 1-IV was dropped from the analysis, as the seeing was too poor to perform a sky subtraction.

which was located far away from the Moon. In addition, the stars were fairly low in the sky during the observations and the seeing conditions were poor; as a result the stars observed in 2006 nearly filled the slit and the sky subtractions proved to be extremely difficult. The final, co-added stellar spectra from 2006 (stars Pal 1-I and -II) thus have lower S/N than expected.

2.3.2 Galactic Clusters

The 47 Tuc spectrum was kindly provided by R. Bernstein & A. McWilliam. It is the same spectrum analyzed in MB08; details on the observations and data reduction can be found in that paper. Additional normalizations with low-order polynomials were performed and the apertures were combined, as described in Chapter 2.4.

The other spectra were observed with HRS on the HET in 2011 and 2012. A slit width of $1''$ was used, leading to an instrumental spectral resolution of $R \approx 30,000$. Given the velocity dispersions of the targets (see Chapter 2.4.3), a higher spectral resolution is unnecessary. The 600 gr/mm cross disperser was used, with a central wavelength of 6302.9 Å; the spectral coverage is therefore $\sim 5320 - 6290$ Å on the blue chip and $\sim 6360 - 7340$ Å on the red chip. This wavelength range was chosen for unresolved targets in order to minimize the effects of improperly modelled HBs, since blue HB stars should contribute less to the integrated light at red wavelengths.

IL observations of distant, point-like targets are relatively simple. Nearby GCs, however, are much more difficult to observe for IL studies, given their large sizes on the sky and the fact that their stars *are* resolved. To overcome these observational

difficulties, the spectra of M3, M13, NGC 7006, and M15 were obtained by scanning the HRS fibres across the cluster cores. A number of specific pointings on the cluster were selected, and the telescope was moved to each position while continuously integrating. The large 3″ fibre was used in order to maximize spatial coverage on the clusters.[2] HRS provides two additional 3″ fibres located 10″ from the centre of the object fibre. In typical observations these extra fibres are intended to observe the sky; however, because of the spatial extent of the Galactic GCs, these sky fibres fall on the GC and provide additional coverage of the objects. Separate sky observations with all three fibres were therefore taken after each GC observation. Telluric standards were also observed for sky absorption line removal.

The pointing patterns on the Galactic GCs are shown in Figure 2.6, along with the clusters' core and half-light radii. For M3, M13, and NGC 7006, the entire core of each cluster was observed, though the clusters were too large to observe the entire area within the half-light radius in a reasonable amount of time. Note that M15 was mapped differently than NGC 7006, M3, or M13; its wedge-shaped map represents an $\sim 80^\circ$ slice of the cluster out to the half-light radius—this should provide a representative IL spectrum of the GC within the half-light radius, assuming the cluster is spherically symmetric. Any differences in the spectra as a result of the different mappings will be negligible, since the input photometry have been selected to reflect the spatial coverage of the IL spectra (see Chapters 4 and 5).

The total exposure times and S/N ratios in blue (5500 Å) and red (7000 Å) regions are shown in Table 2.5. Generally, the exposure times were calculated to allow an observation of a single HB star to reach S/N = 70, though NGC 7006 did not receive sufficient time to meet this goal.

2.3.3 PAndAS Clusters

The PAndAS clusters were observed with the same instrumental setup as the Galactic GCs (i.e. a slit width of 1″, the 600 gr/mm cross disperser set to a central wavelength of 6302.9 Å, and the 3″ fibres). At the distance of M31 the clusters fall within the central 3″ fibre, and the sky fibres actually fall on the sky—thus, no additional sky observations were required, other than the hot star observations for telluric absorption line removal. Exposure times were calculated to obtain a total S/N = 50, although not

[2]Note that the 3″ fibre will observe $\sim$ 225% more sky than the 2″ fibre (`http://hydra.as.utexas.edu`), which will make sky subtraction essential.

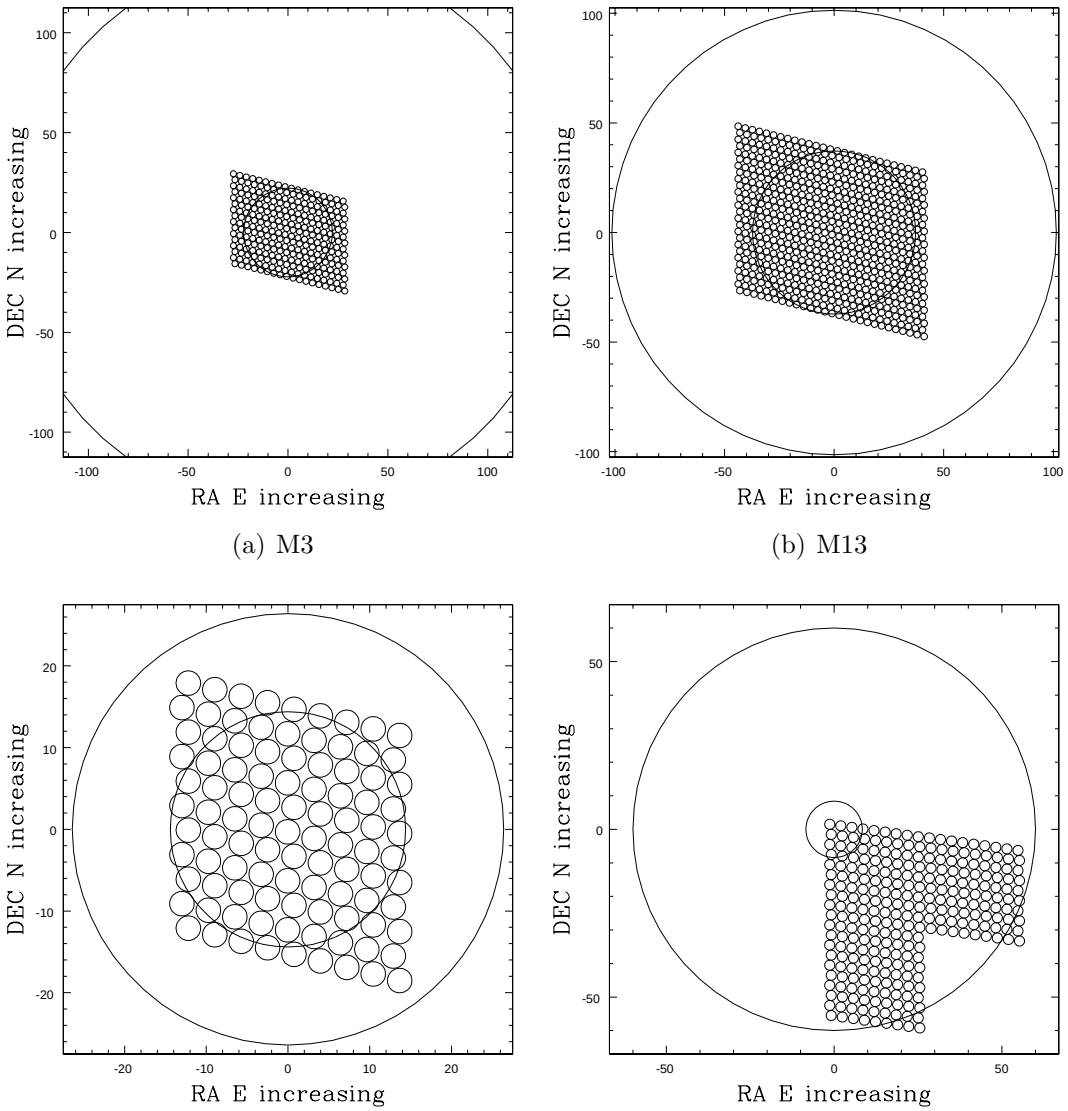

(a) M3 (b) M13

(c) NGC7006 (d) M15

Figure 2.6: Fibre pointings for the HET observations of the target clusters. The small circles show the positions of the 3″ fibres (both sky and object), while the larger circles show the core and half-light radii (from Harris 1996; 2010 edition). The centres of the clusters are shown at $(0, 0)$. Each observation scans the three fibres across the cluster; for an individual GC, each pointing lasts for the same amount of time, and the pointings are not overlapped.

Table 2.5: Galactic GC observations.

Cluster	Observation Dates	Exposure Time (s)	S/N[a] (5500 Å)	S/N[a] (7000 Å)	$r^b_{\rm ILS}$ (r_c)
47 Tuc[c]	2000 Jul 18, 19	11030	120	180	1.1
M3	2012 Mar 25, Apr 16, 17, 18	9940	180	230	1.8
M13	2012 Apr 17, 20, 22	11569	130	250	1.7
NGC 7006	2011 Sep 24, 2012 May 29, Jun 19	8903	65	130	2.4
M15	2011 Sep 27	3280	95	220	7.1

References: Literature values are from the Harris Catalog (Harris, 1996; 2010 edition).

[a]S/N ratios (per pixel) are measured in IRAF.

[b]The quantity $r_{\rm ILS}$ describes the radial extent of the cluster that was observed in the IL spectrum, compared to the core radii.

[c]47 Tuc was observed with the Las Campanas Observatory 2.5 m Du Pont Telescope by R. Bernstein & A. McWilliam; see MB08 for more details.

Table 2.6: PAndAS cluster observations.

Cluster	Observation Dates	Exposure Time (s)	S/N[a] (5500 Å)	S/N[a] (7000 Å)	$r^b_{\rm ILS}$ (r_h)
H10	2011 Jan 2, 10, 11, 22, 23, 28, 30	19180	50	85	2.3
H23	2011 Jul 5, 7, 10, 11, Aug 2, 4, Sep 23	16050	40	50	4.1
PA06	2011 Sep 29, Oct 1, 2, 4, 6, 17, 18, 19, 21, 23	29278	40	65	2.6
PA17	2012 Jan 16, 18, 21	8100	25	30	2.6
PA53	2011 Aug 1, Sep 20, 26	8100	70	90	2.7
PA54	2011 Aug 25, Sep 24, 25, 27	10800	50	80	2.2
PA56	2011 Oct 7, 17, 18, 20, 21, 23, 24, 30 Nov 19, Dec 30, 2012 Feb 10, 11 2012 Feb 10, 11	30623	40	50	2.4

[a]S/N ratios (per pixel) are measured in IRAF.
[b]The coverage radii are based on the half-light radii in Tanvir et al. (2012) and Huxor et al. (2014).

all targets received enough time (particularly PA17). The details of the observations are shown in Table 2.6.

2.3.4 Calibration Spectra

The abundances derived in this thesis rely on calibration analyses of the Sun and Arcturus. The Solar spectrum ($R = 300,000$; Kurucz 2005) comes from the Kurucz 2005 Solar flux atlas.[3] Solar atmospheric parameters of $T_{\rm eff} = 5777$ K, $\log g = 4.44$ dex, $\xi = 0.85$ km s^{-1}, and [M/H] = 0.0 were adopted (Yong et al., 2005).

The Arcturus spectrum is the same one used for the cross-correlation with the target IL spectra (see Chapter 2.4.3). Arcturus atmospheric parameters of $T_{\rm eff} = 4300$ K, $\log g = 1.50$ dex, $\xi = 1.56$ km s^{-1}, and [M/H] = -0.6 (Yong et al., 2005) were

[3]`http://kurucz.harvard.edu/sun.html`

adopted. This Arcturus temperature and surface gravity are in excellent agreement with Fulbright et al. (2006) and Ramírez & Allende Prieto (2011), though the microturbulence values and metallicities differ slightly between the three studies. Both Fulbright et al. and Ramirez & Allende Prieto find higher metallicities and microturbulence values, with $\xi = 1.67$ km s^{-1} and [Fe/H] $= -0.50$, and $\xi = 1.74$ km s^{-1} and [Fe/H] $= -0.52$, respectively. The Yong et al. microturbulence and metallicity are adopted here, because their values agree best with the Fe I and Fe II abundances derived in this thesis.

2.4 Data Reduction

Once images of the spectra have been recorded on the CCD, they must be converted to spectra whose features can be accurately measured. This process, known as data reduction, involves several key steps:

1. Removing signatures of the CCD (e.g. flat-fielding)
2. Eliminating signatures of the instrument (such as scattered light)
3. Instructing the reduction software how to the convert the image to data (for instance tracing the apertures)
4. Converting to physical quantities (e.g. converting angular dispersion to wavelength)
5. Removing spurious features (such as sky subtraction).

All data were reduced in the Image Reduction and Analysis Facility program (IRAF).[4] The basic data reduction procedure for all HET observations has been modified from a basic HRS script (written by M. Shetrone, private communication). A description of the basic script and modifications made for all HRS targets is given in Chapter 2.4.1; the data reduction process for the HDS targets was performed in a similar way. Chapter 2.4.2 provides a description of the special modifications that were made for Galactic GCs. The method for determining velocity dispersions for the IL targets is described in Chapter 2.4.3.

[4]IRAF is distributed by the National Optical Astronomy Observatory, which is operated by the Association of Universities for Research in Astronomy, Inc., under cooperative agreement with the National Science Foundation.

2.4.1 Basic Data Reduction Techniques

An illustration of an ideal spectrum is shown in Figure 2.5, along with an observed image (from the HET). The general idea behind the data reduction procedure is to convert an image like the one in Figure 2.5b into scientifically useful spectra. The steps in this process are described in detail in this section; note that the steps are loosely described in the order in which they are performed. (The precise order depends on the target.)

Bias Removal: Another signature of the CCD is imparted by the different zero - point levels in each pixel. To correct this effect, short ($t_{\rm exp} \approx 0$ sec) exposures are taken and are removed from the science images. Though this is normally a standard part of the data reduction procedure, *this step was not performed on the HET images*, as the process adds noise to images.[5]

Flat fielding: As photons from a target impact a CCD they liberate electrons, which are stored in individual pixels until the end of the exposure when they are transferred to the detector. Charge storage and/or transfer efficiencies differ between pixels, which can make certain pixels appear brighter than others regardless of whether or not the incident flux onto a pixel was higher. In a flat field image the CCD is uniformly illuminated; this image then provides an idea of which pixels appear intrinsically brighter or fainter than the others, and those pixels are adjusted in the final image. To remove these pixel-to-pixel variations the target data is divided by the flat field image.

Defining and tracing apertures: In order to convert an image like Figure 2.5b into a spectrum, the software needs to know where on the CCD the spectra are located. For example, in Figure 2.5b there are thirteen orders spread out over the CCD, which are not perfectly aligned with the dispersion axis—IRAF must be able to locate these thirteen apertures and trace them down the image. If the locations, widths, and traces of the apertures are fairly stable with a given instrumental configuration, they can be defined with a reference image.

Scattered light removal: As the observed light travels through the spectrograph, a small portion of light is scattered out of the defined apertures by the spectro-

[5]Previous tests with the HET CCD showed that the pixel-to-pixel noise introduced by bias removal was actually higher than the bias levels; see the online HRS Data Reduction Tips at `http://hydra.as.utexas.edu/?a=help&h=29#HRS`.

graph. With bright objects the scattered light is insignificant. For faint objects, however, this light can be detected between the spectral orders and therefore affects the target spectra. This light can be removed by modelling the scattered light with a function across the orders. Under the assumption that the light varies continuously across the orders, the magnitude of the scattered light can be modelled and subtracted off.

Spectral extraction: Once an image has been appropriately calibrated and the spectra have been identified, the individual apertures are summed together into one-dimensional spectra. The HET spectra are extracted with two special options:

- *Background fitting.* During the extraction, the sky fibres on either side of the object aperture are fit with a function. The extracted sky spectrum is then saved for sky subtraction (see below).
- *Variance weighting.* During an extraction cosmic ray hits on the spectra will lead to large flux peaks that can obscure the true signal (see the white spots in Figure 2.5b). A special variance weighting procedure can remove many of these cosmic ray hits from the observed spectrum. During the extraction, IRAF considers the gain and read-noise of the CCD and can assign deviant pixels lower weights. IRAF also cleans out pixels that deviate significantly from the noise model. Ultimately this procedure removes many of the bright cosmic rays.

  An unintended consequence of the variance weighting is that the spectrum's flux distribution is altered, i.e. the shape created by the blaze function of the spectrograph is destroyed. To fix this, the variance-weighted spectra are divided by the non-variance-weighted spectra. The output spectrum is fit with a high order polynomial; the variance weighted spectrum is then divided by the polynomial fit, preserving the weighted spectrum *and* the non-weighted continuum. Occasionally the variance weighting can add noise to a spectrum—when this occurs, those regions are replaced with the same regions from the non-variance weighted spectra.

Wavelength calibration: When the light is dispersed across the CCD, the data are in pixels rather than units of wavelength. To convert to a wavelength scale, a thorium-argon (Th-Ar) lamp is observed with the same spectrograph setup. The

locations of the many Th-Ar lines are well known and can be matched up with the lines in the observed Th-Ar spectrum, providing an empirical relationship between dispersion and wavelength for each aperture. Very small changes in the instrumental setup (such as the tilts of the cross-disperser) can lead to errors in a wavelength calibration; therefore, it is important to take Th-Ar observations immediately before or soon after any observation.

Sky subtraction: All spectra taken from ground-based telescopes will suffer from some contamination from the Earth's atmosphere, which has a continuum component as well as emission and absorption lines. These lines are noticeable in Figure 2.5b as the bright emission lines and many of the darkest absorption lines. An analysis of a faint target's spectrum requires removal of these features. The methods for obtaining separate sky exposures (of the continuum component and the emission lines), for each target type are discussed in Chapter 2.3. If the sky spectra are obtained with different fibres (as with HRS) they must be multiplied by some scaling factor to bring them up to the same flux as the sky that was observed in the object fibre. This factor can be determined by performing separate observations of the twilight sky (known as a skyflat).

Once the scaling factor is known, the sky spectra can be subtracted off directly. However, if the targets are particularly faint and noisy, subtracting the sky spectrum will add noise to the spectrum. For faint targets, therefore, the continuum is fit, and the emission lines are added back onto the continuum fit. The emission lines from the UVES sky spectrum database[6] were identified in a reference image and were then applied to the science targets.

The sky's spectrum can vary significantly with time, both in overall sky flux and the relative strengths of the features (since, e.g., the amount of atmospheric water vapor in the line of sight can vary). Thus, removal of any of the sky features will therefore likely be imperfect.

Telluric line removal: The atmospheric absorption lines (also known as *telluric* lines) are identified and removed using separate observations of a telluric standard star. The telluric standard is typically a hot, bright star; its brightness makes it easy to observe in short integration times, while its high temperature means that it should have fewer spectral lines than cooler stars. (The majority

[6] `http://www.eso.org/observing/dfo/quality/UVES/pipeline/sky_spectrum.html`

of a telluric standard's absorption lines should be telluric; any intrinsic absorption lines such as Hα are also likely to have different shapes than the telluric lines.) These factors make it easy to remove the hot, stellar spectrum, leaving only a spectrum of the telluric lines. By dividing the target spectrum by the telluric spectrum, the effects of sky absorption can be minimized. Again, however, atmospheric variations in time mean that the telluric removal will often be imperfect. Note that telluric removal was not performed on the Pal 1 stars because telluric standards were not observed as part of the observing program.

Normalization: At this stage the spectra are still separated into the different echelle orders, each of which has been shaped by the spectrograph's blaze function (see Chapter 2.2). Individual stellar spectra are typically normalized through polynomial fits to the continuum and subsequent smoothing procedures (as was done for Pal 1). However, IL spectra may have undetectable, broad, weak features that depress the continuum; these broad features may be inadvertently removed during a standard normalization. For IL spectral normalization, the spectrograph's blaze function is determined through observations of an extremely metal-poor (EMP) star (i.e. a star with [Fe/H] $\lesssim -3.0$; see Table 2.7) whose continuum is easily identifiable because of its paucity of spectral lines. The IL spectra were first divided by the EMP continua, rendering them relatively flat. However, the shape of the EMP spectrum is also affected by the blackbody function of the star, which depends on its temperature. If the EMP is the same temperature as the cluster's average temperature the blackbody functions should be similar, but they will not match perfectly. The IL spectra were therefore fit with very low-order polynomials to finish the normalization process.

Radial velocity corrections: The target stars or clusters have motions toward or away from the Earth, which leads to Doppler shifts of their spectral lines. The spectra must therefore be shifted to the rest frame. The radial velocities are determined through cross-correlations with a reference rest-frame spectrum (the Arcturus spectrum), and are converted to heliocentric (Sun-centred) velocities based on the time, date, and location of the observation. These radial velocities are shown in Table 2.8.

Combining observations: The individual observations were then combined. Since

Table 2.7: Properties of the observed EMP star, CS29502-092.

Parameter	Value
RA (J2000)	$22^{\rm h}22^{\rm m}36^{\rm s}.0$
Dec (J2000)	$-01°38'27''.5$
V	11.87
$T_{\rm eff}$ (K)	5001
Observation Dates	2011 Nov 16
Exposure Times (s)	690
S/N[a] (5500 Å)	167
S/N[a] (7000 Å)	341
$v^b_{\rm helio}$ (km/s)	-67.0 ± 0.4

References: The position and magnitude are from the SIMBAD database. The stellar temperature is an average from the Stellar Abundances for Galactic Archaeology (SAGA) database (Suda et al., 2008).
[a]S/N ratios (per pixel) are measured in IRAF.
[b]The radial velocity was determined in the same way as the GC targets.

some cosmic ray hits or sky features may remain even after variance weighting, average sigma-clipping rejections were used to ignore highly deviant points. The individual spectra are either averaged or medianed together, depending on the number of spectra.

2.4.2 Modifications for Galactic GCs

The large sizes of Galactic GCs affect the data reduction process, in several ways:

Background extraction: When the "background" (i..e the spectrum observed with the sky fibres) is fit during the spectral extraction, the resulting spectra are additional target IL spectra rather than sky spectra and must be *added* to the observations rather than subtracted. In order to reduce the noise in the image and to reduce the number of cosmic rays, these additional target spectra are averaged with the original target spectra instead of strictly added.

Separate sky reduction: The separate sky observations must then be reduced completely and separately, each with its own background fitting, wavelength solution, etc.

Sky subtraction: The "cleaned" sky spectrum must then be subtracted from the target spectrum. However, the exposure times between the object and the sky may be quite different. The IRAF task *skytweak* is therefore used to find the optimal scaling factor between the target and sky spectra. The red and blue apertures with the most emission lines were used for this scaling, and the resulting scaling factors were then applied to all apertures.

2.4.3 Velocity Dispersions

The IL spectra are composed of light from all the stars in the observed region. Since GC stars have a dispersion, σ, about the net cluster velocity, each star in the cluster has a slightly different radial velocity; this has the effect of broadening the IL spectral lines—in fact, the velocity dispersion often dominates over other sources of broadening at high spectral resolution. The GC velocity dispersions were determined through cross-correlations with the Arcturus spectrum (see Chapter 2.3.4). The strongest correlations occur where the spectral lines are coincident, i.e. when the object spectrum is shifted by the correct radial velocity. The width of the correlation peak depends on

the line broadening and will therefore provide information about the target's velocity dispersion.

The IRAF task *fxcor* is employed for the cross-correlation, using the method described by Tonry & Davis (1979). Continuum subtractions are performed by *fxcor* on both spectra. The task then identifies the peak with the highest correlation; this peak is centred around the radial velocity, while its full width at half-maximum (FWHM) is related to the velocity dispersion (Alpaslan, 2009). The cross-correlation peak is interactively fit with a Gaussian, and the background level is estimated using a wide window. Slight differences in background level or fitting regions can alter the FWHM slightly, so multiple fits are done to minimize random errors. For the radial velocity measurements, the cross-correlation is performed over most of the spectrum, though regions with the strongest telluric lines are masked out. For the velocity dispersion measurements, the range is restricted to 5400-5700 Å—this wavelength region is free of strong sky lines which could affect the analysis. Note that radial velocity measurements are done for each observation, while velocity dispersion measurements are only done on the final, combined spectrum.

The task therefore produces both an observed radial velocity and a peak FWHM, in km s^{-1}, which is related to the velocity dispersion. The velocity dispersion cannot be calculated directly from the FWHM of the correlation peak; instead, a calibration curve must be used. By broadening the Arcturus template spectrum by a known, artificial velocity dispersion and cross-correlating that broadened spectrum with itself, a relation between the measured FWHM and the velocity dispersion can be found. The Arcturus spectrum is broadened by convolving the original spectrum with Gaussians of varying values of σ. The broadened template spectra are then cross-correlated with the original spectrum. The relationship between peak FWHM and velocity dispersion is fit with a spline function, as shown in Figure 2.7. This correlation function shows that Arcturus has an intrinsic broadening of 13.71 km s^{-1} at $\sigma = 0$ km s^{-1}. The FWHM initially increases very slowly as the velocity dispersion increases. With increasing velocity dispersion, however, the relation becomes approximately linear.

The HET targets all have lower spectral resolution than the Arcturus spectrum, making a cross-correlation slightly more difficult. For the correlation the Arcturus spectrum was rebinned to the lower resolution of the object spectrum, as suggested by Alpaslan (2009). The resulting FWHM from the *fxcor* cross-correlation is then inserted into the correlation function, and the resulting velocity dispersion is found. Because the effects of the spectrograph may be significant for globular clusters with

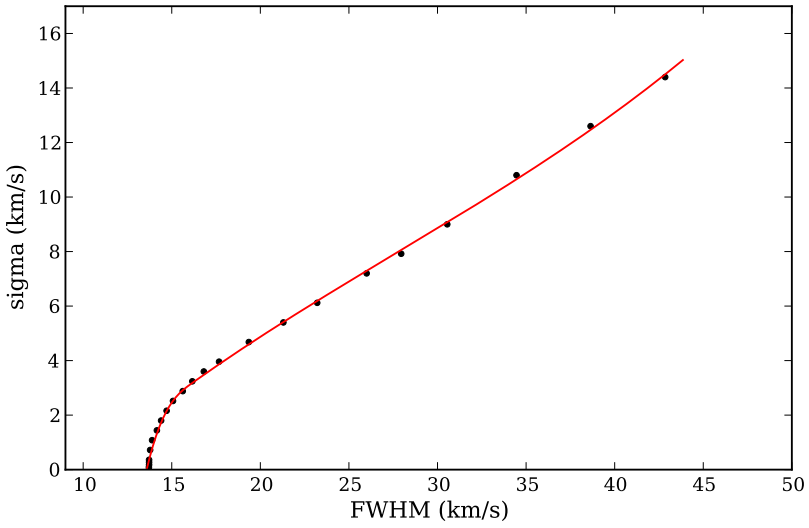

Figure 2.7: The calibration curve relating the measured FWHM of the correlation peak (x-axis) to the broadened width, σ (y-axis). Note that this σ is only equal to the velocity dispersion if the instrumental broadening is close to zero; the HET targets must have an instrumental broadening of 10 km/s removed.

low velocity dispersions, the instrumental broadening must be removed from this total dispersion. The instrumental and velocity dispersion broadenings are described by Gaussians and the observed profile is a convolution of those two Gaussians; the total FWHM is therefore a quadrature sum of the individual Gaussians:

$$\mathrm{FWHM_{tot}} = \sqrt{\mathrm{FWHM_{\sigma}^2} + \mathrm{FWHM_{ins}^2}}. \tag{2.3}$$

Since the spectral resolution of the HRS targets is $R = 30,000$, the resulting instrumental FWHM is 10 km/s. The velocity dispersion can then be found from the total FWHM.

The final velocity information is shown in Table 2.8, along with literature values (where possible). Note that the Pal 1 stars do not have velocity dispersions listed, since they are single stars. The Galactic GC values agree well with those from the literature, though slight discrepancies are to be expected since only the cores are measured in the IL spectra (see Djorgovski et al. 1997). Figure 2.8 compares the IL values to all MW clusters with measured velocity dispersions (from Harris 1996; 2010 edition); there is a clear trend of increasing σ with decreasing M_V, and the MW and PAndAS clusters fall right on this trend.[7]

2.5 Final Spectra

Portions of the fully reduced and normalized spectra are shown in Figures 2.9, 2.10, 2.11, and 2.12, along with notable spectral features.

[7]It should also be noted that Arcturus' high metallicity ([Fe/H] ~ -0.6) complicates the cross-correlation process to determine velocity dispersions, because its intrinsic line profiles are different from those of a metal-poor star. However, the derived velocity dispersion values show no correlation with [Fe/H].

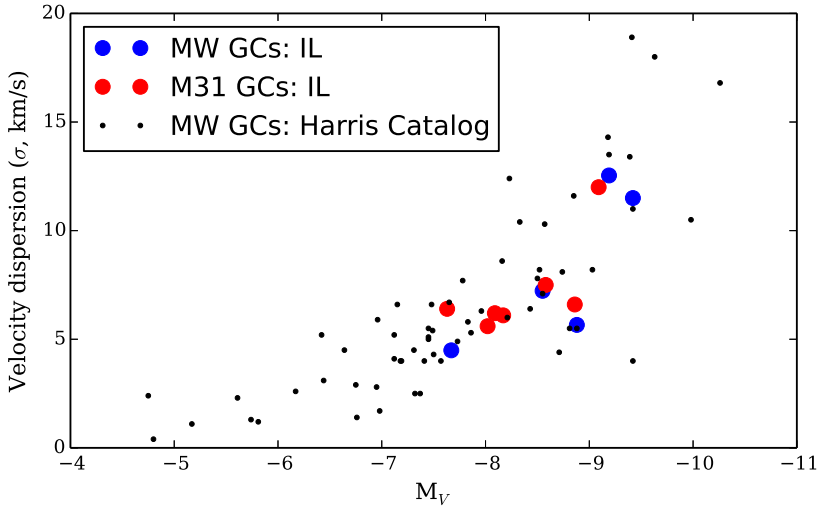

Figure 2.8: Cluster velocity dispersions, σ (in km s^{-1}) versus total cluster magnitude, $M_{\rm V}$ for the Galactic targets (blue circles), the PAndAS targets (red circles), and MW clusters from the literature (black points; from Harris 1996; 2010 edition). There is a clear trend of increasing velocity dispersion with total magnitude; this trend is expected, since both σ and cluster brightness are correlated with cluster mass. The velocity dispersions derived from IL spectra agree well with the values derived from individual stars.

Table 2.8: Velocity information.

Target	$v_{\rm helio,obs}$ (km/s)	$v_{\rm helio,lit}$ (km/s)	$\sigma_{\rm obs}$ (km/s)	$\sigma_{\rm lit}$ (km/s)	Literature References
M67-141	+33.9±1.0	34.1±1.6	n/a	n/a	1, 2
Pal 1-I	−77.2±1.0	−78.5±3.5	n/a	n/a	3, 4
Pal 1-II	−78.0±1.0	−83.2±7.5	n/a	n/a	4
Pal 1-III	−77.2±1.0	−85.5±7.3	n/a	n/a	4
Pal 1-IV	−68.1±1.0	−87.3±11.9	n/a	n/a	4
Pal 1-C	−77.0±1.0	–	n/a	n/a	4
47 Tuc	–	–	11.50±0.30[a]	11.0	5
M3	−146.0±1.1	−147.6	5.66±0.15	5.5	5
M13	−247.5±1.3	−244.2	7.23±0.33	7.1	5
NGC 7006	−380.4±0.7	−384.1	4.49±0.60	–	5
M15	−106.6±0.2	−107.0	12.54±0.60	13.5	5
H10	−351.9±1.5	−352±9	6.6±0.4	–	6
H23	−373.3±0.1	−377±11	6.2±0.4	–	6
PA06	−341.4±0.7	−327±15	5.6±0.4	–	6
PA17	−260.0±1.0	−279±15	6.1±0.5	–	6
PA53	−270.8±0.9	−253±10	12.0±0.4	–	6
PA54	−344.9±0.8	−336±8	7.5±0.4	–	6
PA56	−241.4±1.7	−239±8	6.4±0.4	–	6

References: (1) Yong et al. (2005), (2) Pancino et al. (2010), (3) Monaco et al. (2011), (4) Rosenberg et al. (1998b), (5) the references quoted in Harris (1996; 2010 edition), (6) Veljanoski et al. (2014)

[a]This velocity dispersion has been determined in the same way as the other GCs, for consistency.

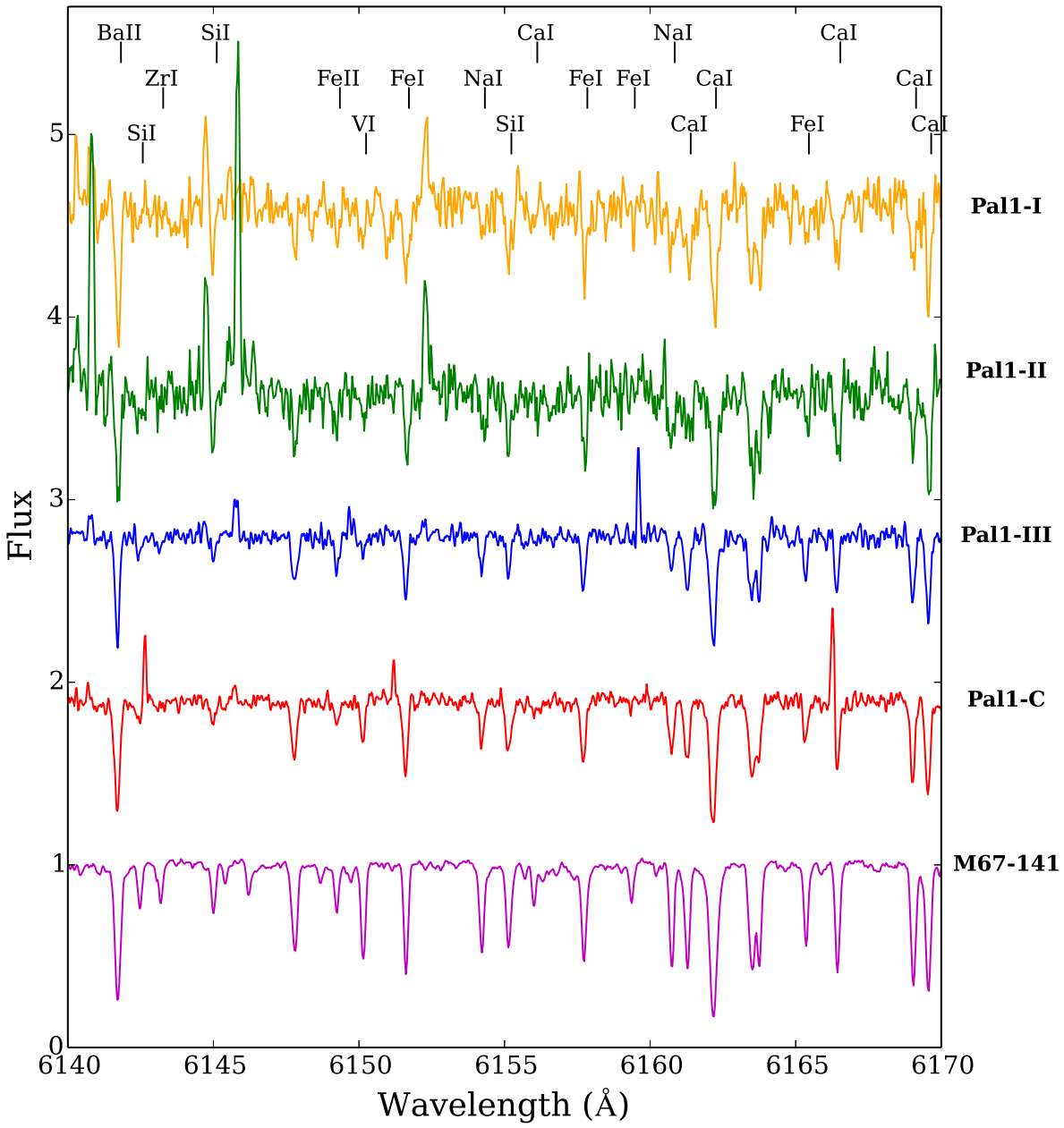

Figure 2.9: Final spectra for the Palomar 1 project. Spectral lines used in typical RGB analyses are identified. Note that Pal 1-I and -II have lower S/N than the other spectra. The brighter points are typically incompletely removed sky lines or cosmic rays.

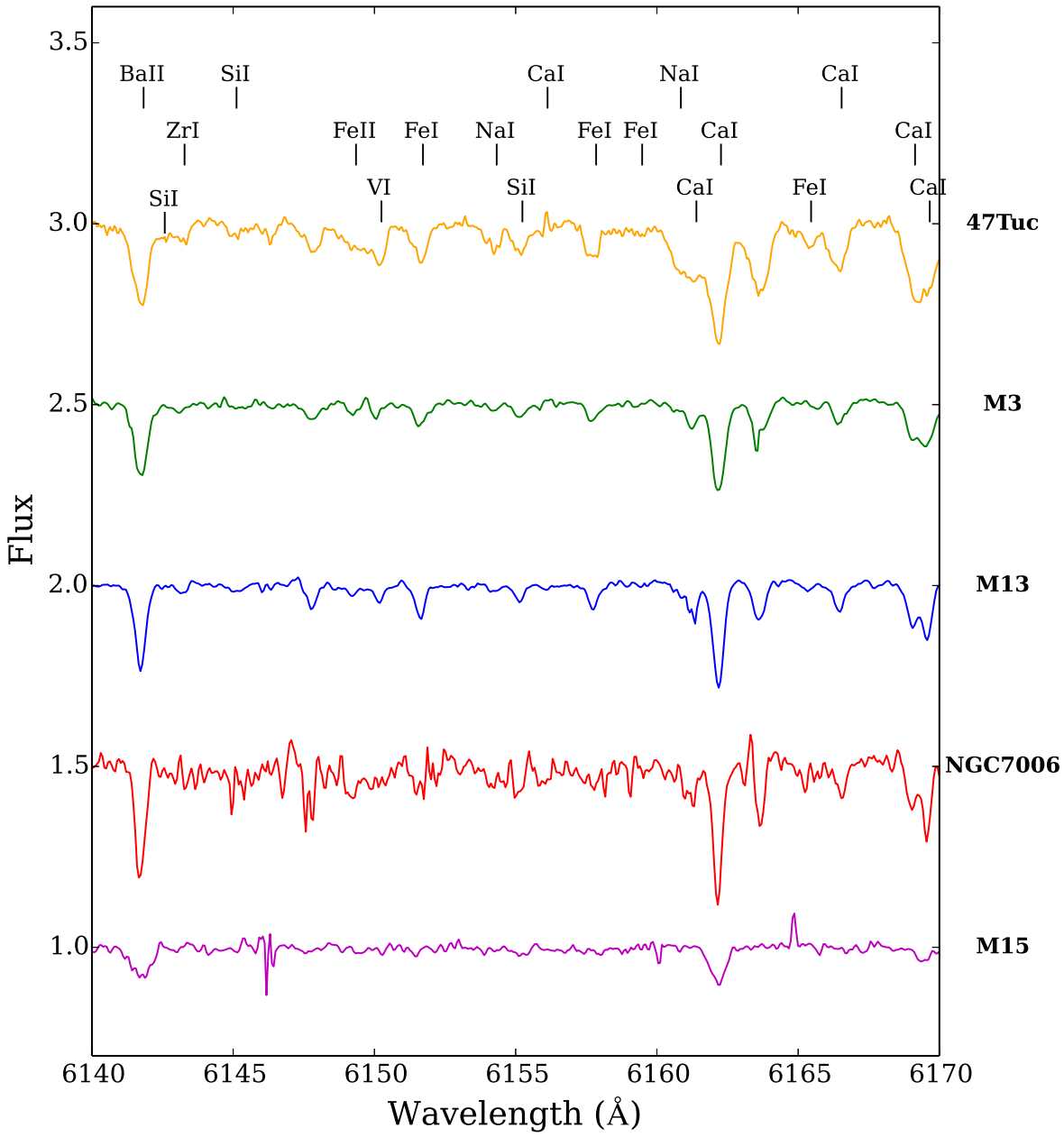

Figure 2.10: Final IL spectra of the Galactic GCs, arranged by metallicity. Spectral lines used in typical RGB analyses are identified.

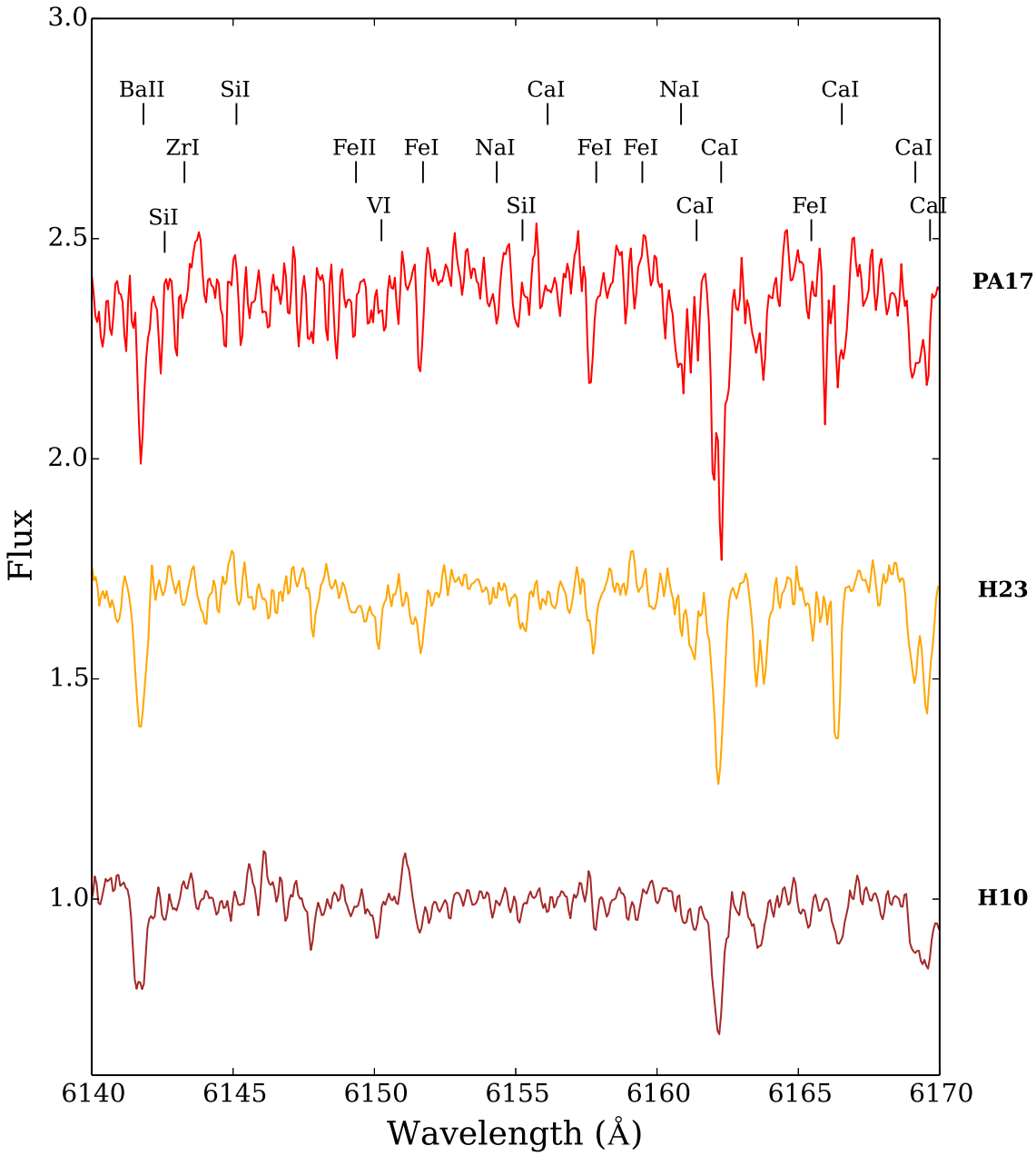

Figure 2.11: Final IL spectra of the metal-rich PAndAS GCs. Spectral lines used in typical RGB analyses are identified.

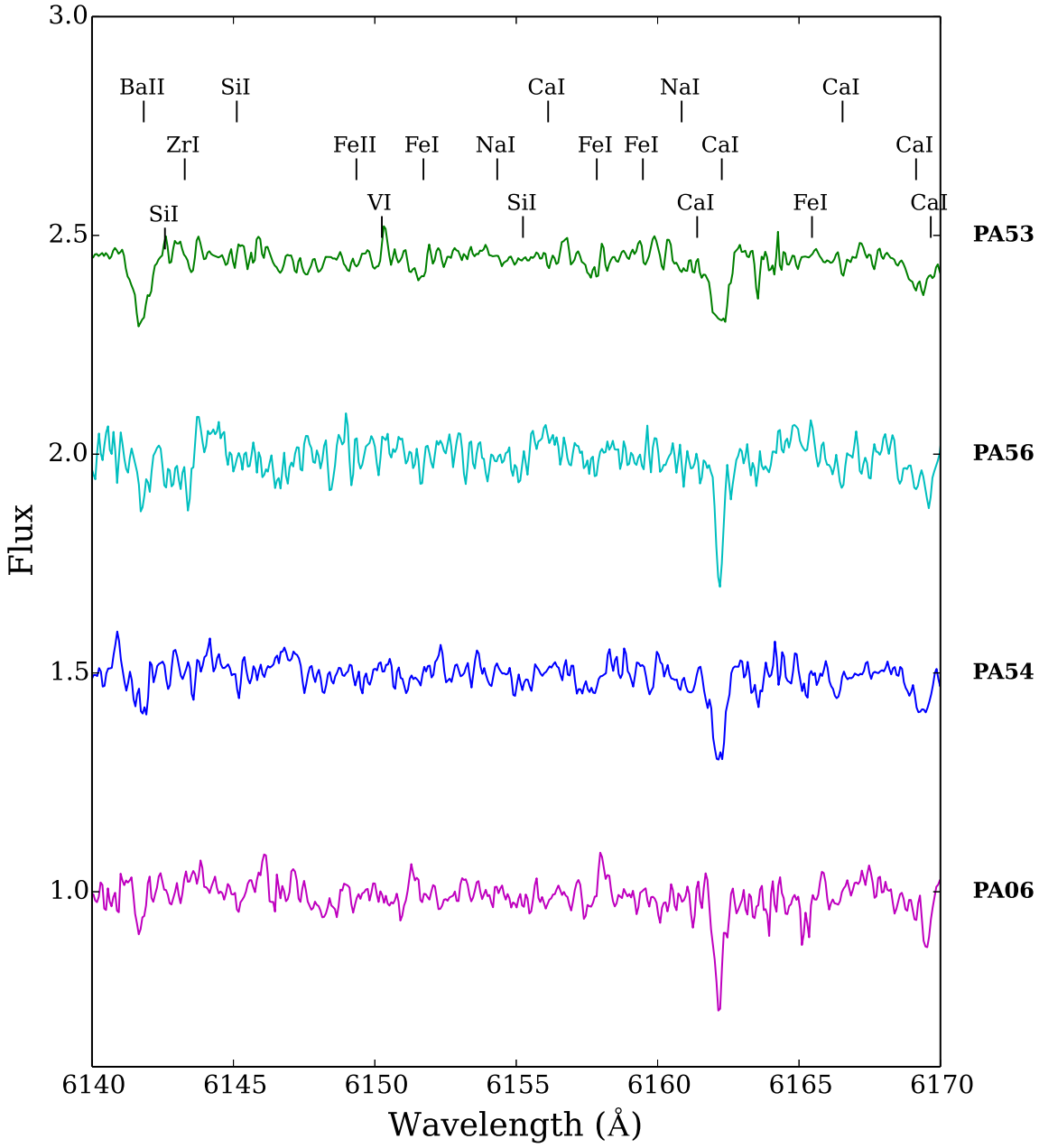

Figure 2.12: Final IL spectra of the metal-poor PAndAS GCs. Spectral lines used in typical RGB analyses are identified.

Chapter 3

A Standard Chemical Tagging Analysis of Four Red Giant Stars in Palomar 1

As mentioned in Chapter 1, Palomar 1 was selected as a target for high resolution spectroscopic observations because it is an unusual cluster. The unusual characteristics of Pal 1 are summarized in Table 3.1, along with an indication of whether the property indicates that Pal 1 is more like a GC or an open cluster (OC). Specifically, Pal 1 was initially classified as a GC (Abell, 1955) because of its location high above the plane, though its paucity of stars, young age, and metallicity indicate that it is not a typical Galactic GC. Figure 3.1 also illustrates that Pal 1's position in the galaxy is unusual given its relatively high metallicity. Spatially, Pal 1 is more similar to Ter 7, Pal 12, Whiting 1, and Rup 106, which are suspected to have been accreted from the Sagittarius (Sgr) dwarf spheroidal. Based on its position and kinematics, Pal 1 has also been tentatively linked with two stellar streams, the Canis Major (CMa) overdensity and the Galactic Anticenter Stellar Stream (GASS), which may be the disrupted remnants of dwarf galaxies. Its unusual properties indicate 1) that Pal 1 is neither a typical GC nor a typical OC, and 2) that it may have originated in a dwarf galaxy.

A spectroscopic analysis is ideal for determining the nature of Pal 1. First of all, Carretta et al. (2009a) argue that all bona fide GCs have stars whose abundances exhibit the Na/O anticorrelation. If Pal 1 does not have signs of the anticorrelation, then it is not a traditional GC. Secondly, if Pal 1 was accreted from a dwarf galaxy, its

Table 3.1: Characteristics of Pal 1 from previous observations.

Parameter	Value	Cluster Type	Reference
$R_{\rm GC}$	17.2 kpc	-	1
Z	3.6 kpc	GC	1
c	2.57	GC	1
$M_{\rm V,tot}$	-2.52	OC[a]	1, 2
age	4-7 Gyr	OC/GC[b]	3, 4, 5
[Fe/H]	-0.6	OC/GC[c]	6

References: (1) Harris (1996; 2010 edition), (2) Carretta et al. (2010b), (3) Chaboyer et al. (1996), (4) Rosenberg et al. (1998a), (5) Sarajedini et al. (2007), (6) Rosenberg et al. (1998b)

[a] Pal 1's low brightness does not preclude it from being a GC (see the discussion in Chapter 3.5.1), but its total magnitude agrees better with OCs, at least in the MW.

[b] Though this age is old for an open cluster, it is comparable to the oldest open clusters, e.g. VandenBerg & Stetson (2004). Similarly, this age is young for a GC, although it is in agreement with Ter 7, Pal 12, and Whiting 1 (Buonanno et al., 1998; Salaris & Weiss, 2002; Carraro et al., 2007; Dotter et al., 2010).

[c] Although there are many metal-rich GCs in the MW, such a high [Fe/H] is quite unusual for an outer halo GC—see Figure 3.1.

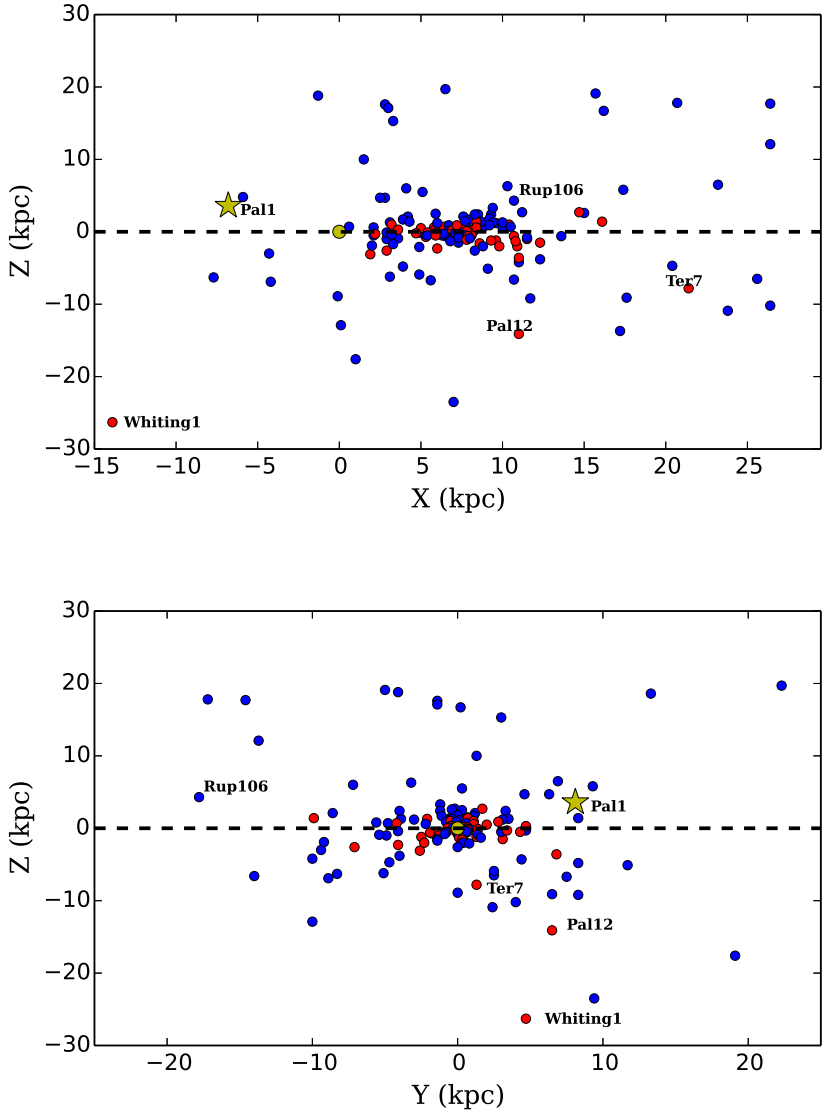

Figure 3.1: The location of GCs in the MW. The blue points are GCs more metal-poor than [Fe/H] $-$ 1, while the red points are the more metal-rich GCs. Pal 1 is indicated with a yellow star. The other unusual GCs (Ter 7, Pal 12, Whiting 1, and Rup 106) are also labelled. The Sun is shown as a yellow point, for reference. *Top:* The X, Z positions of the clusters. The centre of the Galaxy is located at $(\sim 8, 0)$. *Bottom:* The Y, Z positions of the clusters. The centre of the Galaxy is located at $(0, 0)$. Spatially, Pal 1 is clearly dissimilar from the other typical metal-rich (red) GCs (which are closer to the centre of the Galaxy) and is more like the unusual GCs, which may have been accreted from dwarf galaxies.

chemical abundances should be distinct from MW field stars, as described in Chapter 5.5.3. If it belongs to a specific stream, Pal 1's detailed abundances should enable it to be chemically tagged to that host stream. Pal 1 was therefore targeted for high resolution observations. The basic steps of a standard chemical abundance analysis are:

1. Obtain high resolution spectra (discussed in Chapter 2.3.1)
2. Assign model atmospheres to the stars (Section 3.1)
3. Measure spectral features (see Section 3.2 and Appendix C)
4. Determine photospheric abundances for targets (Section 3.3)
5. Compare elemental abundance ratios between systems (Section 3.4)
6. Infer something about the nature of the target (Section 3.5).

This study serves as an example of a standard chemical abundance analysis; later IL analyses will build on the basic techniques described here.

3.1 Model Atmospheres

The goal of a high resolution spectroscopic analysis is to determine the amount of a given element that is present in a stellar atmosphere. As discussed in Chapter 1, this requires understanding what happens to the light from the surface of a star as it travels through the photosphere; thus the stellar atmosphere must be modelled. The stellar atmospheric parameters (effective temperature, $T_{\rm eff}$; surface gravity in its logarithmic form, $\log g$; microturbulence, ξ, in km s^{-1}; and metallicity, [Fe/H], are initially derived from broadband photometry (Section 3.1.1) and revised based on spectral indicators (Section 3.1.2). Once the atmospheric parameters are selected, OSMARCS Local Thermodynamic Equilibrium (LTE) model atmospheres with spherical geometries (Gustafsson et al. 2008, Plez & Lambert 2002) are assigned to each star.

3.1.1 Photometric Parameters

Metallicity

Initial estimates for metallicity ([Fe/H]) for M67-141 are from high resolution spectroscopic analyses ([Fe/H] = 0.01, Yong et al. 2005). For the Pal 1 stars the estimates

from measurements of the Ca II triplet are adopted ([Fe/H] = −0.6, Rosenberg et al. 1998b).

Temperature

The photometric effective temperatures are calculated with empirical metallicity-dependent relations between $(V - K)$ colour and $T_{\rm eff}$, which were determined by Alonso et al. (1999, with the Alonso et al. 2001 correction). The V and K magnitudes in Table 2.1 provide $(V - K)$ colours in the Johnson photometric system. The Alonso et al. colour-temperature relations require $(V - K)$ colours in the TCS photometric systems (named after the Telescopio Carlos Sánchez at the Canarian Observatories); the conversions of Alonso et al. (1999) are therefore applied to the magnitudes in Table 3.2. Because the temperature calibrations are based on the *absolute* colours of the stars, the cluster reddening, $E(B - V)$,[1] must be taken into account. The adopted reddenings for Pal 1 and M67-141 are $E(B-V) = 0.20 \pm 0.03$ and $E(B-V) = 0.033 \pm 0.005$, from the Schlegel et al. (1998) dust extinction maps. The $E(V - K)$ reddening is determined with the conversions of McCall (2004).

The adopted photometric temperatures are shown in Tables 3.2. Errors are determined based on the uncertainties in the input metallicity and reddening.

Surface Gravity

The photometric surface gravity of a star is determined from its luminosity (L, in $\rm L_\odot$), mass (M, in $\rm M_\odot$), and temperature ($T_{\rm eff}$, in K):

$$\log g = \log g_\odot + \log \frac{M}{M_\odot} - \log \frac{L}{L_\odot} + 4 \log \frac{T_{\rm eff}}{T_{\rm eff,\odot}} \tag{3.1}$$

where $\log g_\odot = 4.44$ and $T_{\rm eff,\odot} = 5790$ K. The mass of the target RGB stars can be estimated with stellar isochrones (shown in Figure 2.1b)—in particular, first ascent RGB stars should have approximately the same mass as the turnoff stars. For Pal 1 this mass is $M_{\rm TO} = 1.14 \pm 0.06$ $\rm M_\odot$ (from the DSED isochrones; Dotter et al. 2008). M67 has a similar age (4-5 Gyr; VandenBerg & Stetson 2004), indicating a similar turnoff mass. However, its higher metallicity means that its turnoff mass might be slightly higher than Pal 1's—the slight difference in turnoff mass has a negligible effect on $\log g$.

[1] Recall that reddening is caused by dust; see Chapter 1.2.

The stellar luminosities are determined from their apparent V magnitudes (Table 2.1), which are converted to absolute magnitudes (M_V) via their visual distance moduli, $(m-M)_V$:

$$M_V = V - (m-M)_V. \tag{3.2}$$

For M67-141 the absolute distance modulus quoted in Yong et al. (2005) is adopted: $(m-M)_0 = 9.56$, or $(m-M)_V = 9.66$.[2] For Pal 1 there are two different literature values for the distance modulus: Rosenberg et al. (1998a) give (m-M)$_0 = 15.25 \pm 0.25$ while Sarajedini et al. (2007) give (m-M)$_0 = 15.65 \pm 0.10$. Both are determined through fitting Pal 1's main sequence to 47 Tuc, a Galactic globular cluster with a similar metallicity to Pal 1.[3] Here the Sarajedini et al. (2007) distance modulus, $(m-M)_V = 16.26$ (which is determined from *HST* photometry), is adopted.[4]

The absolute magnitudes are converted to bolometric magnitudes ($M_{\rm bol}$) with bolometric corrections (BCs, which are determined through empirical relationships with $T_{\rm eff}$ and [Fe/H]; Alonso et al. 1999). The BCs are related to bolometric magnitudes by the following expression:

$$M_{\rm bol} = M_V + BC. \tag{3.3}$$

The luminosity is then related to the bolometric magnitude:

$$\log \frac{L}{L_\odot} = 10^{-0.4(M_{\rm bol} - M_{\rm bol,\odot})} \tag{3.4}$$

where the luminosity, L, is expressed in Solar luminosities and the Solar bolometric magnitude is $M_{\rm bol,\odot} = 4.75$. The effective temperatures, masses, and luminosities are then fed to Equation 3.1, leading to the photometric surface gravities listed in Table 3.2.

[2]The relation $A_V = 3.07E(B-V)$ is adopted (McCall, 2004).

[3]As discussed in Rosenberg et al. (1998a), the presence of the sparse horizontal branch is uncertain, preventing accurate determinations of the distance modulus using zero age horizontal branch methods (e.g. VandenBerg et al. 2000).

[4]The discrepancy in distance moduli may be due to the lower quality of the Rosenberg et al. CMD: the equal mass binaries cannot be resolved from the MS, making the MS appear brighter and leading to a lower distance modulus. These binaries are resolved with *HST*, and the Sarajedini et al. (2007) distance modulus is likely to be more accurate.

Table 3.2: Atmospheric Parameters for the Pal 1 stars.

Star	Photometric $T_{\rm eff}$ (K)	$\log g$	Spectroscopic $T_{\rm eff}$ (K)	ξ (km s^{-1})	[Fe/H]	$v \sin i^a$ (km s^{-1})
M67-141	4624 ± 12	2.31 ± 0.06	4750 ± 50	1.4 ± 0.1	0.02 ± 0.02	4.5
Literature:						
M67-141						
Y05	4700 (4604)[b]	2.3	4700	1.34	0.00	-
P10	4590	2.8	4650	1.3	0.06	-
Pal 1-I	4742 ± 81	2.27 ± 0.15	4800 ± 70	1.4 ± 0.3	-0.61 ± 0.08	2.5
Pal 1-II	4725 ± 80	2.33 ± 0.15	4750 ± 135	1.6 ± 0.2	-0.61 ± 0.08	2.5
Pal 1-III	5061 ± 90	2.89 ± 0.15	5050 ± 50	0.9 ± 0.1	-0.60 ± 0.02	0.5
Pal 1-C	4698 ± 79	2.22 ± 0.15	4750 ± 70	1.3 ± 0.1	-0.58 ± 0.03	1.5
Literature:						
Pal 1-I						
M11	4850	2.40	5000	1.0	-0.5	-

Discrepancies between photometric and spectroscopic parameters could indicate, e.g., uncertain photometric transformations.

References: Y05 = Yong et al. (2005), P10 = Pancino et al. (2010), M11 = Monaco et al. (2011)

[a] This parameter was determined for spectrum syntheses, as discussed in Chapter 3.2.

[b] The temperature in parentheses is the photometric temperature with the spectroscopic metallicity.

3.1.2 Spectroscopic Parameters

Once the initial photometric parameters have been determined, they are refined based on the abundances from the iron lines. Iron lines are chosen for this purpose because:

1. There are many Fe I lines available in the optical (up to ~ 100, depending on S/N and [Fe/H])
2. The Fe I lines form over multiple atmospheric layers and cover a wide range of line properties
3. Lines of both Fe I (neutral Fe) and Fe II (singly ionized Fe) are often available.

Thus, the Fe abundances serve as a good indicator of how well the atmosphere is modelled. In particular a star only has a single Fe abundance—therefore, if various Fe lines indicate different Fe abundances, the model parameters are likely to be incorrect.

Temperature

The photometric temperatures are refined based on the trends of Fe I abundance with line excitation potential (EP; see the top panel in Figure 3.2). In general, hotter stars can excite more high energy photons, which are absorbed and produce the highest EP lines. If the highest EP lines predict a larger Fe I abundance (i.e. if the trend is positive), then the model temperature is too low. The temperature can therefore be refined by forcing this trend to be as flat as possible. However, spectral lines form over multiple atmospheric layers. These trends also probe the temperature gradient in the star and are also slightly affected by the other atmospheric parameters.

The trends were calculated with linear least squares fits and the slopes therefore have their own uncertainties. The associated errors in the spectroscopic temperatures were found using these 1σ errors in the slopes. For example, the slope in the top panel of Figure 3.2 is $m = 0.0097 \pm 0.015$. The associated errors in $T_{\rm eff}$ were determined by examining values that led to slopes in the range $[-0.02, +0.02]$.

The spectroscopic temperatures and their errors are shown in Table 3.2.

Microturbulence

The microturbulence, ξ (which does not have a photometric estimate), is a parameter that accounts for small scale motions within a star. These small scale motions broaden

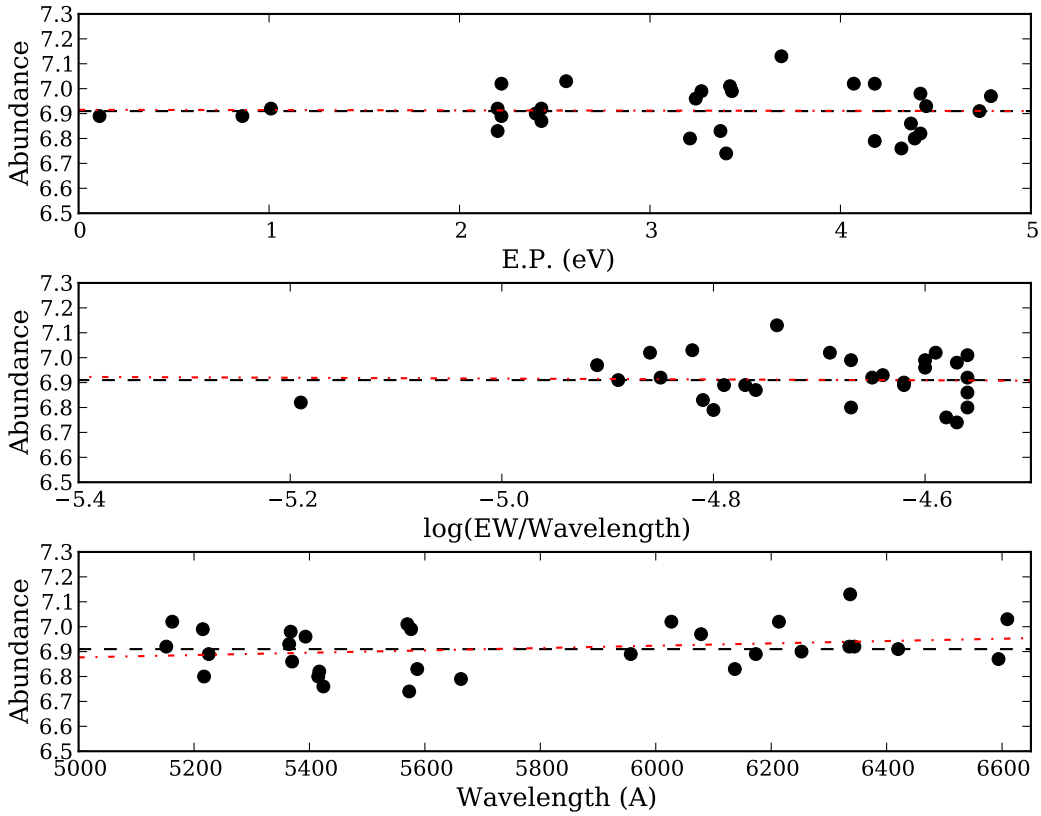

Figure 3.2: The Fe I abundance trends with excitation potential (top), reduced EW (middle) and wavelength (bottom) for Pal 1-I, with the spectroscopic atmospheric parameters listed in Table 3.2. The black dashed line shows a constant trend, while the red dot-dashed line shows the trends of the data; note that in all three panels the trend is essentially constant, though there is still a significant dispersion.

out the spectral lines—the atmospheric microturbulent velocities therefore affect the trends in Fe I abundance with reduced EW (REW,[5] see the middle panel of Figure 3.2, where the fit to the spectral lines has a slope of 0.025 ± 0.12). If a star's microturbulent velocity is too low, the strongest lines require more Fe atoms to match the strengths of the observed features, leading to a positive trend between Fe I abundance and REW. Flattening this trend leads to the correct microturbulence. Uncertainties in the microturbulent velocities were calculated as for $T_{\rm eff}$.

Metallicity

The final metallicity, [Fe/H], is chosen to be the output [Fe I/H] abundance from `MOOG` (see Chapter 3.3), with an error determined from the line-to-line scatter, σ(Fe I), divided by the square root of the number of lines (δ(Fe I) = σ(Fe I)/$\sqrt{N}$; see Section 3.3.2).

Surface Gravity

Other studies have refined the surface gravity by forcing the Fe abundances from the Fe I and Fe II lines to be equal. In principle this should be a valid criterion, since the photosphere can only have a single Fe abundance. However, this may not be a good choice, for two reasons:

1. The Fe I abundance is expected to suffer from non-LTE effects, where interactions with the radiation field reduce the number of Fe I atoms from what would be expected based on the Saha equation.

2. There are few Fe II lines in the spectral range observed with HDS; those that are available are located at blue wavelengths so that reliable Fe II abundance determinations can be difficult, especially in low S/N spectra.

For these reasons, the photometric surface gravities and their associated errors are retained.

[5] REW = EW/λ. The REW is chosen for plotting purposes because the strength of a line also depends on the transition wavelength.

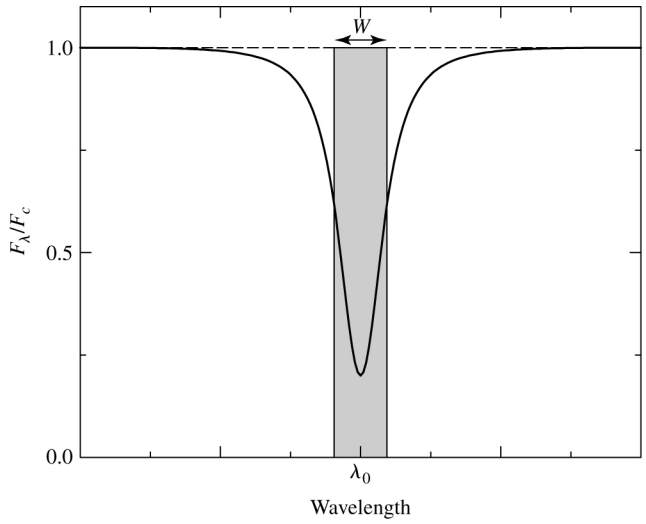

Figure 3.3: An illustration of a spectral line's equivalent width (EW) from Carroll & Ostlie (2006).

3.2 Spectral Measurements

The spectral features in the target stars were measured with two different techniques, which are described below.

Equivalent Widths: One way to parameterize the strength of a line is by its *equivalent width* (EW), which is the width of a rectangle that has a height at the continuum level and the same *area* beneath the continuum as the observed spectral line. This concept is illustrated in Figure 3.2.

EWs are measured through Gaussian fits to the observed spectral lines. The details of this procedure, the EW values themselves, and the associated errors are given in Appendix C. This method is excellent for elements with many spectral lines since the abundance error from a given measurement can be reduced by measuring many lines.

Spectrum Syntheses: For elements with only a few lines, or for elements that only have weak lines, it is preferable to measure the spectral features by synthesizing all lines in a 10 Å region. This enables all lines to be fit simultaneously while taking the broadening, atmospheric parameters, and chemical composition into account. For example, a spectrum synthesis of the Mg I 5528 Å line in Pal 1-I is shown in Figure 3.4.

In each spectrum synthesis the line broadening (which should be approximately the same for all spectral lines[6]) is fixed. With resolutions of $R = 36,000$ and $R = 60,000$, Pal 1 and M67-141 have instrumental broadening values of 8.3 and 5.0 km s^{-1}, respectively. The rotational broadenings for each star were determined by examining nearby lines with known abundances, and adjusting the $v \sin i$ values until the widths and depths matched the points. The derived $v \sin i$ values for M67-141 and the four Pal 1 stars are shown in Table 3.2.

Blends with nearby lines can also be included in spectrum syntheses, as in the case of the 6141.73 Å Ba II line, which is blended with a Ni I line at solar metallicity (Allende Prieto et al., 2001). By using spectrum syntheses, the strength of the Ni line can also be taken into account.

The abundances were then estimated from the best fits to the adopted models, with an error in $\log \epsilon$ equal to the range of abundances that fit the line profiles. Where the spectral lines were particularly noisy, only upper limits are provided.

3.3 Abundances

With the EWs and spectrum syntheses, abundances were determined with the 2010 version of the LTE line analysis program `MOOG` (Sneden, 1973). `MOOG` provides an abundance for element X in the form

$$\log \epsilon(X) = 12 + \log\left(\frac{N_{\rm X}}{N_{\rm H}}\right) \tag{3.5}$$

where $N_{\rm X}$ and $N_{\rm H}$ are the column densities of element X and hydrogen, respectively. These abundances are generally compared to the Solar values through the ratio [X/H]:

$$\begin{aligned} [{\rm X/H}] = &\quad 12 + \log\left(\frac{N_{\rm X}}{N_{\rm H}}\right) - 12 + \log\left(\frac{N_{\rm X,\odot}}{N_{\rm H,\odot}}\right) \\ = &\quad \log \epsilon({\rm X}) - \log \epsilon({\rm X})_\odot. \end{aligned} \tag{3.6}$$

Thus, if a star has [Fe/H] $= -1$, it has 10 times *less* iron (relative to H) than the Sun.

[6]Recall that $R = \lambda/\Delta/\lambda =$ a constant—thus, the instrumental $\Delta\lambda$ varies slightly with wavelength.

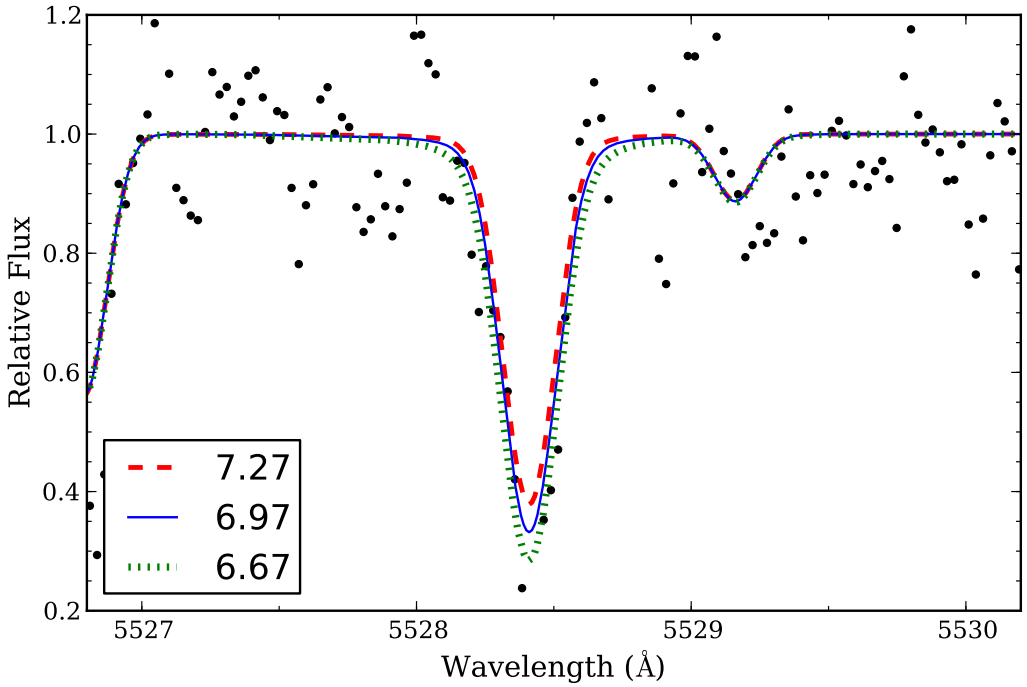

Figure 3.4: A spectrum synthesis of the Mg I 5528 Å line in Pal 1-I, one of the lower S/N targets. Syntheses for three different Mg abundances are shown: $\log \epsilon(\mathrm{Mg}) = 7.27$, 6.97, and 6.67. Note that though the fits match the width of the line well, the bottom-most point is not fit; this point is most likely a noise spike.

Chemical abundance studies also often compare the abundances of various elements other than H to each other. The most common choice is to compare an element X to Fe through the ratio [X/Fe]:

$$\begin{aligned}
[\mathrm{X/Fe}] &= 12 + \log\left(\frac{N_{\mathrm{X}}}{N_{\mathrm{Fe}}}\right) - 12 + \log\left(\frac{N_{\mathrm{X},\odot}}{N_{\mathrm{Fe},\odot}}\right) \\
&= 12 + \log\left(\frac{N_{\mathrm{X}}}{N_{\mathrm{H}}}\right) - \log\left(\frac{N_{\mathrm{Fe}}}{N_{\mathrm{H}}}\right) - 12 + \log\left(\frac{N_{\mathrm{X},\odot}}{N_{\mathrm{Fe},\odot}}\right) - \log\left(\frac{N_{\mathrm{Fe},\odot}}{N_{\mathrm{H},\odot}}\right) \\
&= \log\epsilon(\mathrm{X}) - \log\epsilon(\mathrm{X})_{\odot} - \log\epsilon(\mathrm{Fe}) - \log\epsilon(\mathrm{Fe})_{\odot} \\
&= [\mathrm{X/H}] - [\mathrm{Fe/H}].
\end{aligned} \tag{3.7}$$

Such ratios are useful because the various elements have different nucleosynthetic sites, as discussed in Chapter 1.

3.3.1 Solar Abundances

Equations 3.6 and 3.7 require values for the Solar abundances. These values have been calculated using high precision spectroscopy (e.g. Asplund et al. 2009) and through investigations of meteoritic compositions (e.g. Lodders et al. 2009). Here the Solar abundances are determined *in the same way as for the target stars*—this should minimize the uncertainties due to, e.g., uncertain atomic data or different measurement techniques.

The final Solar abundances are shown in Table 3.3 along with the Asplund et al. (2009) photospheric values and the Lodders et al. (2009) meteoritic values. The results are in excellent agreement, though O, Sc, and Ba are all higher in this analysis, a trend that was also noticed by Yong et al. (2005, for O and Ba), Pancino et al. (2010, for Ba) and Monaco et al. (2011, for Sc and Ba). These high abundances are likely because of differences in, e.g., line selection, model atmospheres, etc., and indicates that the Pal 1 O, Sc, and Ba $\log\epsilon$ abundances could also be high; however, by comparing with the high solar values, the systematic high offsets in [O/Fe], [Sc/Fe], and [Ba/Fe] values will be removed. Because the single Eu line is very weak in the solar spectrum, the Lodders et al. (2009) value is used. These Solar values are adopted in all calculations of [Fe/H] and [X/Fe] in this chapter.[7]

[7]Note that the Solar abundances are treated differently in later chapters.

Table 3.3: Solar abundances compared to those from the literature.

Element	A09	L09	This work
Fe I	7.50	7.45	7.50
Fe II	7.50	7.45	7.49
O I	8.69	8.40	8.83 (8.85)[a]
Na I	6.27	6.24	6.25
Mg I	7.60	7.53	7.59
Al I	6.45	6.43	6.47
Si I	7.51	7.51	7.51
Ca I	6.34	6.29	6.32
Sc II	3.15	3.05	3.19
Ti I	4.95	4.91	4.93
Ti II	4.95	4.91	4.95
V I	3.93	3.96	3.95
Cr I	5.64	5.64	5.63
Cr II	5.64	5.64	5.59
Mn I	5.43	5.48	5.41[b]
Co I	4.99	4.87	4.91[b]
Ni I	6.22	6.20	6.27
Cu I	4.19	4.25	4.28[b]
Zn I	4.56	4.63	4.58
Y II	2.21	2.17	2.18
Ba II	2.18	2.18	2.29
La II	1.10	1.17	1.22
Nd II	1.42	1.45	1.55
Eu II	0.52	0.51	0.51[c]

References: A09 = Asplund et al. (2009), L09 = Lodders et al. (2009)

[a] The number in parentheses is the O abundance as determined with MOOG 2002.

[b] With HFS corrections

[c] From Lodders et al. (2009)

3.3.2 Errors

The errors in the final abundances are separated into statistical errors (due to measurements) and systematic errors (due to uncertain atmospheric parameters).

Statistical Errors

The random abundance errors were calculated as in Shetrone et al. (2003). For each element, three different uncertainties were calculated and compared:

1. The line-to-line abundance scatter. Each elemental abundance has some abundance scatter, σ, about the the mean abundance. The uncertainty in the mean abundance is therefore $\delta_{\rm X} = \sigma/\sqrt{N}$, where N is the number of spectral lines.

2. The EW uncertainty. The error of an EW measurement in a particular spectrum can be estimated with the Cayrel (1988) formula; note that an additional 10% $\times$ EW error is included (see Shetrone et al. 2003). The abundances were recalculated with larger and smaller EWs, and the offset in the mean abundance, $\sigma_{\rm EW}$, was divided by $\sqrt{N}$ to give the uncertainty in the mean abundance, $\delta_{\rm EW}$.

3. The iron line-to-line scatter. Because there are many iron lines, the iron line-to-line scatter provides an estimate of the *minimum* abundance uncertainty, $\delta_{\rm Fe}$. For an element with few detectable spectral lines, the above error types may underestimate the true abundance error.

The largest of these three uncertainties ($\delta_{\rm X}$, $\delta_{\rm EW}$, and $\delta_{\rm Fe}$) is adopted as the final *random* abundance error for that element.

Systematic Errors

The abundances from individual spectral lines in a star are affected by the choice of model atmosphere parameters. Changing each parameter ($T_{\rm eff}$, $\log g$, ξ, [Fe/H]) will affect the average abundance of each species. While the errors in the atmospheric parameters themselves are random, changes in these parameters systematically affect the abundance analyses.

To determine how the abundances are affected by uncertainties in the atmospheric parameters, new model atmospheres were tested by varying one parameter at a time by its 1σ error. It is not obvious how to combine these errors since they are not independent (e.g. increasing $\log g$ affects the $T_{\rm eff}$ and ξ estimates); however, investigating

their effects separately provides a maximum uncertainty estimate. Systematic errors due to continuum placement are also investigated, since continuum placement can result in EW differences that are outside the adopted 1σ errors. As a conservative estimate of these errors, the average offset between the EW measurements presented here and those of Pancino et al. (2010, 4 mÅ, for the high S/N stars) and Monaco et al. (2011, 7 mÅ, for the low S/N stars) are adopted for the continuum uncertainty.

Representative systematic errors in abundances for M67-141, Pal 1 - I, and Pal 1 - III are shown in Tables 3.4, 3.5, and 3.6, individually and added in quadrature. The differences are largest for the continuum and temperature errors in M67-141, while the errors are fairly similar for all parameters in the Pal 1 stars. The total errors in the [X/Fe] ratios are fairly small for all elements. Note that these systematic errors are not included in the errors bars in the following figures and tables.

3.3.3 Hyperfine Structure

The elements Sc, V, Mn, Co, Cu, Ba, La, and Eu were checked for hyperfine structure (HFS) corrections. The majority of the HFS and isotopic data comes from Prochaska et al. (2000, for Sc, V, Mn, and Co), Booth et al. (1983, additional Mn), Biehl (1976, Cu), McWilliam (1998, Ba), and Lawler et al. (2001a,b, La and Eu), with extra lines added from the Kurucz database.[8] The corrections per line were averaged over the entire star and were applied to the average abundances from `MOOG`. If HFS data were not available, then the line was neglected in the correction calculation. When the corrections were less than 0.1 dex, they were ignored. Negligible corrections were found (< 0.1 dex) for Sc, Ba, La, and Eu; moderate corrections ($\lesssim 0.5$ dex) for V and Mn; and large corrections ($\lesssim 1.0$ dex) for Co and Cu.

3.3.4 NLTE Effects

Non-LTE corrections are neglected in this analysis, yet it is well known that many elements do suffer from NLTE effects. This problem has been minimized by eliminating lines which are greatly affected by NLTE. Na is a particularly sensitive element; however, weaker lines tend to have smaller corrections. At Solar metallicity, Lind et al. (2011) recommend the 6154.23/6160.75 Å doublet, with the 5682.65/5688.21 Å doublet for [Fe/H] < -1.0. For the Sun and M67-141, only the former doublet is

[8] `http://kurucz.harvard.edu/linelists.html`

Table 3.4: Errors in M67-141's [X/Fe] ratios due to atmospheric parameter errors.

	ΔT +50 K	$\Delta \log g$ +0.06	$\Delta\xi$ +0.1 km s^{-1}	Δ[M/H] +0.02	Continuum +4 mÅ	Total
Δ[Fe I/H]	+0.07	+0.01	−0.05	+0.01	+0.07	0.11
Δ[Fe II/H]	−0.07	+0.03	−0.05	+0.01	+0.09	0.13
Δ[O I/Fe]	−0.06	+0.02	+0.05	0.0	+0.02	0.08
Δ[Na I/Fe]	+0.01	−0.01	+0.02	−0.01	−0.01	0.03
Δ[Mg I/Fe]	−0.03	0.0	+0.04	0.0	0.0	0.05
Δ[Al I/Fe]	0.0	−0.01	+0.03	−0.01	−0.01	0.03
Δ[Si I/Fe]	−0.10	0.0	+0.03	−0.01	0.0	0.10
Δ[Ca I/Fe]	+0.04	−0.01	0.0	−0.01	−0.01	0.04
Δ[Sc II/Fe]	−0.08	+0.01	0.0	0.0	0.0	0.08
Δ[Ti I/Fe]	+0.09	−0.01	−0.01	−0.01	0.0	0.09
Δ[Ti II/Fe]	−0.08	+0.02	−0.01	0.0	+0.02	0.09
Δ[V I/Fe]	+0.11	0.0	+0.01	0.0	+0.01	0.11
Δ[Cr I/Fe]	+0.08	−0.01	−0.02	−0.01	0.01	0.08
Δ[Cr II/Fe]	−0.13	+0.01	−0.01	−0.01	+0.02	0.13
Δ[Mn I/Fe]	+0.05	0.0	−0.02	0.0	0.0	0.05
Δ[Co I/Fe]	0.0	0.0	−0.02	−0.01	+0.01	0.02
Δ[Ni I/Fe]	−0.03	0.0	0.0	−0.01	0.0	0.03
Δ[Cu I/Fe]	0.0	−0.01	−0.01	0.0	−0.02	0.02
Δ[Zn I/Fe]	−0.11	+0.01	0.0	0.0	+0.03	0.11
Δ[Y II/Fe]	−0.07	+0.02	−0.02	0.0	+0.03	0.08
Δ[Ba II/Fe]	−0.04	+0.02	−0.03	+0.01	0.0	0.05
Δ[La II/Fe]	−0.05	+0.02	+0.04	0.0	+0.02	0.07
Δ[Nd II/Fe]	−0.06	+0.02	+0.02	0.0	+0.05	0.08
Δ[Eu II/Fe]	−0.08	+0.02	+0.04	0.0	+0.02	0.09

All columns show the difference between the new [X/Fe] ratio and the adopted one, i.e. Δ[X/Fe] = [X/Fe]$_{\rm new}$ - [X/Fe]$_{\rm original}$. For Fe, [Fe/H] is shown. The total error shows the individual errors added in quadrature.

Table 3.5: Errors in Pal 1-I's [X/Fe] ratios due to the atmospheric parameter errors.

	ΔT +70 K	$\Delta \log g$ +0.15	$\Delta\xi$ +0.3 km/s	Δ[M/H] +0.08	Continuum +7 mÅ	Total
Δ[Fe I/H]	+0.07	0.0	−0.18	+0.01	+0.12	0.23
Δ[Fe II/H]	−0.04	+0.05	−0.08	+0.02	+0.11	0.15
Δ[Na I/Fe]	−0.01	−0.02	+0.08	−0.01	−0.01	0.08
Δ[Mg I/Fe]	−0.02	−0.05	+0.08	0.0	−0.06	0.11
Δ[Si I/Fe]	−0.08	+0.02	+0.12	0.0	−0.01	0.15
Δ[Ca I/Fe]	0.0	−0.02	+0.03	−0.01	−0.02	0.04
Δ[Sc II/Fe]	−0.08	+0.06	+0.09	+0.01	+0.01	0.14
Δ[Ti I/Fe]	+0.04	+0.01	0.0	−0.01	+0.04	0.06
Δ[V I/Fe]	+0.05	0.0	+0.14	−0.01	0.0	0.15
Δ[Ni I/Fe]	−0.01	+0.02	+0.01	−0.01	+0.01	0.03
Δ[Ba II/Fe]	−0.05	+0.05	−0.08	+0.02	0.0	0.11
Δ[Nd II/Fe]	−0.05	+0.07	+0.09	+0.01	+0.05	0.13

All columns show the difference between the new [X/Fe] ratio and the adopted one, i.e. Δ[X/Fe] = $[X/Fe]_{new}$ - $[X/Fe]_{original}$. For Fe, [Fe/H] is shown. The total error shows the individual errors added in quadrature.

Table 3.6: Errors in Pal 1-III's [X/Fe] ratios due to the atmospheric parameter errors.

	ΔT +50 K	$\Delta \log g$ +0.15	$\Delta\xi$ +0.1 km/s	Δ[M/H] +0.02	Continuum +4 mÅ	Total
Δ[Fe I/H]	+0.05	−0.01	−0.04	0.0	+0.08	0.10
Δ[Fe II/H]	−0.03	+0.06	−0.04	0.0	+0.14	0.16
Δ[O I/Fe]	−0.04	+0.08	+0.04	+0.01	+0.14	0.17
Δ[Na I/Fe]	−0.02	−0.01	+0.02	0.0	−0.03	0.04
Δ[Mg I/Fe]	−0.02	−0.02	+0.03	0.0	−0.02	0.05
Δ[Al I/Fe]	−0.02	+0.01	+0.04	0.01	+0.03	0.05
Δ[Si I/Fe]	−0.04	+0.03	+0.04	+0.01	+0.02	0.07
Δ[Ca I/Fe]	0.0	−0.02	+0.01	0.0	−0.04	0.05
Δ[Sc II/Fe]	−0.05	+0.07	0.0	0.0	+0.05	0.10
Δ[Ti I/Fe]	+0.02	+0.01	0.0	0.0	+0.02	0.03
Δ[Ti II/Fe]	−0.05	+0.06	0.0	0.0	+0.05	0.09
Δ[V I/Fe]	+0.02	+0.02	+0.03	0.0	+0.03	0.05
Δ[Cr I/Fe]	+0.02	−0.01	−0.01	0.0	−0.01	0.03
Δ[Cr II/Fe]	−0.07	+0.07	0.0	+0.01	+0.07	0.12
Δ[Mn I/Fe]	+0.01	−0.01	0.0	+0.01	−0.02	0.03
Δ[Co I/Fe]	0.0	+0.03	+0.02	+0.01	+0.04	0.05
Δ[Ni I/Fe]	−0.02	+0.01	0.0	0.0	+0.01	0.02
Δ[Cu I/Fe]	0.0	+0.01	−0.02	0.0	+0.01	0.02
Δ[Zn I/Fe]	−0.07	+0.04	0.0	0.0	+0.05	0.09
Δ[Y II/Fe]	−0.05	+0.07	0.0	+0.01	+0.08	0.12
Δ[Ba II/Fe]	−0.04	+0.04	−0.02	+0.01	−0.01	0.06
Δ[La II/Fe]	−0.04	+0.07	+0.03	0.0	+0.10	0.13
Δ[Nd II/Fe]	−0.05	+0.07	+0.01	0.0	+0.08	0.12
Δ[Eu II/Fe]	−0.05	+0.08	+0.04	+0.01	+0.14	0.17

All columns show the difference between the new [X/Fe] ratio and the adopted one, i.e. Δ[X/Fe] = $[X/Fe]_{new}$ - $[X/Fe]_{original}$. For Fe, [Fe/H] is shown. The total error shows the individual errors added in quadrature.

used; for Pal 1, however, both sets are used. Any corrections to these lines should be < -0.10 dex at most (Mashonkina et al., 2000).

The NLTE effects for Mn can also be quite large. However, Bergemann & Gehren (2007) note that the corrections are strongest for the weak and intermediate lines (i.e. those with EW < 80 mÅ). All of the lines considered here are stronger than 80 mÅ—such corrections are then "scattered around zero or negative."

Barium is another element that suffers from NLTE effects which affect the lines. The 6496.91 Å line has been eliminated from this analysis, since it has large corrections. However the corrections for 5853.69 Å and 6141.73 Å are negligible for Pal 1's metallicity range, and the 4554.03 Å correction is small at solar metallicity (Short & Hauschildt, 2006).

3.3.5 Final Abundances: M67-141

M67-141's final abundance ratios are shown in Table 3.7. The [X/Fe] values agree very well with those of Yong et al. (2005)—the only inconsistent abundances are those of O and Mg. The Mg difference may be due to the choice of lines. The O abundance, however, relies on molecular equilibrium calculations within `MOOG`; these calculations seem to differ between the 2002 version used by Yong et al. and the 2010 version used in this analysis. The O abundances are increased with `MOOG` 2002, bringing [O/Fe] into better agreement with Yong et al. These abundances are shown in Tables 3.3, 3.7, and 3.8, in parentheses following the 2010 versions. Note that the Solar O abundance is only slightly affected between `MOOG` 2002 and 2010. Since many of the comparison studies in Chapter 3.4 use the 2002 version of `MOOG`, that version is utilized for all O abundances in this chapter.

The [X/Fe] ratios do not agree as well with Pancino et al. (2010) for Na, Mg, Ca, Ti, V, Co, and Ba. For Na, Al, Ti, and Ba the discrepancies seem to be due primarily to the different atmospheric parameters. Pancino et al. (2010) also do not appear to have applied HFS corrections to V or Co, which could explain why their abundances are much higher. Mg is again discrepant because of the choice of lines and atomic data. Ca is also quite low in their analysis, also apparently due to atomic data.

A spectral comparison of a solar twin in M67 (Önehag et al., 2010) suggests that the entire cluster should have roughly Solar abundances, with a slightly elevated [Fe/H] ~ 0.02 dex. With the exceptions of Na and Si, all elements in Table 3.7 are within 0.08 dex of Solar values (i.e. within the 1σ errors, [X/Fe] ~ 0). Na could very

well be elevated in red clump stars like M67-141; Tautvaišienė et al. (2000) suggested that mixing could take place in open clusters after the He-flash, which could bring up material from the Na-Ne cycle. Alternatively this high Na abundance could indicate a need for a negative NLTE correction.

3.3.6 Final Abundances: Pal 1

The final abundances for the Pal 1 stars are listed in Table 3.8, while Table 3.9 provides a comparison with the Pal 1-I abundances from Monaco et al. (2011).

A Comparison with Monaco et al.

As shown in Table 3.9, the Monaco et al. (2011) abundances differ for Mg, Al, Sc, and Ti. The significantly different atmospheric parameters affect most of these ratios, particularly Al (note that the Pal 1-I spectrum does not have a sufficiently high S/N ratio to determine the Al abundance, and the Pal 1-III and -C values are therefore used for that comparison; this assumes there is not an abundance spread within Pal 1). In addition, different atomic data for Mg, Al, and Ti causes additional discrepancies. The Sc II abundance seems to differ due to the Solar Sc abundances; the measured Solar EWs in Monaco et al. (2011) are considerably higher than the ones measured in this thesis (see Appendix C), leading to a higher solar Sc abundance and therefore a lower [Sc/Fe] for Pal 1-I.

The abundance offsets between data sets can be rather large; however, while spectral line selection can differ significantly between studies, much of the atomic data used here agree with those of Fulbright (2000) and Reddy et al. (2003, 2006), who provide the majority of the metal-rich Galactic stars for the comparisons in Chapter 3.4. Thus, systematic offsets because of atomic data should be minimal in later comparisons.

Cluster Means

The mean cluster abundances are shown in Table 3.10, along with the star-to-star dispersion in [X/Fe] (σ), the average uncertainty in a single star's [X/Fe] ratio ($\sigma_{\rm obs}$), and the spread ratio, a comparison of σ and $\sigma_{\rm obs}$. Large values of the spread ratio imply that the star-to-star variations are larger than the average uncertainty for an individual star, suggesting that the cluster has a genuine abundance spread. The Pal 1 stars do not show a significant spread for most elements (a spread ratio > 1.0

Table 3.7: A comparison of the derived abundances in M67-141.

	P10	Y05	This work		
X	[X/Fe][a]	[X/Fe][a]	[X/Fe][a]	δ	N
Fe I	0.06±0.01	−0.01±0.12	0.02	0.02	91
Fe II	0.01±0.03	0.01±0.09	−0.03	0.04	24
O I	−0.0±0.09	0.10±0.06	−0.15 (0.03)[b]	0.09	2
Na I	0.10±0.02	0.24±0.10	0.29	0.13	4
Mg I	0.29±0.03	0.18±0.04	0.04	0.07	3
Al I	0.06±0.06	0.16±0.06	0.14	0.15	2
Si I	0.09±0.02	0.11±0.08	0.13	0.05	10
Ca I	−0.1±0.02	0.09±0.03	0.07	0.06	15
Sc II	−0.0±0.08		0.09	0.06	12
Ti I	−0.0±0.02	0.05±0.05	0.02	0.05	35
Ti II	−0.0±0.02		0.10	0.05	33
V I	0.13±0.04		−0.05	0.05	17
Cr I	0.01±0.03		−0.04	0.09	8
Cr II			0.18	0.18	2
Mn I		−0.20±0.03	−0.08	0.13	4
Co I	0.11±0.02	0.01±0.09	−0.15	0.21	2
Ni I	0.06±0.05	0.06±0.09	0.08	0.04	26
Cu I			0.16	0.13	3
Zn I			0.05	0.12	3
Y II	−0.0±0.02		−0.04	0.11	5
Ba II	0.26±0.05	0.02	0.0	0.17	2
La II	0.06±0.05	0.13±0.04	0.04	0.06	4
Nd II	0.01±0.29		0.04	0.08	5
Eu II		0.05	0.0	0.12	1

References: Y05 = Yong et al. (2005), P10 = Pancino et al. (2010)

[a] [X/H] is given instead for Fe I and Fe II.

[b] The [O/Fe] value in parentheses is the value calculated with the 2002 version of `MOOG` (see the text).

Table 3.8: [X/Fe] ratios, 1δ errors, and the number of lines used for the Pal 1 stars.

	Pal 1-I		Pal 1-II		Pal 1-III		Pal 1-C	
X	[X/Fe][a]	N	[X/Fe][a]	N	[X/Fe][a]	N	[X/Fe][a]	N
Fe I	−0.61±0.08	30	−0.61±0.08	21	−0.60±0.03	81	−0.58±0.03	60
Fe II	−0.46±0.30	1	−0.64±0.44	2	−0.61±0.05	23	−0.68±0.05	23
O I	< 0.82	1	< 0.32	1	< 0.42	1	0.20±0.11[b]	2
Na I	0.26±0.34	2	0.23±0.31	2	0.20±0.09	4	0.16±0.09	4
Mg I	−0.11±0.20	1	−0.13±0.30	1	−0.02±0.08	5	0.02±0.07	6
Al I					0.0±0.10	2	0.07±0.10	2
Si I	0.24±0.24	1	0.13±0.23	1	0.09±0.06	8	0.19±0.06	8
Ca I	0.16±0.16	6	−0.04±0.22	4	0.15±0.06	17	0.12±0.06	18
Sc II	0.28±0.26	3	0.21±0.33	2	0.30±0.09	8	0.21±0.07	12
Ti I	−0.03±0.34	3	−0.14±0.38	4	0.02±0.06	24	−0.08±0.06	24
Ti II			−0.13±0.51	2	−0.08±0.05	32	0.08±0.07	23
V I	−0.05±0.21	1	0.08±0.14	4	0.14±0.07	6	0.06±0.05	14
Cr I					0.01±0.09	11	−0.16±0.11	9
Cr II					0.17±0.20	2	0.19±0.21	2
Mn I			−0.16±0.36	1	−0.21±0.12	4	−0.11±0.10	8
Co I					−0.10±0.18	2	0.03±0.20	2
Ni I	0.05±0.25	3	0.09±0.14	5	0.08±0.05	20	0.03±0.05	21
Cu I			−0.05±0.33	1	0.04±0.18	2	−0.08±0.32	1
Zn I					0.08±0.14	3	0.15±0.15	3
Y II	< 0.04	1	< 0.34	1	−0.45±0.12	4	−0.36±0.12	5
Ba II	0.27±0.24	2	0.19±0.26	2	0.22±0.12	3	0.26±0.18	2
La II	< 0.38	1	< 0.78	1	0.42±0.16	1	0.24±0.14	3
Nd II	0.19±0.65	1			0.13±0.16	2	0.12±0.14	2
Eu II	< 0.78	1	< 0.78	1	0.50±0.20	1	0.50±0.20	1

[a] [X/H] is given instead for Fe I and Fe II.

[b] `MOOG` 2002 has only a small effect on Pal 1-C's [O/Fe].

Table 3.9: A comparison with the M11 Pal 1-I abundances.

	M11 Pal 1-I [X/Fe][a]	This work Pal 1-I [X/Fe][a]
Fe I	−0.49	−0.61±0.08
Fe II	−0.53	−0.46±0.30
Na I	0.38	0.26±0.34
Mg I	0.11	−0.11±0.20
Al I	0.25	
Si I	−0.01	0.24±0.24
Ca I	0.04	0.16±0.16
Sc II	−0.01	0.28±0.26
Ti I	0.10	−0.03±0.34
V I	−0.06	−0.05±0.21
Cr I	−0.23	
Mn I	−0.22	
Co I	−0.06	
Ni I	−0.03	0.05±0.25
Zn I	0.38	
Y II	−0.32	< 0.04
Ba II	0.24	0.27±0.24
La II	0.29	< 0.38

References: M11 = Monaco et al. (2011).
[a] [X/H] is given instead for Fe I and Fe II.

would be considered significant; Cohen 2004). The Cr I abundance has a spread ratio > 1.0; however, abundances are only available for 2 stars, suggesting that this is not a significant result. Thus, Pal 1 does not appear to show any signs of star-to-star variations in any of the 21 elements investigated here.

3.4 Discussion: Chemical Abundances

Chapter 1.3.3 gave a basic introduction to the nucleosynthetic origins of the elements. This section breaks down each abundance ratio, discussing in more detail the nucleosynthetic origins of the elements and the implications for the formation of Pal 1.

3.4.1 Metallicity

Iron is expected to form both in Type II SNe (from the core collapse of massive stars) and Type Ia SNe (from the explosion of a white dwarf that has exceeded the Chandrasekhar limit). In a closed-box chemical evolution model (i.e. where no gas enters or leaves the system) Fe should be correlated with age. In reality this is not necessarily a valid assumption. However, it is useful to compare Pal 1's metallicity to other known GCs. As discussed by Monaco et al. (2011), this average metallicity is high for a GC so far from the Galactic centre—the only metal-rich Galactic halo GCs are Pal 12 and Ter 7, both of which are associated with the Sgr dSph. However, there are bulge and disk clusters in this metallicity regime, including 47 Tuc. This metallicity is also low for an OC, though Berkeley 20 (Be 20) and Be 29 are nearly as metal-poor.

3.4.2 α-elements

The α-elements form via the capture of ^{4}He nuclei. This happens primarily during hydrostatic burning in massive stars, and the α-elements are subsequently released into the interstellar medium by Type II supernovae. The lighter α-elements are not expected to form in Type Ia SNe and less Ca and Ti are expected to form, compared to Fe; the [α/Fe] ratio therefore probes the relative contributions from Type II and Type Ia SNe. Figures 3.5 and 3.6 compare the [α/Fe] ratios of the Pal 1 stars (red star symbols) and M67-141 (red circle) to those of Galactic field stars (field stars; grey points, from the sources assembled by Venn et al. 2004, with additions from Reddy

Table 3.10: Mean abundances and spread ratios for the four stars in Pal 1, according to the method described in Cohen (2004).

	Mean $\log \epsilon$	Mean [X/Fe][a]	Number of stars	σ	σ(obs)	Spread Ratio
Fe I	6.90	−0.60	4	0.014	0.055	0.26
Fe II	6.89	−0.60	4	0.096	0.21	0.46
Na	5.86	0.21	4	0.043	0.21	0.21
Mg	6.93	−0.06	4	0.072	0.16	0.44
Al	5.91	0.04	2	0.049	0.10	0.49
Si	7.07	0.16	4	0.066	0.15	0.45
Ca	5.84	0.10	4	0.093	0.13	0.75
Sc	2.80	0.25	4	0.047	0.19	0.25
Ti I	4.27	−0.06	4	0.068	0.21	0.33
Ti II	4.31	−0.04	3	0.11	0.21	0.52
V	3.41	0.06	4	0.079	0.12	0.68
Cr I	4.94	−0.09	2	0.12	0.10	1.20
Cr II	5.17	0.18	2	0.014	0.21	0.07
Mn	4.65	−0.16	3	0.050	0.18	0.27
Co	4.27	−0.04	2	0.092	0.20	0.47
Ni	5.73	0.06	4	0.038	0.12	0.22
Cu	3.65	−0.03	3	0.062	0.28	0.23
Zn	4.10	0.12	2	0.049	0.15	0.34
Y	1.17	−0.41	2	0.064	0.12	0.53
Ba	1.93	0.24	4	0.037	0.20	0.18
La	0.95	0.33	2	0.13	0.15	0.85
Nd	1.10	0.15	3	0.038	0.32	0.12
Eu	0.41	0.50	2	0.0	0.20	0.0

Note: A spread ratio > 1 indicates that a significant spread exists (i.e. that the star-to-star dispersion is larger than the typical uncertainty in a single measurement); Pal 1 shows no evidence for any abundance spreads.
[a] [X/H] is given instead for Fe I and Fe II.

et al. 2006 and Simmerer et al. 2004), Galactic GCs (black solid symbols, from the sources assembled in Pritzl et al. 2005, plus Sbordone et al. 2007 and Cohen 2004), and old, metal-poor Galactic OCs (open circles, from Carraro et al. 2004, Yong et al. 2005, and Friel et al. 2010). The two old, most metal-poor OCs are Be 20 and Be 29; the latter has been linked to the Sgr dSph based on its location, chemistry, and kinematics (Carraro & Bensby, 2009) and its location on the Sgr age-metallicity relation (Forbes & Bridges, 2010). The bulge and thin/thick disk GCs (circles) are distinguished from the halo clusters Pal 12 (plus signs) and Ter 7 (crosses), both of which are associated with the Sgr dSph. The bulge and disk cluster abundances are averaged over the entire cluster, while the individual stars in the halo clusters are separate. Those studies that do not perform their own Solar abundance analyses have been shifted to the Asplund et al. (2009) abundances. The total α abundance shown in Figure 3.6 is an average of Mg, Ca, and Ti. Note that O was excluded from this average because of its weak lines, while Si was excluded because the [Si/Fe] may be systematically high, as shown in Chapter 3.3.5. Note that the [α/Fe] values from Venn et al. (2004) and Pritzl et al. (2005) have been re-calculated using this definition.

Figures 3.5 and 3.6 show that the Milky Way stars exhibit the well-known behavior described in Chapter 1.3.5: the [α/Fe] ratio is $\sim +0.4$ at the low [Fe/H] end and remains relatively constant until [Fe/H] ~ -1, when it starts to decrease. This knee is typically interpreted as the point when lower mass stars have evolved enough for Type Ia SNe to occur. Figures 3.5 and 3.6 show that the M67-141 [α/Fe] ratios agree well with the Milky Way field stars, while Pal 1's α-abundances are slightly lower than the field stars, except for [Si/Fe] and [Ca/Fe]. The calculated [Si/Fe] ratio is also a bit high in M67-141 (as compared to the literature values; see Table 3.7), suggesting that Pal 1's [Si/Fe] may be systematically high. Calcium is not very low and does not follow the other α-elements; however, Ca may have other nucleosynthetic sites that affect [Ca/Fe] (e.g. SNe Ia; Woosley & Weaver 1995).

As discussed in Chapter 1, low [α/Fe] ratios are a signature that a star or cluster formed in a low mass dwarf galaxy. This is shown in Figures 3.7 and 3.8, which plot the Pal 1 *average* [O/Fe], [Mg/Fe], [Si/Fe], [Ca/Fe], [Ti/Fe], and [α/Fe] ratios along with Milky Way field stars and dwarf galaxy field stars. The Galactic field stars are shown in grey. Dwarf galaxies are also included, with their field stars as small symbols and their GCs as larger open symbols. Again, abundances have been averaged over an entire cluster. Black points are Fornax stars (Letarte et al., 2010); cyan triangles

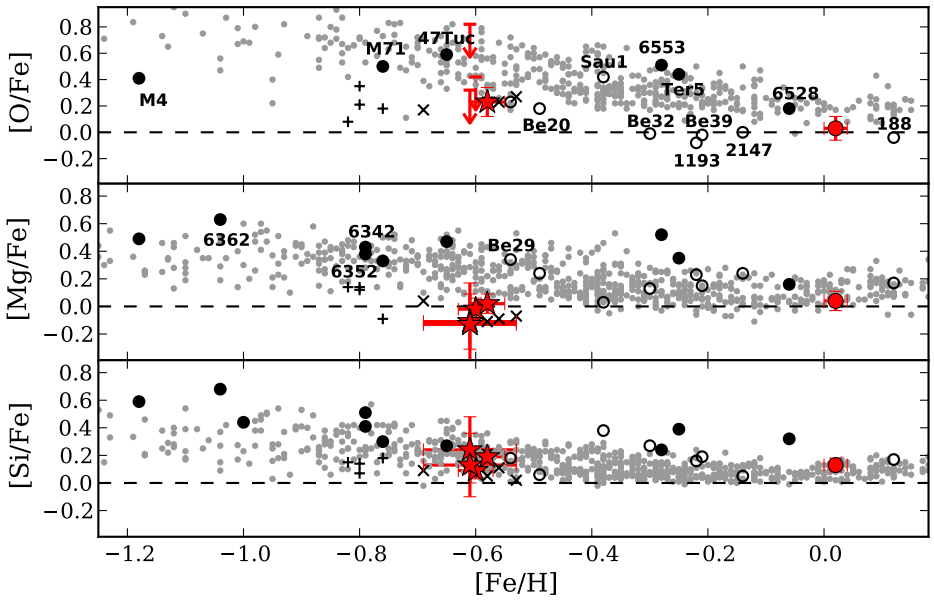

Figure 3.5: [X/Fe] ratios of α-elements O, Mg, and Si versus metallicity for the stars in this study as well as Galactic field stars and clusters. The red star symbols are the four Pal 1 stars. M67-141 is the red circle. Points with arrows represent upper (or lower) limits. The grey points are Galactic field stars, from the sources assembled by Venn et al. (2004) with additions from Reddy et al. (2006). Black open circles are Galactic OCs from Carraro et al. (2004), Yong et al. (2005), and Friel et al. (2010). Black filled circles are bulge and disk GCs from the sources assembled by Pritzl et al. (2005). Note that most Galactic GCs are more metal-poor than [Fe/H] ~ -1.2, and therefore do not appear in these plots. Plus signs are stars in Palomar 12 (from Cohen 2004) while crosses are stars in Ter 7 (from Sbordone et al. 2007); both are classified as halo GCs. The dashed lines show Solar values.

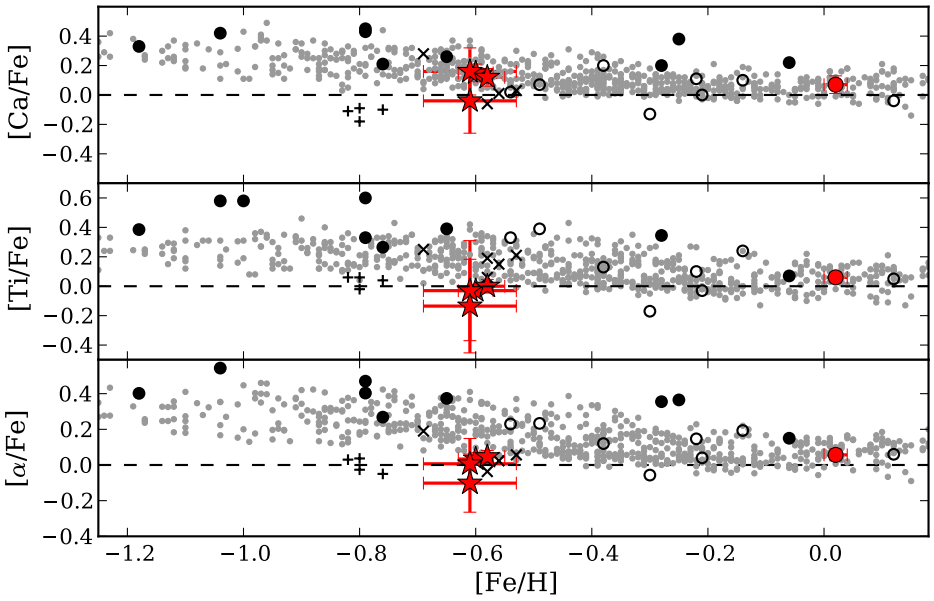

Figure 3.6: [X/Fe] ratios of the α-elements Ca and Ti, as well as of the average α from Mg, Ca, and Ti. The Ti abundance is an average of Ti I and Ti II, except for Pal 1-I, whose Ti I abundance is shown since its Ti II abundance is abnormally high. The points are as in Figure 3.5.

are Sgr stars (field stars are from Sbordone et al. 2007, Monaco et al. 2007, and Chou et al. 2010a, while GC stars are from Cohen 2004 and Sbordone et al. 2005b); blue squares are Large Magellanic Cloud stars (field stars from Pompéia et al. 2008; cluster stars from Johnson et al. 2006 and Mucciarelli et al. 2008); green crosses are Galactic Anticenter Stellar Stream (GASS; Chou et al. 2010b) stars; and orange diamonds are field stars in the Canis Major overdensity (Sbordone et al., 2005a). While other dwarf galaxy data are available in this metallicity range, plotting all of it makes these plots nearly illegible, and only the most relevant dwarf data (i.e. galaxies with many stars and many elemental abundances in the same metallicity range as Pal 1) are included.

Pal 1's slightly low [α/Fe] ratios place it with the dwarf galaxies (with the possible exception of Ca). This suggests that Type Ia supernovae began to contribute to Pal 1's host environment at a lower [Fe/H] than for stars in the Galaxy or that Pal 1 was deficient in the highest mass stars. In general, Pal 1's [α/Fe] ratios agree best with the Sgr and LMC clusters. The slightly subsolar [Ti/Fe] value agrees with the GASS stars while the slightly low [Mg/Fe] and [Ti/Fe] and slightly higher [Ca/Fe] and [Si/Fe] ratios agree with the [Fe/H] = -0.44 CMa star.

3.4.3 Sodium and Aluminum

Na and Al are produced in massive stars during nucleosynthesis through carbon burning and hydrogen shell burning (Woosley & Weaver, 1995).

Abundances

The [X/Fe] ratios are shown in Figure 3.9. (Note that Galactic GCs all show star-to-star variations in Na, and possibly Al; therefore, the average abundances of the GCs may not reflect the actual primordial abundances.) Both Pal 1 and M67-141 have slightly higher [Na/Fe] values than the MW field stars, in agreement with the old OCs and GCs. The Pal 1 [Na/Fe] ratios are distinctly higher than the halo GCs Pal 12 and Ter 7. M67-141's [Al/Fe] agrees with the field stars, while Pal 1's [Al/Fe] is slightly low for field stars, bulge/disk GCs, and OCs. As with sodium, the [Al/Fe] ratios in the Pal 1 stars are distinct from those of stars in Ter 7.

Comparisons with the dwarf galaxies are shown in Figure 3.10. Pal 1's Na and Al abundances agree well with the low-metallicity CMa star. The Na abundances are higher than the Fornax and Sgr values but overlap with the LMC stars. For the few available [Al/Fe] abundances, Pal 1 is higher than the Sgr and LMC clusters; however,

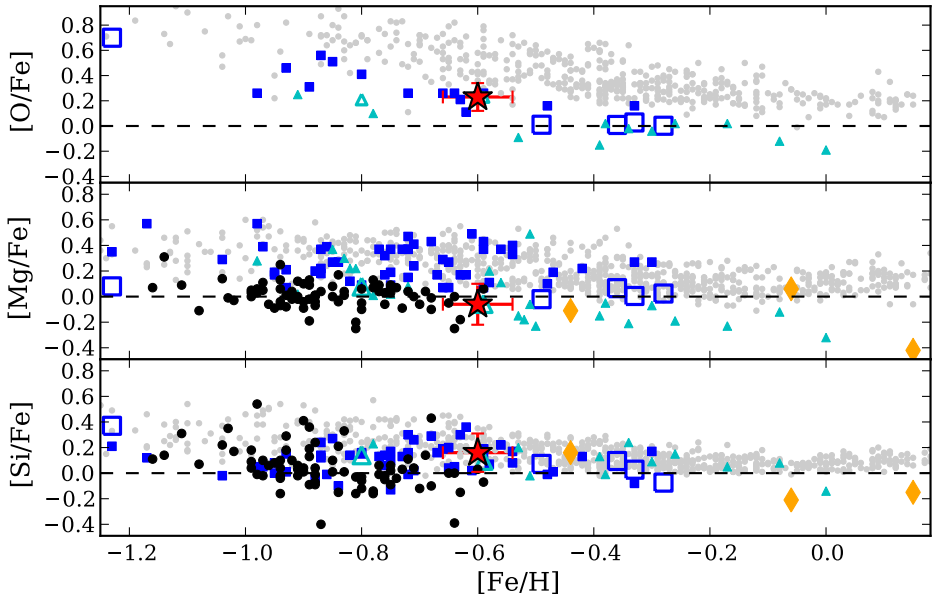

Figure 3.7: [X/Fe] ratios of α-elements O, Mg, and Si versus metallicity for the Pal 1 stars, Galactic field stars (grey; as in Figure 3.5), and stars in other galaxies. Black points are Fornax stars (Letarte et al., 2010); cyan triangles are Sagittarius (Sgr) stars (field stars are from Sbordone et al. 2007, Monaco et al. 2007, and Chou et al. 2010a, while GC stars are from Cohen 2004 and Sbordone et al. 2005b); blue squares are Large Magellanic Cloud stars (field stars from Pompéia et al. 2008; cluster stars from Johnson et al. 2006 and Mucciarelli et al. 2008); and orange diamonds are field stars in the Canis Major overdensity (Sbordone et al., 2005a).

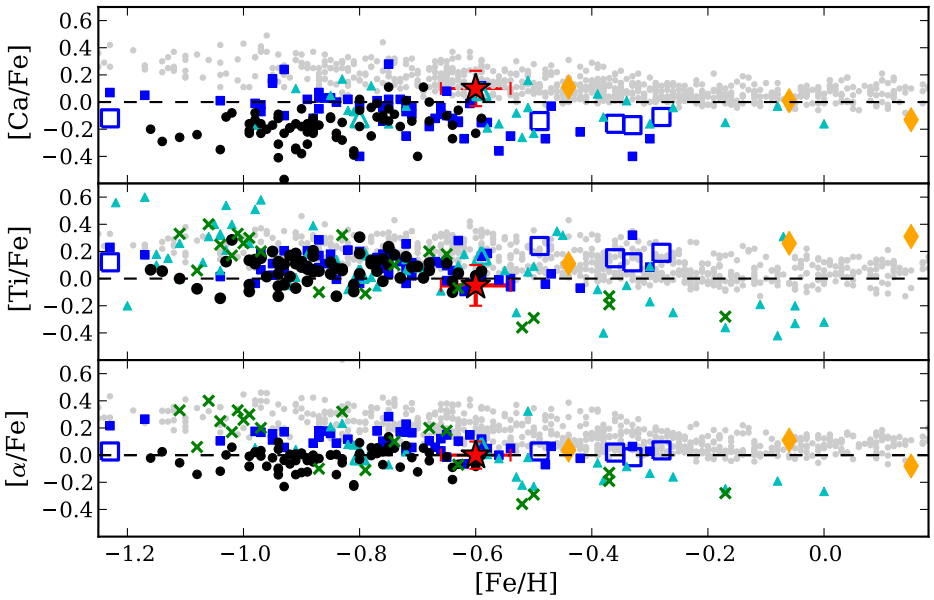

Figure 3.8: [X/Fe] ratios of the α-elements Ca and Ti, as well as of the average α from Mg, Ca, and Ti. The Ti abundance is an average of Ti I and Ti II, except for Pal 1-I, whose Ti I abundance is shown since its Ti II abundance is abnormally high. The points are as in Figure 3.7, with the addition of Galactic Anticenter Stellar Stream (GASS; green crosses) stars from Chou et al. (2010b).

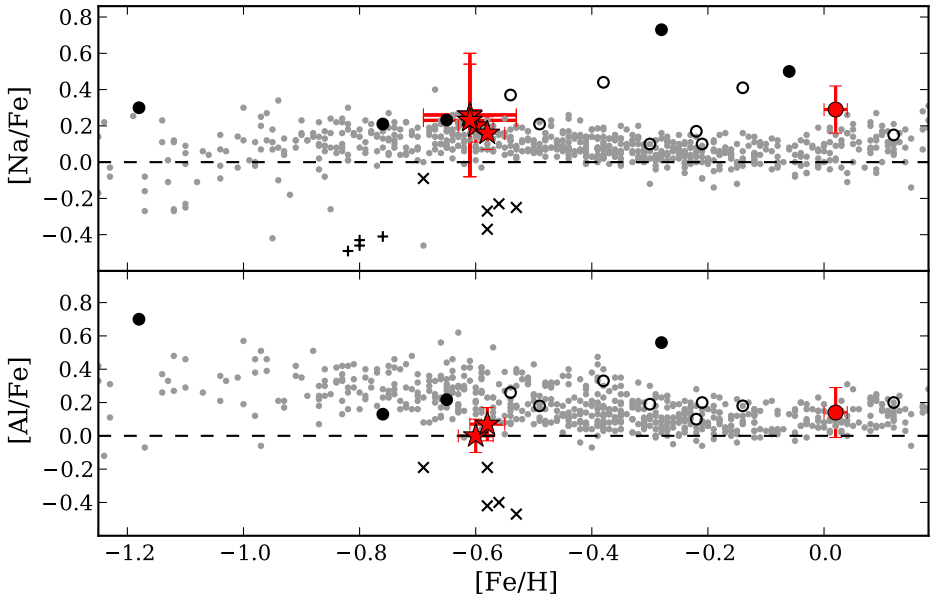

Figure 3.9: [X/Fe] ratios of the light elements Na and Al versus metallicity in MW field stars and clusters. The points are as in Figure 3.5.

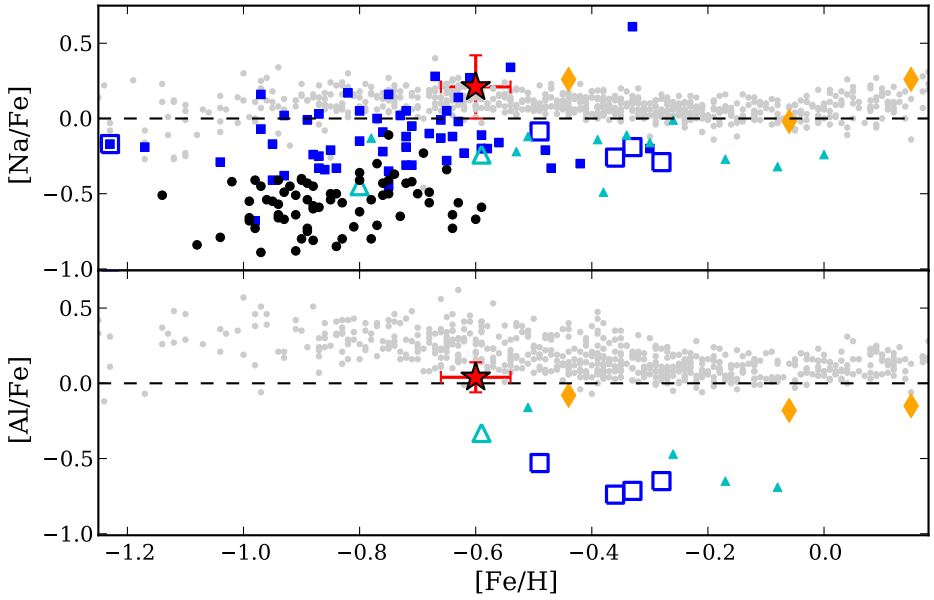

Figure 3.10: [X/Fe]ratios of the light elements Na and Al versus metallicity. The points are as in Figure 3.7.

the available Al abundances are too sparse to conclude that Pal 1 is dissimilar from dwarf galaxy stars.

Abundance Anticorrelations

Anticorrelations between Na/O (and occasionally Al/Mg) are seen in nearly all Galactic GCs, and Carretta et al. (2010b) suggest that the presence of a Na/O anticorrelation is a necessary criterion for a cluster to be classified as a globular. Table 3.10 clearly shows that there is not a significant range in [Na/Fe] or [Mg/Fe] for the four stars. This could be due to the small sample size, or could indicate that there are no Na/O or Al/Mg anticorrelations in Pal 1.

There is little evidence supporting the presence of an Al/Mg anticorrelation: Al is clearly not enhanced in Pal 1-III and Pal 1-C, and the [Al/Fe] ratios are slightly low for Galactic stars. The [Mg/Fe] ratio is low (see Chapter 3.4.2) but is most likely due to a low primordial [α/Fe], since without significant Al overabundances Mg depletion is not expected to occur (Carretta et al., 2009a). Therefore, the Al and Mg abundances are consistent with the absence of an anticorrelation—however, this is not surprising given Pal 1's [Fe/H], since the Al/Mg anticorrelation is not observed in metal-rich GCs (see, e.g., Carretta et al. 2010b).

The Pal 1 Na abundances, however, *are* slightly enhanced in Pal 1, lying just above the Galactic field stars. In the absence of any evolutionary effects (which could lead to a Na enhancement), Na should behave like the α-elements, which are also created in massive stars and are subsequently distributed by Type II supernovae. Thus Pal 1's high Na abundances may indicate that Na-Ne cycled gas is present (though recall that M67-141's [Na/Fe] ratio is also high, hinting at the possibility of a systematic offset). Even though only upper limits on [O/Fe] are available for three stars, Pal 1-C's [O/Fe] is slightly low. Again, this could be consistent with a low primordial [α/Fe]. Ultimately, because there is no significant range in the Na abundances there is no conclusive evidence for a Na/O anticorrelation in Pal 1.[9] The implications of this will be discussed further in Chapter 3.5.1.

[9]It should be noted that Na-enhanced, O-deficient stars in GCs are typically more centrally concentrated than the primordial populations (e.g. Vesperini et al. 2013; Cordero et al. 2014). The Pal 1 targets cover the inner and outer regions, so that the target stars should sample the two populations (if there are indeed two).

3.4.4 Iron-peak Elements

The iron-peak elements are formed in both Type Ia and Type II supernovae, though the precise contributions of the different types are unknown. In Pal 1's metallicity regime Type Ia supernovae should be the dominant contributors; Iwamoto et al. (1999) estimate that a Type II supernova may create ~ 0.1 $M_\odot$ of iron-peak material while a Ia may contribute ~ 0.8 $M_\odot$.[10] The odd-Z elements (scandium, vanadium, manganese, and cobalt) are similar because they have only a single stable isotope each; these elements also require corrections for hyperfine splitting. Note that Sc is included in this discussion, even though it is not a traditional iron-peak element, as its production site is primarily Type II supernovae.

Figures 3.11 and 3.12 show the [X/Fe] ratios of the iron-peak elements. Note that in the single plot for [Cr/Fe] both Cr I (red) and Cr II (yellow) are shown. All of Pal 1's odd iron-peak elements agree with the Galactic field stars. Sc is slightly higher than the general Galactic trend, putting Pal 1 in closer agreement with 47 Tuc than with Ter 7 or Pal 12. The V abundances are slightly lower than the Galactic trend, in agreement with field stars and Ter 7. [Mn/Fe] is slightly higher than all the GCs, but agrees with field stars and the old OCs Be 20 and 29. Finally, [Co/Fe] is slightly low, in agreement with the halo clusters but still within range for OCs and field stars—a comparison cannot be made with the GCs as Co abundances are not available for all clusters.

Cr abundances are only available for M67-141, Pal 1-III, and Pal 1-C—their Cr I abundances are in good agreement with each other and with the literature. M67 - 141's Cr I abundance agrees with Galactic field stars and GCs, while Pal 1 lies slightly below the field stars and agrees with the halo GCs. However, the Cr II abundances are considerably higher (identified as yellow in Figure 3.12), an effect that has been observed in previous studies of Galactic stars (e.g. Zhang et al. 2009). The Cr II abundances may not be reliable because the lines are in the blue; however, the discrepancy between Cr I and Cr II may be due to NLTE effects for Cr I (Sobeck et al., 2007; Bergemann & Cescutti, 2010). Therefore, neither [Cr I/Fe] nor [Cr II/Fe] may be valuable choices for chemical tagging purposes. Both M67-141 and Pal 1's [Ni/Fe] values match those of field stars and clusters, with the exceptions of Ter 7 and Pal 12, which are slightly lower.

[10] Though of course the relative rate of SNe Ia is difficult to determine without understanding the nature of the progenitors or the mechanisms of mass transfer.

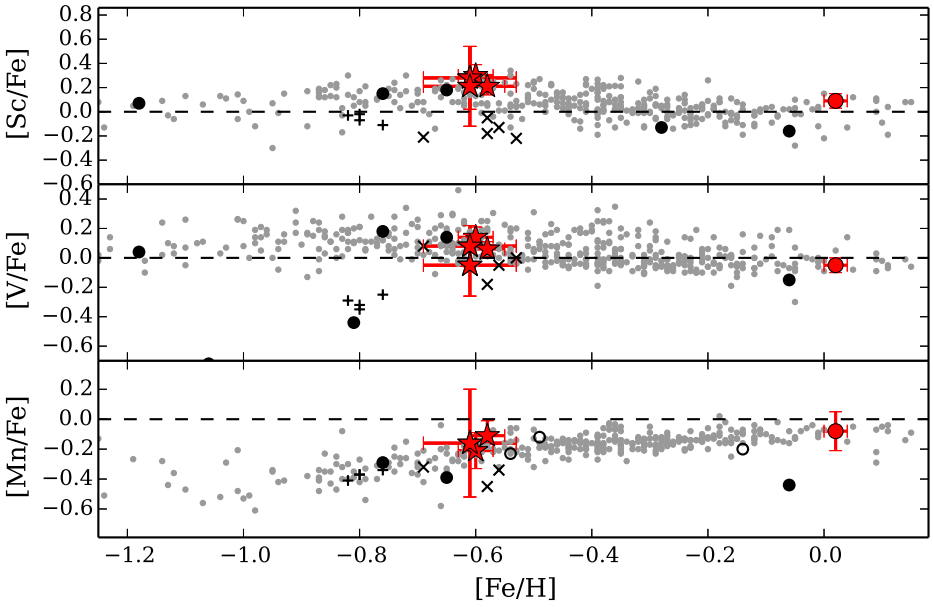

Figure 3.11: [X/Fe] ratios of the iron-peak elements Sc, V, and Mn versus metallicity. The points are as in Figure 3.5.

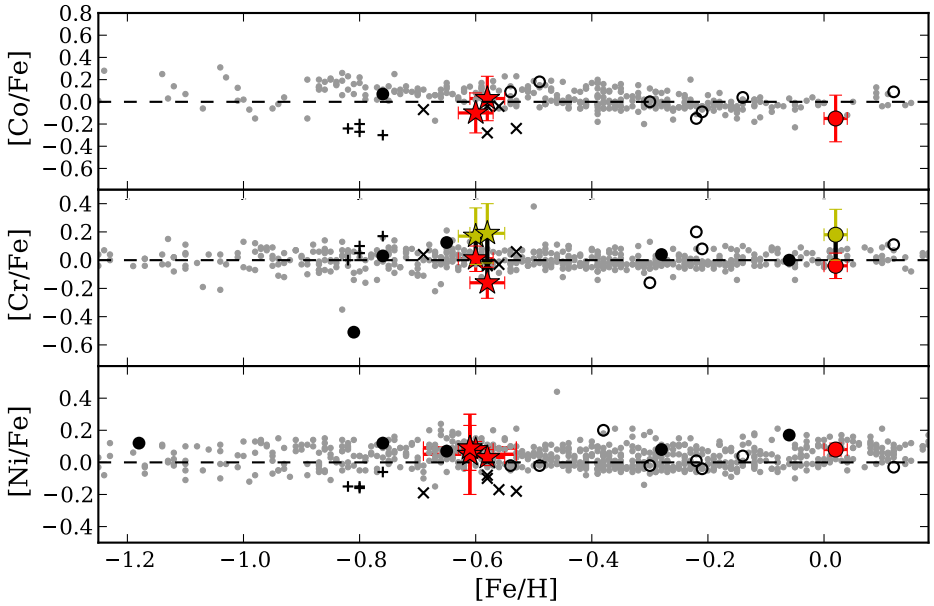

Figure 3.12: [X/Fe] ratios of the iron-peak elements Co, Cr, and Ni versus metallicity. Both Cr I and Cr II are shown (Cr I in red, Cr II in yellow); note that the low S/N stars Pal 1-I and -II only have Cr I abundances. The points are as in Figure 3.5.

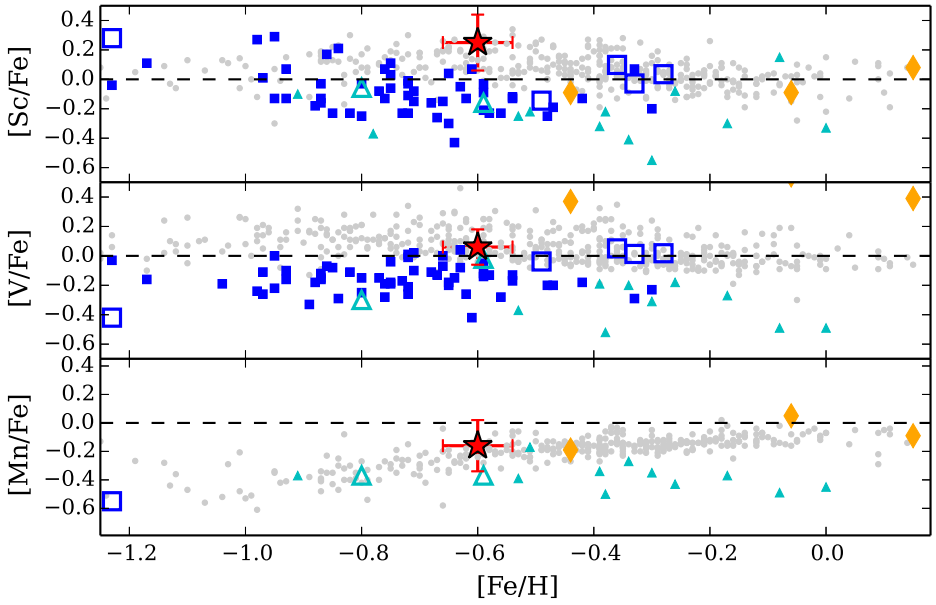

Figure 3.13: [X/Fe] ratios of the iron-peak elements Sc, V, and Mn versus metallicity. The points are as in Figure 3.7.

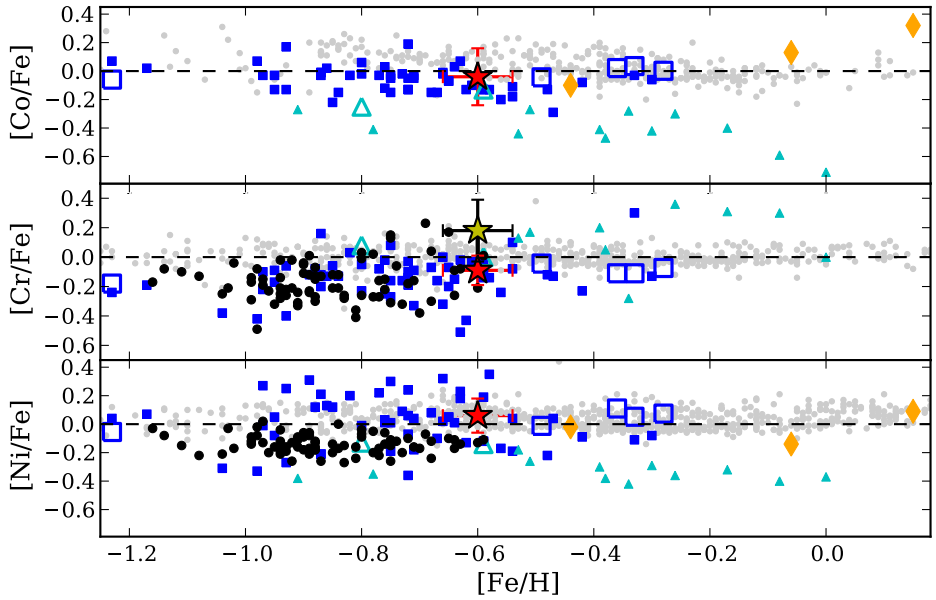

Figure 3.14: [X/Fe] ratios of the iron-peak elements Co, Cr, and Ni versus metallicity. Both Cr I and Cr II are shown (Cr I in red, Cr II in yellow). The points are as in Figure 3.7.

Comparisons with dwarf galaxy stars are shown in Figures 3.13 and 3.14. Pal 1's [Sc/Fe] remains clearly distinct from the dwarf galaxy stars. Pal 1's [V/Fe] ratio is in good agreement with the dwarfs, with the exception of the CMa stars, which may be due to HFS corrections. Overall the Pal 1 Fe-peak elements show the best agreement with the Galactic stars rather than the dwarf galaxy stars. Variations in [Fe-peak/Fe] with metallicity have been suggested to be due to metallicity-dependent supernovae yields, e.g. metal-poor Type Ia supernovae will produce less Mn than metal-rich ones (Cescutti et al., 2008), as seen in the Sgr field stars. However, Pal 1's agreement with the Galactic and dwarf galaxy stars at a similar metallicity suggests no significant dispersion in the Type Ia contributions.

3.4.5 Copper and Zinc

The nucleosynthetic origins of Cu and Zn are varied, and the precise yields from various sites depend on the models used. Explosive burning in Type Ia and II supernovae can create Cu and Zn, as can neutron captures. Given the uncertainty surrounding the formation of these elements, they are discussed separately from the rest. Their [X/Fe] ratios are shown in Figure 3.15. The three Pal 1 [Cu/Fe] ratios agree with the Galactic field stars—the [Cu/Fe] values are *not* within 1δ of Ter 7 and Pal 12. M67-141's [Cu/Fe] is a bit high, but its 1δ errors place it with the Galactic field stars. Both M67-141 and Pal 1 have [Zn/Fe] ratios that agree with field stars and GCs but are higher than Ter 7 and Pal 12.

The comparisons to dwarf galaxy stars are shown in Figure 3.16. Both Cu and Zn (Figure 3.16) are in better agreement with the Galactic stars and possibly CMa and are clearly distinct from the Sgr and LMC stars.

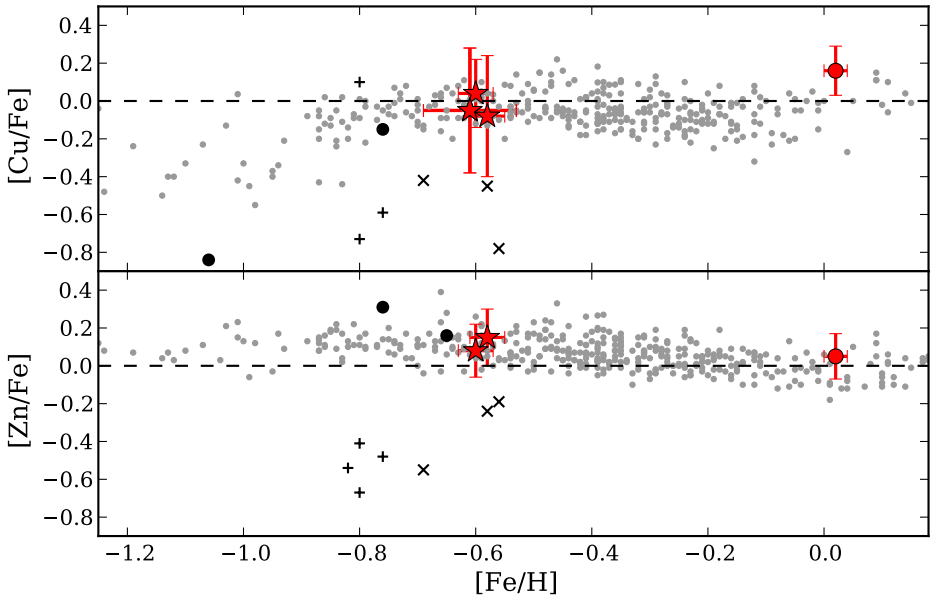

Figure 3.15: [X/Fe] ratios of the elements Cu and Zn versus metallicity. The points are as in Figure 3.5.

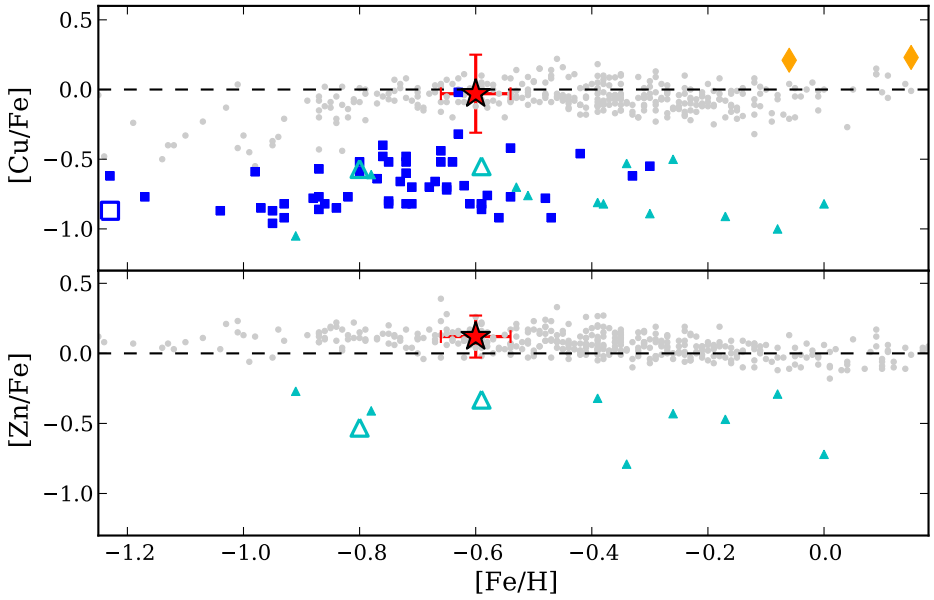

Figure 3.16: [X/Fe] ratios of the elements Cu and Zn versus metallicity. The points are as in Figure 3.7.

3.4.6 Neutron Capture Elements

The heavier elements are formed through neutron captures onto iron-peak nuclei, either via the rapid (r-) process in Type II supernovae, or via the slow (s-) process, e.g. in low mass AGB stars. In the Sun, the percentages of Y, Ba, La, Nd, and Eu that come from the s-process are 75%, 85%, 72%, 47%, and 3%, respectively (Burris et al., 2000); thus Eu is an important r-process indicator.

s-process Elements

The [X/Fe] ratios for the elements that are primarily due to the s-process (Y, Ba, and La) are shown in Figure 3.17. While M67-141 agrees well with the field stars, the Pal 1 stars are deficient in [Y/Fe] compared to field stars and globular clusters. The Pal 1 [Y/Fe] ratios are in better agreement with those from Ter 7 and Pal 12. [Ba/Fe] and [La/Fe] show a similar trend in Figure 3.17: both are higher in Pal 1 than in the field stars, but both are in agreement with 47 Tuc, Ter 7, Pal 12, and the old OCs, particularly Be 29.

High s-process yields have been observed in Galactic GCs (e.g. M4, Yong et al. 2008), and have typically been explained by primordial variations, i.e. the cluster happened to be born in a region where all s-process yields were particularly high. However, in Pal 1 not all the s-process elements are high: Y, a first-peak s-process element, shows the opposite trend from Ba and La, which are second-peak elements. To compare the relative contributions of second-peak to first-peak, [Ba/Y] vs. [Fe/H] is shown in the top panel of Fig. 3.18. Though only lower limits are available for Pal 1-I and -II, it is still evident that Pal 1 has higher [Ba/Y] ratios than the field stars and GCs, though it is in good agreement with the ratios for Ter 7 and Pal 12.

Comparisons with dwarf galaxy stars are shown in Figures 3.19 and 3.20, and show that the Pal 1 stars agree better with the dwarf galaxies than with the Galactic stars. Pal 1's low [Y/Fe] and high [Ba/Fe], [La/Fe], and [Ba/Y] ratios suggest that like the Sgr dSph, Pal 1 was enriched by metal-poor AGB stars. (This effect is also seen in the [La/Y] ratios of the Sgr stars; McWilliam & Smecker-Hane 2005). With an excess of neutrons per Fe atom in metal-poor AGB stars, more heavy second-peak s-process elements such as Ba and La can be created, leaving a deficit of first-peak elements like Y (Gallino et al., 1998; Bisterzo et al., 2010). This further suggests that Pal 1 has not been enriched by its own metal-rich AGB stars, which is perhaps not surprising given its lack of evolved stars (see Figure 2.1b). The GASS field stars do

not have high [La/Fe] like Pal 1, suggesting that the stream does not have an excess of second-peak to first-peak s-process elements. The CMa stars do seem to have high [Ba/Fe] and [La/Fe], and arguably have low [Y/Fe], in agreement with Pal 1.

r-process Elements

The [X/Fe] ratios of elements with larger r-process contributions (Nd and Eu) are shown in Figure 3.21, which shows that M67-141 follows the Galactic field star trend for both Nd and Eu, while Pal 1, though slightly high, is still in agreement with the Galactic field stars within its 1δ errors. Pal 1's [Nd/Fe] ratio may be a bit low compared to Ter 7—no comparisons are available for the other Galactic GCs. The [Eu/Fe] of the Pal 1 stars is in good agreement with Pal 12, though both are much higher than 47 Tuc and the other Galactic GCs and OCs.

Since 97% of Eu is produced via the r-process in the Sun (Burris et al., 2000), it is primarily an r-process indicator. The site of the r-process is believed to be Type II supernovae, which also distribute the α-elements; in this framework, Eu should trace the α-elements. However, this is not seen in Pal 1: the middle panel in Figure 3.18 shows [Eu/α] vs. [Fe/H]. Pal 1 has higher [Eu/α] ratios than the Galactic field stars, GCs, and OCs, but is in good agreement with the [Eu/α] ratios in Ter 7 and Pal 12.

Dwarf galaxy comparisons are shown in Figures 3.20 and 3.22. Pal 1 has slightly higher [Eu/Fe], [Nd/Fe], and [Eu/α] ratios than Galactic stars, in agreement with the LMC, Sgr, and Fornax. While the CMa stars do show an excess of Nd, they do not appear to have an excess of Eu; CMa therefore has a normal value for [Eu/α]. The high [Nd/Fe] and [Eu/Fe] ratios can be understood in terms of small s-process contributions to the dominantly r-process elements (e.g. McWilliam & Smecker-Hane 2005; McWilliam et al. 2013). The high [Eu/α] suggests either that dwarf galaxies have an additional source of r-process elements compared to the Galaxy (see e.g. Letarte et al. 2010) or that dwarfs are lacking the most massive stars that make the α-elements (e.g. McWilliam et al. 2013). Regardless of the cause, Pal 1's [Eu/α] ratio agrees best with the dwarf galaxy stars.

s-process versus r-process

The ratio [Ba/Eu] provides a clue of the ratio of the s- to r-process contributions. Given the strengths of the Ba lines and the possibilities for NLTE corrections, [La/Eu] may be a more suitable ratio; however, since Pal 1 - I and -II only have upper limits

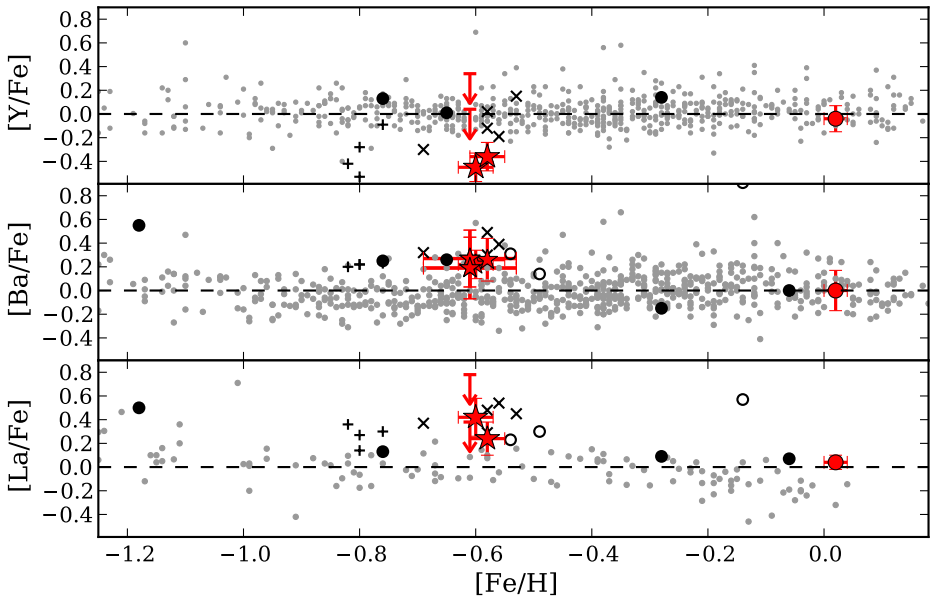

Figure 3.17: [X/Fe] ratios of the elements Y, Ba, and La versus metallicity. The points are as in Figure 3.5, with additional Galactic abundances from Simmerer et al. (2004).

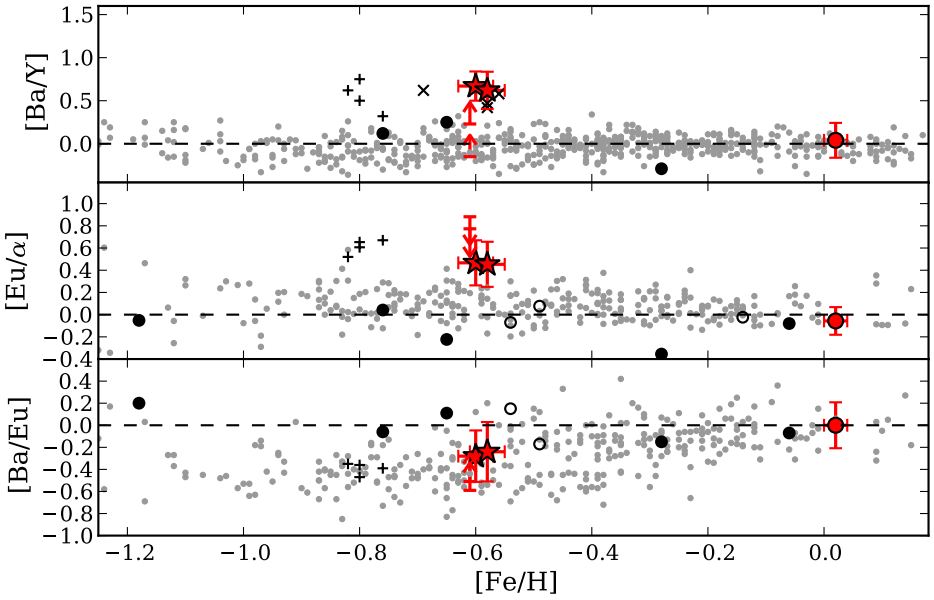

Figure 3.18: [Ba/Y], [Ba/Eu], and [Eu/α] versus metallicity. The points are as in Figure 3.17.

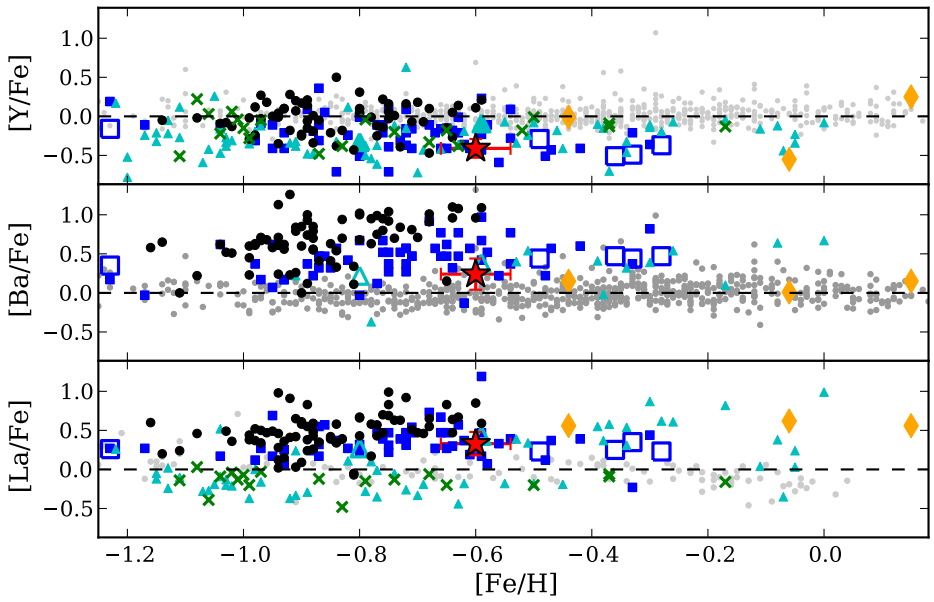

Figure 3.19: [X/Fe] ratios of the elements Y, Ba, and La versus metallicity. The points are as in Figure 3.8.

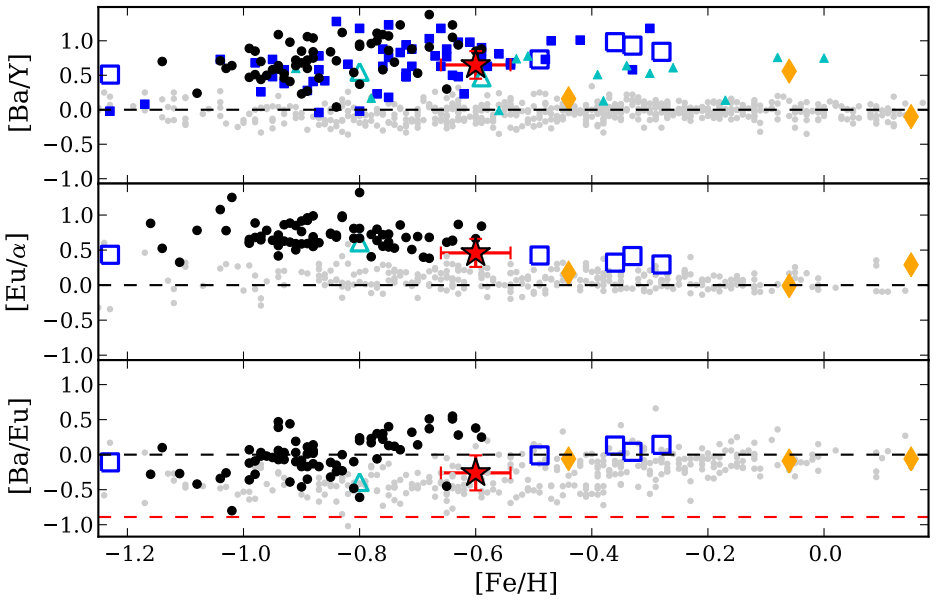

Figure 3.20: [Ba/Y], [Ba/Eu], and [Eu/α] versus metallicity. The dashed red line shows the r-process-only [Ba/Eu] ratio (from Burris et al. 2000). The points are as in Figure 3.7.

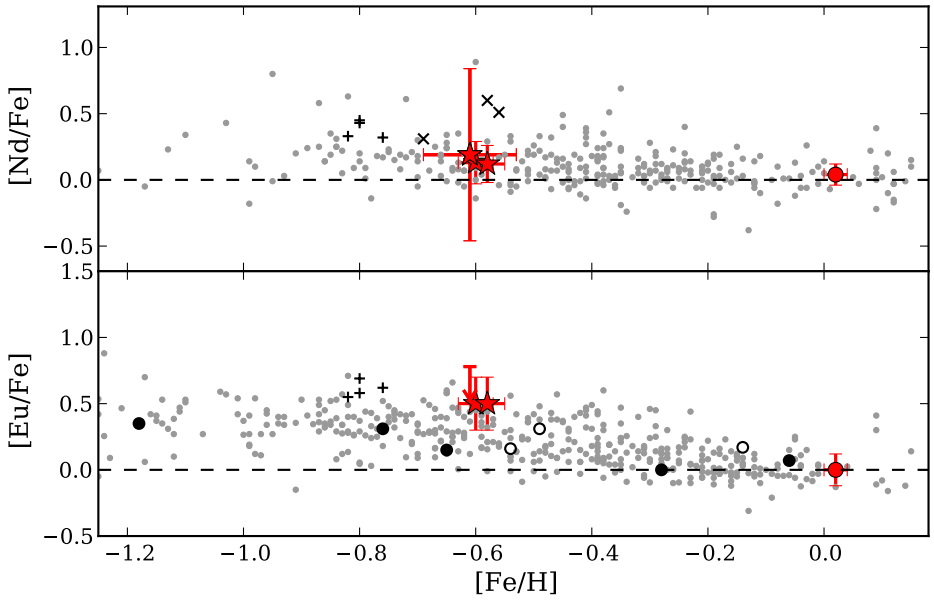

Figure 3.21: [X/Fe] ratios of the elements Nd and Eu versus metallicity. The points are as in Figure 3.17.

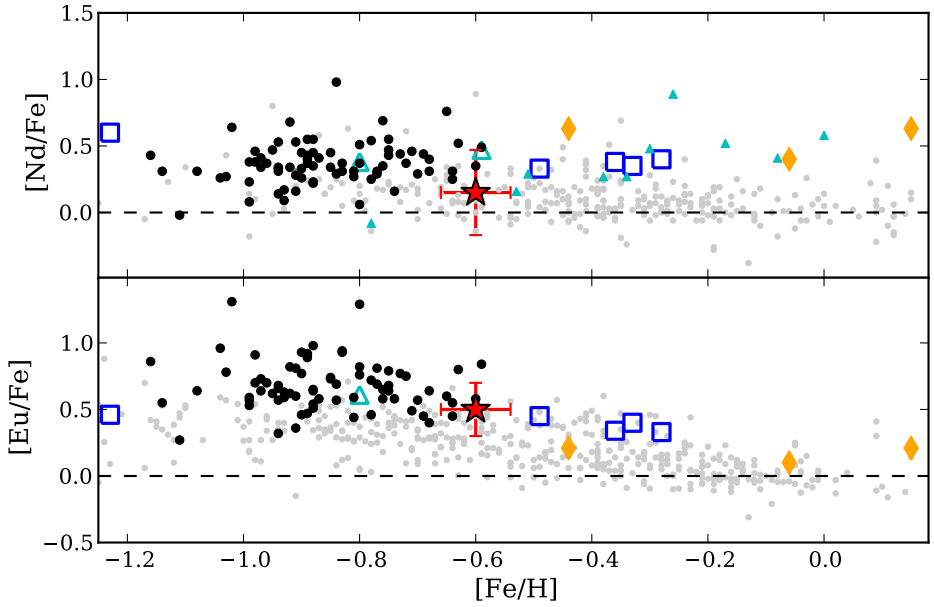

Figure 3.22: [X/Fe] ratios of the elements Nd and Eu versus metallicity. The points are as in Figure 3.7.

for La, [Ba/Eu] is used. The bottom panel in Figure 3.18 shows that Pal 1 is in good agreement with the Galactic field star distribution, suggesting that in Pal 1 the s-process contributes to the chemical evolution in a similar way as in the Galaxy. It is interesting that Pal 1's [Ba/Eu] ratios are similar to Pal 12 and Be 20, but that those are all slightly lower than the rest of the Galactic GCs and OCs.

Despite its discrepant values for [Ba/Fe] and [Eu/Fe], the [Ba/Eu] ratio in Pal 1 agrees better with the Galactic stars than with the dwarf galaxies (see Figure 3.20), though the Fornax dispersion and Pal 12 do extend down to Pal 1's value. Again, CMa's [Ba/Eu] values are in fair agreement with Pal 1.

As discussed in Chapter 1.3.3, the [Ba/Eu] ratio provides an indication of the relative contributions of the s-process to the r-process. Before the s-process begins to contribute Ba is initially produced solely through the r-process; as time goes on the s-process creates more Ba but little Eu, and [Ba/Eu] increases. The theoretical r-process–only lower limit for [Ba/Eu] is shown as the dashed red line in Figure 3.20. Pal 1's slightly high Ba and Eu abundances lead to a [Ba/Eu] value that agrees with the classical prediction for a system that has had little contribution from the s-process. This is not likely to be true given Pal 1's other abundance ratios, particularly the neutron capture ratios (e.g. [Ba/Y]). Taken together, the high [Eu/Fe], [Ba/Fe], and [Eu/α] suggest that the [Ba/Eu] ratio is affected by the extra Eu in Pal 1 (relative to the Galactic FSs). Whatever the case, Pal 1 has clearly not followed the "classical" chemical evolution models.

3.5 Discussion: The Nature of Palomar 1

With the detailed chemical abundances and comparisons with other stars, the nature of Pal 1 can be examined. Ultimately, the guiding questions of the abundance analysis are:

1. Is Pal 1 a globular cluster, an open cluster, or something else altogether? Do the traditional classifications of star clusters need to be re-examined?

2. Did Pal 1 form in the Milky Way, or was it accreted from a dwarf galaxy?

3.5.1 Cluster Type

Given that the cluster types are not well-defined, it is difficult to distinguish between the two types of clusters, particularly when examining chemical abundances. However, the question can be approached by considering abundance spreads within Pal 1, abundance comparisons with other clusters, and kinematic properties of the Pal 1 stars.

Abundance Anticorrelations

Multiple populations have been observed in nearly all Galactic GCs but not in open clusters. Thus, signs of the Na/O and/or the Mg/Al anticorrelations would be positive indicators for a GC. As discussed in Chapter 3.3.6, there is no evidence to suggest that either anticorrelation is present in Pal 1. Certain models (e.g. Conroy & Spergel 2011) suggest that the formation of a second population in a GC depends on the cluster mass, since more massive clusters can retain more gas to form a second population—Pal 1's current mass, $\log(M/\mathrm{M}_\odot) \approx 3.2$ (Niederste-Ostholt et al., 2010), is below the critical mass for retaining the gas to form a second population (i.e. one that is Na/Al enhanced and O/Mg deficient). It has been known for some time that Pal 1 is in the process of evaporating (Rosenberg et al., 1998a); Niederste-Ostholt et al. (2010) further show that the mass in Pal 1's tidal tails is roughly equal to its current mass, suggesting that the cluster might have been at least twice as massive in the past. In the Conroy & Spergel (2011) context, however, Pal 1's lack of a second generation implies that it was *never* more massive than $\log(M/\mathrm{M}_\odot) = 4.0$, regardless of its current size. This restriction is not necessarily prohibitive for a GC: the GC Pal 12 does not show signs of abundance spreads (Cohen, 2004) and five intermediate age

(< 2 Gyr) LMC GCs show no evidence for multiple populations in their CMDs. All that can be said is that Pal 1 is unlike the classical Galactic GCs.

Comparisons with Other Clusters

Pal 1's detailed abundances can also be compared to the well-established GCs in the Galaxy. Its metallicity alone puts it in an unusual regime: while there are many metal-rich GCs, they are usually centrally concentrated in the bulge or disk, while Pal 1 is located much further from the centre and far above the disk ($R_{\rm GC} = 17.2$ kpc and $Z = 3.6$ kpc; Harris 1996; 2010 edition, 2010 edition).[11] Most of the iron-group (Figures 3.11 and 3.12), α- (Figures 3.5 and 3.6), and neutron capture elements (Figures 3.17, 3.21, and 3.18) are in good agreement between Pal 1 and the Sgr clusters; however, the Na, Al, Cu, and Zn abundances (Figures 3.9 and 3.15) are distinctly different. Thus, the chemical pattern of Pal 1 is not clearly similar to either the metal-rich Galactic GCs or the Sgr GCs. Of the GCs, Pal 1 is most similar to Pal 12 and Ter 7, both known to be associated with the Sgr dSph.

There are several old, metal-poor OCs with detailed abundances in the literature, though most are more metal-rich than Pal 1. Several of these clusters are located in the outer disk, and may have been accreted from a dwarf galaxy or formed during a major merging event (Yong et al., 2005). Be 20 and 29, the two clusters in this sample that lie closest to Pal 1's metallicity, have similar abundance ratios as the Galactic stars, with the exceptions of the s-process neutron capture elements. Thus, the only elements that are clearly discrepant between Be 20, Be 29, and Pal 1 are the α-elements (Figures 3.5 and 3.6) and Eu (and by extension [Eu/α] and [Ba/Eu]; Figures 3.21 and 3.18). Cu, Zn, and Y abundances are not available for Be 20 and 29; however, Pal 1's Na and Al abundances (Figure 3.9) agree better with Be 20 and 29 than with the Sgr clusters.

It is then natural to ask if Pal 1 looks more like the GCs Pal 12 and Ter 7 or the OCs Be 20 and 29. In terms of the α-elements and neutron capture elements Pal 1 looks more like the GCs, while Na and Al agree more with the OCs. However, *chemically* comparing Pal 1 to the two cluster types is not an accurate way of determining Pal 1's cluster type, as Pal 1, Be 20, and Be 29 are not conclusively associated with dwarf galaxies while Pal 12 and Ter 7 are associated with the Sgr dSph. Furthermore, the

[11] Recall that previous classifications have labeled Pal 1 as a bulge/disk cluster (e.g. Mackey & van den Bergh 2005) based on its [Fe/H] and HB morphology rather than its location, though its unusual location does distinguish it from the bulge/disk GCs.

chemical abundances of stars depend on their host galaxies' star formation histories, etc., and these quantities are unique to individual galaxies. Thus, unless all of the clusters originated in the Sgr dSph, this comparison is not straightforward.

Table 3.11 shows various quantities that *can* be compared between the clusters: the Galactocentric radius, $R_{\rm GC}$ (in kpc); the distance above the Galactic plane, Z (in kpc); distance from the Sun, d (in kpc); the age (in Gyr; though note that these ages are assembled from different sources, and may not be valid for absolute comparisons); metallicity, [Fe/H]; absolute visual magnitude, M_V; half-light radii, r_h (in pc; note that the distance was used to convert the half-light radius from arcminutes to pc); and concentration parameter, c. The last two parameters are only available for the GCs. Note that Whiting 1, a GC associated with Sgr (Carraro et al., 2007) is also included, though there are no chemical abundances available for this cluster at this time. The values of $R_{\rm GC}$ are similar for all the clusters in the table. The OCs, while more than 1 kpc away from the plane, are still closer than the GCs, with Pal 1 lying between the two. The ages and metallicities are similar, but again Pal 1 is still quite young for a GC. Though Pal 1 is fainter than the OC Be 29, its brightness is comparable to the GC Whiting 1. Finally, Pal 1 has a very small half-light radius compared to Pal 12 and Ter 7, but in agreement with Whiting 1, and Pal 1 is very concentrated, much more so than Ter 7 and Whiting 1.

The distinctions between OC and GC in Table 3.11 seem to be based primarily on distance from the Galactic plane. Considering that Pal 12, Ter 7, and Whiting 1 have been accreted from Sgr, this is not a particularly valid criterion. Consequently, the distance above the Sgr plane, $|Z_{\rm Sgr}|$, is also plotted for clusters that are (or might be) associated with the Sgr dSph (from Law & Majewski 2010; note that Pal 1's $|Z_{\rm Sgr}|$ is also included, although it is most likely *not* associated with Sgr). Examined this way, the clusters look very similar, i.e. *the young, metal-rich GCs that are close to the Sgr plane are similar to the old, metal-poor OCs that are close to the Galactic plane, suggesting that these clusters may be classified as open (or intermediate-aged) clusters in the Sgr frame of reference.* Carretta et al. (2010b) also cast doubt upon the GC classification for Pal 12 and Ter 7, given the lack of a definite Na/O anticorrelation. Under the Carretta et al. definition, Pal 1 is not a bona fide GC; however, it is not an obvious Galactic OC either, suggesting that the historical definitions for star clusters are incomplete.

Table 3.11: Parameters for the GCs and OCs used in this study.

Cluster	R_{GC} (kpc)	Z (kpc)	d (kpc)	age[a] (Gyr)	[Fe/H]	M_V	r_h^b (pc)	c	$\lvert Z_{\rm Sgr}\rvert^c$ (kpc)	Refs
Pal 1	17.2	3.6	14.2	5.0	-0.6	-2.52	1.8	2.57	9.8	
Traditional GCs										
Pal 12	15.8	−14.1	19.0	9.5	-0.80	-4.47	9.1	2.99	3.24	1, 2
Ter 7	15.6	−7.8	22.8	8.0	-0.60	-5.01	4.9	0.93	1.09	1, 3
Whit 1	34.5	−26.3	30.1	6.5	-0.65	-2.46	1.8	0.55	0.22	4
Traditional OCs										
Be 20	15.8	−2.5	-	5.8	-0.44	-2.06	-	-	–	5, 6, 7
Be 29	21.6	1.8	-	4.5	-0.54	-4.64	-	-	1.79	4, 6, 8
Sau 1	19.2	1.7	-	5.0	-0.38	-	-	-	5.25	4, 9

References: If no references are given then the data comes from this study (in the case of Pal 1) or the Harris (1996; 2010 edition) catalog (2010 edition). The other sources are: (1) Dotter et al. (2010); (2) Cohen (2004); (3) Sbordone et al. (2005a); (4) from the sources assembled by Forbes & Bridges (2010); (5) Andreuzzi et al. (2011); (6) Yong et al. (2005); (7) De Marchi et al. (2006); (8) Lata et al. (2002); (9) Frinchaboy et al. (2006)

[a] Note that the ages are assembled from different sources and therefore might not be directly comparable.

[b] The distance d was used to convert the half-light radius (r_h) from arcminutes to parsecs.

[c] All values of $|Z_{\rm Sgr}|$ are from Law & Majewski (2010).

A Connection with Ultra-Faint Dwarfs?

Given Pal 1's previous identification as an ultra faint globular cluster and its proximity to the ultra-faint dwarfs (UFDs) in a plot of absolute magnitude vs. half-light radius (Figure 1 in Niederste-Ostholt et al. 2010), it is tempting to consider whether Pal 1 is related to these other ultra-faint objects. The UFDs are distinguished by their larger-than-expected velocity dispersions, which imply high mass/light ratios and large amounts of dark matter. The velocities for the five Pal 1 stars (including Pal 1-IV) listed in Table 2.8 imply a velocity dispersion of 3.6 ± 1.5 km s^{-1} (using the formula from Walker et al. 2006), *assuming that all five velocities are orbital velocities of cluster members.* Under this assumption, Pal 1's velocity dispersion is in agreement with the velocity dispersions of several UFDs, including Segue II, Leo V, Leo IV, and Hercules (see the summary of UFD properties by McConnachie & Côté 2010).

As tempting as this comparison may be, it is not altogether appropriate. Firstly, Pal 1 has tidal tails and is therefore not in dynamical equilibrium (Niederste-Ostholt et al., 2010). Secondly, only one star out of five (Pal 1-IV) has a discrepant velocity, and this difference is easily explained if Pal 1-IV is a binary; McConnachie & Côté (2010) showed that the presence of binaries can significantly boost the velocity dispersion of a low-mass system. A binary fraction of 20% is not at all unusual for a globular cluster (see, e.g., Côté et al. 1996). Alternatively, Pal 1-IV could be a nonmember—its location in the CMD (Figure 2.1b) is separate from the other stars—however its consistent chemistry and close radial velocity make this seem unlikely. Therefore, Pal 1 remains an ultra faint cluster, and though it would be interesting if it were an extrapolation of the UFDs its current velocity dispersion is best explained by its tidal disruption or by the presence of a binary.

3.5.2 Galactic vs. Extragalactic

The chemical comparisons in Chapter 3.4 indicate that Pal 1 likely originated in a dwarf satellite that was later accreted by the Milky Way (about 500 Myr ago; Niederste-Ostholt et al. 2010). Though the light elements ($Z \leq 30$) are arguably in agreement with Galactic disk stars within the 1δ errors, the neutron capture elements are distinct enough to conclude that Pal 1 does have an extragalactic origin.

Pal 1 has been tentatively associated with both the GASS (Crane et al., 2003) and the CMa overdensity (e.g. Martin et al. 2004, Forbes & Bridges 2010), two streams of stars that could be from disrupted dwarf galaxies. Alternatively, Pal 1 could have

originated in a now-disrupted system that was similar to Sgr, the LMC, or Fornax. The GCs Pal 12 (Cohen, 2004) and Ter 7 (Sbordone et al., 2005b) have both been chemically linked to the Sgr dSph; if Pal 1 is associated with a dwarf galaxy or either of the streams, then it should have similar chemical abundances to the associated field stars and clusters.

Given the low [La/Fe] abundance in the GASS, it is not likely that Pal 1 is a member of this stream. The few stars analyzed in the CMa overdensity are more promising (even if the stars analyzed so far in CMa are more metal-rich): the general trends in the α-abundances, the odd-Z elements Na, Al, Cu, and Zn, the iron-peak elements (with the exception of Sc and V possibly due to HFS corrections), and the neutron capture elements (possibly with the exception of Eu) are in fair agreement. Based on this analysis, it is possible that Pal 1 could be associated with this stream, as suggested by Saviane et al. (2010) and Forbes & Bridges (2010). The slight differences between individual elements could be due to the choices of spectral lines and atomic data. However, it must be noted that none of the CMa stars are guaranteed members, as disk contamination is extremely likely (Sbordone et al., 2005a). In particular, the star with an [Fe/H] closest to Pal 1 seems identical to the Galactic disk stars based on its chemistry, and may not be a true member of the stream. Analyses of more stars in the CMa overdensity, particularly in the metallicity range of Pal 1, would help establish potential membership.

A comparison with the LMC intermediate-age clusters must also be considered, as they are also young and in a similar metallicity regime as Pal 1. There are several low-mass GCs that appear to be similar to Pal 1: in their sample of sixteen intermediate-age clusters, Milone et al. (2009) found five with no signs of multiple populations in their CMDs, suggesting that they were not massive enough to retain gas for a second generation of stars (Conroy & Spergel 2011; see Section 3.4). Though the Na, Al, Cu, and Zn abundances in these clusters are slightly different from Pal 1, the rest of the elements are in good agreement. Pal 1 does not appear to have been accreted from the LMC; however, it is possible that its formation mechanisms were similar to the intermediate-age LMC clusters, i.e. that Pal 1 was accreted from a dwarf galaxy similar to the LMC.

Finally, with the exceptions of [Na/Fe], [Al/Fe], [Cu/Fe], and [Zn/Fe] (which are all higher in Pal 1), Pal 1 agrees well with Pal 12 and Ter 7 in Sgr. Thus, regardless of its uncertain association with either the GASS or CMa, its abundances imply that Pal 1 likely originated in a fairly massive dwarf satellite (i.e. a satellite that had a mass

somewhere between Sgr and the LMC). If this is the case, the progenitor galaxy likely brought in more GCs, although they could be metal-poor and have indistinguishable abundances from Galactic field stars.

3.6 Conclusions

Detailed chemical abundances have been determined for 21 elements in four red giant stars in the unusual GC Palomar 1. The findings are summarized below.

- Pal 1 is an outer halo, young (5 ± 1 Gyr) cluster whose age, metallicity, location, and structural parameters distinguish it from the standard Galactic globular or open clusters. However, Pal 1 does appear to be similar to the known extragalactic GCs and OCs that have been accreted during mergers (i.e. from the Sgr dSph).

- Pal 1's young age and single stellar population suggest a resemblance to the low-mass, intermediate-age LMC clusters. Chemical abundances further suggest that Pal 1 may have shared a similar formation history.

- Pal 1 shows several unusual chemical characteristics, including

  - Lower [α/Fe] ratios than Galactic stars of the same [Fe/H]
  - A lack of evidence for a Na/O anticorrelation, though marginally high Na is found
  - Similar [Fe-peak/Fe] ratios to Galactic stars
  - An excess of second-peak s-process neutron capture elements over first-peak elements
  - Low [Ba/Eu] and high [Eu/α] values that suggest Pal 1's host galaxy had an additional r-process site (possibilities could be inhomogeneous mixing, a truncated IMF that is missing the most massive stars, or variable nucleosynthetic yields).

- Chemically, Pal 1 does not behave like the typical Galactic bulge/disk GCs or the old, metal-poor OCs. The closest agreement seems to be with the Sgr clusters Pal 12 and Ter 7 and the LMC intermediate-age clusters; however the Na, Al, Cu, and Zn abundances do not agree with the LMC or Sgr clusters.

- Comparing the [X/Fe] of the Pal 1 stars to those of stars in known streams show that
  - It is unlikely that Pal 1 originated in the Galactic Anticenter Stellar Stream, given the differing [La/Fe] ratios
  - Pal 1 may have originated in the Canis Major overdensity, if the [X/Fe] ratios of the three possible CMa stars are extrapolated to slightly more metal-poor stars.

Overall, chemical tagging has established that Pal 1 likely had an extragalactic origin, though its chemistry remains unique compared to the known globular and open clusters.

The abundance analysis techniques introduced in this chapter are next expanded to integrated analyses of entire populations.

Chapter 4

Chemical Abundances of Galactic Globular Clusters

Chapter 1.4 outlined the importance of high resolution IL spectroscopy for studying extragalactic GC systems, namely that high resolution is necessary for:

1. Investigating chemical abundances that cannot be accessed with low resolution IL spectra
2. Studying the detailed abundances of individual GCs (e.g. for chemical tagging)
3. Verifying lower resolution techniques.

The first two goals require that high resolution IL abundances be *precise* (i.e. that the random uncertainties be reduced as much as possible) and *accurate* (i.e. that there are no significant systematic offsets in the abundances) so that IL abundances can be compared between clusters and between studies. These tests of precision and accuracy are first performed on well-studied, resolved Galactic GCs—*it is necessary to understand the errors in an IL analysis technique before these methods are applied to unresolved systems.*

This chapter presents the key steps of an IL abundance analysis:

1. The methods for generating model atmospheres are described
2. `ILABUNDS`, the code used to determine integrated abundances, is introduced
3. The EW-based abundances for Fe, Ca, Ti, Ni, and Ba are presented

4. Spectrum synthesis-based abundances for Na, Mg, and Eu are determined, and the precision in SS-derived abundances is investigated

5. The integrated abundances are compared to literature abundances from individual stars

6. The implications for unresolved systems are discussed.

Chapter 5 then presents an analysis of the potential systematic errors in these integrated abundances.

4.1 Model Atmospheres

Chapter 3.1 describes the process of assigning atmospheric parameters to individual stars given their observed colours. For IL observations, atmospheric parameters can be assigned to all the stars in a population via the same techniques *if the population is resolved and a CMD can be obtained*. (If a CMD cannot be obtained, the atmospheric parameters have to be modelled with theoretical isochrones; this technique is deferred to Chapter 4.7.) The *Hubble Space Telescope* (*HST*) photometry used in the CMD - based analyses comes from two sources. The 47 Tuc B, V data is from Guhathakurta et al. (1992) and Howell et al. (2000), and was provided by R. Schiavon—this is the same photometry presented in MB08. The V, I data for all clusters are from the ACS Survey of Galactic Globular Clusters (Sarajedini et al. 2007; Anderson et al. 2008; Dotter et al. 2011). The *HST* magnitudes were converted to Johnson-Cousins V, I magnitudes via the transformations in Sirianni et al. (2005). Stars within the maximum radii observed in the IL spectra were selected for input to `ILABUNDS`, using the cluster centres from Goldsbury et al. (2010). The necessity for cleaning the input photometry is demonstrated by the luminosity functions (LFs; i.e. the number of stars per magnitude bin) for 47 Tuc in Figure 4.1. The core region (i.e. the region within the core radius) is missing the lowest mass stars and is slightly enhanced in AGB stars as a result of mass segregation.[1]

The stars in a CMD are grouped together into boxes to speed up computing time. Each box is assigned the average $T_{\rm eff}$, $\log g$, and ξ of the stars in that box, and the

[1]Mass segregation is a dynamical process where the highest mass stars migrate to the centres of GCs and the lowest mass stars migrate outward. This means that IL spectra of core regions will be biased to contributions from massive stars. Mass segregation has been observed in, e.g., 47 Tuc, and is significant enough to effect dynamical models of the cluster (e.g. Goldsbury et al. 2013).

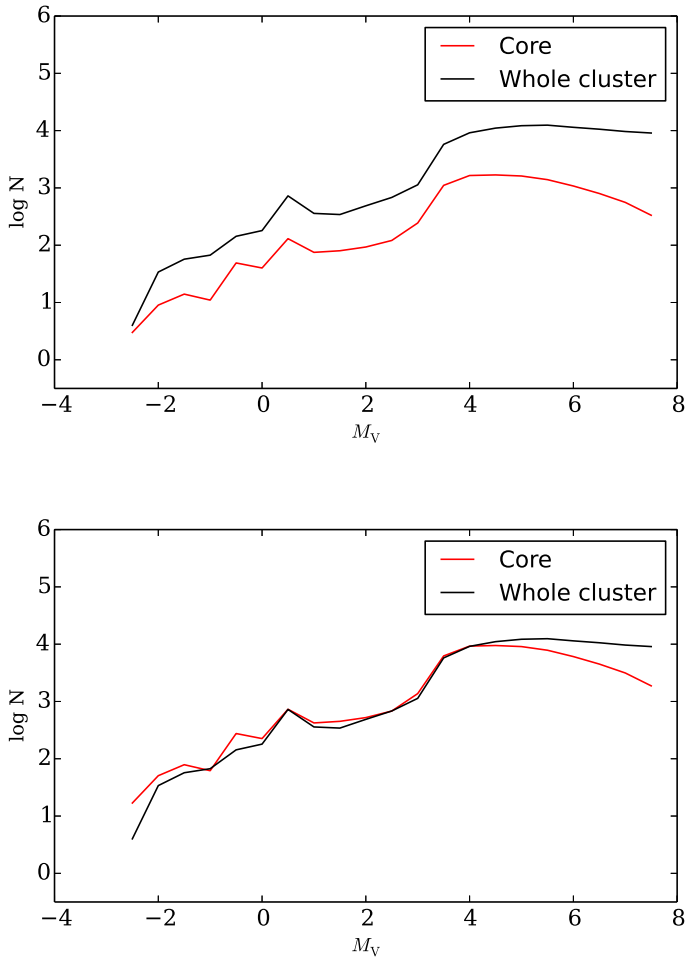

Figure 4.1: Luminosity functions (the number of stars per magnitude bin). The black line show the LF of the entire cluster, based on the V, I data, while the red line shows the LF from the core region scanned by the IL spectrum. *Top:* The true $\log N$ values, illustrating that the core has fewer stars than the entire cluster. *Bottom:* A LF where the core has been scaled up to match the entire cluster. This illustrates the AGB enhancement and the deficiency in MS stars.

box is weighted by the number of stars in that box. Figure 4.2 shows the *HST* CMDs and the boxes. The 47 Tuc boxes are listed in MB08; Tables 4.1 through 4.4 show the parameters of M3, M13, NGC 7006, and M15's boxes, which are determined in the same way as the Pal 1 stars (see Chapter 3.1) except that Ramirez & Melendez (2005) colour-temperature relations are utilized. Distance moduli and reddening values were adopted from Harris (1996; 2010 edition) and turnoff masses of 0.8 $M_{\odot}$ were assumed (a reasonable assumption given that the clusters are all old). Microturbulent velocities are assigned to each box with on an empirical relationship between ξ and $\log g$, based on the Sun and Arcturus (see MB08; the effects of this relationship are examined in Chapter 5.3.2).

Once the atmospheric parameters of a box are known, a corresponding Kurucz model atmosphere[2] (Castelli & Kurucz, 2004) is then assigned. The grid values are interpolated to each box's $T_{\rm eff}$ and $\log g$.

4.2 A Description of `ILABUNDS`

`ILABUNDS` (first developed and presented by MB08) is an IL modification of the 1997 version of `MOOG` (Sneden 1973; see Chapter 3). `ILABUNDS` functions in a similar way as `MOOG`, and can perform both EW and SS analyses. Like `MOOG`, `ILABUNDS` requires input:

1. *Model atmospheres.* Instead of a single model atmospheres, `ILABUNDS` requires model atmospheres for the entire stellar population (see Chapter 4.1).

2. *A line list.* Depending on the analysis type (EW or SS), `ILABUNDS` requires a line list, either with EW measurements or with lines to synthesize.

4.2.1 The Equivalent Width Version of `ILABUNDS`

Integrated EWs are measured with the program `DAOSPEC` (Stetson & Pancino, 2008) and checked by hand, as described in Appendix C. With an integrated EW of a single line and the model atmosphere boxes, `ILABUNDS`:

1. Assumes an initial abundance (either a scaled Solar value or one specified separately)

[2] `http://kurucz.harvard.edu/grids.html`

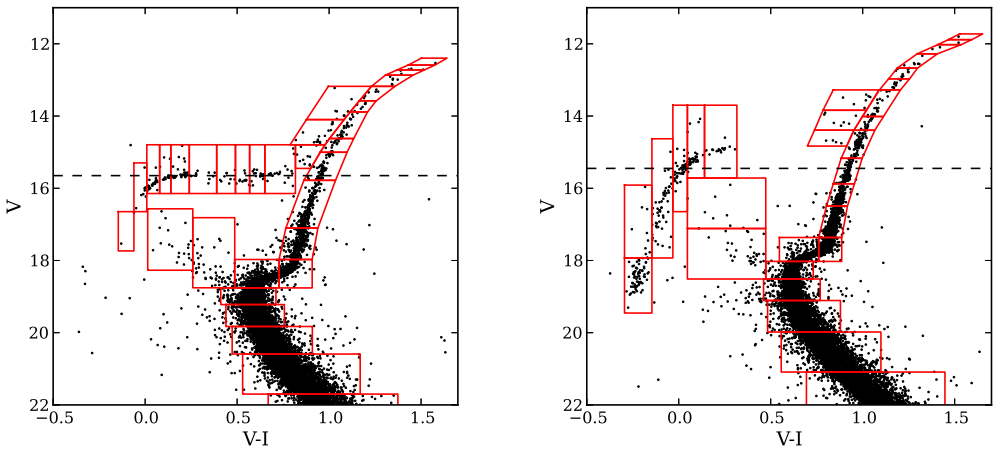

(a) M3

(b) M13

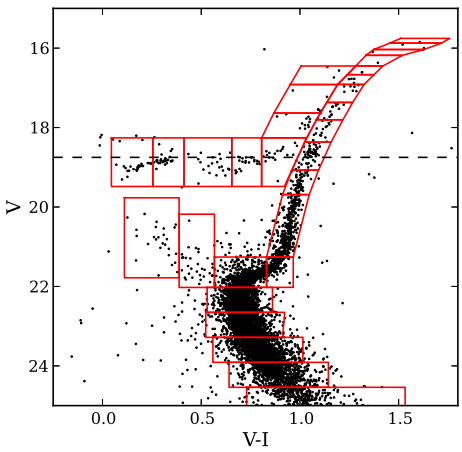

(c) NGC7006

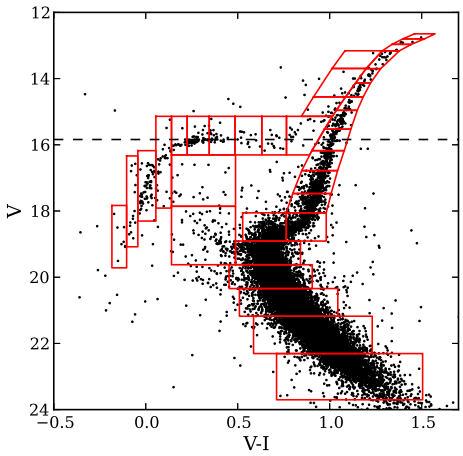

(d) M15

Figure 4.2: *HST* Johnson-Cousins V, I CMDs of the target clusters (Sarajedini et al., 2007; Anderson et al., 2008; Dotter et al., 2010, 2011). The stars have been selected based on their distances from the cluster centre, to reflect the populations sampled by the IL spectrum. Overlaid are the boxes used to assign model atmospheres to the stars. The 50% V-band light levels are shown by the horizontal dashed lines. The brightest stars that lay outside the boxes may be field stars—the possible effects of these field stars are investigated in Chapter 5.3.5, and are unlikely to have a significant effect on the syntheses presented here.

Table 4.1: M3's CMD Boxes

	$V_{0,\mathrm{avg}}$	$(V-I)_{0,\mathrm{avg}}$	T_{eff} (K)	$\log g$	ξ (km/s)	R ($\mathrm{R}_\odot$)	$f(V)$	N
RGB	12.502	1.564	3995	0.333	1.87	100.95	0.0141	1
	12.675	1.450	4125	0.517	1.83	81.63	0.0361	3
	12.754	1.377	4218	0.627	1.81	71.90	0.0224	2
	12.981	1.334	4266	0.759	1.78	61.81	0.0544	6
	13.332	1.218	4437	1.023	1.73	45.60	0.0394	6
	13.683	1.164	4521	1.220	1.69	36.34	0.0332	7
	14.270	1.081	4676	1.547	1.62	24.94	0.0761	28
	14.748	1.014	4686	1.745	1.57	19.86	0.0284	16
	15.398	0.952	4810	2.072	1.50	13.63	0.0712	74
	16.446	0.879	4975	2.575	1.40	7.64	0.0695	197
	17.470	0.824	5114	3.047	1.30	4.43	0.0419	296
SGB	18.185	0.769	5265	3.400	1.22	2.96	0.0252	338
	18.512	0.619	6166	3.850	1.13	1.76	0.0530	960
MS	18.959	0.568	6403	4.098	1.07	1.32	0.0630	1720
	19.475	0.588	6336	4.283	1.03	1.07	0.0707	3120
	20.147	0.651	6075	4.472	0.99	0.86	0.0552	4557
	20.992	0.773	5586	4.647	0.96	0.70	0.0323	5928
	22.113	0.999	4716	4.700	0.94	0.66	0.0067	3549
AGB/HB	13.697	1.052	4757	1.364	1.65	30.79	0.0363	8
	14.471	0.948	4820	1.707	1.58	20.75	0.0362	16
	15.084	0.861	5018	2.051	1.51	13.96	0.0129	10
	15.468	0.733	5374	2.360	1.44	9.78	0.0170	19
	15.615	0.599	5855	2.599	1.39	7.43	0.0144	18
	15.718	0.521	6438	2.829	1.34	5.70	0.0080	11
	15.654	0.436	6773	2.902	1.33	5.24	0.0069	9
	15.610	0.292	7360	3.043	1.30	4.46	0.0097	12
	15.481	0.179	7886	3.110	1.28	4.13	0.0267	30
	15.529	0.103	8372	3.217	1.26	3.65	0.0111	13
	15.834	0.028	9168	3.450	1.21	2.79	0.0163	25
	15.953	−0.021	10189	3.584	1.18	2.39	0.0045	8
	17.501	−0.144	15471	4.506	0.99	0.83	0.0001	1
BS	18.145	0.355	7309	4.022	1.09	1.44	0.0042	57
	17.356	0.146	8264	3.922	1.11	1.62	0.0030	20

The average V and $(V-I)$ colours of each box are shown, along with the average effective temperature, surface gravity, microturbulence, radius, fractional V-band flux, and number of stars assigned to each box. The different evolutionary stages of the boxes are also shown. Note that the 50% light level for M3 is $V_{1/2} = 15.65$, which reaches the middle of the HB.

Table 4.2: M13's CMD Boxes

	$V_{0,\mathrm{avg}}$	$(V-I)_{0,\mathrm{avg}}$	T_{eff} (K)	$\log g$	ξ (km/s)	R ($\mathrm{R}_\odot$)	$f(V)$	N
RGB	11.739	1.494	4083	0.400	1.86	93.39	0.0158	1
	11.907	1.494	4070	0.458	1.85	87.35	0.0136	1
	12.059	1.373	4221	0.649	1.81	70.16	0.0236	2
	12.474	1.257	4377	0.933	1.75	50.57	0.0561	7
	12.740	1.192	4477	1.110	1.71	41.23	0.0565	9
	13.035	1.155	4541	1.269	1.67	34.36	0.0526	11
	13.601	1.061	4717	1.600	1.60	23.46	0.0556	20
	14.123	1.003	4707	1.803	1.56	18.58	0.0350	20
	14.681	0.952	4809	2.081	1.50	13.48	0.0808	78
	15.469	0.890	4948	2.467	1.42	8.65	0.0506	101
	16.134	0.852	5040	2.776	1.35	6.06	0.0369	135
	16.839	0.816	5133	3.100	1.29	4.17	0.0486	346
SGB	17.525	0.779	5247	3.424	1.22	2.87	0.0196	257
	17.809	0.662	5987	3.808	1.13	1.85	0.0357	608
MS	18.213	0.585	6329	4.074	1.08	1.36	0.0677	1676
	18.738	0.580	6369	4.295	1.03	1.05	0.0805	3249
	19.441	0.635	6146	4.507	0.99	0.83	0.0812	6352
	20.367	0.762	5633	4.710	0.94	0.65	0.0478	8903
	21.594	1.007	4699	4.778	0.93	0.60	0.0158	9561
AGB	13.473	0.969	4776	1.581	1.61	23.99	0.0223	7
	14.022	0.841	5069	1.947	1.53	15.74	0.0134	7
	14.646	0.817	5133	2.224	1.47	11.43	0.0044	4
HB	14.851	0.194	7816	3.139	1.28	3.99	0.0153	17
	14.879	0.054	8836	3.322	1.24	3.23	0.0261	32
	15.389	−0.013	9951	3.649	1.17	2.22	0.0247	46
	16.169	−0.105	13400	4.157	1.06	1.24	0.0122	53
	16.745	−0.214	20818	4.733	0.94	0.64	0.0013	10
	18.333	−0.247	24467	5.000	0.78	0.27	0.0024	67
BS	16.465	0.193	7980	3.809	1.13	1.85	0.0019	10
	17.656	0.341	7408	4.144	1.06	1.25	0.0022	34

The 50% light level for M13 is $V_{1/2} = 15.45$, which is slightly below the reddest HB stars.

Table 4.3: NGC 7006's CMD Boxes

	$V_{0,\mathrm{avg}}$	$(V-I)_{0,\mathrm{avg}}$	T_{eff} (K)	$\log g$	ξ (km/s)	R ($\mathrm{R}_\odot$)	$f(V)$	N
RGB	15.694	1.539	4022	0.371	1.87	96.61	0.0197	1
	15.800	1.504	4058	0.445	1.85	88.69	0.0357	2
	15.941	1.300	4333	0.726	1.79	64.21	0.0157	1
	16.215	1.327	4271	0.793	1.78	59.40	0.0122	1
	16.455	1.247	4389	0.975	1.74	48.20	0.0195	2
	16.645	1.196	4469	1.107	1.71	41.40	0.0327	4
	16.855	1.194	4465	1.188	1.69	37.69	0.0472	7
	17.400	1.096	4644	1.517	1.62	25.82	0.0568	14
	17.896	1.049	4735	1.768	1.57	19.33	0.0460	18
	18.517	0.987	4738	2.018	1.52	14.50	0.0895	62
	19.211	0.930	4856	2.357	1.44	9.81	0.0465	61
	20.276	0.876	4981	2.845	1.34	5.59	0.0871	328
SGB	21.312	0.808	5156	3.339	1.23	3.17	0.0196	177
	21.607	0.663	5978	3.765	1.14	1.94	0.0664	792
MS	22.181	0.627	6151	4.048	1.08	1.40	0.0748	1516
	22.774	0.660	6022	4.243	1.04	1.12	0.0491	1722
	23.392	0.722	5774	4.409	1.01	0.92	0.0237	1467
	23.998	0.812	5439	4.530	0.98	0.80	0.0070	759
	24.733	0.955	4804	4.534	0.98	0.80	0.0021	454
AGB	16.429	1.101	4668	1.141	1.70	39.81	0.0299	3
	17.233	1.008	4697	1.481	1.63	26.91	0.0281	6
	17.694	0.941	4833	1.739	1.57	19.99	0.0372	12
HB	18.496	0.823	5115	2.197	1.48	11.81	0.0265	18
	18.718	0.663	5612	2.489	1.42	8.43	0.0266	22
	18.747	0.493	6542	2.809	1.35	5.83	0.0244	21
	18.638	0.244	7564	3.040	1.30	4.47	0.0363	28
	18.713	0.093	8451	3.240	1.26	3.55	0.0308	26
BS	21.184	0.407	7063	3.912	1.11	1.63	0.0039	33
	20.583	0.209	7923	3.883	1.12	1.69	0.0053	26

The 50% light level is $V_{1/2} = 18.75$, i.e. in the middle of the HB.

Table 4.4: M15's CMD Boxes

	$V_{0,\mathrm{avg}}$	$(V-I)_{0,\mathrm{avg}}$	T_{eff} (K)	$\log g$	ξ (km/s)	R ($\mathrm{R}_\odot$)	$f(V)$	N
RGB	12.452	1.361	4349	0.446	1.85	88.58	0.0107	1
	12.599	1.271	4464	0.594	1.82	74.73	0.0373	4
	12.830	1.228	4513	0.724	1.79	64.33	0.0151	2
	13.061	1.157	4617	0.884	1.76	53.51	0.0967	16
	13.569	1.082	4735	1.160	1.70	38.93	0.0532	14
	14.008	1.018	4710	1.323	1.66	32.29	0.0532	21
	14.484	0.967	4805	1.566	1.61	24.41	0.0278	17
	14.941	0.921	4898	1.796	1.56	18.73	0.0706	66
	15.503	0.880	4987	2.064	1.51	13.75	0.0487	77
	16.136	0.843	5073	2.356	1.44	9.83	0.0383	108
	16.814	0.800	5180	2.673	1.38	6.82	0.0518	274
	17.448	0.766	5270	2.963	1.31	4.88	0.0342	323
SGB	18.069	0.702	5460	3.285	1.25	3.37	0.0344	576
	18.366	0.556	5985	3.588	1.18	2.38	0.0427	939
MS	18.947	0.520	6612	4.009	1.09	1.46	0.0863	3261
	19.649	0.554	6495	4.252	1.04	1.11	0.0621	4473
	20.399	0.633	6164	4.451	1.00	0.88	0.0414	5994
	21.285	0.770	5617	4.627	0.96	0.72	0.0183	6062
	22.352	0.971	4797	4.715	0.94	0.65	0.0021	1886
AGB/HB	12.923	1.100	4721	0.892	1.75	53.02	0.0069	1
	13.840	0.962	4814	1.312	1.67	32.69	0.0260	9
	14.632	0.864	5022	1.733	1.58	20.14	0.0171	12
	15.168	0.740	5345	2.087	1.50	13.39	0.0171	20
	15.570	0.562	5959	2.474	1.42	8.58	0.0071	12
	15.490	0.414	6832	2.716	1.37	6.49	0.0084	13
	15.399	0.244	7537	2.864	1.34	5.47	0.0174	25
	15.520	0.147	8051	3.021	1.30	4.57	0.0383	61
	15.637	0.052	8853	3.195	1.26	3.74	0.0090	16
	15.966	−0.032	10589	3.491	1.20	2.66	0.0101	28
	16.613	−0.111	13883	3.958	1.10	1.55	0.0073	33
	16.661	−0.199	19831	4.232	1.04	1.13	0.0016	8
	18.304	−0.273	23306	4.983	0.88	0.48	0.0003	7
BS	16.809	0.143	8198	3.557	1.19	2.47	0.0038	21
	18.375	0.228	7923	4.115	1.07	1.30	0.0046	110

The 50% light level for M15 is $V_{1/2} = 15.84$, which runs through the red HB stars.

2. Calculates EWs for each box, given the initial abundance and the atmospheric parameters for each box

3. Combines the EWs from each box (weighted by luminosity and the number of stars) to produce a synthetic, integrated EW

4. Compares that EW to the observed EW; if the two do not match within 1% the initial abundance is altered and Steps 2-4 are repeated.

In this sense the `ILABUNDS` EW version is quite similar to `MOOG`: given an input EW `ILABUNDS` finds the integrated abundance that best matches that EW.

4.2.2 The Spectrum Synthesis Version of `ILABUNDS`

As in `MOOG`, `ILABUNDS` requires a list of lines to synthesize over a given wavelength region. No line measurements are provided—instead, initial abundances are fed to `ILABUNDS`. In the SS version, `ILABUNDS`

1. Generates a synthetic spectrum for each box given the input abundances, model atmospheres, and line lists

2. Combines the synthetic spectra, weighted by the luminosity of each box, to create a synthetic IL spectrum

3. Broadens the synthetic IL spectrum by the velocity dispersion.

The synthetic IL spectrum is then compared to the observed IL spectrum, and the abundances are altered, if necessary.

4.2.3 Input Line Lists

Spectral lines and atomic data were assembled from five different sources:

1. The IL line lists from MB08 and Colucci et al. (2009)

2. The RGB line line lists from Sakari et al. (2011) and Venn et al. (2012)

3. The Vienna Atomic Line Database[3] (VALD; Kupka et al. 2000)

[3] `http://www.astro.uu.se/~vald/php/vald.php`

4. The Kurucz database[4]

5. The National Institute of Standards and Technology (NIST)[5] database.

Only lines from the first two sources were used to determine the integrated abundances. The lines from the last three sources were used to synthesize lines in the regions around the line of interest, when SS methods were used to determine abundances (see Section 4.5). When the same lines were present in multiple lists the atomic data from the IL and RGB line lists were prioritized, because those lists have been carefully tested and refined.

Hyperfine Structure and Isotopic Information

HFS occasionally affects the lines that are being measured, as well as lines in the synthesized spectral regions. HFS and isotopic components are included for the Ba II and Eu II lines using the components from McWilliam (1998), Lawler et al. (2001a), and Lawler et al. (2001b). All HFS corrections were found to be negligible ($\lesssim 0.05$ dex) and were not applied to any of the Ba II or Eu II abundances presented in this thesis. HFS blends were not included for other lines in the synthesized regions; instead, regions with HFS are noted (see Chapter 4.5).

Damping

Damping (e.g., from pressure broadening) can affect the abundances derived from strong lines. For consistency, damping is included for the strongest lines from the RGB line lists. The damping is implemented in `ILABUNDS` in a similar way as the 2010 version of `MOOG`, i.e. the damping parameters from Barklem et al. (2000) and Barklem & Aspelund-Johansson (2005) were converted to C6 parameters. When damping data were not available from the Barklem sources (or when they did not provide satisfactory fits to the Solar/Arcturus spectra), values from the VALD or Kurucz databases were included.

Molecular Lines

Several abundant molecules (e.g., CH, CN, and MgH) have detectable spectral lines near the lines of interest. The CH, CN, and MgH molecular features were included

[4] `http://kurucz.harvard.edu/linelists.html`
[5] `http://www.nist.gov/index.html`

in all final spectrum syntheses when the features were noted in the Arcturus Atlas (Hinkle, 2003). The MOOG 1997 default values for the molecular equilibrium calculations were employed, with the exception of the MgH dissociation energy, for which the MOOG 2010 value was adopted.

Syntheses of these molecular features require input C and N abundances, and $^{12}C/^{13}C$ and $^{24}Mg{:}^{25}Mg{:}^{26}Mg$ ratios. For each cluster, "integrated" C and N abundances are derived to best fit the molecular lines—each integrated abundance is adopted for the whole cluster, and star-to-star variations are not considered. The observed isotopic ratios from individual stars can vary significantly, even within a single cluster. The $^{12}C/^{13}C$ ratio has been observed to vary from > 50 down to ~ 4 (Lambert & Ries, 1981; Gilroy & Brown, 1991; Gratton et al., 2000; Pilachowski et al., 2003). In M 13, NGC 6752, and M 71, Yong et al. (2003, 2006) found $^{24}Mg{:}^{25}Mg{:}^{26}Mg$ ratios ranging from $48 : 13 : 39$ to $83 : 10 : 7$. Figure 4.3 shows the effects of varying the isotopic ratios, as well as the effects of neglecting all molecular lines, in the regions around the 5528 Å Mg I and the 6645 Å Eu II lines in the Arcturus spectrum. The plots are zoomed in to highlight the weak molecular feature. Here $^{12}C/^{13}C$ ratios of 4, 9, and 50 are considered, as well as $^{24}Mg{:}^{25}Mg{:}^{26}Mg$ ratios of $48 : 13 : 39$ and $83 : 10 : 7$. In these regions, the isotopic ratios do not significantly affect the continuum levels, or the specific lines that are being synthesized, though the inclusion of the molecular lines is necessary to properly fit the regions. Hence, different isotopic ratios are not investigated in these IL spectrum syntheses.

It should also be noted that none of the molecular lines have been calibrated to the Solar and Arcturus spectra (i.e. none of the atomic data, etc. were changed from the Kurucz values). Any regions with mismatching/uncertain molecular features (whether from isotopic ratios or atomic data) are identified in the syntheses with the Final Line List.

4.2.4 Computing Abundances

In both the EW and SS cases, ILABUNDS outputs the $\log \epsilon$ abundances (see Chapter 3.3). The [X/H] ratios are calculated differentially *for each line* (i.e. the abundance from a single line was compared to the Solar abundance for that line, which was derived with the same techniques). This should lessen the potential systematic offsets that could occur because of atomic data, choices of model atmospheres, etc. The [X/Fe] ratios are calculated by comparing elements of similar ionization states. Thus,

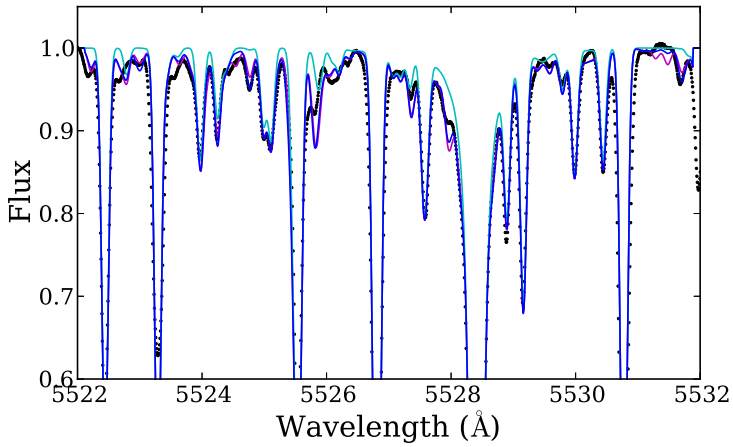

(a) Mg I 5528 Å region

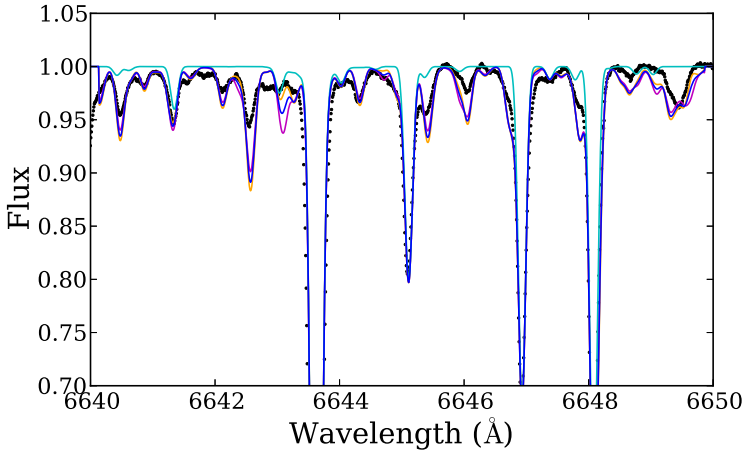

(b) Eu II 6645 Å region

Figure 4.3: Syntheses of the Arcturus spectral regions around the 5528 Å Mg I (top) and 6645 Å Eu II (bottom) lines. The cores of the lines are not shown, since the purpose of the plot is only to highlight the weaker features around the lines of interest. The cyan lines show syntheses of only atomic lines (i.e. no molecular lines were included), with isotopic and HFS components included for the Eu II line in Figure 4.3b. It is evident that atomic lines do not account for all the lines in the regions; in particular, the Mg I region contains MgH lines, while the Eu II region contains many CN lines. The blue lines in the top image indicate Mg isotopic ratios of 48 : 13 : 39 for ^{24}Mg:^{25}Mg:^{26}Mg (Yong et al., 2006), while the magenta lines indicate Mg isotopic ratios of 83 : 10 : 7 (Yong et al., 2003). The orange, blue, and magenta lines in the right-hand image show ^{12}C/^{13}C ratios of 50, 9, and 4, respectively. The varying isotopic ratios do not have a significant effect on the continuum or the lines of interest, though the molecular lines must be included.

the [X/Fe] ratios of neutral species are relative to Fe I and those of singly ionized species are relative to Fe II. In RGB stars, comparing singly ionized species to Fe II reduces systematic uncertainties, as this compares the dominant ionization stages. IL is dominated by RGB stars, and this methodology is therefore adopted.

The random abundance errors were calculated as in Shetrone et al. (2003) and Chapter 3. For each element, three different uncertainties were calculated and compared:

1. The line-to-line abundance scatter. For a single element there is some standard deviation, σ, about the the mean abundance. The uncertainty in the mean abundance is therefore $\delta_{\rm X} = \sigma/\sqrt{N}$, where N is the number of spectral lines.

2. The EW uncertainty. The error of an EW measurement in a particular spectrum can be estimated with the Cayrel (1988) formula; note that an additional 10% $\times$ EW error is included (see Shetrone et al. 2003 and Chapter 3). The abundances were recalculated with larger and smaller EWs, and the offset in the mean abundance, $\sigma_{\rm EW}$, was divided by $\sqrt{N}$ to give the uncertainty in the mean abundance, $\delta_{\rm EW}$.

3. The iron line-to-line scatter. Because there are many iron lines, the iron line-to-line scatter provides an estimate of the *minimum* abundance uncertainty, $\delta_{\rm Fe}$. For an element with few detectable spectral lines, the above error types may underestimate the true abundance error.

The largest of these three uncertainties ($\delta_{\rm X}$, $\delta_{\rm EW}$, and $\delta_{\rm Fe}$) is adopted as the final *random* abundance error for that element.

4.3 Fe Abundances

The average [Fe I/H] and [Fe II/H] ratios for Arcturus and the target GCs are shown in Table 4.5, along with their 1δ random errors.

4.3.1 A Comparison with Literature Abundances

The Arcturus values in Table 4.5 agree well with Yong et al. (2005), while the GC [Fe/H] values agree quite well with the literature values quoted in Harris (1996; 2010 edition, also shown in Table 4.5; note that these values are a compilation of literature

values based on spectroscopic studies). With the exception of 47 Tuc, the [Fe I/H] and [Fe II/H] ratios agree with each other within their 1δ errors.

The 47 Tuc integrated light [Fe I/H] value in Table 4.5 is slightly different from the value from MB08 (which is also shown in Table 4.5), though the [Fe II/H] ratio is in excellent agreement with MB08. Given that the EWs (Figure C.3b) and CMD boxes are nearly identical, and since both [Fe I/H] ratios have been computed differentially, it is puzzling that the [Fe I/H] values are not in agreement. The two $\log \epsilon$(Fe) values *are* actually in agreement ($\log \epsilon$(Fe) = 6.73 compared to MB08's 6.77)—this suggests that there are differences in how the differential [Fe/H] ratios are computed. The low [Fe I/H] ratio in 47 Tuc (compared to [Fe II/H]) may also be due to damping problems in the older version of `MOOG` (A. McWilliam, private communication).

4.3.2 EW Fraction per Box

Each IL spectral line is affected by all the stars in the GC. The precise contributions from each box depend on the luminosity of the box and the parameters of the lines. Figures 4.4 and 4.5 break down the contributions from each box, for two Fe I lines. Figure 4.4 shows the contributions to a low EP Fe I at 6648.121 Å, which has an integrated EW of 15 and 12 mÅ in M3 and M13, respectively. The stars on the upper RGB contribute the most to the integrated EW, with contributions $\sim$ 20%; these bright RGB boxes have EWs from 16-80 mÅ. The scatter between boxes is due to stochastic sampling and boxing of the upper RGB. In all clusters the AGB and HB boxes contribute a small portion to the integrated 6648.121 Å line. Figure 4.5 then shows the contributions to a higher EP Fe I line at 6419.956 Å, which has an integrated EW of 34 and 28 mÅ in M3 and M13, respectively. The contributions from fainter and hotter stars are more significant for the higher EP line; however, the line strength is still dominated by the RGB stars. These results suggest that a trend in Fe I abundance with EP may help constrain the properties of the brightest stars in a cluster.

Table 4.5: Fe Abundances.

	[Fe I/H]	N	[Fe II/H]	N
Arcturus	-0.65 ± 0.02	91	-0.60 ± 0.04	5
Literature	-0.58 ± 0.03		-0.58 ± 0.03	
47 Tuc	-0.81 ± 0.02	68	-0.69 ± 0.07	4
MB08	-0.75 ± 0.03		-0.72 ± 0.06	
Literature	-0.72		-0.72	
M3	-1.51 ± 0.02	95	-1.58 ± 0.05	5
Literature	-1.50		-1.50	
M13	-1.57 ± 0.02	71	-1.55 ± 0.07	3
Literature	-1.53		-1.53	
NGC 7006	-1.52 ± 0.03	73	-1.56 ± 0.07	5
Literature	-1.52		-1.52	
M15	-2.30 ± 0.03	31	-2.38 ± 0.10	1
Literature	-2.37^a		-2.37	

References: Literature values are from Yong et al. (2005) and Harris (1996; 2010 edition) for Arcturus and the target GCs, respectively. The MB08 values for 47 Tuc are also shown.

[a] The literature average is shown here, though note that different studies find [Fe/H] values that differ by ~ 0.3 dex (e.g. Preston et al. 2006 and Sobeck et al. 2011 find [Fe/H] ~ -2.6 while Carretta et al. 2009b find [Fe/H] ~ -2.3). These differences likely reflect systematic offsets between studies, not significant intrinsic [Fe/H] variations.

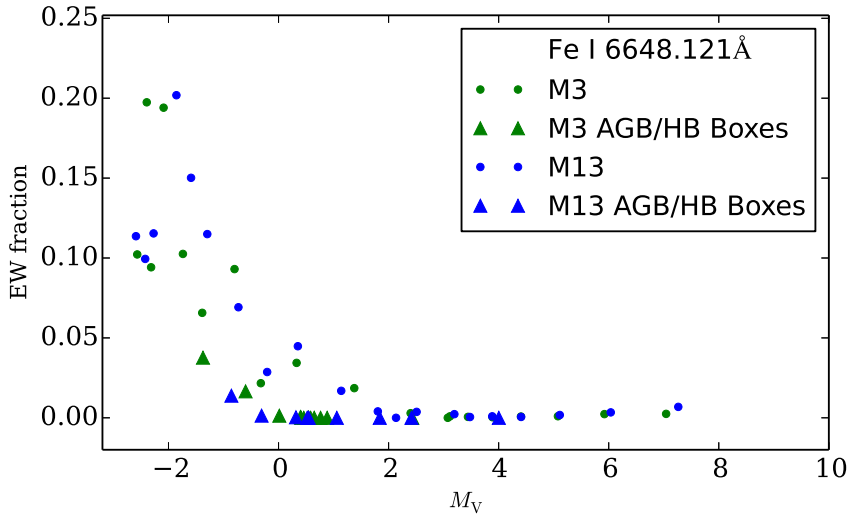

Figure 4.4: EW fraction from each box for the low EP Fe I line at 6648.121 Å, as a function of the average M_V of that box, for M3 (green points) and M13 (blue points). The AGB and HB boxes are indicated with larger triangles. It is clear that the strength of this low EP Fe I line is dominated by stars on the upper RGB, with the largest boxes contributing $\sim 20\%$ to the integrated EW. The scatter in EW fraction at low M_V is due to sampling and boxing effects, where the number of stars per box changes.

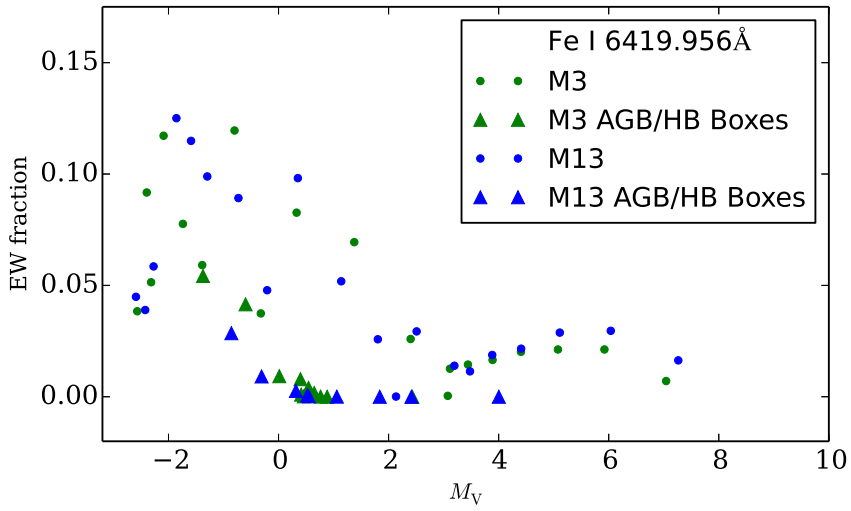

Figure 4.5: EW fraction from each box for the high EP Fe I line at 6419.956 Å, as a function of the average M_V of that box, for M3 (green points) and M13 (blue points). The AGB and HB boxes are indicated with larger triangles. It is clear that this higher EP Fe I is dominated by stars further down the RGB. The lower MS boxes have a non-negligible contribution.

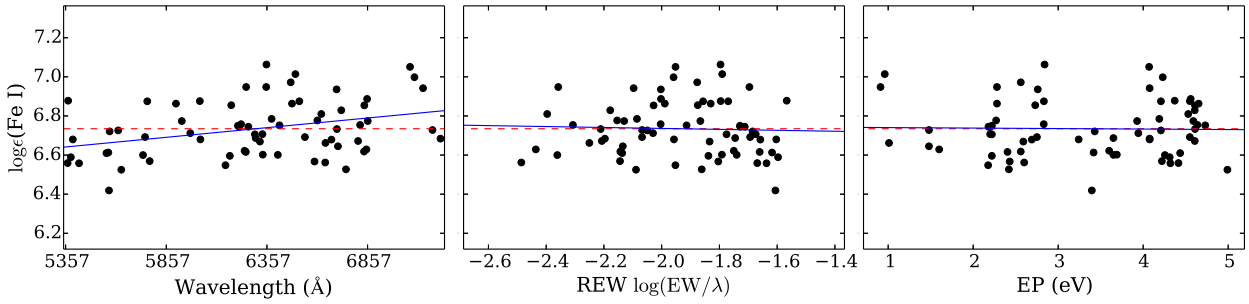

Figure 4.6: Trends in Fe I line abundances in 47 Tuc. Each black point represents a separate spectral line. The dashed red line shows the average Fe I abundance. The solid blue line shows the linear least squares fit to the points.

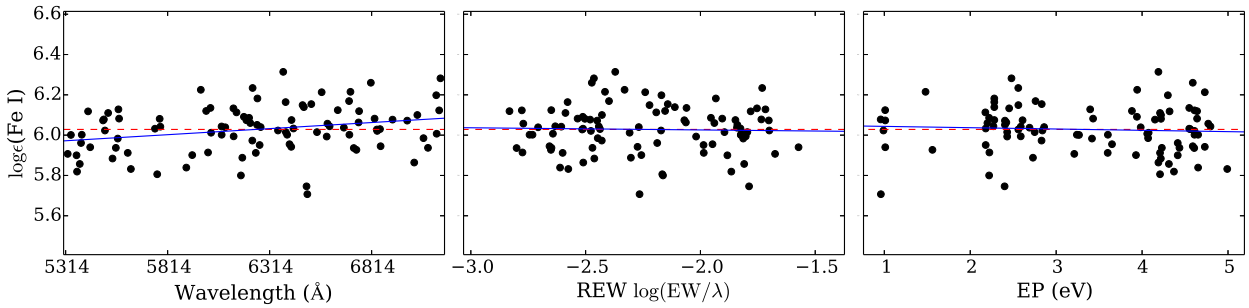

Figure 4.7: Trends in Fe I line abundances in M 3. Lines are as in Figure 4.6.

4.3.3 Trends in Fe Abundance

The trends in the integrated Fe I line abundances are shown in Figures 4.6 through 4.10. The trends are not perfectly flat, though the slopes are sufficiently small (see Table 4.6), except for in the case of M15; however, with only 31 Fe I lines M15's trends in the slopes may not be significant. These (mostly) flat trends for all GCs show that the cleaned CMDs accurately reflect the distributions of stars scanned in the IL spectrum. It is therefore safe to proceed to other abundances.

Table 4.6: Trends in Fe I abundance for the Galactic GCs

Cluster	Wavelength Slope	REW Slope	EP Slope
47 Tuc	$9.9 \times 10^{-5} \pm 3.3 \times 10^{-5}$	-0.024 ± 0.075	-0.0025 ± 0.016
M3	$6.0 \times 10^{-5} \pm 2.3 \times 10^{-5}$	-0.011 ± 0.036	-0.0063 ± 0.011
M13	$7.2 \times 10^{-5} \pm 3.1 \times 10^{-5}$	-0.028 ± 0.053	-0.029 ± 0.015
NGC 7006	$6.7 \times 10^{-5} \pm 4.9 \times 10^{-5}$	-0.071 ± 0.085	0.019 ± 0.023
M15	$-2.9 \times 10^{-5} \pm 4.7 \times 10^{-5}$	0.017 ± 0.091	-0.041 ± 0.022

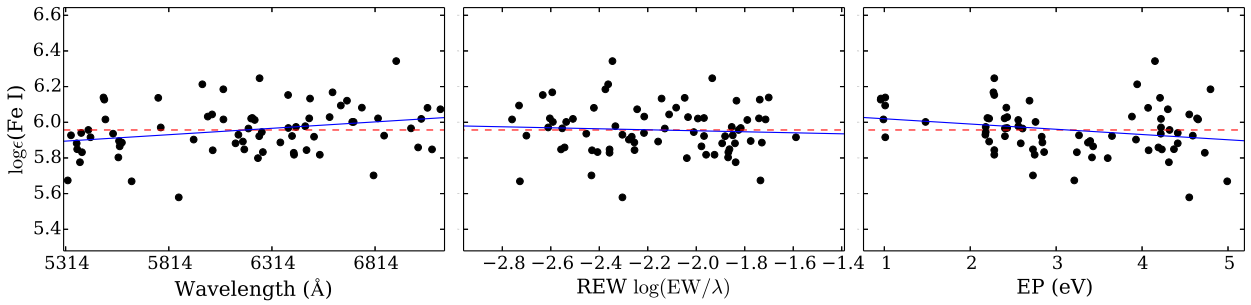

Figure 4.8: Trends in Fe I line abundances in M 13. Lines are as in Figure 4.6.

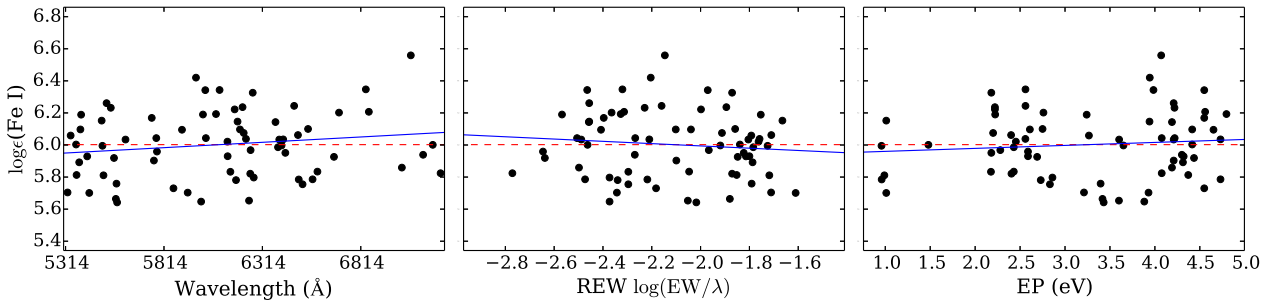

Figure 4.9: Trends in Fe I line abundances in NGC 7006. Lines are as in Figure 4.6.

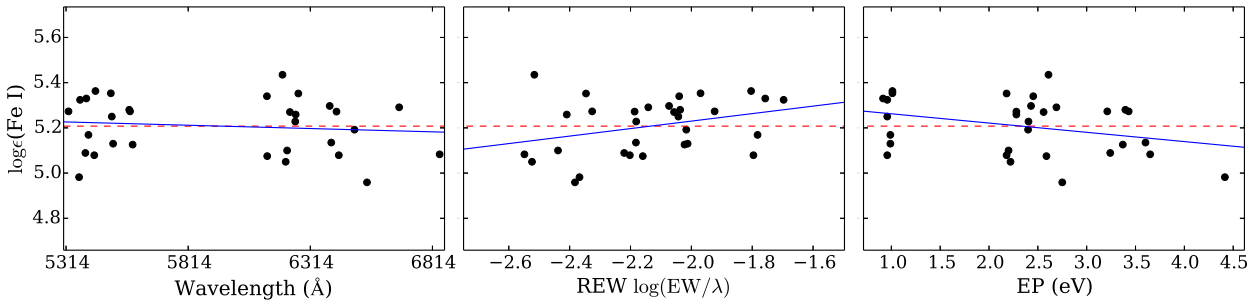

Figure 4.10: Trends in Fe I line abundances in M 15. Lines are as in Figure 4.6.

4.4 EW-based Abundances

In most of the target clusters there are a sufficient number of Ca I, Ti I, Ti II, Ni I, and (possibly) Ba II lines to justify EW analyses.[6] In several cases (particularly for metal-poor GCs like M15 and for elements like Ba II), spectrum synthesis might be preferable in lower S/N GCs because of problems with continuum identifications and blends. For the same reasons spectrum synthesis is necessary for GCs with higher velocity dispersions. The [X/Fe] ratios for the EW-based elements are shown in Table 4.7, along with 1δ errors and the number of lines used. Recall that the Ba II lines were examined for isotopic and HFS corrections (Chapter 4.2.3), which were all negligible.

The 47 Tuc IL abundances are in excellent agreement with the MB08 abundances, with the exception of [Ti I/Fe I] and [Ti II/Fe II]. The MB08 [Ti I/Fe I] ratios are calculated with slightly different lines: MB08 utilized four Ti I lines blueward of 5300 Å (which are inaccessible in the IL spectra of the other targets), while this analysis adds two lines that were not used by MB08. The [Ti II/Fe II] abundances differ partly because of an EW mismatch for the 5381 Å line. Furthermore, MB08 did not combine the spectral orders (see Chapter 2.4) and measured lines in those overlapping regions twice; the 5381 Å line was one of those lines that was included twice. Secondly, if the MB08 EWs are adopted the $\log \epsilon$ ratios agree though the [Ti II/Fe II] still differ by ~ 0.07 dex. This suggests that the [Ti II/Fe II] ratios also differ because of how the differential ratios (with respect to Solar abundances) are calculated. Despite its uncertain EW, the 5381 Å line is retained for this analysis because of the paucity of Ti II lines.

Table 4.7 and Figure 4.11 demonstrate that for the most part the integrated abundances of the other clusters agree well with the literature abundances from individual stars, while Figure 4.12 shows that the IL GC [Ca/Fe] abundances agree with the MW field stars, and have fairly small random errors. Ultimately, all the target GCs are enhanced in α-elements (Ca, Ti I, Ti II), and are roughly Solar in [Ni/Fe] and [Ba/Fe].

[6] Recall that in an IL spectrum most of the lines are blended, making spectrum synthesis essential for determining precise abundances from individual lines.

Table 4.7: Galactic GC abundances derived from EWs.

	[Ca I/Fe I]	[Ti I/Fe I]	[Ti II/Fe II]	[Ni I/Fe I]	[Ba II/Fe II]
47 Tuc	0.28 ± 0.05	0.27 ± 0.09	0.29 ± 0.07	-0.04 ± 0.07	-0.01 ± 0.08
N	9	6	2	7	2
MB08	0.31 ± 0.08	0.41 ± 0.07	0.54 ± 0.09	0.0 ± 0.06	0.02 ± 0.02
Lit.	0.19	0.24	0.36	0.0	0.31
M3	0.37 ± 0.06	0.30 ± 0.09	0.36 ± 0.06	-0.03 ± 0.08	-0.06 ± 0.09
N	17	6	2	7	2
Lit.	0.27	0.32	0.32	-0.02	0.17
M13	0.33 ± 0.06	0.29 ± 0.13	0.42 ± 0.06	-0.02 ± 0.08	0.06 ± 0.08
N	13	6	2	7	2
Lit.	0.26	0.39	0.39	0.02	0.24
NGC 7006	0.46 ± 0.12	0.29 ± 0.17	0.33 ± 0.04	-0.04 ± 0.09	0.19 ± 0.08
N	14	7	1	6	2
Lit.	0.30	0.32	0.32	0.02	0.33
M15	0.31 ± 0.09	$-$[b]	0.33 ± 0.12	$+0.01 \pm 0.08$	-0.21 ± 0.06
N	6	$-$	2	1	2
Lit.	0.27	0.32	0.32	0.01	0.11

[Fe/H] and [X/Fe] values were calculated *line by line* relative to the Solar values, which were derived with the EWs in Appendix C.1.

References: Literature abundances are from the sources assembled in Pritzl et al. (2005), with additional values from Sneden et al. (1997), Kraft et al. (1998), Carretta et al. (2004), Jasniewicz et al. (2004), Cohen & Melendez (2005).

[a] The Ba and Eu abundances vary between stars in some of these GCs, such that the integrated abundances may not match the GC averages.

[b] M15's Ti I lines were not sufficiently strong to determine a robust [Ti I/Fe I] ratio.

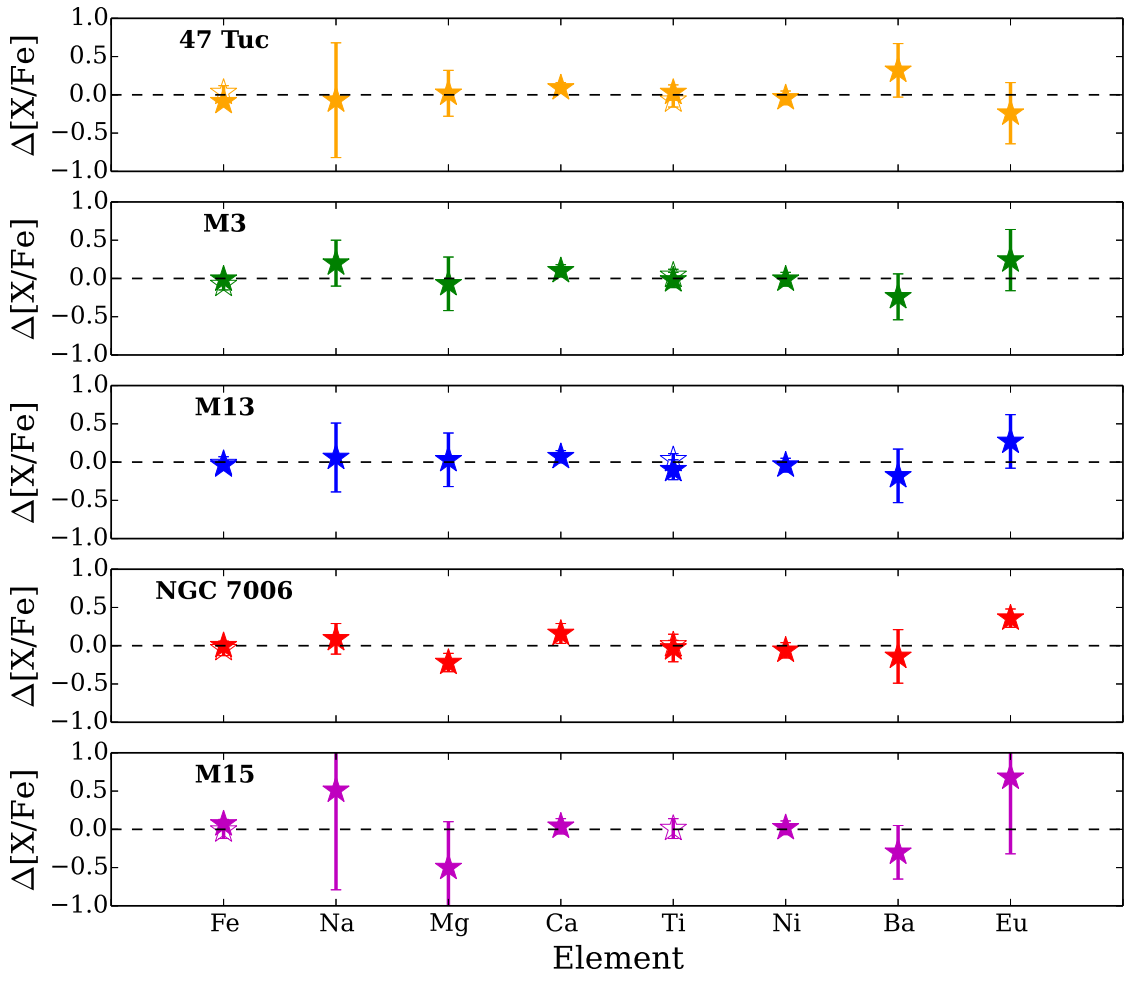

Figure 4.11: Comparisons between the derived integrated [X/Fe] ratios for the Galactic GCs and the literature abundances for individual stars; Δ[Fe/H] is given for Fe. Literature abundances are given in Tables 4.5, 4.7, 4.8, 4.9, and 4.10. The errors bars represent random errors in integrated abundances, added in quadrature with the uncertainties in the literature means, *except for Na, Mg, Ba, and Eu*, for which the error bars show the observed literature ranges.

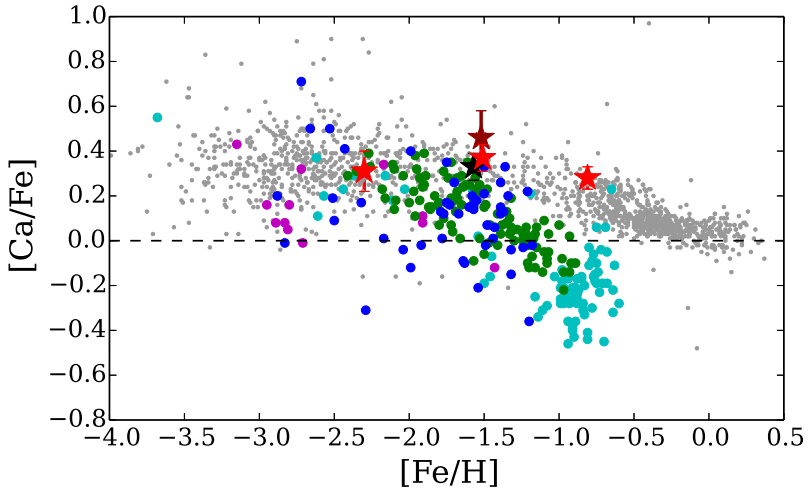

Figure 4.12: [α/Fe] vs. [Fe/H] for the Galactic GCs (red, maroon, and black stars) versus Milky Way field stars (grey points) and dwarf galaxy field stars (coloured solid symbols). The integrated abundances of the Galactic GCs agree best with the Milky Way field stars, in agreement with analyses of individual stars (see, e.g., Pritzl et al. 2005). References are as in Figure 1.7.

4.5 SS-based Abundances

Many of the interesting elements for chemical analyses have only 1-2 detectable lines in an optical spectrum; many of these lines are also weak and difficult to measure. As for individual stars, an EW analysis is undesirable for these lines, particularly in low S/N spectra. Spectrum synthesis (SS) enables the continuum and line strengths to be fit simultaneously, while fixing the FWHM and considering the presence of nearby lines.

Any rigorous spectrum synthesis method should produce abundances with random errors that are less than or equal to the standard error from an equivalent width analysis, whether for individual stars or an IL spectrum (though an equivalent width analysis may still be the preferable choice when the lines are blended, the profiles are uncertain, or the S/N is quite low). An equivalent width analysis of Fe I lines from a $R \approx 30,000$ and S/N $\sim$ 100 spectrum of an RGB star results in a line to line scatter of $\sim \pm 0.1$ dex (see Chapter 3). Therefore ± 0.1 dex is adopted as the minimum uncertainty in the abundance of any single spectral line in an $R = 30,000$ and S/N = 100 spectrum. Since the GC IL spectra have these same qualities, the spectrum synthesis abundance uncertainties should be reduced to this minimum, if possible.

Chapters 4.5.1, 4.5.2, and 4.5.3 show the integrated light syntheses of Mg, Na, and Eu lines in the IL spectra of the five Galactic GCs. Each section begins with syntheses of the 47 Tuc IL spectrum using three different line lists:

Minimal List: This list includes only the standard lines used in IL and RGB analyses. These lines have been selected for other analyses (e.g. MB08, Colucci et al. 2009, Venn et al. 2012) because the lines are well studied, calibrated, detectable, and reasonably free from blends with strong lines. The tests presented in this section show that syntheses with only these lines are incapable of achieving the desired precision, because there are not enough lines to fit the continuum level or to match known blends.

VALD List: This list consists of additional RGB lines from the VALD. These are lines that VALD has determined would appear (to at least 2%) in a tip of the RGB star at 47 Tuc's metallicity. None of the atomic data were changed from the VALD values. This list is included to illustrate that even a reasonably comprehensive line list may not be sufficient without calibrated atomic data or

molecular lines.

Final List: The Final Line List consists of lines from the Minimal List, with supplements from VALD for the coolest RGB stars, warmer RGB stars, and hot stars, all at 47 Tuc's metallicity. Lines that should appear in the Solar spectrum were also included. As shown below, the atomic data from VALD are not capable of reproducing the strengths or profiles of all the lines in the Solar and Arcturus spectra. Thus, atomic data (i.e. $\log gf$ values, damping parameters, and wavelengths) were checked in both the Kurucz and NIST databases. These atomic data were then adjusted so that the Solar and Arcturus spectra were accurately reproduced in the syntheses. The Final Line List also contains the molecular lines from the Kurucz database.

For each case, the errors due to continuum placement and profile fitting are discussed in detail, and it is shown that neither the Minimal nor VALD Line Lists are sufficient for reducing the errors to a satisfactory level in 47 Tuc. Each section then presents syntheses on the other Galactic GCs, using only the Final Line List.

4.5.1 Magnesium

There are two strong Mg I lines that can be detected in IL spectra from GCs of all metallicities. The 5528 Å feature is typically strong in metal-rich ([Fe/H] $\gtrsim -1.0$) stars. In the 47 Tuc spectrum, the equivalent width of this line is ~ 230 mÅ, making the line too strong for an abundance analysis since the uncertainties in damping, atmospheric structure, and NLTE corrections become too large. However, this 5528 Å feature is not as strong in the more metal-poor clusters (such as M3, M13, NGC 7006, and M15), and the spectral region must therefore be calibrated. The 5711 Å line is weaker, and will not be strong enough to measure in the most metal-poor clusters.

5528 Å

Figure 4.13 shows syntheses of the 5528 Å line in 47 Tuc with the three line lists. The top panel shows the syntheses with lines only from the Minimal List, while the middle panel shows the syntheses with the VALD Line List. In addition to the Mg I line, only two other lines are in the Minimal List (an Fe I line at 5522.45 Å, and a Sc II line at 5526.82 Å). The scarcity of lines makes it very difficult to distinguish weak lines

from noise. This leads to large uncertainties in continuum placement, as shown by the large vertical offsets. This uncertainty leads to Mg abundance errors that are ~ 0.20 dex, which is insufficient for distinguishing between a Mg-enhanced and non-Mg-enhanced cluster. The VALD line list (which includes more lines) helps significantly with continuum identification. However, different continuum shifts are still necessary in order to fit the different features, and it is still difficult to distinguish weak features from noise. In this case, the best-fitting synthesis leads to Mg abundance errors that are ± 0.15 dex—this uncertainty is lower than before, but is still large.

The 47 Tuc syntheses with the Final Line List are shown in Figures 4.13, while the syntheses of the Solar and Arcturus spectra are shown in Figure 4.14. The addition of the MgH features in the Final Line List helps improve the continuum identification, particularly for the blended features in 47 Tuc. Despite the strength of the line, the synthesis of the 5528 Å feature fits the Solar and Arcturus spectra quite well. In the 47 Tuc spectrum, the complete, calibrated line list leads to a synthetic spectrum that is an excellent fit to the observed spectrum, as shown in Figure 4.14. This is due to two reasons: first, most of the lines in the region now fit better than before they were calibrated, and second, the best continuum regions are evident in the Solar and Arcturus spectra, and can be used to fit the 47 Tuc continuum.

The fits to the 5528 Å line in the other IL spectra are shown in Figure 4.15, and are quite good for M3 and M13, but are much more uncertain for NGC 7006 (owing to its lower S/N) and M15 (as a result of its weaker lines). The 5528 Å line is easily detectable in all spectra, and there are enough additional lines to help isolate the continuum.

5711 Å

The only RGB line from the Minimal List that appears in this spectral region is the 5711 Å Mg I line itself. Without any additional lines in the region, it is difficult to locate the continuum level in the region, as illustrated by the top synthesis of 47 Tuc in Figure 4.16. In particular, it is unclear whether the peak blueward of the 5711 Å line is the true continuum, noise, an improperly removed cosmic ray, etc. It is also unclear whether the width or depth of the line should be fit. Considering all these factors, the uncertainty in the best-fitting abundance ends up being ± 0.25. As before, the increased number of lines in the VALD Line List helps to isolate the continuum level. However, many of the synthesized lines in the region do not match the observed

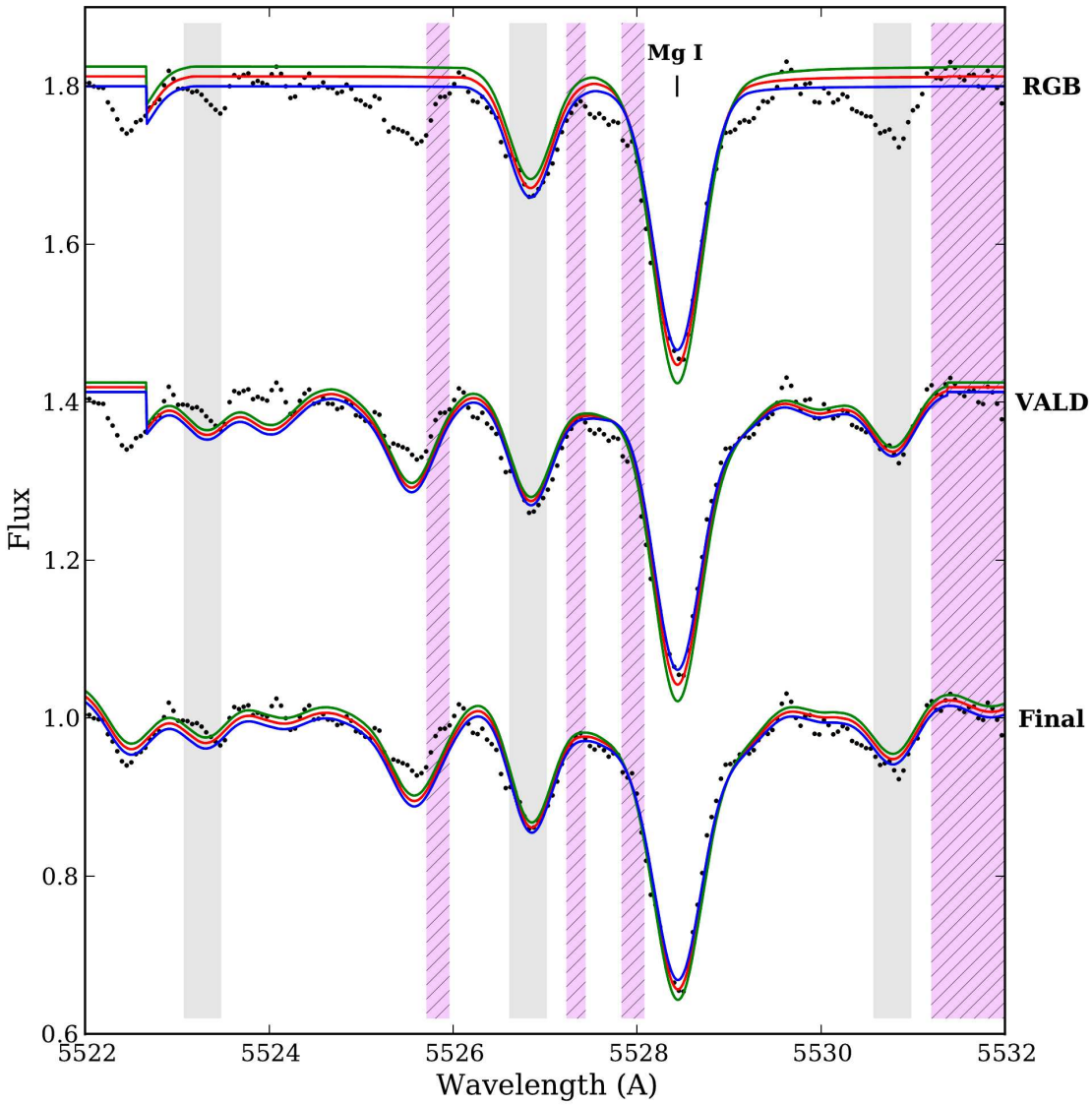

Figure 4.13: Spectrum syntheses of the 5528 Å Mg I line in the 47 Tuc IL spectrum with the Minimal, VALD, and Final Line Lists. Uncertainties in continuum location and line profile fitting are both considered. The red lines show the average abundance, while the green/blue lines show the $\pm 1\sigma$ abundances, respectively. The shaded grey regions indicate areas with possible HFS components, while the hatched light purple regions indicate uncertain molecular features. Both types of regions have been ignored for continuum fits. Note that the abrupt edges of the syntheses are where `ILABUNDS` has truncated the syntheses.

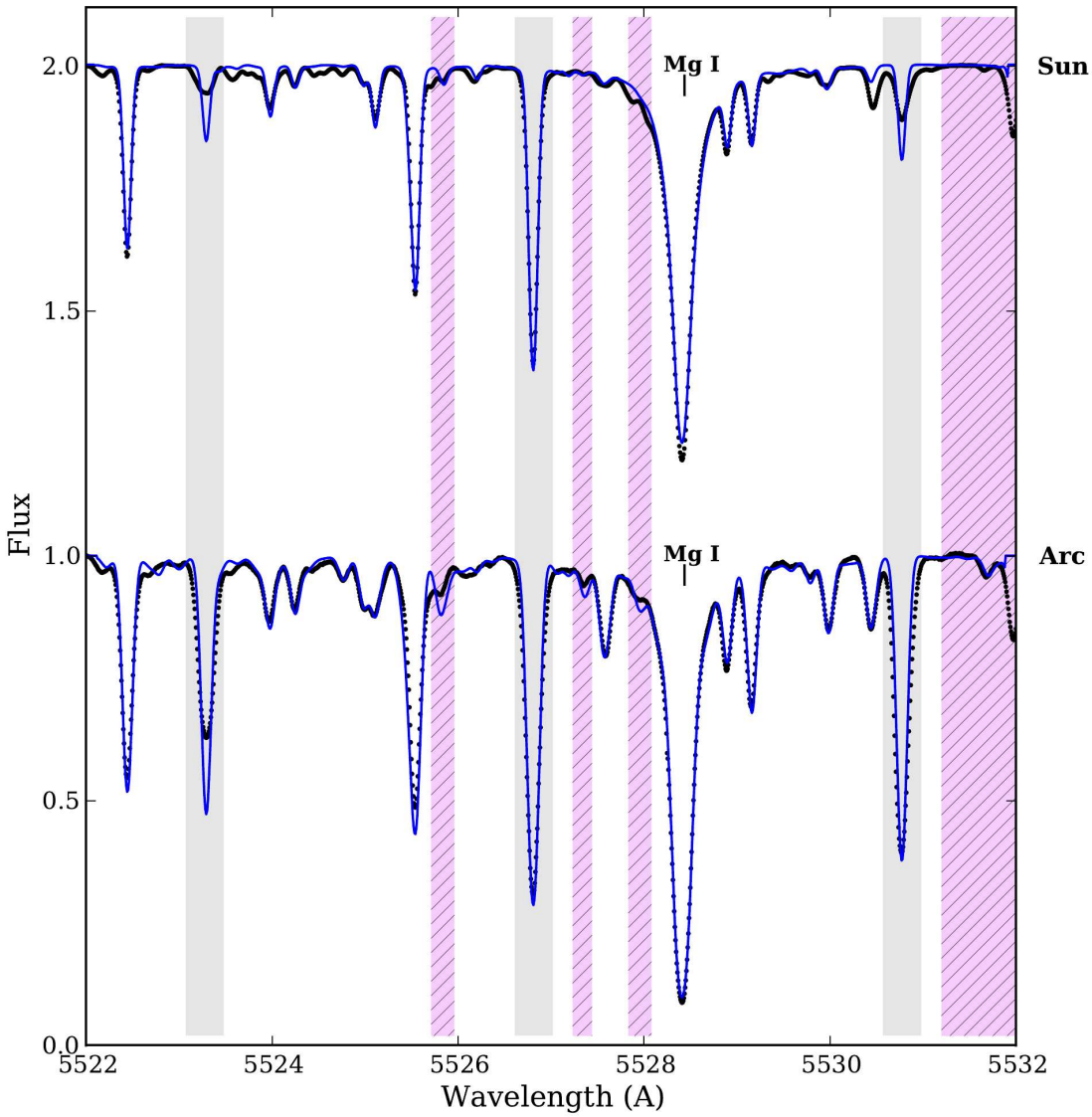

Figure 4.14: Spectrum syntheses of the 5528 Å Mg I line in the Solar (top) and Arcturus (bottom) spectra. Lines are as in Figure 4.13. Note that only the best fits are shown, as the differences in the $\pm 1\sigma$ syntheses are generally too small to see.

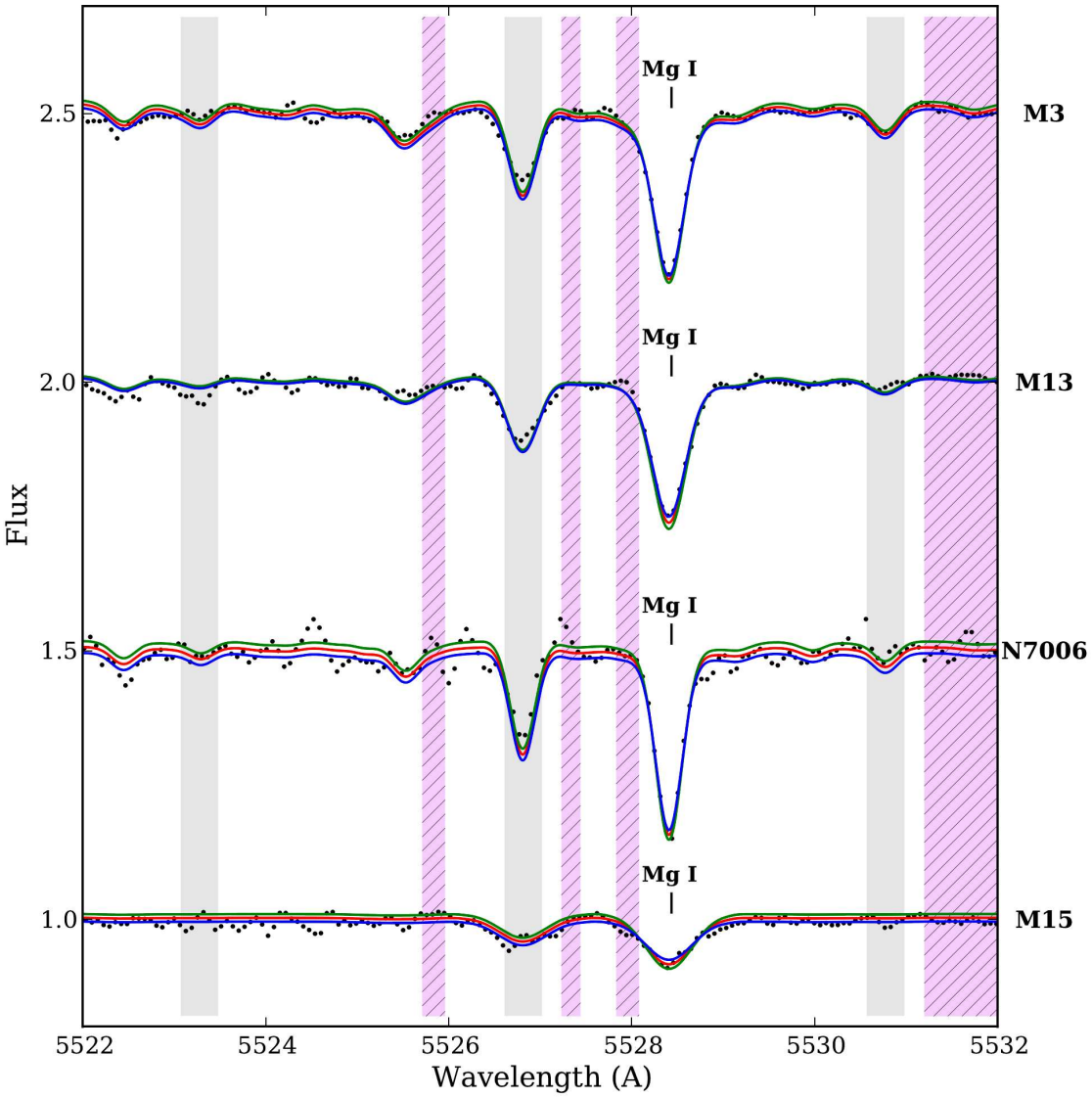

Figure 4.15: Spectrum syntheses of the 5528 Å Mg I line in M3, M13, NGC 7006, and M15. Lines are as in Figure 4.13.

ones—some are stronger, others are weaker, and some are missing altogether. With the VALD lines, the error in the best fitting abundance becomes ±0.17. This level of uncertainty is better, but is still more than expected for a spectrum synthesis on such a high S/N spectrum (~ 100).

Thus, the Minimal and VALD line lists are insufficient for the IL spectrum syntheses of the regions around these two Mg I lines, primarily because the continuum level cannot be clearly identified. These lists may be missing spectral lines (which are blended together in the IL spectrum)—furthermore, the lines that *are* in the lists do not all fit the observed lines properly. This confirms that the line lists *must* be tested and calibrated on well-studied stars, such as the Sun and Arcturus.

The syntheses of the 5711 Å Mg I line with the Final Line Lists are shown in Figures 4.16 and 4.17. These fits show that there are missing lines in the syntheses of this region of the Solar and Arcturus spectra, even with a reasonably complete, calibrated line list. Several lines in the region also require HFS components, e.g. the V I and Sc I lines. Despite the missing features, the strong lines are generally matched well in both the individual and 47 Tuc spectra, with the exception of the feature at 5709 Å. This feature is a blend of Ti I, Fe I, Ni I, and Ti II features, where the Fe I and Ni II features dominate the line strength. It is unclear why the lines match in the Solar spectrum, but not in the Arcturus or 47 Tuc spectra. Regardless, these features can be disregarded in the analyses.

The fits to the 5711 Å Mg I line in the other GCs are shown in Figure 4.18. While the fits are excellent for M3, M13, and NGC 7006, the 5711 Å line is much more difficult to fit for M15 because the GC is metal-poor; this line only provides an upper limit for the Mg abundance in M15.

Comparison with Literature Mg Abundances

The derived Mg abundances are tabulated in Table 4.8, along with comparison literature abundances. The Solar abundances from both lines are in excellent agreement with the Asplund et al. (2009) value. The Arcturus [Mg/Fe] ratios are slightly higher than the average literature value, but the values agree within the errors.

Taken together, the two Mg I lines provide a total [Mg I/Fe I] $= 0.46 \pm 0.14$ for 47 Tuc. This *qualitatively* agrees with the literature stellar abundances assembled by Pritzl et al. (2005), i.e. 47 Tuc is Mg-enhanced, as expected for a Galactic GC at its metallicity, and the IL value is in good agreement with the literature average. Ulti-

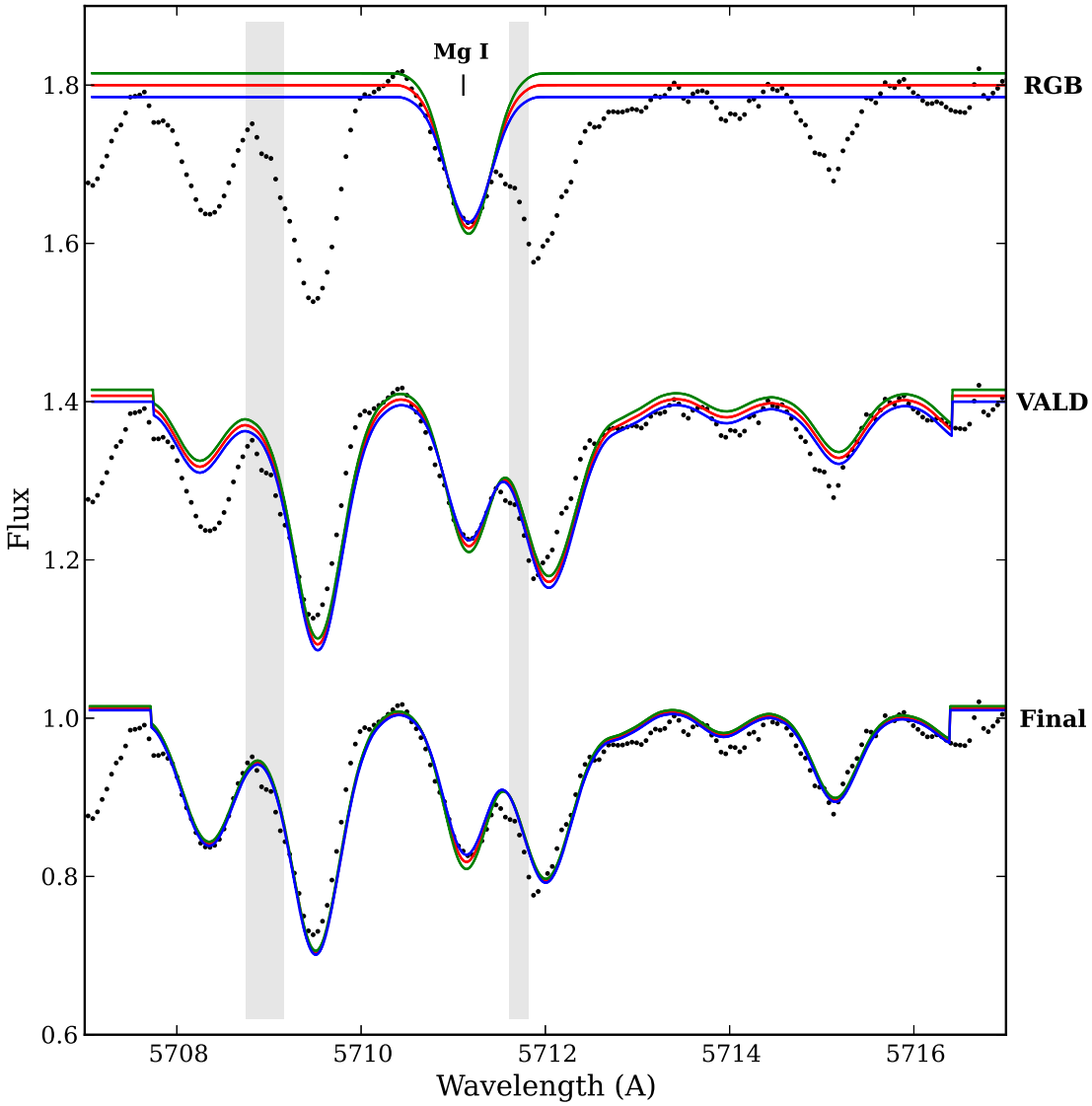

Figure 4.16: Spectrum syntheses of the 5711 Å Mg I line on the 47 Tuc IL spectrum with the Minimal, VALD, and Final Line Lists. Lines are as in Figure 4.13.

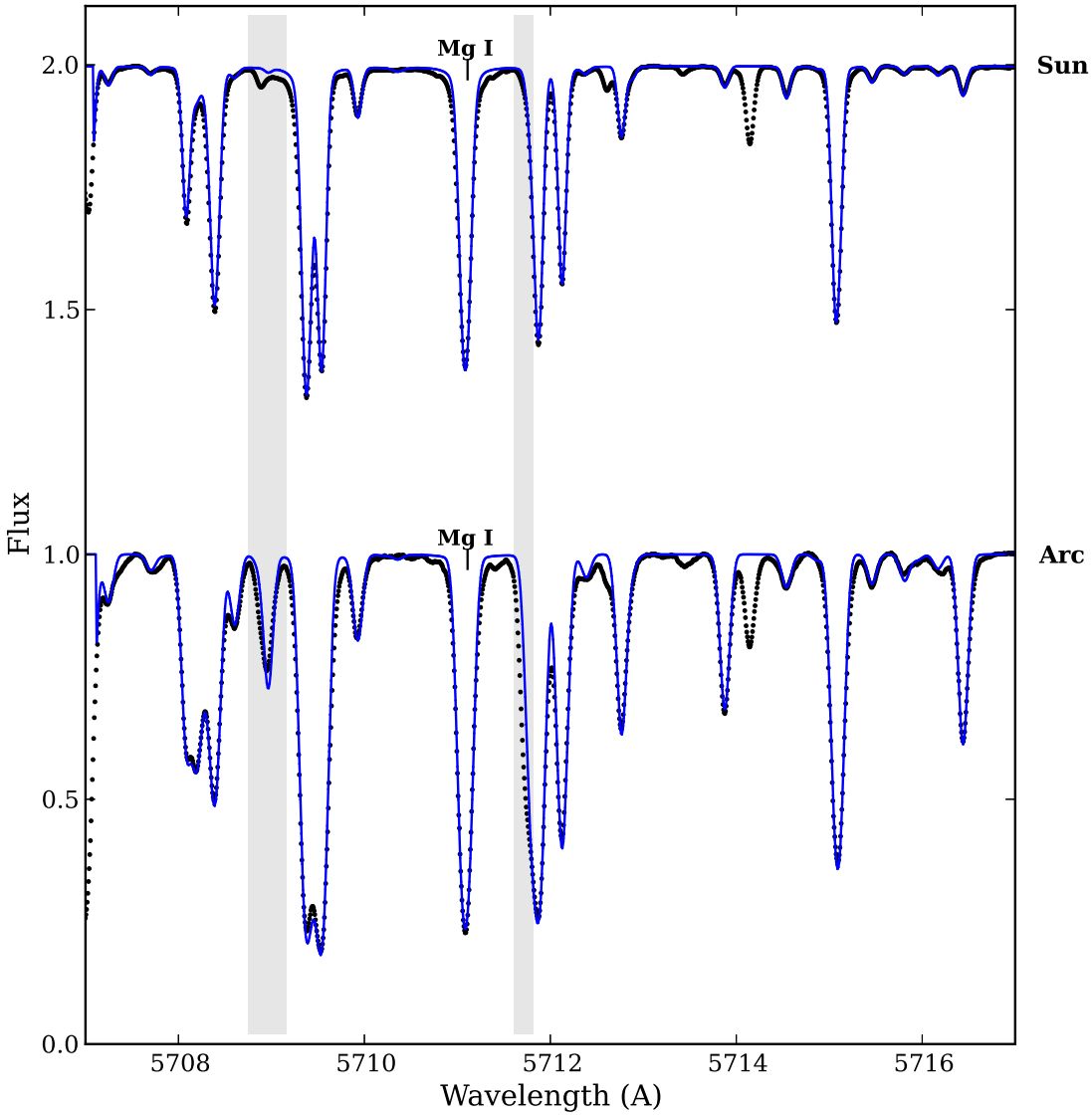

Figure 4.17: Spectrum syntheses of the 5711 Å Mg I line in the Sun and Arcturus. Lines are as in Figure 4.14.

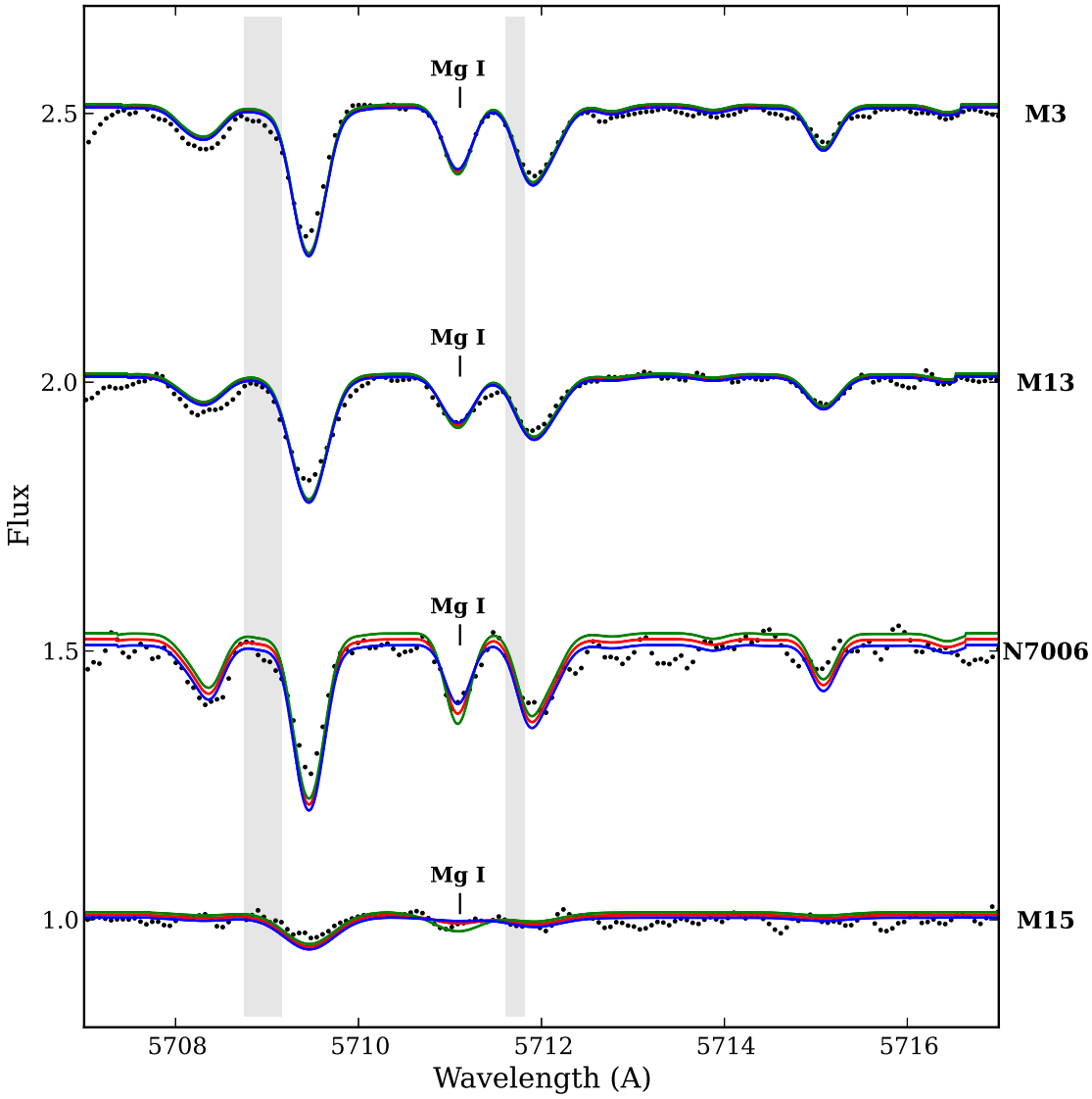

Figure 4.18: Spectrum syntheses of the 5711 Å Mg I line in M3, M13, NGC 7006, and M15. Lines are as in Figure 4.13.

mately, the calibrated Final Line List has reduced uncertainties in the Mg abundance ratios from the Minimal and VALD Lists from ~ 0.2 and ~ 0.18 to ~ 0.14. Thus, spectrum synthesis techniques with the carefully calibrated Final Line List are able to provide improved and precise abundances. However, the 47 Tuc syntheses indicate a best-fitting [Mg/Fe] ratio that is higher than the MB08 value of [Mg/Fe] $= 0.22$ (which was determined from the EW of the 7387 Å Mg I line, and which was not calculated differentially). Adjusting the MB08 Solar abundance leads to a higher [Mg/Fe] ratio in 47 Tuc, as shown below.

The average Mg I IL abundance ratios for M3, M13, and NGC 7006 are in excellent agreement with each other. With the exception of M13, all the IL values are slightly lower than the average literature abundances, especially M15. These differences between the IL abundances and the "average" literature abundances are likely due to the known star-to-star Mg variations within metal-poor clusters (recall the discussion of the Mg/Al anticorrelation in Chapter 3). For example, the M15 Mg abundance quoted in Pritzl et al. (2005) is an average of eighteen bright RGB stars observed by Sneden et al. (1997); the latter analysis showed that M15 has strong star-to-star Mg variations, ranging from $-0.4 \lesssim$ [Mg/Fe] $\lesssim +0.8$, with [Mg/Fe] decreasing for stars higher up the RGB. Furthermore, the Sneden et al. (1997) sample mainly consists of stars from the outer regions of M15, and may be primarily from the "first generation" (see, e.g., Vesperini et al. 2013, Cordero et al. 2014); the [Mg/Fe] variations might be stronger if more second generation stars are observed. Since IL spectra are dominated by the brightest stars in the core regions, the M15 IL spectrum is most likely dominated by the most Mg-poor giants, which decreases the integrated Mg abundance. The derived IL [Mg/Fe] ratio for M15 *does* fall at the lower end of the observed abundance range. M3 and M13 also show signs of Mg variations (Sneden et al., 2004; Cohen & Melendez, 2005) which most likely accounts for their slightly low average [Mg/Fe] abundances in comparison to Milky Way field stars. However, even though these clusters also have star-to-star variations, their abundances *do* agree with the literature averages. This shows that caution must be taken when comparing IL abundances to "average" literature abundances from a limited sample of stars, as discussed in Chapter 4.6.3. This also shows that for chemical tagging purposes [Mg/Fe] might not be the best indicator of the [α/Fe] ratio for metal-poor GCs. Regardless, these comparisons with the literature abundances *do* show that spectrum syntheses of the 5528 and 5711 Å lines are capable of producing Galactic GC Mg I abundances that fall within the observed ranges from individual stars, provided that the lines are

sufficiently strong, and that the S/N is sufficiently high.

7387 Å

To compare the above Mg I integrated light abundances for 47 Tuc with the value quoted in MB08, the 7387 Å line was synthesized in the Solar, Arcturus, and 47 Tuc spectra using the VALD RGB Line List only (Figure 4.19). This region was not calibrated because it falls outside the observed spectral region of the HET clusters, and will not be used in this analysis. Many of the lines in the region do not fit well, precisely because they have not been calibrated. Molecular lines and HFS components were also not included, although the Arcturus Atlas (Hinkle, 2003) shows that there are CN lines in the region.

The Solar synthesis in Figure 4.19 shows that a Solar abundance of $\log \epsilon_{\rm Mg} = 7.30 \pm 0.02$ is required to fit the observed feature; this value is significantly lower than the Asplund et al. (2009) Mg abundance. The line profile also cannot be fit perfectly, as there seem to be extra components in the red wing of the Mg I line. The Arcturus synthesis fits better, but the Mg abundance ($\log \epsilon_{\rm Mg} = 7.15 \pm 0.03$) is lower than from the other Mg lines; a differential comparison with the lower Solar abundance leads to a normal [Mg I/Fe I] $= 0.50 \pm 0.04$. This suggests that the atomic data is systematically offset for this line, and illustrates the importance of using differential abundances and of checking all important lines in the Solar and Arcturus spectra.

Syntheses of the 47 Tuc IL spectrum yield $\log \epsilon_{\rm Mg} = 7.21 \pm 0.20$, which corresponds to [Mg I/Fe I] $= 0.72 \pm 0.20$. The large uncertainty in the abundance reflects the uncertainty in the continuum level, the uncertain line profile, and the low S/N at the line centre. With the Solar Mg abundance from the 7387 Å line, the MB08 value (which comes from an EW analysis of this line) can be recalculated *differentially* to [Mg I/Fe I] $= 0.56$—this value now agrees with the 7388 Å, 5528 Å, and 5711 Å syntheses. Thus, the value quoted in MB08 is systematically lower than it should be, as a result of the lower Solar abundance.

Table 4.8: Solar, Arcturus, and Globular Cluster Mg Abundances

	[Mg I/Fe I] 5528 Å	[Mg I/Fe I] 5711 Å	Total [Mg I/Fe I]
Sun	7.75 ± 0.05^a	7.58 ± 0.04^a	-
Literature Avg			7.60 ± 0.04
Arcturus	0.55 ± 0.18	0.59 ± 0.06	0.57 ± 0.13
Literature Avg			0.46 ± 0.09
47 Tuc	0.39 ± 0.13	0.44 ± 0.14	0.42 ± 0.14
MB08			*0.22/0.56*^{c}
Lit. Avg			0.40 ± 0.03
Lit. Range			$[0, +0.6]$
M3	0.12 ± 0.11	0.20 ± 0.07	0.16 ± 0.11
Lit. Avg			0.23 ± 0.03
Lit. Range			$[-0.1, +0.6]$
M13	0.13 ± 0.11	0.14 ± 0.08	0.14 ± 0.10
Lit. Avg			0.11 ± 0.03
Lit. Range			$[-0.2, +0.5]$
NGC 7006	0.10 ± 0.14	0.13 ± 0.20	0.12 ± 0.17
Lit. Avg			0.34 ± 0.02
Lit. Range			$[+0.3, +0.4]$
M15	-0.15 ± 0.21	< 0.55	-0.15 ± 0.21^c
Lit. Avg			0.35 ± 0.05
Lit. Range			$[-0.4, +0.8]$

The mean literature values are un-weighted averages. The quoted $\pm 1\sigma$ errors in the literature mean do not reflect the observed range in the abundances. The literature ranges show the approximate extremes that have been observed.

References: Literature Solar values are from Asplund et al. (2009). Arcturus literature values from Yong et al. (2005), Fulbright et al. (2007), and Ramírez & Allende Prieto (2011) after shifting to a common [Fe/H] = −0.6. The GC literature data are from MB08 and Pritzl et al. (2005), with supplements from Brown & Wallerstein (1992); Sneden et al. (1997); Kraft et al. (1998); Sneden et al. (2004); Carretta et al. (2004); Jasniewicz et al. (2004); Cohen & Melendez (2005); Alves-Brito et al. (2005); Preston et al. (2006); Wylie et al. (2006); Koch & McWilliam (2008); Carretta et al. (2009a); Worley et al. (2009); Sobeck et al. (2011); Gratton et al. (2013).

[a]Solar values are $\log \epsilon$ abundances, not [X/Fe] ratios.

[b]The first value is from in MB08; the second is the re-derived *differential* value.

[c]This IL abundance is likely to be affected by star-to-star variations within M15.

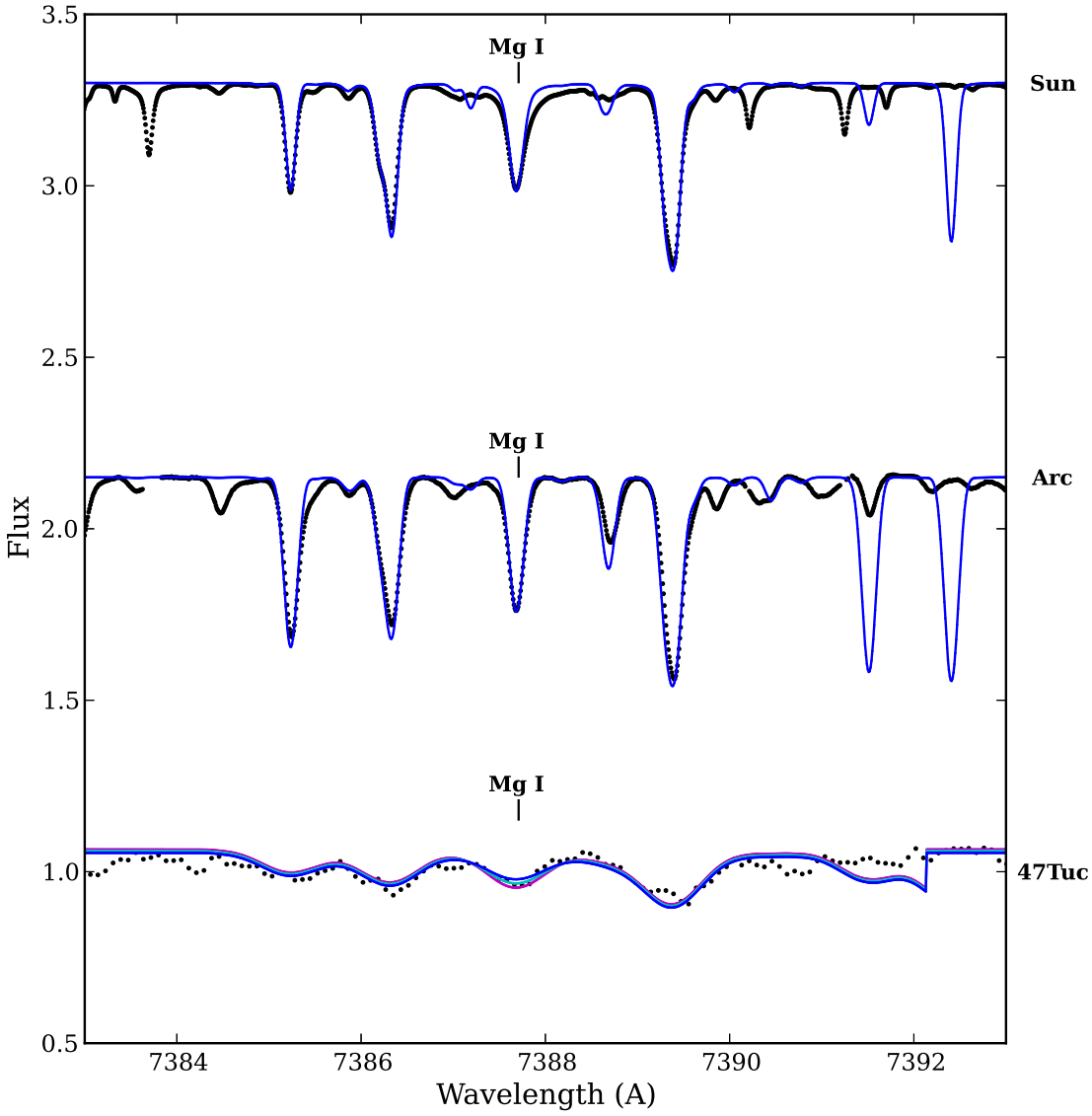

Figure 4.19: Spectrum syntheses of the 7388 Å Mg I line in the Solar (top), Arcturus (middle), and 47 Tuc (bottom) spectra. The HFS regions are not shown, though there are several in this region. Molecular lines are also not included. Lines are as in Figure 4.13.

4.5.2 Sodium

There are several strong Na lines in the optical portions of IL spectra. The strong Na D lines are too strong in all but the most metal-poor GCs, and have not been included in this analysis.[7] As discussed in Chapter 3, Na lines are known to suffer from strong non-LTE effects. No NLTE corrections are applied to these IL Na abundances—to avoid necessary NLTE corrections, Lind et al. (2011) suggest that analyses at Solar metallicity should use the 6154/6160 Å doublet, while analyses of more metal-poor stars ([Fe/H] $\lesssim -1.0$) should use the 5682/5688 Å lines. However, literature results use both sets of lines, often without any NLTE corrections. Here the results for the 6154/6160 doublet are presented for all the GCs. The NLTE effects make it difficult to fit the Solar 5682/5688 Å lines (in agreement with, e.g., Baumüeller et al. 1998), which prevents a differential analysis from being done. Without a differential analysis the atomic data can lead to systematic offsets between lines.

6154/6160 Å

Figure 4.20 shows spectrum syntheses of the 6154/6160 Å doublet in 47 Tuc. The synthesis with the Minimal Line List (the top synthesis in Figure 4.20) only has a few strong lines available for continuum identification. Furthermore, the features are strongly blended in the 47 Tuc spectrum, and there are few obvious continuum locations. The 6160 Å line, in particular, is blended with the nearby Ca I line in most of the targets. With only these strong lines, the errors in the best-fitting abundances are ±0.30 and ±0.13 for 6154 and 6160 Å, respectively. The VALD lines (shown in the the middle syntheses in Figure 4.20) help slightly, bringing the abundance errors to ±0.25 and ±0.12, respectively.

Figures 4.20 and 4.21 show syntheses of the 6154 and 6160 Å Na I lines in the 47 Tuc, Solar, and Arcturus spectra with the Final Line List. With so many lines (both strong and weak) and blends in the region, it is easy to see how fitting becomes very difficult with IL spectra. In particular, it is difficult to isolate continuum regions and to know which regions *should* match the synthetic spectra, and which could be different as a result of improper atomic data, missing atomic or molecular lines, or HFS. Without Solar and Arcturus calibrations to identify the best areas for continuum fitting, such a region is quite difficult to fit. With the Final List, it is clear that HFS contamination seems to be minimal in this region. The Solar and Arcturus syntheses

[7] Furthermore, the Na D lines are occasionally affected by interstellar absorption.

show that there are clearly lines missing from the line list, though they are mostly weak. The Solar and Arcturus spectra also show that the syntheses cannot perfectly reproduce the shape of the 6154 Å Na I line—there seems to be a missing component slightly redward of the line centre. Thus, the syntheses to the 47 Tuc spectrum focused primarily on fitting the depth of the line rather than the width.

For the 6154 Å sodium line, the Final Line List has reduced the errors from 0.30 (from the Minimal Line List) and 0.25 (from the VALD Line List) to 0.15. In the case of the 6160 Å line the improvements are similarly excellent, with decreases from 0.13 and 0.13 to 0.07. Again, the Final Line List provides a significant improvement in the precision of the derived IL abundances. The Na 6154/6160 Å syntheses on M3, M13, NGC 7006, and M15 with the Final Line List are shown in Figure 4.22.

Comparisons with Literature Na Abundances

The best fitting abundances to the 6154/6160 Å Na I lines are shown in Table 4.9, along with comparison literature abundances. The Solar values are in reasonable agreement with the Asplund et al. (2009) value. The Arcturus value is also in excellent agreement with the average literature value, after shifting to a common [Fe/H].

For the GCs, literature abundances were determined with both the 6154/6160 and 5682/5688Å lines (and occasionally also the Na D lines). In the case of M3, M13, and NGC 7006, the literature abundances have *not* had NLTE corrections, while some of the M15 stars did have NLTE corrections. The M3/M13 literature abundances are from 36 and 60 stars from the base of the RGB up to the tip of the RGB while the NGC 7006 literature abundances are only from six tip of the RGB stars. M15's literature abundances are mainly from more evolved stars (e.g. RGB, HB, and AGB stars). Most literature abundances are from stars in the outer regions of the clusters.

The 47 Tuc value is in agreement with the MB08 value, which was derived from the same lines. The IL abundance also agrees well with the average literature abundance in Table 4.9. As a Galactic GC, 47 Tuc is one of the many Galactic GCs that have shown star-to-star variations in Na, as mentioned earlier (e.g. Carretta et al. 2009a). However, in this case the Na abundance is not overly high, suggesting that 47 Tuc's integrated light is not dominated by Na-enhanced stars. While M13 and NGC 7006's IL abundances are in good agreement with the literature averages, the IL Na abundance in M3 is quite a bit higher than the average literature value. The 6160 Å line is not well-resolved in the M15 IL spectrum, and hence provides only

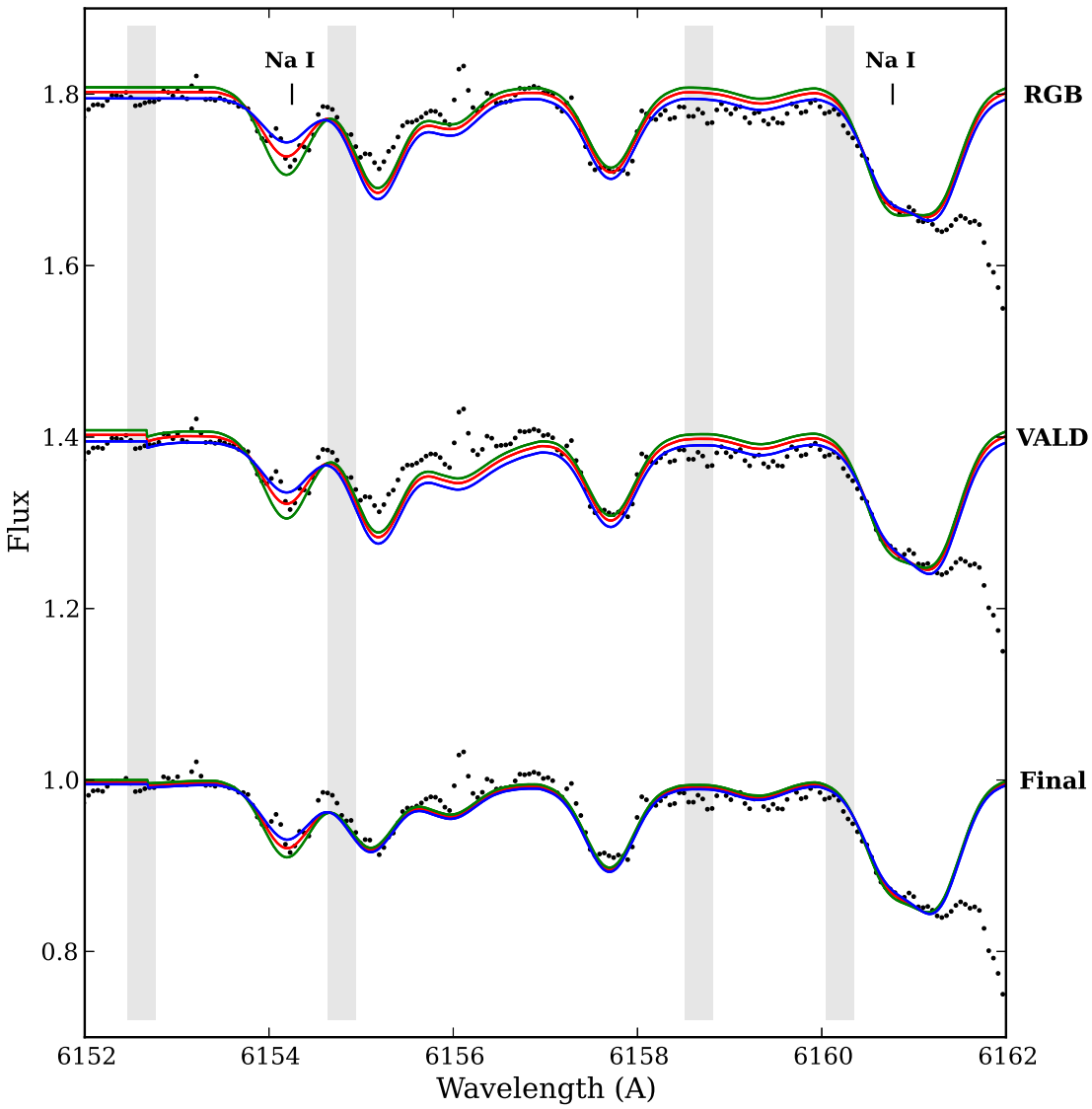

Figure 4.20: Spectrum syntheses of the 6154/6160 Å Na I lines in 47 Tuc, with the Minimal, VALD, and Final Line Lists. Lines are as in Figure 4.13. The Ca I lines redward of 6162 Å were not included in the syntheses; the syntheses therefore diverge from the observed spectra at 6162 Å.

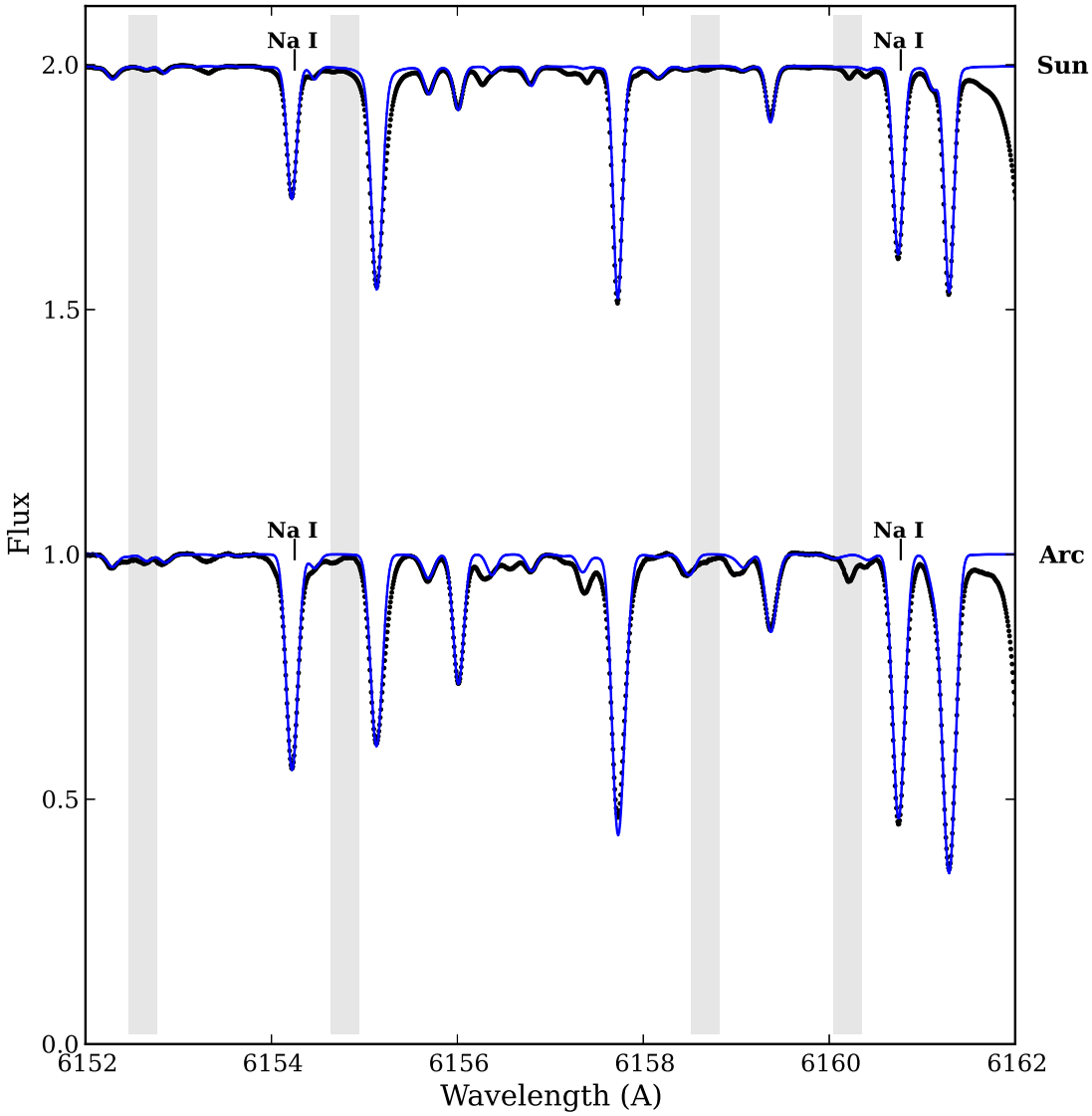

Figure 4.21: Spectrum syntheses of the 6154/6160 Å Na I lines on the Solar and Arcturus spectra. Lines are as in Figure 4.13.

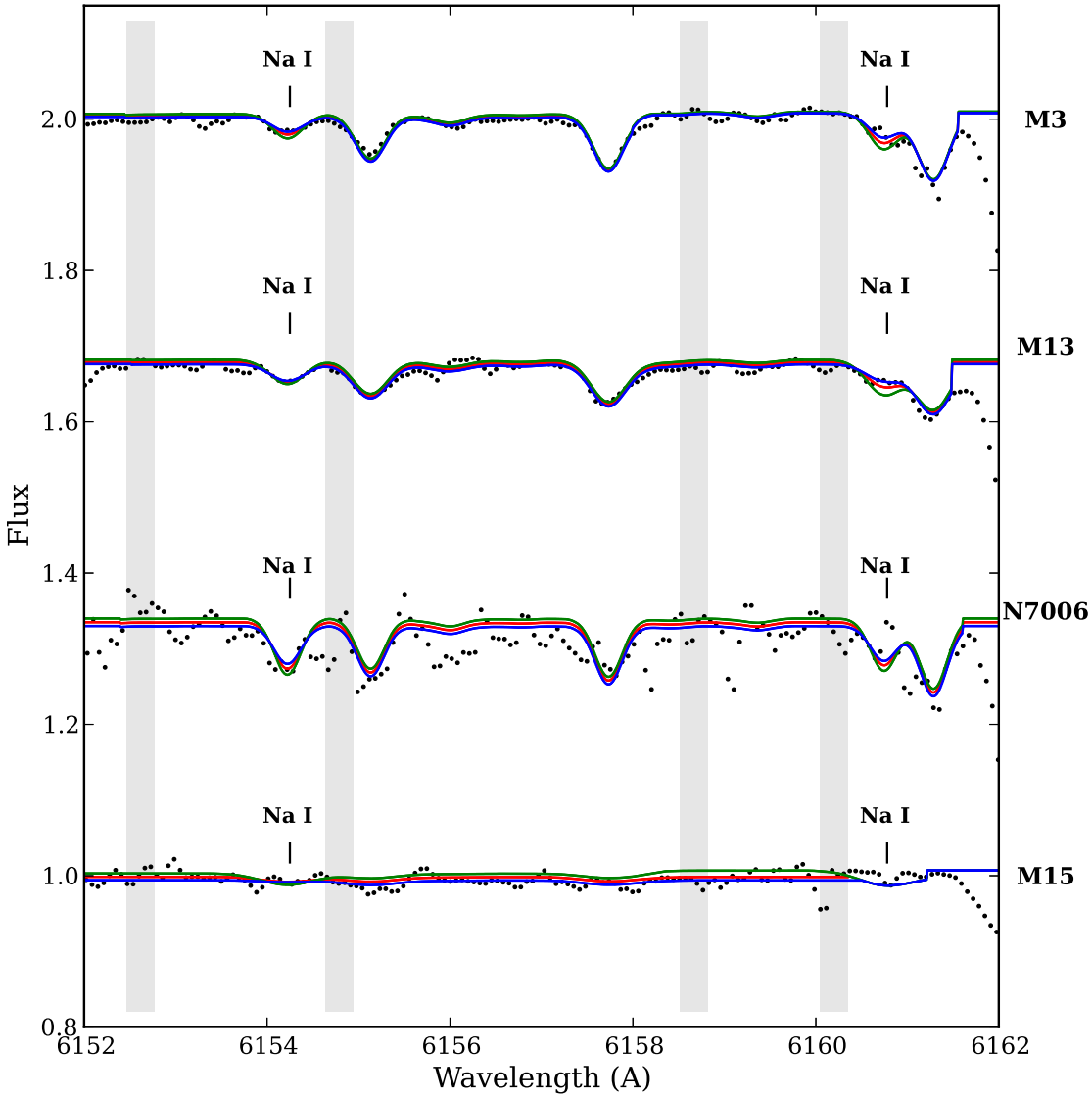

Figure 4.22: Spectrum syntheses of the 6154/6160 Å Na I lines on the M3, M13, NGC 7006, and M15 spectra. Lines are as in Figure 4.13. The 6160 Å line provides only an upper limit in M15.

an upper limit. The 6154 Å line in M15, however, provides a larger Na abundance than the literature average. Again, these discrepancies with the literature averages are results of the intercluster Na variations, which vary from $-0.6 \lesssim$ [Na/Fe] $\lesssim 2$ (Sneden et al., 1997; Preston et al., 2006).

4.5.3 Europium

The weak 6645 Å Eu II feature is commonly synthesized in spectroscopic analyses, since it provides important constraints on contributions from the r- (rapid) neutron capture process.[8] Because there are no other Eu II lines or lines from other dominantly r-process elements in the observed spectral region, the 6645 Å is a crucial line, even though it is often quite weak.

CN Molecules

As discussed earlier, CN molecular lines are present throughout the region around the 6645 Å Eu II line; their presence is likely to affect the integrated Eu II abundances, since the features are blended in an IL spectrum. For the Solar syntheses the C and N abundances from Asplund et al. (2009) are used, while scaled-Solar C and N abundances are adopted for Arcturus. For IL syntheses it is less clear which C and N abundances to use. The effects of dredge-up in RGB stars (e.g. C depletion and N enhancement; Lambert & Ries 1981) are likely to influence the integrated light abundance. In addition, all the stars in 47 Tuc show a well-established CN bimodality, from the RGB (e.g. Briley 1997) down to the main sequence (e.g. Briley et al. 2004). To determine the extent to which the input C and N abundances affect the IL results, spectrum syntheses were performed with the extreme 47 Tuc values determined from individual stars, i.e. [C/Fe] ≈ -0.8 and [N/Fe] $\approx +2.0$ vs. [C/Fe] $\approx +0.4$ and [N/Fe] ≈ 0.0 (Briley et al., 2004).

Sample 47 Tuc spectrum syntheses with different C and N abundances are presented in Figure 4.23. All syntheses were individually vertically shifted to fit the continuum regions, and the Eu II abundances were re-derived to best fit the line profile. The differences in the strengths of the CN lines are quite striking—in general the CN-weak case (in blue, i.e. the higher carbon abundance) has stronger spectral lines than the CN-strong case (in cyan). The unfortunate presence of a blended CN line redward of the Eu II line makes the Eu abundance particularly sensitive to the input

[8] Recall that at solar metallicity 97% of Eu comes from the r-process (Burris et al., 2000).

Table 4.9: Solar, Arcturus, and Globular Cluster Na Abundances

	[Na I/Fe I] 6154 Å	[Na I/Fe I] 6160 Å	Total [Na I/Fe I]
Sun	6.28 ± 0.02^a	6.33 ± 0.03^a	-
Literature Avg			6.24 ± 0.04
Arcturus	0.20 ± 0.03	0.20 ± 0.04	0.20 ± 0.04
Literature Avg			0.18 ± 0.05
47 Tuc	0.38 ± 0.15	0.37 ± 0.08	0.38 ± 0.12
MB08			0.45 ± 0.10
Lit. Avg			0.45 ± 0.01
Lit. Range			$[-0.3, +1.0]$
M3	0.27 ± 0.13	0.17 ± 0.13	0.22 ± 0.13
Lit. Avg			0.02 ± 0.06
Lit. Range			$[-0.3, +0.3]$
M13	0.45 ± 0.10	0.20 ± 0.20	0.33 ± 0.16
Lit. Avg			0.27 ± 0.06
Lit. Range			$[-0.3, +0.6]$
NGC 7006	0.66 ± 0.14	0.26 ± 0.13	0.41 ± 0.14
Lit. Avg			0.32 ± 0.06
Lit. Range			$[0, +0.4]$
M15	0.90 ± 0.40	< 1.05	0.90 ± 0.40
Lit. Avg			0.39 ± 0.06
Lit. Range			$[-0.6, +2.0]$

The mean literature values are straight, un-weighted averages from all available sources. The quoted $\pm 1\sigma$ errors in the literature mean do not reflect the observed range in the abundances. The literature ranges show the approximate extremes that have been observed in the clusters.

References: References are as in Table 4.8.

[a]Solar values are $\log \epsilon$ abundances, not [X/Fe] ratios.

C abundance. In order to force the CN-weak syntheses to best match the observed line profile, a Eu II abundance that is ~ 0.2 dex lower than the CN-strong case must be adopted. However, if the carbon abundance is treated as a free parameter, and is determined by fitting the CN lines in the region (the magenta line in Figure 4.23), the systematic errors in abundance can be reduced.

6645 Å

The need to include the CN molecular features is further supported by the 47 Tuc syntheses with the Minimal and VALD Lists (Figure 4.24). With these lists there appear to be fewer lines in this region, making it easier to identify the continuum level—however, the CN lines are blended together and are undetectable in the IL spectrum, and the continuum is not trivial to locate. Altogether, the errors in the abundances are $\pm$ 0.17 and $\pm$ 0.15 for the Minimal List and the VALD RGB List, respectively.

With the Final Line List, syntheses of the Eu II line in the Solar, Arcturus, and 47 Tuc spectra are shown in Figures 4.24 and 4.25. HFS and isotopic components for the Eu II line are included, using the data from Lawler et al. (2001b)—these corrections alter the shape of the line slightly, but have a negligible effect on its strength. There are several other lines with HFS components in the region of the Eu II line which are not included. The precision of the abundance from the weak Eu II line has significantly improved with the use of the Final Line List, with the error decreasing to 0.10 from 0.18 and 0.15 for the Minimal and VALD Lists, respectively. The spectrum synthesis technique has also improved the accuracy of the derived abundance, as compared to the EW analysis.

The syntheses of the Eu II line in the IL spectra of the other GCs are shown in Figure 4.26. The input carbon abundances is less important for these GCs, since the CN lines are weaker. However, the Eu II feature may also be weaker, making it even more difficult to synthesize the line.

Comparisons with Literature Eu Abundances

The Eu abundances are given in Table 4.10, along with the [Ba II/Eu II] ratios and literature averages. The Solar Eu abundance is slightly lower than the Asplund et al. (2009) value. The Arcturus abundance again agrees with the average literature value.

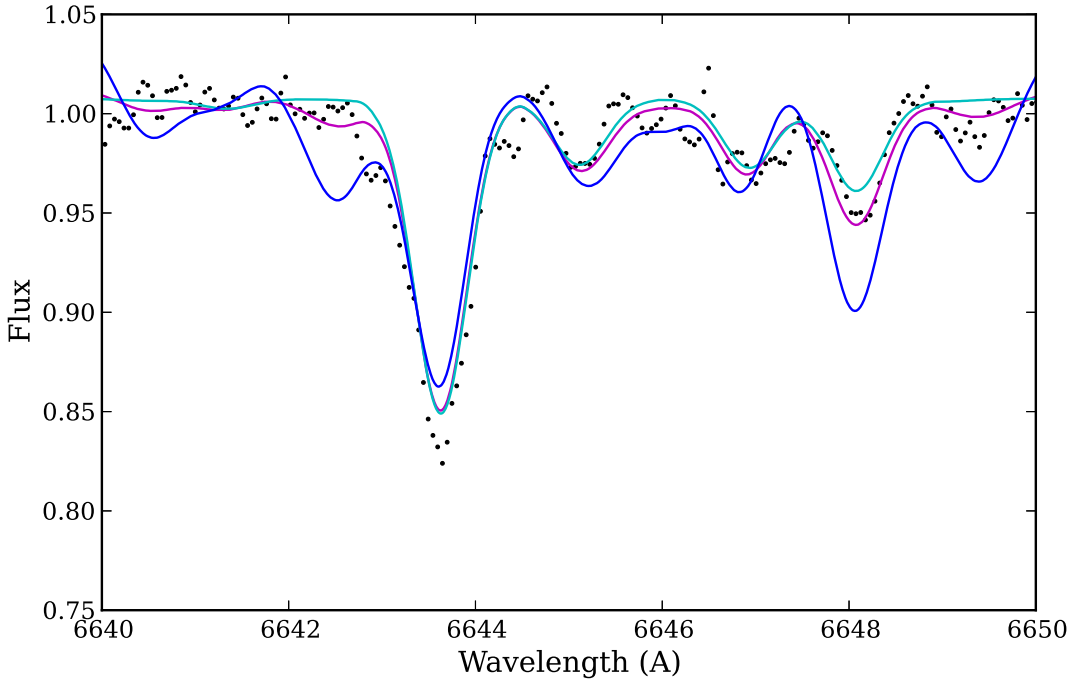

Figure 4.23: Syntheses of the region around the Eu II line in 47 Tuc with the CN molecules, and assuming a carbon isotopic ratio of $^{12}C/^{13}C = 9$. The cyan line assumes [C/Fe] $= -0.8$ and [N/Fe] $= +2.0$, typical of the CN-strong stars in 47 Tuc, while the blue synthesis represents the CN-weak abundances, [C/Fe] $= 0.4$ and [N/Fe] $= 0.0$ (Briley et al., 2004). For each abundance combination the syntheses were vertically shifted to fit the continuum; the Eu abundances were then altered to best fit the Eu II 6645 Å line. The Eu abundances differ by nearly 0.2 dex as a result of the differing input carbon abundances. The magenta line shows the synthesis with the best-fitting carbon abundance, as determined by fitting all the CN lines in the region; this case yields a Eu abundance similar to the CN-strong case.

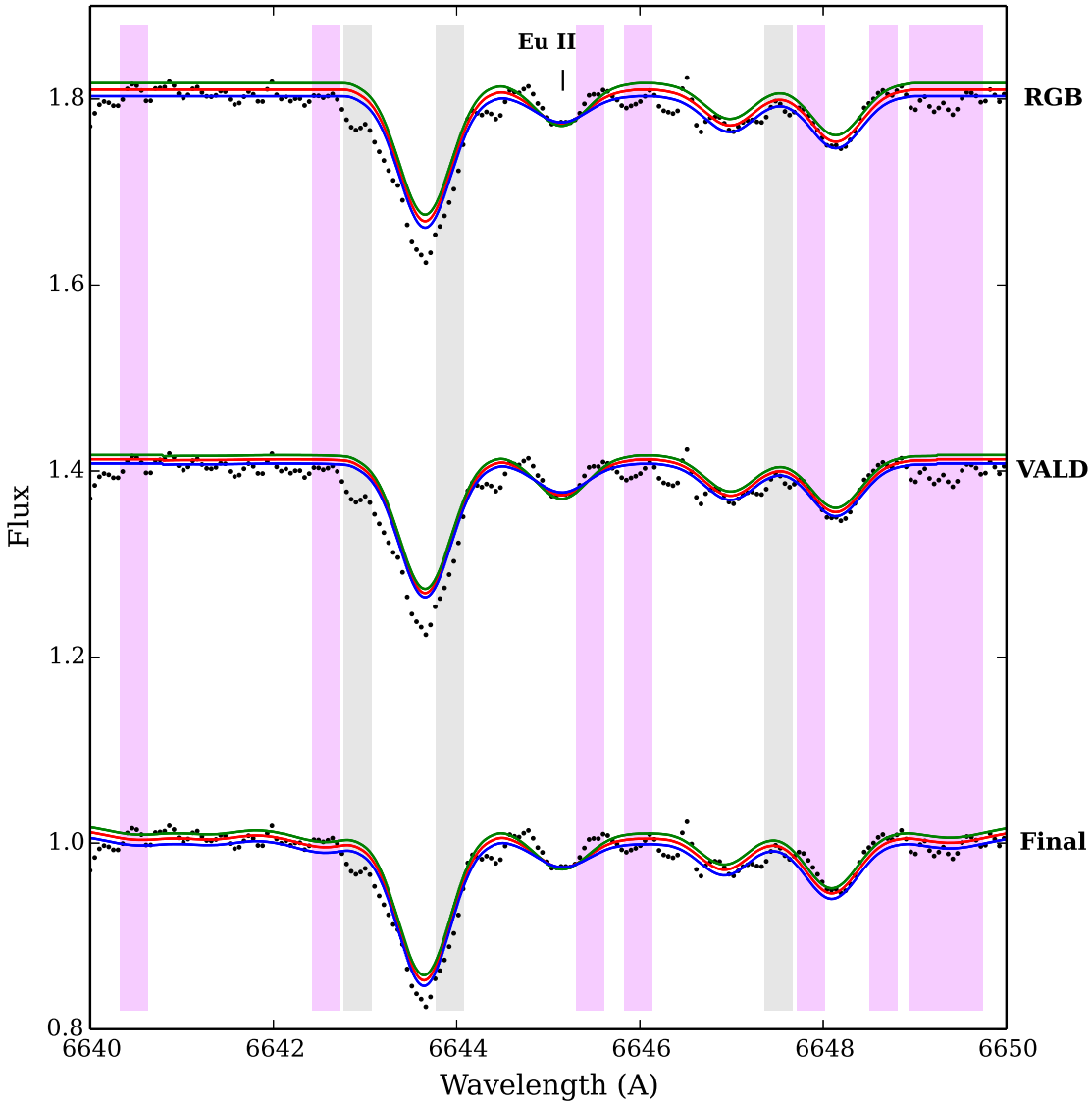

Figure 4.24: Spectrum syntheses of the 6645 Å Eu II line with the Minimal, VALD, and Final Line Lists. Lines are as in Figure 4.13.

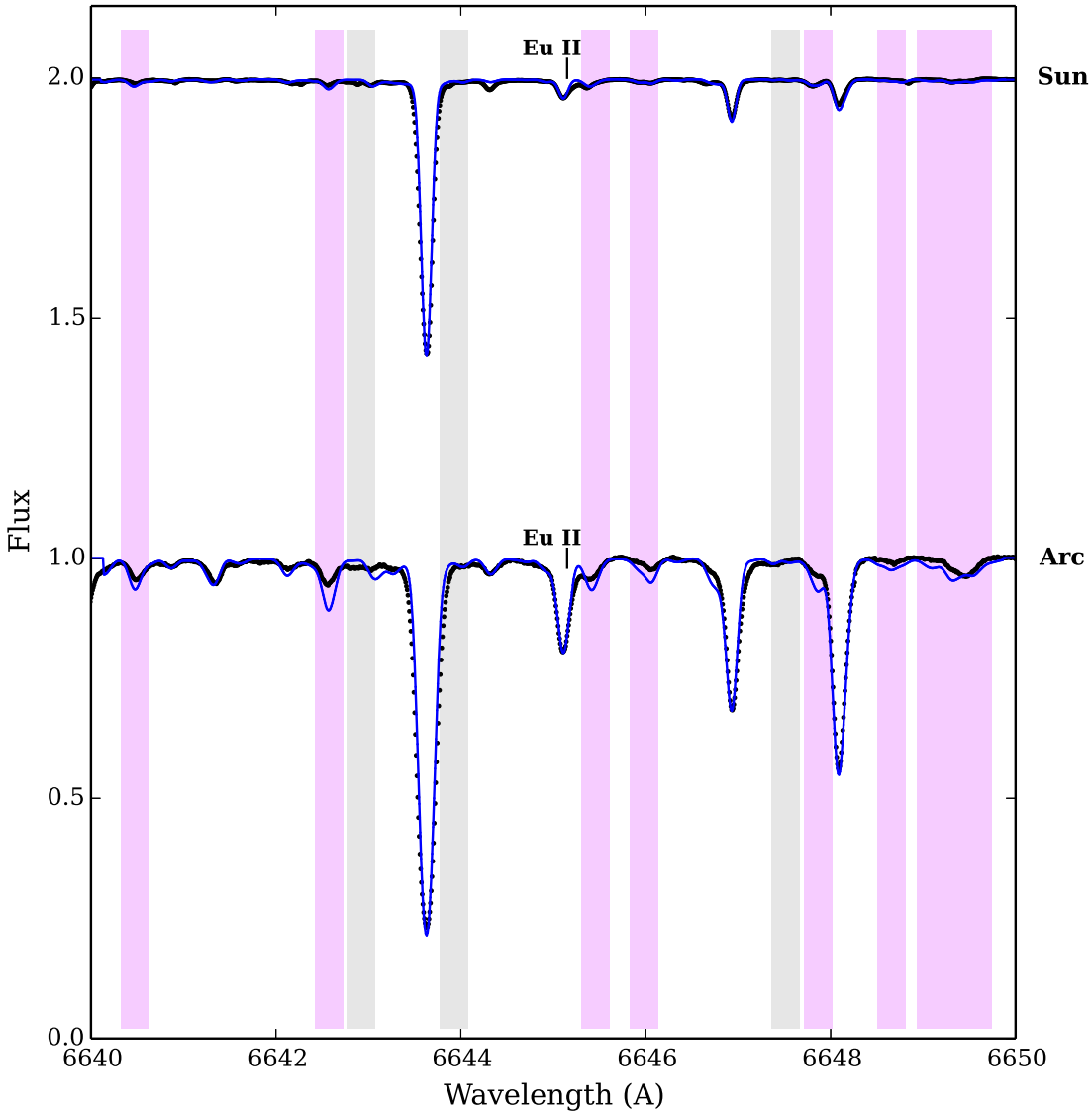

Figure 4.25: Spectrum syntheses of the 6645 Å Eu II line on the Solar and Arcturus spectra with the Final Line List. Lines are as in Figure 4.14.

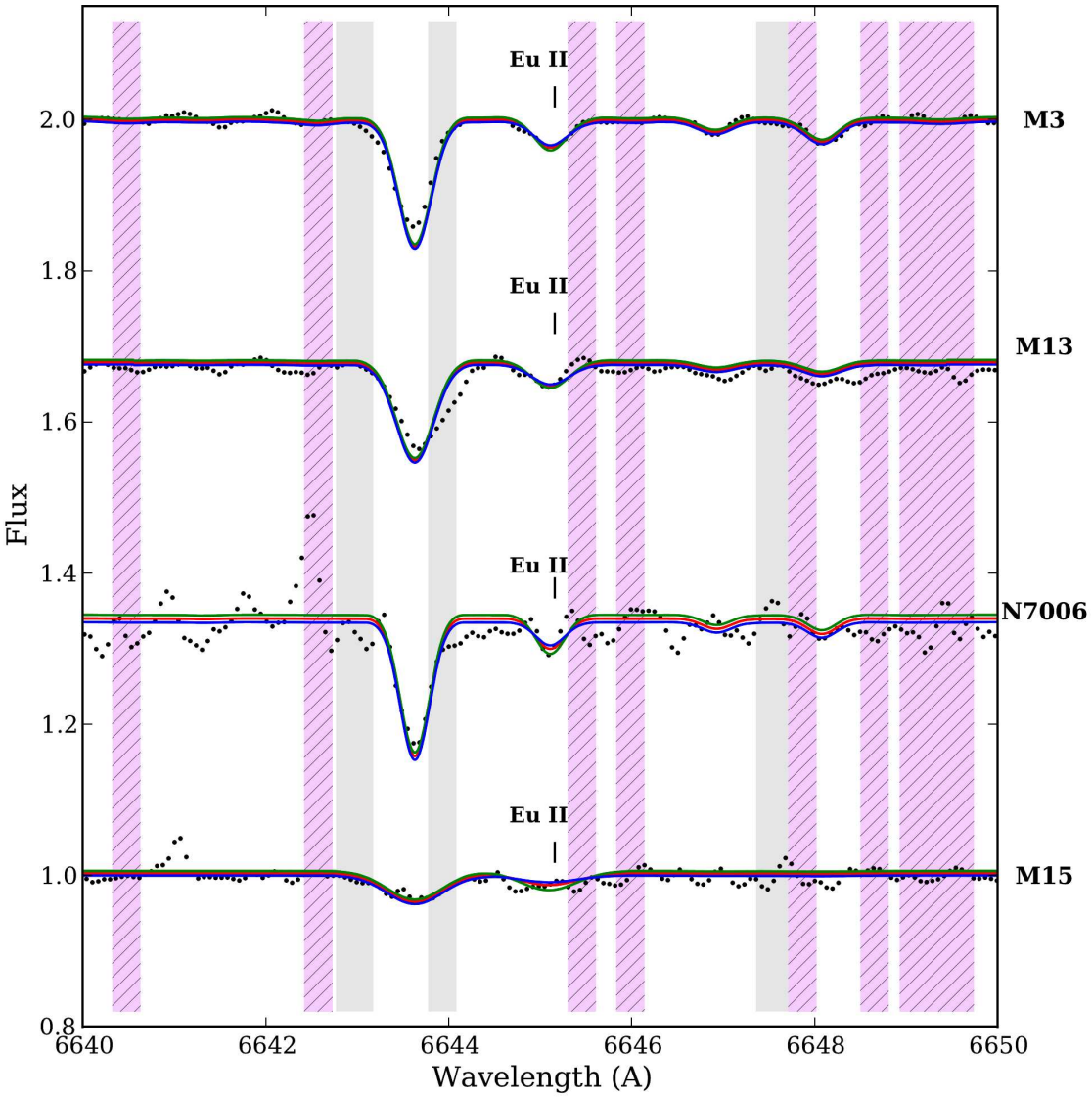

Figure 4.26: Spectrum syntheses of the 6645 Å Eu II line on the M3, M13, NGC 7006, and M15 IL spectra. Lines are as in Figure 4.14.

The 47 Tuc integrated [Eu/Fe] value is higher than MB08's [Eu/Fe] = 0.04, which is based on an equivalent width analysis with the same spectrum; an EW measurement of this weak line may be more difficult than originally realized (especially given the CN lines in the region). The syntheses presented here show that the width of the synthesized line is wider than the observed feature (see Figure 4.25), indicating that noise may have distorted the shape of the Eu II line. In this case, the spectrum syntheses (with a fixed FWHM, HFS components, and the inclusion of CN lines) does a better job of fitting the true line profile. The integrated Eu abundance in 47 Tuc is slightly higher than the average literature value, though the values do agree within the errors. The average literature 47 Tuc [Eu/Fe] abundance in Pritzl et al. (2005) is based on the abundances of 5 giants, 8 subgiants, and 3 turnoff stars whose abundances range from $-0.39 \lesssim$ [Eu/Fe] $\lesssim +0.44$. The IL abundance falls at the upper end of this observed range, suggesting that the Eu-enhanced stars are dominating the IL Eu II line strength.

Table 4.10 shows that the other clusters are all enhanced in Eu, and that these enhancements are considerably greater than the literature averages. However, these literature averages do not reflect the Eu variations that exist within the clusters. Roederer (2011) has shown that large Eu dispersions are present in many Galactic GCs, including M3 ($0.4 \lesssim$ [Eu/Fe] $\lesssim 0.8$), M13 ($0.2 \lesssim$ [Eu/Fe] $\lesssim 1.0$), and M15 ($0.2 \lesssim$ [Eu/Fe] $\lesssim 2.2$). NGC 7006 does not show a significant dispersion in Eu ($0.30 \lesssim$ [Eu/Fe] $\lesssim +0.44$) but these abundances are based on observations of only six giants (Kraft et al., 1998). All of the integrated light synthesis-based abundances fall at the upper end of the literature ranges, again suggesting that the integrated abundances are dominated by the most Eu-rich stars in the GCs.

These integrated Eu II abundances can be compared to the Ba II abundances from Chapter 4.4. The [Ba II/Eu II] values in Table 4.10 show that these Galactic GCs agree well with the Galactic field stars, with the exception of M15 (which has strong star-to-star Ba and Eu variations; Sneden et al. 1997, Roederer 2011).

Table 4.10: Solar, Arcturus, and Globular Cluster Eu Abundances

	[Eu II/Fe II] 6645 Å	[Ba II/Eu II]
Sun	0.45 ± 0.02^a	1.67 ± 0.09
Literature Avg	0.52 ± 0.04	
Arcturus	0.28 ± 0.05	-0.4 ± 0.05
Literature Avg	0.26 ± 0.04	
47 Tuc	0.27 ± 0.11	-0.28 ± 0.11
MB08	0.04^b	-0.02^b
Lit. Avg	0.51 ± 0.02	-0.20
Lit. Range	$[-0.4, +0.4]$	
M3	0.75 ± 0.11	-0.81 ± 0.10
Lit. Avg	0.51 ± 0.02	-0.34
Lit. Range	$[+0.4, +0.8]$	
M13	0.76 ± 0.10	-0.70 ± 0.10
Lit. Avg	0.49 ± 0.03	-0.25
Lit. Range	$[+0.3, +1.0]$	
NGC 7006	0.72 ± 0.15	-0.53 ± 0.12
Lit. Avg	0.36 ± 0.02	-0.03
Lit. Range	$[+0.3, +0.4]$	
M15	1.31 ± 0.20	-1.40 ± 0.15
Lit. Avg	0.63 ± 0.03	-0.52
Lit. Range	$[+0.2, +2.2]$	

The mean literature values are straight, un-weighted averages from all available sources. The quoted $\pm 1\sigma$ errors in the literature mean do not reflect the observed range in the abundances. The literature ranges show the approximate extremes that have been observed in the clusters.

References: References are as in Table 4.8.

[a]Solar values are $\log \epsilon$ abundances, not [X/Fe] ratios.

[b]These discrepancy with MB08's abundances may be due to the difficulties in measuring the EW of the weak Eu II line.

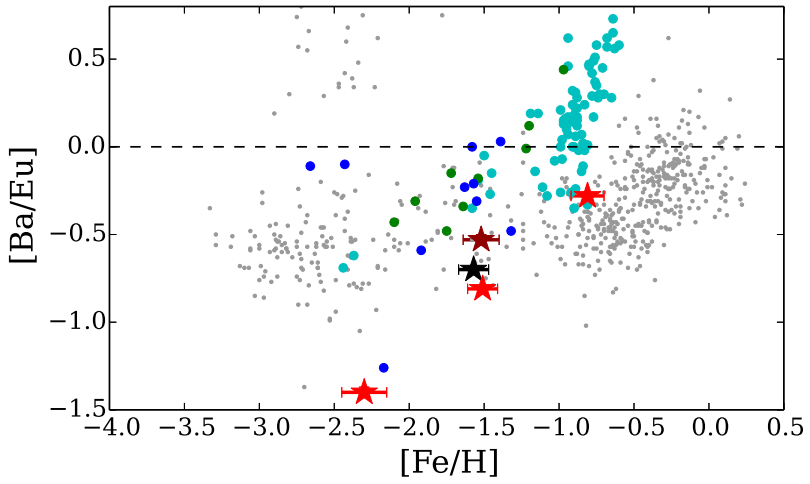

Figure 4.27: [Ba/Eu] vs. [Fe/H] for Galactic GCs (red, maroon, and black stars) versus Milky Way field stars (grey points) and dwarf galaxy field stars (coloured solid symbols). References are as in Figure 1.8. The Galactic GCs generally agree well with the MW field stars; M15's low [Ba/Eu] is a result of its high [Eu/Fe] ratio, which is likely due to strong star-to-star Eu variations.

4.6 Discussion

This chapter has presented IL abundances for the five Galactic GCs 47 Tuc, M3, M13, NGC 7006, and M15, as well as comparisons with literature abundances. This section now discusses the important findings from these syntheses.

4.6.1 The Nature of Integrated Light EW Analyses

Chapter 4.4 showed that integrated EW analyses were capable of reproducing literature abundances for elements that are not expected to vary within a cluster, such as Fe, Ca, Ti, and Ni, with $\sim 0.02 - 0.1$ dex precision. However, the spread in abundances can be quite large with an EW analysis (see the spread in Fe I abundances in Figures 4.6 through 4.10, for example). This is likely because of difficulty in continuum placement, blends of multiple lines, and the presence of molecules—because the IL line widths are dominated by the cluster velocity dispersion, these effects will be much more significant in IL analyses. For elements with few detectable, weak lines (e.g. Fe II in M15 or Ti I in NGC 7006) an EW analysis can therefore lead to large random errors if the line-to-line dispersion is large, or can lead to significant systematic offsets if there are too few lines. Accurate integrated abundances of such elements require spectrum syntheses.

4.6.2 The Nature of Integrated Light Spectrum Syntheses

The results from Chapter 4.5 clearly show that determining abundances from spectrum syntheses of IL spectra is more difficult than with individual, resolved stars. As with an EW analysis, the severe blends in an IL spectrum make fitting lines and identifying the continuum level difficult, although it is much easier to fit lines when entire regions are synthesized. These difficulties are even worse in low S/N spectra. Comparisons between the individual Solar/Arcturus spectra and the 47 Tuc IL spectrum clearly show that 47 Tuc does not have "traditional" continuum regions (i.e. regions that are free of any spectral lines)—even the most featureless regions in the 47 Tuc spectrum are blends of continuum *and* weak absorption features. This is particularly evident in Figure 4.28, which shows syntheses of the 6154/6160 Å Na I lines in the 47 Tuc IL spectrum; both the unbroadened and broadened (by the velocity dispersion and instrumental broadening; see Chapter 4.2.2) spectra are shown. In this crowded region, the broadened spectrum never reaches the continuum level of

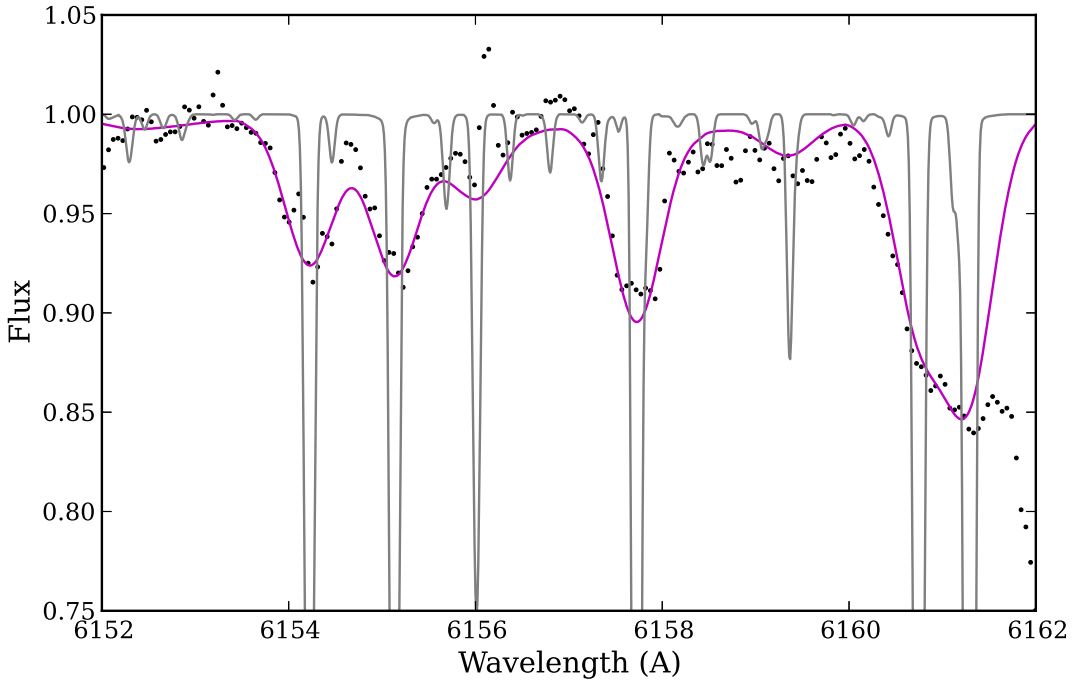

Figure 4.28: Syntheses of the Na I 6154/6160 Å doublet in the 47 Tuc spectrum. The magenta line shows the best-fitting abundance from Chapter 4.5.2. The grey line shows the same synthesis, *before it has been broadened by the velocity dispersion and instrumental broadening*. It is clear that the magenta line never fully reaches the continuum level of the grey synthesis, due to blending of the weak features.

the unbroadened spectrum. Thus, even the basic step of fitting the continuum level requires some *a priori* knowledge of the weak lines that are involved in the blending, and the abundances of the elements that cause those spectral lines. This once again illustrates that for high precision it is *necessary* to use a complete and calibrated input line list.

Despite this concern, the uncertainties in continuum placement introduced by blended weak features may not be significant in all cases. The target GCs are all more metal-poor than the Sun and Arcturus, suggesting that fewer spectral lines are present throughout the GC spectra. The cluster velocity dispersion, which blends the lines together, also makes the weak lines weaker. Even if weak lines are present and are strong enough to influence the continuum, the lines in the Final Line List have been calibrated to the Sun and Arcturus, meaning that once the integrated light abundances of the elements with the most lines (e.g., Fe, Ca, Ti, and Ni) have been

determined (e.g., through an EW analysis), the synthesized lines should match the observed ones. Thus, the well-calibrated strong lines from these well-known elements may also be used to fit the continuum. Ultimately, however, this problem is unavoidable in IL spectrum syntheses, and continuum level uncertainty should be considered as an important source of uncertainty in the integrated light abundances.

4.6.3 Comparisons with Literature Abundances

As is clear from the abundances presented in Chapter 4.5, caution must be taken when comparing IL abundances to average literature values. *The IL abundances do not represent average cluster abundances.* The stellar contributions to an IL spectrum are flux-weighted, meaning that the brightest RGB and AGB stars contribute the most light to the observed spectrum (and therefore have more influence on a line's shape and strength). Furthermore, the contributions to individual *line strengths* can also depend on line properties (e.g. wavelength, ionization state, excitation potential, etc.; see Figure 4.6). For elements that are not expected to vary significantly between stars in a given cluster (e.g. Fe), these effects will be unimportant (assuming the population is properly modelled). For elements that *are* expected to vary (such as Mg, Na, and Eu), the observed line strengths will also depend on the abundance spreads in the stars that dominated the light. The literature averages will depend on the number and types of stars observed. It is important to consider these effects when comparing with literature abundances. Flux-weighted literature averages may help with comparisons with IL abundances, but this requires a reasonably complete sample of stars that are selected only from the observed regions.

For elements with star-to-star variations within a GC, such as Mg, Na, and Eu, it is therefore more instructive to consider the observed literature *ranges*, especially those observed among the brightest evolved stars that dominate the integrated light. These ranges will reflect any star-to-star abundance variations, whether due to effects that may occur up the RGB (e.g. mixing, Korn et al. 2007) or as a result of separate populations throughout the cluster. With this caveat in mind, the `ILABUNDS` spectrum synthesis method presented here provides accurate abundances that fall within the ranges of literature abundances from individual stars.

4.6.4 The Chemical Signatures of Multiple Populations?

As standard Galactic GCs, 47 Tuc, M3, M13, NGC 7006, and M15 all show signs of multiple populations (under the definition of multiple populations as "synonymous with 'multiple generations of stars' that can be distinguished either from their spectra or from multiple sequences in the colour magnitude diagram;" Gratton et al. 2012). These multiple populations are often distinguished through star-to-star C, N, O, Na, Mg, and/or Al abundance variations (e.g. Carretta et al. 2009a). These abundance variations are known to affect certain features in lower resolution IL spectra (for instance, Coelho et al. 2011 find that the Ca 4227, G4300, CN_1, CN_2, and NaD Lick indices are all affected by the second generation abundance differences). The high-resolution integrated light Na and Mg abundances presented here are therefore likely affected by these multiple populations within the GCs.

The abundance results from the syntheses are generally qualitatively similar among the GCs. With the exception of M15, the GCs are all found to be Mg-enhanced in their integrated light, as compared to the Sun. Similarly, all GCs were found to be Na-enhanced. The magnitudes of these enhancements vary between the clusters. For example, 47 Tuc has the highest integrated Mg enhancement and a moderate integrated Na enhancement, while M15 shows Mg depletion and a much stronger Na enhancement. These findings qualitatively agree with the Na and Mg star-to-star variations in Galactic GCs, and suggest that in the observed regions, *stars from different populations may be dominating the integrated light in these clusters* (e.g. "normal" stars may dominate the 47 Tuc light, while more "second generation" Na-rich/Mg-poor stars may dominate the M15 integrated light). Although the second generation stars are more centrally concentrated (and may therefore have more of an effect on an IL spectrum of a GC's core) this may be a stochastic effect, and the integrated abundances may depend on the area observed in the IL spectrum. Furthermore, the IL abundances of the light elements will depend on the area scanned by the IL spectrum, the properties of the GC (e.g. [Fe/H]), and the properties of the two populations (e.g. relative numbers of stars). More theoretical work with multiple populations must be done in order to understand exactly how these effects will alter the integrated light abundances.

4.7 HRD-based Analyses

The integrated abundances presented in this chapter so far are derived with high quality resolved photometry down to the lower MS, and were sampled to represent the scanned populations. However, high quality CMDs are not available for the distant extragalactic GCs that can only be observed as IL targets. For those targets isochrones must be used to generate theoretical HRDs, and spectral diagnostics must be developed to constrain the properties of the most appropriate HRD. This section examines the HRD-based abundances and compares them to the CMD-based abundances.

MB08 and Colucci et al. (2009, 2011a, 2012, 2013) have pioneered high resolution IL spectral analyses of unresolved GCs. Their algorithm for identifying the HRD that best represents an underlying stellar population involves iterating upon isochrone parameters until the following criteria are met:

1. The isochrone [Fe/H] matches the output integrated [Fe I/H] ratio
2. Any trends in Fe I abundance with wavelength, REW, or excitation potential (EP) are minimized (similar to individual stellar analyses; see MB08 and the Pal 1 analysis in Chapter 3)
3. The line-to-line abundance spreads from Fe I and Fe II lines are minimized.

Colucci et al. have demonstrated that a suitable HRD can be identified based on these criteria. Furthermore, Cameron (2009) argue that HRD-based abundances of Galactic GCs are in good agreement with CMD-based ones (which are, in turn, in agreement with literature abundances from individual stars). This section focuses on the abundance offsets that arise as a result of uncertainties in spectroscopically identifying the best input isochrones for an unresolved population. These tests assume that *the Galactic GCs are completely unresolved*, i.e. that there is no information about HB morphology, no constraints on [Fe/H] or age, and no observed LFs to help populate the isochrones.

First, the spectroscopically-determined "best fitting" standard BaSTI isochrones (i.e. the HRDs that best satisfy the above criteria) are identified for the targets GCs. No modifications were made to the default BaSTI HBs (see Chapter 5.2.3). As in Colucci et al, isochrones with extended AGBs and mass loss parameters of $\eta = 0.2$ were initially adopted (see Chapter 5.2.4 for tests with other AGB prescriptions,

though note that MB08 utilize $\eta = 0.4$ isochrones based on the tests by Maraston 2005). In order to match 47 Tuc's observed luminosity function MB08 manually enhanced the number of AGB stars; however, no AGB enhancements were included in these tests. When the [Ca I/Fe I] ratio indicated α-enhancement, α-enhanced isochrones were used. The "best-fitting" solution was deemed to be the one for which all slopes are minimized—note that this choice is subjective, since the slopes are rarely simultaneously minimized.

Tables 4.11 and 4.12 presents the parameters for the best-fitting HRDs and comparisons with the CMD-based abundances. Note that none of the REW slopes are sufficiently flat for M15. With the exception of M13, all solutions are younger than isochrone fits to the resolved CMDs indicate (see, e.g., Dotter et al. 2010; VandenBerg et al. 2013). The best-fitting HRD abundances can be significantly offset from the CMD-based abundances—in particular, the [Ti I/Fe I] values are persistently lower than those from the CMD analyses and those from individual stars. The [Fe I/H], [Fe II/H], [Ti II/Fe II], [Ba II/Fe II], and [Eu II/Fe II] ratios are also significantly affected. Only [Ca I/Fe I] and [Ni I/Fe I] consistently agree well with the CMD-based abundances. These offsets illustrate two important points.

1. Without CMDs it is difficult to know which isochrones to use to populate the HRDs. The spectroscopically-determined "best-fitting" isochrones will not necessarily fit the resolved CMDs.

2. These differences between models and reality lead to significant abundance offsets for some elements. It is therefore imperative to quantify these offsets, identify elements that are least sensitive to uncertainties in the underlying populations, and/or develop diagnostics to refine the input models.

These effects will be discussed in more detail in Chapter 5.

Table 4.11: Parameters of the spectroscopically-determined HRDs, assuming that the GCs are completely unresolved.

	Age[a]	[Z/H]
47 Tuc	10	-0.35
M3	9	-1.27
M13	12	-1.27
NGC 7006	7	-1.27
M15	9	-1.79

Notes: The default α-enhanced BaSTI isochrones were used, with no modifications to HB morphology, etc. [a] These ages disagree with the ages from resolved photometry; because the the adopted isochrones do not perfectly match the underlying stellar populations, there may be errors in the derived abundances.

Table 4.12: Parameters of the "best-fitting" HRDs, and abundance comparisons with the CMD-based abundances.

	Δ[X/H]		Δ[X/Fe]					
	Fe I	Fe II	Ca I	Ti I	Ti II	Ni I	Ba II	Eu II
47 Tuc	**+0.07**	**+0.19**	**−0.05**	**−0.10**	−0.01	+0.02	**−0.05**	**−0.08**
M3	**−0.05**	−0.04	−0.01	**−0.20**	**−0.05**	−0.03	**−0.10**	**−0.06**
M13	**−0.11**	**−0.13**	+0.03	**−0.19**	**−0.10**	−0.04	**−0.12**	−0.02
NGC 7006	**+0.06**	−0.02	−0.02	**−0.14**	**+0.05**	−0.03	+0.03	**−0.05**
M15	+0.02	**+0.06**	−0.01	−0.04	0.0	+0.01	+0.04	+0.03

Notes: Abundance differences are calculated relative to the baseline abundances in Tables 4.5, 4.7, and 4.10; offsets larger than 0.05 are shown in bold.

4.8 Conclusions

This chapter has presented the integrated abundances of five Galactic globular clusters over a wide range of metallicities and HB morphologies, and has compared these abundances to the literature values from individual stars. In particular, this work has produced the following key findings:

- EW analyses can successfully reproduce the literature abundances for Fe, Ca, Ti, Ni, and Ba, to within 0.1 dex in most cases. However, for elements with only a handful of spectral lines the line-to-line dispersion is significant; because of uncertainties in continuum identification and unresolved blends, spectrum syntheses must be used to achieve the high precision necessary for, e.g., chemical tagging.

- Spectrum syntheses of GC IL spectra can yield abundances with ~ 0.1 dex precision, comparable to the accuracy obtained with high quality spectral analyses of individual stars. To achieve this level of precision, attention must be given to the completeness of the input line list, which needs to be calibrated, e.g., to the Solar and Arcturus spectra. Molecular features do affect spectral lines of interest and the continuum levels, and need to be included in the syntheses.

- The abundances determined here from the IL spectra of 47 Tuc, M3, M13, NGC 7006, and M15 fall within the abundance ranges in the literature from individual cluster member stars.

- The integrated light abundances may not represent the average cluster abundances in the literature, due to star-to-star abundance variations within each GC. The signatures of star-to-star abundance variations in Mg, Na, and Eu seem to be evident in the integrated light abundances of all the target GCs.

- HRD-based abundances (from isochrones) do not always agree with the CMD-based abundances (or the literature abundances) when the GCs are treated as completely unresolved targets. This suggests that there are systematic differences in how the populations are modelled and that these offsets have nonnegligible effects on certain abundance ratios.

This work shows that high resolution IL spectral analyses can be used to determine precise elemental abundances in GCs, at least for Fe, Mg, Na, Ca, Ti, Ni, Ba and

Eu lines in the $5300 - 7300$ Å region. This method can reproduce individual stellar abundances for GCs of range of metallicities and HB morphologies, *provided that the underlying stellar populations are well modelled.* It may not be possible to model populations of unresolved targets perfectly; furthermore, even if the populations are well modelled, as with individual stellar analyses there are unavoidable systematic errors associated with the atmospheric parameters. The next chapter describes the systematic errors in abundance that could occur as a result of uncertainties in the underlying stellar populations.

Chapter 5

Systematic Errors in Integrated Chemical Abundances

Chapter 4 demonstrated that *precise* integrated chemical abundances can be determined from spectrum syntheses with complete, calibrated line lists, and from EWs when a given element has a sufficient number of clean lines. These IL abundances were shown to agree with literature abundances from individual stars for elements that do not vary within a cluster; for those elements that *are* expected to vary the IL abundances fall within the observed ranges from individual stars. These detailed abundances are not free from systematic errors—like the Pal 1 abundances in Chapter 3, the IL abundances are affected by uncertainties in the stellar atmospheric parameters.

This chapter presents a detailed analysis of the systematic errors in the integrated abundances of 47 Tuc, M3, M13, NGC 7006, and M15 as a result of uncertainties in the underlying stellar populations. First the uncertainties in the CMD-based abundances in Chapters 4.3, 4.4, and 4.5 are discussed in Chapter 5.1. Chapter 5.2 then turns to the uncertainties that occur when isochrones are used to generate synthetic HRDs, as in Chapter 4.7. Uncertainties that are expected to occur in both types of analyses are presented in Chapter 5.3. Finally, a hybrid technique for nearby clusters is presented in Chapter 5.4, and the results are discussed in Chapter 5.5.

The methodology for all tests in Chapters 5.1 through 5.4 is the same, regardless of analysis type. In each case, specific modifications are made to the underlying populations, `ILABUNDS` is rerun with the new populations (and the same EW measurements), and these new abundances are compared to the baseline abundances in

Chapter 4 (unless otherwise noted). These differences are calculated as

$$\Delta[\mathrm{X/Fe}] \;=\; [\mathrm{X/Fe}] \;-\; [\mathrm{X/Fe}]_{\mathrm{orig}}. \tag{5.1}$$

Not all GCs are utilized for all tests. For computationally intensive tests only 47 Tuc is considered. In cases where only metallicity effects are investigated 47 Tuc, M3, and M15 are used; similarly, to investigate HB morphology effects only M3, M13, and NGC 7006 are used. Finally, some tests only apply to metal-rich GCs (47 Tuc) or clusters with hot stars (M13 or M15).

Because the integrated Na and Mg abundances are extremely sensitive to star-to-star abundance variations in metal-poor GCs, those lines were not considered in this systematic error analysis. Ba and Eu are retained, however, as the star-to-star variations within a cluster are not always significant. Roederer (2011) demonstrated that Eu variations are only large for the most *massive* GCs. Furthermore, these dispersions are not seen in all massive, metal-poor GCs—for instance, Cohen (2011) detect no heavy element dispersion in M92. Furthermore, evidence suggests that Ba and Eu may vary together, such that the ratio of [Ba/Eu] may still be useful for chemical tagging purposes (Worley et al., 2013). The Eu SS-based abundance was converted to an EW for these tests (i.e. EWs were found to match the SS-derived Eu abundance). Note that M15's Ti I lines were undetectable—to investigate the effects on Ti I at M15's metallicity EWs of Ti I lines were found to force [Ti I/Fe I] to equal [Ti II/Fe II].

5.1 Uncertainties in CMD-based IL Analyses

As in Chapter 4, CMDs can be used to determine the parameters of stars in a GC. The main advantage of a CMD-based analysis is that the basic properties (i.e. age and [Fe/H]) may be estimated from the CMD. The distribution of stars in the CMD is also known, removing the need to model difficult subpopulations (e.g. the HB or the AGB) or the relative numbers of dwarfs and giants. The main disadvantages of a CMD-based analysis are that observable properties must be converted to intrinsic, physical quantities and that the CMDs might not completely represent the observed regions. Errors in observed quantities can lead to cluster-to-cluster systematic errors, while differences in the employed conversion techniques/relations can lead to offsets between studies. Discrepancies between photometric and spectroscopic observations (e.g. sampled regions or incompleteness) can also lead to systematic uncertainties, as can poor resolution in cluster cores.

Two sources of error in CMD-based analyses are considered:

1. Errors that occur when observable quantities are converted to physical values (Chapters 5.1.1, 5.1.2, and 5.1.3)

2. Errors that occur when the input photometry does not exactly match the population observed in the IL spectra (Chapters 5.1.3, 5.1.4, 5.1.5; also see Chapter 5.3).

5.1.1 Minimum Errors in Photometric Parameters

Conversions to photometric stellar parameters require estimates of a cluster's distance modulus, reddening, turnoff mass, etc., all of which have associated uncertainties that lead to unavoidable minimum uncertainties in the photometric effective temperature, $T_{\rm eff}$, and surface gravity, $\log g$. Detailed abundance analyses with individual stars also show that the spectroscopically-determined microturbulence, ξ, and metallicity, [Fe/H], cannot be perfectly constrained. These errors in the atmospheric parameters are typically on the order of $\Delta T_{\rm eff} = \pm 100$ K, $\Delta \log g = \pm 0.2$ dex, $\Delta\xi = \pm 0.2$ km/s, and Δ[M/H] $= \pm 0.1$ dex *regardless of the methods used to determine these parameters* (see Chapter 3). These abundance differences are therefore good estimates of the minimum systematic errors that would occur in a CMD-based integrated light abundance analysis. This section investigates the magnitudes of the

abundance errors that occur as a result of these unavoidable, minimum uncertainties in the atmospheric parameters.

These minimum changes to the atmospheric parameters lead to the abundances shown in Table 5.1. Significant errors (≥ 0.05 dex) are shown in bold. Note that the surface gravity and microturbulence were changed independently from each other, even though the microturbulence is determined through an empirical relationship with the surface gravity.[1] With the empirical relation, a change in the surface gravity of $\Delta \log g = 0.2$ dex would only lead to $\Delta\xi = 0.04$ km/s.

The abundance differences in Table 5.1 indicate that:

1. The largest offsets in [Fe/H] and [X/Fe] are ~ 0.1 dex
2. The model atmosphere metallicity has a negligible effect on all abundance ratios
3. The differences in the [Fe I/H] and [Fe II/H] ratios are generally < 0.1 dex, except in 47 Tuc and M15, whose offsets are ~ 0.1 dex
4. The [Fe I/H] and [Fe II/H] ratios can be significantly (i.e. $|\Delta$[Fe/H]$| > 0.05$) affected by the changes in temperature, surface gravity, and microturbulence
5. The relative [Ca I/Fe I] and [Ni I/Fe I] ratios are largely unaffected by these errors in the atmospheric parameters
6. The [Ti I/Fe I] ratios are moderately affected by temperature, while the [Ti II/Fe II] ratios are affected primarily by microturbulence (though the [Ti/Fe] errors are all < 0.1 dex); surface gravity effects are negligible
7. The [Ba II/Fe II] and [Eu II/Fe II] ratios are most affected by temperature and microturbulence, though [Ba II/Fe II] is constrained to within 0.12 dex, and [Eu II/Fe II] to within 0.07 dex.

Thus, the systematic errors from the intrinsic uncertainties in atmospheric parameters are $\lesssim 0.1$ dex for [Fe I/H], [Fe II/H], [Ti I/Fe I], [Ti II/Fe II], [Ba II/Fe II], and [Eu II/Fe II], and are < 0.05 dex for [Ca I/Fe I] and [Ni I/Fe I].

Of course, the atmospheric parameters are not independent. It is thus instructive to see how the final abundances change as two parameters are varied together—these tests were performed only on 47 Tuc (which has the largest individual offsets). For

[1] The effects of the microturbulence relation are investigated in Chapter 5.3.2.

Table 5.1: Offsets in the CMD-based abundances due to the atmospheric parameters.

	Δ[X/H]		Δ[X/Fe]					
	Fe I	Fe II	Ca I	Ti I	Ti II	Ni I	Ba II	Eu II
47 Tuc								
$+\Delta T$	+0.04	**−0.10**	+0.04	**+0.07**	**+0.07**	0.0	**+0.10**	**+0.07**
$-\Delta T$	−0.03	**+0.11**	−0.04	**−0.08**	**−0.07**	0.0	**−0.11**	−0.06
$+\Delta \log g$	+0.01	**+0.10**	−0.02	0.0	−0.02	+0.03	−0.03	−0.02
$-\Delta \log g$	−0.02	**−0.11**	+0.03	+0.02	+0.03	−0.02	+0.04	+0.03
$+\Delta \xi$	**−0.09**	**−0.05**	−0.01	+0.02	**−0.07**	+0.01	**−0.11**	+0.02
$-\Delta \xi$	**+0.08**	**+0.06**	+0.03	0.0	**+0.07**	+0.01	**+0.11**	−0.04
$+\Delta$[M/H]	0.0	+0.03	0.0	0.0	−0.01	+0.01	0.0	0.0
$-\Delta$[M/H]	−0.02	−0.04	+0.03	+0.02	+0.01	0.0	+0.01	0.0
M3								
$+\Delta T$	**+0.08**	**−0.05**	0.0	**+0.06**	+0.04	0.0	**+0.07**	**+0.05**
$-\Delta T$	**−0.06**	**+0.07**	−0.02	**−0.09**	−0.04	0.0	**−0.07**	−0.03
$+\Delta \log g$	−0.01	**+0.09**	−0.02	0.0	−0.02	+0.02	−0.04	+0.01
$-\Delta \log g$	+0.01	**−0.08**	+0.01	−0.01	+0.02	−0.03	+0.03	+0.02
$+\Delta \xi$	**−0.05**	−0.02	−0.02	+0.01	**−0.05**	0.0	**−0.12**	+0.02
$-\Delta \xi$	**+0.05**	+0.03	+0.01	−0.02	**+0.05**	+0.01	**+0.11**	+0.01
$+\Delta$[M/H]	0.0	+0.04	−0.01	−0.02	−0.01	+0.01	−0.01	+0.02
$-\Delta$[M/H]	0.0	−0.01	0.0	0.0	+0.01	0.0	−0.01	0.0
M13								
$+\Delta T$	**+0.09**	**−0.05**	−0.01	**+0.05**	+0.03	−0.01	**+0.07**	**+0.05**
$-\Delta T$	**−0.07**	**+0.07**	0.0	**−0.07**	−0.04	0.0	**−0.08**	−0.02
$+\Delta \log g$	0.0	**+0.09**	−0.02	−0.01	−0.02	+0.02	−0.04	+0.02
$-\Delta \log g$	+0.01	**−0.08**	+0.02	0.0	+0.02	−0.02	+0.03	+0.02
$+\Delta \xi$	**−0.05**	−0.03	−0.01	+0.02	−0.04	0.0	**−0.10**	+0.03
$-\Delta \xi$	**+0.06**	+0.03	0.0	−0.03	**+0.05**	−0.01	**+0.10**	+0.02
$+\Delta$[M/H]	0.0	+0.03	0.0	−0.01	−0.01	0.0	0.0	+0.03
$-\Delta$[M/H]	0.0	−0.02	+0.01	+0.01	+0.01	0.0	0.0	+0.02
NGC 7006								
$+\Delta T$	**+0.08**	**−0.06**	+0.01	**+0.05**	+0.04	0.0	**+0.09**	**+0.05**
$-\Delta T$	**−0.07**	**+0.06**	−0.02	**−0.07**	−0.04	0.0	**−0.07**	−0.03
$+\Delta \log g$	−0.01	**+0.08**	−0.02	0.0	−0.01	+0.03	−0.03	+0.01
$-\Delta \log g$	+0.01	**−0.08**	+0.02	0.0	+0.01	−0.02	+0.04	+0.01
$+\Delta \xi$	**−0.06**	−0.03	+0.02	+0.03	−0.03	+0.01	**−0.11**	+0.02
$-\Delta \xi$	**+0.06**	+0.02	+0.01	−0.03	**+0.05**	0.0	**+0.12**	+0.01
$+\Delta$[M/H]	0.0	+0.03	−0.01	−0.02	0.0	+0.01	+0.01	+0.01
$-\Delta$[M/H]	0.0	−0.02	0.0	0.0	+0.01	0.0	0.0	0.0
M15								
$+\Delta T$	**+0.10**	−0.03	−0.04	+0.02	+0.03	+0.02	**+0.06**	**+0.07**
$-\Delta T$	**−0.11**	+0.02	+0.03	−0.02	−0.02	−0.02	**−0.06**	−0.02
$+\Delta \log g$	−0.03	**+0.06**	0.0	+0.01	−0.01	+0.02	−0.02	+0.02
$-\Delta \log g$	+0.02	**−0.07**	0.0	0.0	+0.01	−0.01	+0.01	+0.02
$+\Delta \xi$	**−0.06**	−0.01	+0.01	**+0.06**	−0.02	+0.03	**−0.09**	+0.01
$-\Delta \xi$	**+0.06**	0.0	−0.01	**−0.05**	+0.04	−0.03	**+0.11**	+0.03
$+\Delta$[M/H]	−0.01	0.0	0.0	0.0	+0.01	0.0	+0.01	+0.03
$-\Delta$[M/H]	+0.01	−0.01	−0.01	0.0	0.0	0.0	0.0	+0.01

Notes: Abundance differences are calculated relative to the baseline abundances in Tables 4.5, 4.7, and 4.10. Significant offsets (≥ 0.05 dex) are shown in bold.

Table 5.2: The offsets in the 47 Tuc CMD-based abundances when two atmospheric parameters are varied together.

	Δ[X/H]		Δ[X/Fe]					
	Fe I	Fe II	Ca I	Ti I	Ti II	Ni I	Ba II	Eu II
47 Tuc								
$\Delta T, \log g$	–	**<0.20**	**<0.06**	–	–	<0.04	–	–
$\Delta T, \xi$	**<0.12**	–	–	**<0.06**	**<0.14**	–	**<0.22**	**<0.11**

Notes: The maximum abundance differences that occur when two parameters are changed together. The selected parameters for a given element were those that individually had the strongest effects. Abundance differences are calculated relative to the baseline abundances in Tables 4.5, 4.7, and 4.10.

each element ratio, the two parameters that individually showed the strongest changes in Table 5.1 were varied *together*. The maximum differences for all abundance ratios are shown in Table 5.2.

These results show that within the 1σ boxes, [Ni I/Fe I] is negligibly affected by the atmospheric parameters, while [Ca I/Fe I] and [Ti I/Fe I] are moderately affected ($\lesssim 0.1$ dex). The [Fe I/H], [Fe II/H], [Ti II/Fe II], [Ba II/Fe II], and [Eu II/Fe II] ratios are all significantly ($0.1 < \Delta$[X/Fe] < 0.22) affected by the changes in atmospheric parameters.

5.1.2 Colour-Temperature Relations

In a CMD-based analysis, the observed stellar colours are transformed to effective temperatures via Colour-Temperature Relations (CTRs). Several groups have calibrated these relations for different photometric filters and different stellar types, over ranges in colour and metallicity (see Figure 5.1). This section investigates the effects on the abundances caused by changing these CTRs. To investigate metallicity dependencies, 47 Tuc, M3, and M15 were used for these tests. The relations of Alonso et al. (1996, 1999, for dwarfs and giants, respectively), Ramirez & Melendez (2005, for dwarfs and giants), and Casagrande et al. (2010, for dwarfs only—the Ramírez & Melendez relation was used for giants) are considered. Recall that for the CMD-based abundances presented in MB08 and Chapter 4 the $(B-V)$ relations of Alonso et al. (1996, 1999) were used for 47 Tuc, while the $(V-I)$ relations from Ramirez & Melendez (2005) were used for the other clusters. The CTRs are only valid for the re-

Table 5.3: Differences in CMD-based abundance ratios with various Colour-Temperature Relations.

	Δ[X/H]		Δ[X/Fe]					
	Fe I	Fe II	Ca I	Ti I	Ti II	Ni I	Ba II	Eu II
47 Tuc								
Ext. A96/99	0.0	0.0	0.0	0.0	0.0	0.0	0.0	+0.01
RM05	−0.01	+0.01	−0.01	−0.03	−0.01	0.0	−0.02	0.0
C10+RM05	+0.01	0.0	+0.01	0.0	+0.01	0.0	+0.01	+0.01
Kurucz only	**+0.08**	−0.04	+0.03	**+0.05**	**+0.07**	+0.01	**+0.10**	**+0.07**
M3								
A96/99[a]	**+0.46**	**−0.05**	**−0.05**	**+0.25**	**+0.17**	**+0.08**	**+0.36**	**+0.21**
Ext. RM05	−0.03	+0.01	0.0	−0.01	−0.02	0.0	**−0.05**	+0.01
C10+RM05	+0.01	0.0	0.0	−0.01	+0.01	−0.01	+0.01	0.0
Kurucz only	+0.01	**−0.08**	**+0.06**	**−0.09**	**+0.11**	**−0.10**	**−0.05**	**−0.15**
M15								
A96/99[a]	**+0.44**	+0.02	**−0.17**	-	**+0.15**	**+0.12**	**+0.34**	**+0.25**
Ext. RM05	**−0.07**	0.0	+0.02	-	−0.03	+0.04	**−0.06**	−0.03
C10+RM05	0.0	0.0	+0.01	-	+0.01	0.0	0.0	−0.01
Kurucz only	**+0.14**	0.0	**−0.05**	+0.02	**+0.05**	+0.04	**+0.10**	**−0.06**

Notes: Extrapolated relations carry the CTRs outside the colour ranges in which they were calibrated. Abundance differences are calculated relative to the baseline abundances in Tables 4.5, 4.7, and 4.10.

References: A96 = Alonso et al. (1996), A99 = Alonso et al. (1999), RM05 = Ramirez & Melendez (2005), C10 = Casagrande et al. (2010), Kurucz = Kurucz grid of stellar atmospheres

[a] Note that the A96/A99 relations are significantly offset from the RM05 relations—at the tip of the RGB [$(V-I) \sim 1.5$ in M3] the $T_{\rm eff}$ offset is $\sim 300-400$ K, which is much larger than the estimated 1σ error in $T_{\rm eff}$ (Chapter 5.1.1).

gions in which they were calibrated; for stars whose colours fall outside the calibrated regions, MB08 and Paper I utilized the Kurucz grid of stellar models to determine effective temperatures. The effects of extrapolated relations and only values from the Kurucz grid are also considered.

Table 5.3 shows the offsets that occur when different CTRs are used. With the exception of the Kurucz-only case, the differences for 47 Tuc are all negligible ($\lesssim 0.03$ dex). The M3 and M15 results are *very* discrepant when the Alonso et al. (1996, 1999) relations are employed. This is consistent with the large offsets between the Alonso et al. (1996, 1999) CTRs versus the Ramirez & Melendez (2005) and Casagrande et al. (2010) CTRs (see Figure 5.1). Of the three relations, the Ramirez & Melendez (2005) and Casagrande et al. (2010) relations are likely to be more accurate, since Alonso et al. had to rely on uncertain transformations between photometric systems (see

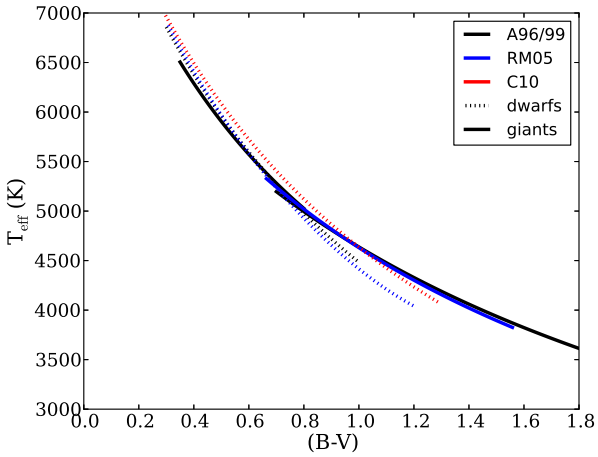

(a) CTRs for 47 Tuc

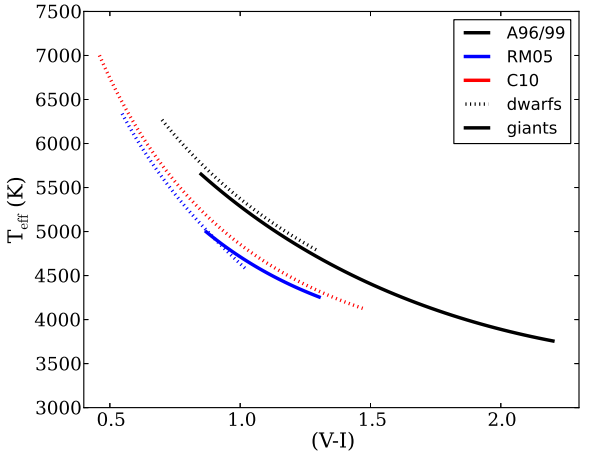

(b) CTRs for M3, M13, NGC 7006, and M15

Figure 5.1: CTRs for B and V filters (top, for $-1.5 <$ [Fe/H] < -0.5) versus those for V and I filters (bottom, for $-2.5 <$ [Fe/H] < -1.5), from Alonso et al. (1996, 1999, black), Ramirez & Melendez (2005, blue), and Casagrande et al. (2010, red). The dotted lines show the relations for dwarfs, while the solid lines show the relations for giants.

the discussion by Casagrande et al. 2010). The Kurucz only relations are also quite discrepant, suggesting that empirical relations (specifically the Ramirez & Melendez 2005 and/or Casagrande et al. 2010 CTRs) may be a better choice for CMD-based studies.

Other than the large offsets from the $(V-I)$ Alonso et al. relations and from the Kurucz only abundances, the differences between the other CTRs (including the extrapolated relations) are insignificant, except for [Ba II/Fe II], which is affected by ~ 0.05 when the Ramirez & Melendez (2005) relation is extrapolated outside the calibrated regions in M3 and M15.

5.1.3 Different Photometric Data Sets

This section investigates the effects of different photometric data sets (i.e. V, I instead of B, V, taken with different instruments at different times). This test is only performed on 47 Tuc since B, V CMDs of the cores are not available for the other GCs. Recall that the original 47 Tuc abundances were determined with the B, V photometry from Guhathakurta et al. (1992). Figure 5.2a presents the boxed *HST* 47 Tuc V, I CMD from the ACS Galactic Globular Cluster Treasury (e.g. Sarajedini et al. 2007). The CTRs of Ramirez & Melendez (2005) were used to determine atmospheric parameters for the V, I photometry; an HRD showing the box averages for the two data sets is shown in Figure 5.2b. The agreement between the parameters of each box is generally good, with the exception of the brightest RGB and BS boxes.

The bright RGB boxes in the V, I CMD contain cool M giants. Due to TiO line blanketing,[2] and the breakdown of the M giant $(B-V)$ CTR, the M giants appear mixed with the K giants in the B, V CMD. For this reason, M giants need to be treated differently if a B, V CMD is employed. MB08 showed that, for the core of 47 Tuc, the TiO blanketing in the M giant spectra significantly reduced their impact on the IL spectrum, such that only small errors in the derived abundances would result from the omission of the two M giants.[3] The M giants were *not* removed from

[2]Line blanketing occurs when there are so many absorption lines that they blend together and become almost undetectable—this makes the continuum level look lower than it actually is. Cool stars have many absorption lines from molecules such as TiO, which can lead to line blanketing, particularly in the red.

[3]However, the mostly negligible abundance effects of the two M giants in the 47 Tuc spectrum may not translate to similar effects in more metal-rich GCs, which have a larger fraction of M giants. Therefore the presence of M giants needs to be considered carefully when analyzing the IL spectra of GCs more metal-rich than 47 Tuc.

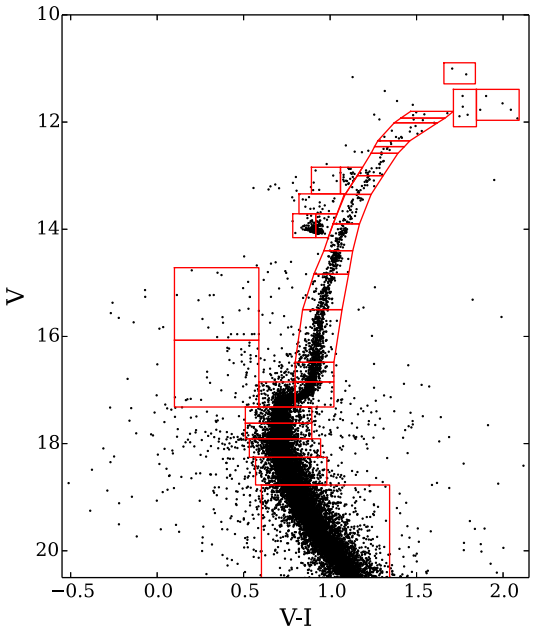

(a) V, I CMD

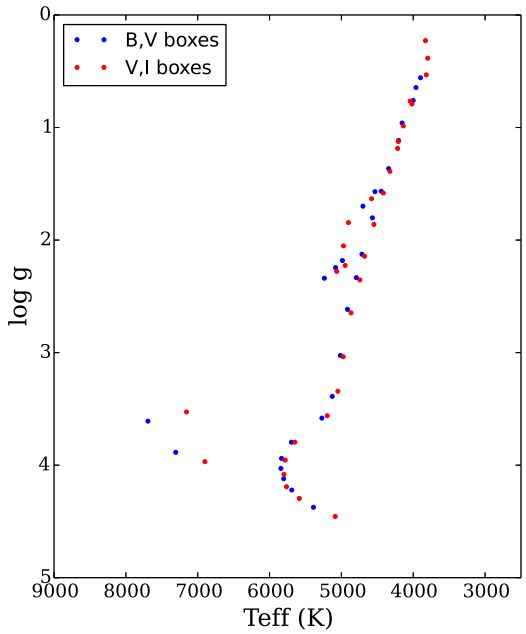

(b) HRD for B, V and V, I photometry

Figure 5.2: The V, I photometry for 47 Tuc. *Top:* The thirty CMD boxes on top of the Johnson-Cousins V, I photometry from the ACS Galactic Globular Cluster Treasury (Sarajedini et al., 2007). *Bottom:* An HRD of the B, V (blue) and V, I (red) CMD boxes, illustrating the general agreement between the two data sets.

Table 5.4: Differences in CMD-based abundance ratios as a result of various alterations to the input photometry.

	Δ[X/H]		Δ[X/Fe]					
	Fe I	Fe II	Ca I	Ti I	Ti II	Ni I	Ba II	Eu II
V, I data								
47 Tuc	−0.04	**+0.07**	−0.02	−0.04	−0.04	+0.01	**−0.07**	+0.02
Completeness								
47 Tuc	**+0.07**	**+0.07**	+0.01	**+0.06**	**+0.07**	+0.04	**+0.07**	+0.03
M3	0.0	+0.01	+0.01	0.0	0.0	+0.01	−0.01	0.0
M13	−0.01	0.0	−0.01	−0.01	+0.01	−0.01	0.0	+0.01
NGC 7006	+0.03	+0.01	**−0.05**	+0.01	+0.02	−0.02	+0.01	0.0
M15	−0.03	0.0	−0.02	+0.03	+0.01	+0.04	0.0	−0.01
Sampling								
M15	**<0.22**	**<0.10**	**<0.09**	**<0.06**	**<0.10**	<0.03	**<0.21**	**<0.09**

Notes: Abundance differences are calculated relative to the baseline abundances in Tables 4.5, 4.7, and 4.10.

the V, I photometry, which accounts for the differences in the brightest boxes.

The differences in BS boxes are likely only due to sampling. These boxes represent a small ($\lesssim 1\%$) portion of the total light, and therefore have an insignificant effect on the final abundances. Small variations between B, V and V, I photometry may also be due to the Bond-Neff effect (Bond & Neff, 1969), since 47 Tuc does have a significant population of CN-strong stars.

The abundance differences with different photometric data sets are listed in Table 5.4. In general, these differences are not drastic, with the exception of [Fe I/H] and [Ba II/Fe II], which differ by ~ 0.07 dex. The small differences in Fe I and Ba II and the negligible differences in the other abundances indicate that the M giants do not need to be removed from the V, I data, and that (as in MB08) the TiO molecular lines do not need to be included for GCs at 47 Tuc's metallicity. Only 47 Tuc was considered for this test—however, variations between B, V and V, I may be metallicity dependent, or dependent upon the populations in a given GC.

5.1.4 Incompleteness

Even the highest quality *HST* data suffer from incompleteness of the faintest stars. The effects of incompleteness were tested by increasing the numbers of stars in the lower main sequence boxes in order to match the theoretical luminosity functions

(assuming no mass segregation; this means that this test may add more low mass stars than are actually present in the observed core regions). The abundance differences (tabulated in Table 5.4) are all $\lesssim 0.1$ dex. The only GC affected by incompleteness is 47 Tuc; it is also the GC whose IL spectra covers the smallest portion of the cluster (see Table 2.6), suggesting that mass segregation may affect 47 Tuc's IL spectrum more than the other clusters. In 47 Tuc, the [Fe I/H], [Fe II/H], [Ti I/Fe I], [Ti II/Fe II], and [Ba II/Fe II] ratios are affected by < 0.1 dex—the other abundances are largely unaffected.

5.1.5 Sampling the Input Photometry

The input photometry may not perfectly match the population observed in the IL spectra. This is especially problematic in cases where the spectrograph fibres must be scanned across the cluster (see Figure 2.6). The input photometry can be cleaned based on distance from the cluster centre, but irregular coverage patterns will lead to differences between the input photometry and the observed population.

As a test of this effect, it is assumed that there are no constraints on the area that was scanned in M15's wedge-shaped coverage pattern. Note that this is a somewhat unrealistic worse case scenario; however, it serves as a useful test of how sensitive the abundances are to stochastic effects on the upper RGB. To select the input photometry, one hundred 80° wedges were selected by assuming a random[4] starting angle between 0 and 360°. `ILABUNDS` was then rerun on each of the one hundred wedges, producing new abundances for each run. The largest offsets from the mean are listed in Table 5.4. These abundance differences can be quite large, especially for [Fe I/H] and [Ba II/Fe II], where the maximum offsets are ~ 0.2 dex. However, the [Fe II/H], [Ca I/Fe I], [Ti II/Fe II], [Ni I/Fe I], and [Eu II/Fe II] abundances are less sensitive to this effect (with maximum differences $\lesssim 0.1$ dex). The primary differences between each run are the numbers and properties of bright RGB stars. Thus, these tests indicate that [Fe I/H] and [Ba II/Fe II] are particularly sensitive to sampling of the upper RGB.

This test on M15's wedge-shaped pointing pattern illustrates the importance of adequately selecting stars that truly match the observed population. The relative numbers of stars at various evolutionary stages are important, as are slight differences in colours and magnitudes. Because each cluster is unique, this effect cannot be

[4]A random value was selected using the numerical Python (NumPy) *random* routine.

removed through a differential analysis. However, observations that cover more of the cluster (e.g. extragalactic observations; Chapter 6) or whose pointing patterns are more regular (e.g. in the case of M3, M13, and NGC 7006) will not suffer from the problem as severely as M15 since the sampling differences between photometric data sets will be less extreme. Additionally, the IL observations of M3, M13, NGC 7006, and M15 utilized discrete pointings across the cluster (see Figure 2.6), albeit with short integration times. This means that the IL spectra are non-trivially weighted by the stars at those pointings. This effect is extremely difficult to account for—however, as the exposure times were short and the uncovered areas were small, this effect should not be too large.

In a CMD-based analysis of resolved GCs sampling problems can be alleviated by 1) symmetrically observing GCs and 2) using deep photometry that has been accurately sampled to match the IL spectra. Unfortunately, the second option is not possible for unresolved extragalactic targets. The next section investigates systematic offsets that occur when populations are unresolved, and have to be modelled with theoretical isochrones.

5.2 Uncertainties in HRD-based IL Analyses

CMDs cannot be obtained for unresolved clusters, and theoretical isochrones must be used to generate HRDs (i.e. temperatures and surface gravities) for the underlying populations. The main advantage of an HRD-based analysis is that the stars are modelled in the theoretical plane, and there is no need to convert observable properties to physical quantities. The main disadvantage in a HRD-based analysis of an unresolved target is that very little is known about the GC *a priori*, and diagnostics must be used to refine the model of the underlying stellar population. This section investigates systematic errors that occur when the stellar populations are incorrectly modelled. These errors include:

1. Uncertainties in identifying the best-fitting isochrones (Chapter 5.2.1)
2. Uncertainties that occur when the theoretical isochrones are populated with stars (Chapter 5.2.2)
3. Uncertainties in modelling evolved stars (Chapters 5.2.3 and 5.2.4) and main sequence stars (Chapters 5.2.5 and 5.2.6).

Discrepancies between the real population and the modelled population may vary between clusters in the same study, making it difficult to remove these effects though differential analyses.

5.2.1 HRD-based Abundances

Uncertainties in identifying the best HRDs

Chapter 4.7 outlines the criteria for identifying the HRDs that best fit the populations. The best-fitting HRDs in Table 4.11 are those which *best* meet the spectroscopic criteria; however, multiple solutions meet these criteria, and there is therefore a range of possible abundances. In this section, the selection criteria of Colucci et al. are broadened to assess the possible abundance ranges.

The first criterion for identifying the best HRD (isochrone [Fe/H] = IL [Fe I/H]) is uncertain: not only does the integrated [Fe I/H] have its own uncertainty, there may be systematic offsets between spectroscopically determined [Fe/H] values and between those determined from isochrone fits—these [Fe/H] values could be off by as much as 0.2 dex.[5] Additionally, [Fe I/H] is not necessarily indicative of the cluster [Fe/H], because of NLTE effects. Thus, it may not be correct to force the integrated [Fe I/H] abundance to equal the isochrone [Fe/H].

The least-squares fits to the Fe I abundances versus wavelength, REW, and EP also have their own uncertainties, such that multiple solutions produce "flat" fits (i.e. with no significant trend in the Fe I abundances). Furthermore the dispersion in Fe I abundances ensures that multiple solutions can produce sufficiently flat slopes, even in individual stellar analyses. This means that it may not be reasonable to consider only the isochrones that produce the flattest slopes.

Possible HRD solutions are identified in a similar way as Colucci et al.:

1. BaSTI isochrones of all ages and metallicities were used to generate synthetic stellar populations.

2. For each isochrone, `ILABUNDS` was run on the synthesized population.

3. Any isochrones whose output [Fe I/H] ratios were within 0.2 dex of the input isochrone [Fe/H] were deemed to be possible solutions. Note that Colucci et

[5]For example, from high resolution spectroscopic analyses of M3, Cohen & Melendez (2005) find an average [Fe/H] ~ -1.4 while Sneden et al. (2004) find [Fe/H] ~ -1.6. Isochrone fits with the DSED isochrones also indicate values of [Fe/H] ~ -1.6 (Dotter et al., 2010), while Galactic GC fiducials give [Fe/H] ~ -1.5 (VandenBerg et al., 2013).

Table 5.5: Abundance ranges when all acceptable HRD solutions are considered.

	Δ[X/H]		Δ[X/Fe]					
	Fe I	Fe II	Ca I	Ti I	Ti II	Ni I	Ba II	Eu II
47 Tuc	**<0.12**	**<0.12**	**<0.07**	**<0.13**	**<0.12**	<0.03	**<0.19**	**<0.08**
M3	**<0.08**	**<0.15**	<0.04	**<0.07**	**<0.05**	<0.04	**<0.10**	**<0.05**
M13	**<0.06**	<0.02	<0.01	**<0.06**	**<0.05**	<0.01	**<0.06**	<0.02
NGC 7006	**<0.07**	**<0.16**	**<0.07**	**<0.12**	**<0.08**	<0.04	**<0.08**	<0.03
M15	**<0.16**	**<0.05**	**<0.05**	<0.02	**<0.05**	<0.03	**<0.10**	**<0.07**

Notes: Abundance differences are calculated relative to the best-fitting HRD abundances in Table 4.12.

al. find the best [Fe/H] solution for each age; for the purposes of this errors analysis, *all* possible [Fe/H]/age combinations are retained if they meet this criterion.

4. For each possible solution, the fits to the Fe I abundances vs. wavelength, REW, and EP were calculated. All solutions whose slopes were $|m| \leq 0.04$ (within the uncertainty) were considered to be alternate solutions.

Table 5.5 presents the maximum offsets of the alternate solutions from the best-fitting HRD solutions. The spreads around the best-fitting HRD abundances are quite large, with every element except Ni having significant differences. The [Ca I/Fe I] and [Eu II/Fe II] ratios are fairly robust, with differences less than 0.07 and 0.08 dex, respectively. The other abundances ratios can be significantly affected by the isochrone parameters, depending on the cluster. It is also important to note that the offsets from the CMD-based abundances (Table 4.12) are sometimes larger than the uncertainties quoted in Table 5.5, suggesting that the differences between HRD and CMD-based abundances are due to systematic offsets between the two methods.

Comparisons between different isochrones

Different sets of isochrones predict slightly disparate distributions of stars in an HRD, even for a common age and metallicity, which could lead to slight discrepancies in the integrated abundances. Here the DSED (Dotter et al., 2008) and Victoria-Regina isochrones (VandenBerg et al., 2006) are compared to the BaSTI isochrones (Pietrinferni et al., 2004, 2006). Tests are run on 47 Tuc, M3, and M15 to investigate metallicity effects. Because neither the DSED nor the Victoria-Regina models include evolved HB or AGB stars in their models, the HB/AGB boxes from the resolved photome-

Table 5.6: Abundance offsets with different isochrones.

	Δ[X/H]		Δ[X/Fe]					
	Fe I	Fe II	Ca I	Ti I	Ti II	Ni I	Ba II	Eu II
47 Tuc								
Victoria-Regina	+0.02	+0.03	−0.01	+0.01	0.0	0.0	0.0	0.0
DSED $\alpha + 0.2$	+0.02	−0.01	+0.01	+0.02	+0.01	0.0	+0.03	+0.01
DSED $\alpha + 0.4$	+0.03	+0.02	−0.01	+0.02	0.0	+0.01	+0.02	+0.02
M3								
Victoria-Regina	−0.01	+0.04	−0.01	−0.01	−0.01	+0.01	−0.01	−0.01
DSED $\alpha + 0.2$	**−0.15**	**−0.06**	+0.02	**−0.09**	**−0.05**	−0.04	**−0.11**	**−0.07**
DSED $\alpha + 0.4$	**−0.05**	+0.04	−0.02	−0.01	−0.04	+0.03	**−0.06**	−0.03
M15								
Victoria-Regina	−0.01	+0.04	0.0	−0.04	0.0	−0.02	0.0	−0.02
DSED $\alpha + 0.2$	**−0.35**	**−0.14**	**+0.13**	**+0.07**	**−0.14**	−0.01	**−0.27**	**−0.14**
DSED $\alpha + 0.4$	**+0.05**	+0.04	−0.02	−0.03	+0.01	0.0	**+0.05**	+0.04

Notes: Abundance differences are calculated relative to the abundances derived with the BaSTI isochrones and resolved boxes of the HB and AGB (see the text).

try are used instead of HRD boxes *in all cases* (even with the BaSTI isochrones). The isochrones were sampled such that the number of RGB stars agreed with the number of resolved RGB stars—this was necessary to ensure that the relative number of HB/AGB and RGB stars was approximately correct. The isochrones with the best-fitting BaSTI parameters (from Chapter 4.7) were used.

The offsets from the BaSTI abundances are shown in Table 5.6. The differences between the BaSTI and Victoria-Regina isochrones are insignificant in all cases. The DSED isochrones have larger offsets at low [Fe/H], depending on the input [α/Fe] ratio. The BaSTI and Victoria-Regina models use [α/Fe] = +0.4 and +0.3, respectively, while DSED isochrones can have [α/Fe] = $+0.2$ or +0.4. The [α/Fe] = +0.4 DSED isochrones are in much better agreement than the +0.2 ones, although the [α/Fe] = $+0.4$ isochrone offsets can be ~ 0.05 dex. This suggests that the slight differences in the treatment of the upper RGB, subgiant branch, and main sequence turnoff do not have a strong effect on any of the final, integrated abundances, though the input [α/Fe] abundance may be important.

5.2.2 Populating an Isochrone

An isochrone provides the temperature and surface gravity at certain mass intervals for a cluster of a given age and chemical composition. To determine the integrated

Table 5.7: Abundance differences as a result of the input IMF.

	Δ[X/H]		Δ[X/Fe]					
	Fe I	Fe II	Ca I	Ti I	Ti II	Ni I	Ba II	Eu II
47 Tuc								
Salpeter	−0.04	0.0	−0.01	−0.04	−0.04	0.0	**−0.05**	−0.03
Chabrier	−0.04	−0.01	−0.02	**−0.06**	**−0.05**	−0.02	**−0.07**	**−0.05**
M3								
Salpeter	+0.02	0.0	0.0	+0.04	+0.01	+0.01	+0.02	+0.02
Chabrier	+0.01	−0.01	0.0	+0.03	+0.01	+0.01	+0.02	+0.02
M15								
Salpeter	+0.03	0.0	−0.01	**−0.08**	+0.01	+0.01	+0.02	+0.02
Chabrier	+0.01	0.0	0.0	**−0.06**	0.0	+0.02	0.0	+0.02

Notes: Abundance differences are calculated relative to the best-fitting HRD abundances in Table 4.12, which were determined with a Kroupa (2002) IMF.

abundances of a cluster, `ILABUNDS` must also know the number of stars in each mass bin. Stars are assigned to each bin assuming that the stellar masses are distributed according to an initial mass function (IMF), with the total number of stars determined from a cluster's total absolute V magnitude.

IMF

For their analyses of unresolved systems, MB08 and Colucci et al. utilize a Kroupa (2002) IMF. However, other forms of the IMF exist, for example the Salpeter (1955) and Chabrier (2003) IMFs, which differ most from the Kroupa IMF at the high mass end ($M \gtrsim 0.5 M_{\odot}$). These alternate IMFs are used to assign stars to the best-fitting HRDs from Chapter 5.2.1. The abundance differences are shown in Table 5.7. The different IMFs have no significant effect on M3. For 47 Tuc, the Salpeter IMF only significantly alters the [Ba II/Fe II] abundance (by 0.05 dex), while the Chabrier IMF has a $0.05 \lesssim \Delta$[X/Fe] < 0.1 dex effect on [Ti I/Fe I], [Ti II/Fe II], [Ba II/Fe II], and [Eu II/Fe II]. The [Fe I/H] ratio is also slightly affected by the Chabrier IMF. M15's [Ti I/Fe I] ratios are affected by both IMFs. These results suggest that Fe I, Ti, Ba, and Eu are sensitive to the sampling of the highest mass stars.

Total Magnitude

The total magnitude of the GC, M_V, determines the total number of stars in the populated HRD. Fainter GCs will have fewer stars to populate the HRD; certain

boxes along the isochrone may then have no stars, while others may be rounded up to one star, and the relative flux contributions from the boxes will be disrupted. This is shown in Table 5.8, where the abundance differences from the best-fitting HRD values are shown when different values of M_V are considered.

It is clear from Table 5.8 that lowering the total magnitude (i.e. making the cluster brighter) only leads to small offsets ($\lesssim 0.1$ dex) while making the cluster fainter can lead to large offsets in the [Fe I/H], [Ti I/Fe I], [Ba II/Fe II], and [Eu II/Fe II] ratios ($0.1 < \Delta$[X/Fe] < 0.4 dex, with the largest differences occurring for M13 and M15). The [Fe II/H], [Ca I/Fe I], [Ti II/Fe II], and [Ni I/Fe I] ratios are somewhat affected ($\lesssim 0.1$ dex) when the GC is made fainter. These abundance differences are driven by how the isochrone is populated, such that fainter GCs do not adequately populate the upper RGB. The Galactic GCs (and the PAndAS GCs in Chapter 6) are at the bright end of the GC luminosity function, suggesting that these effects will not be significant for the abundances derived in this thesis. Observations of the fainter GCs, however, will suffer from sampling problems.

This test indicates that fainter clusters will be more susceptible to abundance offsets if the cluster M_V is not well constrained. These problems can be reduced by using photometry of the bright RGB, AGB, and HB stars, and/or by sampling as much of the GC as possible. However, additional tests show that these errors can be dramatically reduced if *fractional* stars are used to populate the HRDs, instead of integer numbers of stars. Although this choice is distinctly non-physical it seems to work for IL spectra of bright, well-sampled GCs. Whether it will be applicable to real, intrinsically poorly-sampled GCs is uncertain.

5.2.3 Horizontal Branch Morphology

As discussed in Paper I, it is difficult to model the HBs of unresolved GCs, given the uncertain effects of the "second parameter" (Dotter, 2008; Dotter et al., 2010; VandenBerg et al., 2013). Synthetic HBs with a range of morphologies can be generated (e.g. from the BaSTI database; Pietrinferni et al. 2004, 2006), but require inputs for the average HB mass and the spread in HB masses, both of which are not known *a priori* and may not exactly match the true HB stars. In particular, if blue HB stars are not properly accounted for, spectroscopic ages will be skewed to younger ages to compensate for the absence of the hot stars (e.g. Lee et al. 2000; Ocvirk 2010). At high resolution, MB08 argued that blue HB stars could also confuse trends in Fe I

Table 5.8: Abundance offsets when the GC total magnitude is adjusted.

	Δ[X/H]		Δ[X/Fe]					
	Fe I	Fe II	Ca I	Ti I	Ti II	Ni I	Ba II	Eu II
47 Tuc								
$\Delta M_V = +1$	−0.03	+0.02	−0.03	**−0.06**	**−0.05**	−0.02	**−0.07**	**−0.05**
$\Delta M_V = +0.5$	+0.04	0.0	+0.01	**+0.05**	+0.03	+0.01	+0.04	+0.03
$\Delta M_V = -0.5$	+0.02	0.0	0.0	+0.01	+0.02	0.0	+0.02	+0.01
$\Delta M_V = -1$	+0.01	0.0	−0.01	0.0	+0.01	0.0	0.0	0.0
M3								
$\Delta M_V = +1$	**+0.36**	**+0.05**	0.0	**+0.41**	**+0.14**	**+0.10**	**+0.33**	**+0.23**
$\Delta M_V = +0.5$	**+0.21**	+0.02	+0.02	**+0.29**	**+0.08**	**+0.06**	**+0.20**	**+0.14**
$\Delta M_V = -0.5$	**+0.06**	0.0	+0.01	**+0.10**	+0.03	+0.02	**+0.06**	**+0.05**
$\Delta M_V = -1$	**+0.06**	+0.02	0.0	**+0.05**	+0.02	+0.01	+0.04	+0.02
M15								
$\Delta M_V = +1$	**+0.25**	**+0.10**	**−0.10**	**+0.05**	**+0.07**	**+0.07**	**+0.20**	**+0.15**
$\Delta M_V = +0.5$	**+0.12**	+0.04	**−0.05**	+0.03	+0.03	+0.04	**+0.10**	**+0.07**
$\Delta M_V = -0.5$	**−0.11**	0.0	+0.02	**−0.21**	−0.02	**−0.07**	**−0.10**	**−0.08**
$\Delta M_V = -1$	−0.03	+0.02	0.0	**−0.14**	0.0	−0.04	−0.03	−0.03

Notes: Abundance differences are calculated relative to the best-fitting HRD abundances in Table 4.12. Note that most of the abundance offsets for the low magnitude clusters are dramatically reduced if fractional stars are used to populate the HRDs.

abundances with EP, leading to incorrect [Fe/H] and age determinations.

It is therefore possible that HB morphology could measurably affect the derived chemical abundances. Lower resolution studies have concluded that IL spectral features can help constrain HB morphology, e.g. the Balmer line ratios (Schiavon et al., 2004) or specific indices from ionized atoms (e.g. the Mg II doublet at 2800 Å or the Ca II H and K index; Percival & Salaris 2011). However, the IL spectra presented here do not extend blueward enough to access these features.

The purpose of the tests presented below is not to identify or test the best way to constrain HB morphology, but to isolate and examine the abundance effects from HB morphology. With an M31 GC at [Fe/H] = −2.2, Colucci et al. (2009) tested the effects of HB morphology by manually moving red HB stars to blue HB star boxes in their best-fitting HRDs. For that particular GC, they found that individual Fe I abundances changed by < 0.05 dex and that the effect on the best-fitting isochrone parameters was negligible. Here these results are tested on the Galactic GCs.

The Direct Effects of HB Stars on Abundances

To test the direct effects of HB morphology on chemical abundances, the IL spectra and resolved photometry of the second parameter triad M3, M13, and NGC 7006 are used. The HB boxes for the three GCs are swapped, while maintaining the same total number of HB stars for each cluster. Worst case scenarios of purely red and purely blue HBs were also considered for M13 and NGC 7006, respectively. Finally, synthetic HBs from the BaSTI database were assigned to M13 and NGC 7006, using masses of 0.5 and 0.8 $M_\odot$ and mass dispersions of 0.02 $M_\odot$. These differences are shown in Table 5.9; the tests are first organized by GC, then by HB morphology.

Table 5.9 shows that:

1. The slight differences between M3 and NGC 7006's HBs lead to negligible abundance offsets.

2. HBs that are too red raise the integrated [Fe I/H], while HBs that are too blue lower the [Fe I/H]. The largest differences are ~ 0.1 dex.

3. The [Fe II/H] ratios are most affected when red HB stars are added (or when intermediate HB stars are removed). The largest offsets are ~ 0.2 dex.

4. The [Ca I/Fe I] and [Ni I/Fe I] ratios are mostly unaffected by HB morphology.

Table 5.9: Abundance differences as a result of HB morphology.

	Δ[X/H]		Δ[X/Fe]					
	Fe I	Fe II	Ca I	Ti I	Ti II	Ni I	Ba II	Eu II
M3								
M13's HB	**−0.05**	0.0	0.0	0.0	−0.02	−0.01	**−0.06**	−0.02
NGC 7006's HB	0.0	0.0	0.0	+0.01	−0.01	+0.01	−0.01	+0.01
M13								
Purely blue HB	−0.04	−0.02	0.0	+0.01	−0.03	+0.01	−0.04	+0.01
Synthetic Blue	**−0.06**	**−0.09**	+0.02	−0.01	+0.01	−0.04	−0.03	−0.02
M3's HB	**+0.06**	−0.01	−0.01	+0.01	+0.02	0.0	**+0.05**	**+0.05**
NGC 7006's HB	**+0.07**	−0.01	−0.01	+0.01	0.0	0.0	**+0.05**	**+0.06**
Synthetic Red	+0.02	**−0.17**	−0.01	**+0.05**	**−0.06**	+0.02	+0.01	**+0.11**
Purely red HB	+0.02	**−0.08**	−0.02	**+0.08**	**−0.07**	+0.04	−0.01	**+0.10**
NGC 7006								
Purely blue HB	**−0.11**	−0.02	−0.01	+0.03	**−0.07**	+0.02	**−0.11**	**−0.04**
Synthetic Blue	**−0.08**	−0.02	0.0	+0.02	−0.03	+0.01	**−0.07**	−0.03
M13's HB	**−0.07**	0.0	0.0	+0.01	−0.03	0.0	**−0.07**	**−0.05**
M3's HB	0.0	0.0	0.0	+0.01	0.0	0.0	−0.01	−0.02
Synthetic Red	−0.03	**−0.05**	0.0	+0.04	−0.03	+0.03	−0.03	+0.01
Purely red HB	−0.04	−0.04	−0.01	**+0.06**	**−0.05**	+0.03	**−0.05**	+0.01

Notes: Abundance differences are calculated relative to the baseline abundances in Tables 4.5, 4.7, and 4.10. Tests are organized by cluster, then by HB morphology, with the bluest HBs listed first.

5. The [Ti/Fe] ratios are significantly affected only when the HBs are significantly different from reality (e.g. the pure and synthetic red cases for M13).

6. The total offsets in [Ba II/Fe II] are $\lesssim 0.1$ dex. HBs that are too blue lower the output [Ba II/Fe II]. However, HBs that are too red do not always raise [Ba II/Fe II], because of the varying effects on Fe II. When intermediate HB stars are added to M13, the [Ba II/Fe II] ratio is increased; when they are removed or altered in M3 and NGC 7006 [Ba II/Fe II] is decreased. It therefore appears that [Ba II/Fe II] is most affected by the presence or absence of intermediate HB stars. This is not only driven by the differences in the [Fe II/H] abundances.

7. HBs that are too blue lower [Eu II/Fe II], while redder HBs raise [Eu II/Fe II]. Again, these effects are not driven by [Fe II/H] differences.

The Indirect Effects of HB Stars on Isochrone Age and [Fe/H]

The alternate HBs also affect the trends of Fe I abundances with wavelength, REW, and EP, such that the slopes are generally made steeper when the HB is improperly modelled. These slope changes imply that different HB models will lead to alternate best-fitting isochrones. To test the indirect effects of HB stars on isochrone age and [Fe/H], the default HBs were replaced with extremely blue and extremely red synthetic HBs (from the BaSTI synthetic HB generator), and `ILABUNDS` was rerun on the new populations. The parameters of the new isochrones and the subsequent abundance offsets are shown in Table 5.10.

These results show that:

1. For the GCs with intermediate HB morphologies (M3 and NGC 7006), HBs that are too red lead to underpredictions of the GC age (most likely to compensate for the lack of hot, blue stars in the input models) while HBs that are too blue lead to overpredictions of the GC age (likely for the opposite reason). These findings agree well with the findings of Lee et al. (2000) and Ocvirk (2010), i.e. that when blue HB stars are not properly accounted for, IL analyses will converge on ages that are too young.

2. For the blue HB GCs M13 and M15, the extreme blue and extreme red cases both converge on old ages. To understand this effect, the default HB morphologies of the original best-fitting isochrones must be investigated. For M13 and M15 the original HBs are significantly redder than the real HBs; M15's default HB also extends slightly blueward of the synthetic red HB tested here. The fact that the synthetic pure red and blue HBs both push the isochrones to old ages for these blue HB clusters may be because the bluest HB stars are fainter than their intermediate or red counterparts, such that they have less of an effect on the IL spectrum. Adding brighter intermediate HB stars to these GCs could then have a significant affect on the IL ages. This agrees with the findings of Colucci et al. (2009), who tested these effects on a GC with both blue and red HB stars and found that the bluest HB stars had a negligible effect.

These examples illustrate that convergence on a correct age (within ~ 5 Gyr) requires modelling the intermediate age HB stars (at least approximately) correctly.

However, regardless of how the HBs are modelled, all isochrones converge on reasonable isochrone metallicities with the Fe I lines in the $5300 - 7300$ $\AA$ region. Fur-

Table 5.10: Abundance differences and parameters of the best-fitting HRDs when synthetic HBs are used.

	Age	[Z/H]	Δ[X/H]		Δ[X/Fe]					
			Fe I	Fe II	Ca I	Ti I	Ti II	Ni I	Ba II	Eu II
M3										
Red HB	8	-0.96	**+0.11**	**+0.05**	−0.02	**+0.15**	0.0	**+0.07**	**+0.11**	**+0.12**
Blue HB	14	-1.27	**+0.08**	+0.01	+0.02	**+0.16**	**+0.07**	+0.03	**+0.12**	**+0.06**
M13										
Red HB	12	-1.27	**+0.18**	−0.02	−0.02	**+0.20**	**+0.05**	**+0.05**	**+0.16**	**+0.13**
Blue HB	14	-1.27	**+0.10**	+0.04	0.0	**+0.10**	**+0.08**	0.0	**+0.10**	+0.02
NGC 7006										
Red HB	5	-0.96	**+0.13**	**+0.06**	0.0	**+0.10**	+0.03	**+0.05**	**+0.14**	**+0.09**
Blue HB	14	-0.96	+0.02	**+0.28**	−0.03	**−0.12**	+0.01	+0.01	−0.04	**+0.08**
M15										
Red HB	14	-1.79	**+0.06**	−0.02	−0.03	**+0.06**	+0.01	**+0.07**	+0.03	**+0.08**
Blue HB	14	-1.79	+0.01	+0.03	0.0	+0.02	+0.02	0.0	0.0	−0.01

Notes: Abundance differences are calculated relative to the best-fitting HRD-based abundances in Table 4.12.

thermore, certain abundance ratios are relatively insensitive to the adopted isochrone age and HB morphology. While [Fe I/H], [Ti I/Fe I], [Ba II/Fe II], and [Eu II/Fe II] are very sensitive to changes in HB morphology (with offsets $\gtrsim 0.1$ dex), [Ca I/Fe I], [Ti II/Fe II], and [Ni I/Fe I] are much less sensitive, with offsets < 0.1 dex. Given the significant effects of HB morphology on age and various abundance ratios, for extragalactic targets it may be worthwhile to first obtain partially resolved photometry (Chapter 5.4) or lower resolution IL spectra that access the Balmer lines, in order to constrain the HB morphology (and age).

5.2.4 Asymptotic Giant Branch Stars

With the BaSTI isochrones the AGB can be modelled in various ways. Firstly, different mass loss parameters of $\eta = 0.2$ or $\eta = 0.4$ can be selected. Secondly, the AGB can be extended through all thermal pulse phases or can be terminated after the first few pulses (where the former is denoted as the "Extended" case and the latter as the "Normal" case; see the BaSTI website). Given their tests with Galactic GCs (Cameron, 2009), Colucci et al. (2009, 2011a) utilize Extended AGB isochrones with $\eta = 0.2$. This section investigates the abundance offsets that arise when the other AGB prescriptions are used. Note that MB08 required an enhancement in the

number of AGB stars in order to match the observed luminosity function and abundances of 47 Tuc. That enhancement is not included here, nor was it included for the HRD-based abundances in Chapter 4.7.

The Direct Effects of AGB Stars on Abundances

The AGB prescriptions were first altered while maintaining the best-fitting isochrone parameters from Chapter 5.2.1. These offsets are shown in Table 5.11. The AGB prescription has a small effect on 47 Tuc's abundances and a much larger effect on M3 and M15's abundances. The ratios that are most affected by the AGB models are [Fe I/H], [Ti I/Fe I], [Ba II/Fe II], and [Eu II/Fe II] (with offsets $\sim 0.1 - 0.2$ dex, depending on the cluster), while [Fe II/H], [Ti II/Fe II], and [Ni I/Fe I] are occasionally affected ($0.1 - 0.15$ dex). For all GCs, the [Ca I/Fe I] ratio is largely insensitive ($\lesssim 0.05$ dex) to the AGB prescription.

The abundance offsets are not the same for a given AGB prescription. For 47 Tuc, only the Normal, $\eta = 0.4$ case significantly alters the abundances. For M3 both of the Normal AGB cases ($\eta = 0.2$ and 0.4) lead to large offsets, while for M15 both $\eta = 0.4$ cases create significant offsets. In some cases the various AGB prescriptions bring the HRD-based abundances into better agreement with the CMD-based abundances; for example, Normal AGBs raise M3's [Ti I/Fe I] ratio; however, other abundance ratios are then sometimes brought out of agreement. Thus, the systematic uncertainties from a given AGB prescription are not the same for all clusters, and adopting a uniform treatment of the AGB will not remove intra-cluster systematic offsets. Without resolved photometry of the brightest AGB stars, it would be difficult to determine which AGB prescription is most representative of a given cluster.

The Indirect Effects of AGB Stars on Isochrone Age and [Fe/H]

To test how the AGB models affect the parameters for the best-fitting HRDs, the isochrone parameters were allowed to vary. These new best-fitting parameters for each AGB prescription and the resulting abundance differences are also shown in Table 5.11. In all cases new ages and/or metallicities are favoured, though they are not significantly different from the original values. This indicates that the AGB prescription is not responsible for the young isochrone ages for M3 and M15.

When the new isochrone parameters are selected for a given AGB treatment, the abundances are generally brought into *slightly* better agreement with the original

Table 5.11: Abundance differences from modelling the AGB.

AGB[a]	Age[b]	[Fe/H]	Δ[X/H]		Δ[X/Fe]					
			Fe I	Fe II	Ca I	Ti I	Ti II	Ni I	Ba II	Eu II
47 Tuc										
E-0.4	10[c]	-0.70	+0.01	+0.02	−0.03	−0.04	−0.01	−0.01	−0.03	−0.03
N-0.2	10[c]	-0.70	+0.03	+0.02	−0.01	+0.01	+0.01	+0.01	+0.02	+0.01
N-0.4	10[c]	-0.70	**+0.07**	0.0	+0.01	**+0.06**	**+0.06**	+0.01	**+0.08**	**+0.05**
E-0.4	11	-0.70	+0.03	0.0	−0.01	+0.01	+0.01	+0.01	+0.02	+0.02
N-0.2	12	-0.70	+0.01	+0.03	−0.02	−0.01	−0.01	0.0	−0.03	−0.02
N-0.4	11	-0.60	+0.03	**+0.09**	**−0.05**	−0.04	−0.02	+0.01	−0.04	−0.03
M3										
E-0.4	9[c]	-1.62	**+0.06**	+0.03	0.0	0.0	+0.04	+0.02	**+0.05**	+0.01
N-0.2	9[c]	-1.62	**+0.14**	+0.01	+0.02	**+0.23**	**+0.06**	**+0.05**	**+0.15**	**+0.10**
N-0.4	9[c]	-1.62	**+0.18**	+0.02	+0.01	**+0.22**	**+0.09**	**+0.05**	**+0.19**	**+0.11**
E-0.4	10	-1.62	+0.04	+0.02	0.0	0.0	+0.03	+0.01	+0.03	0.0
N-0.2	8	-1.31	**+0.08**	**+0.15**	+0.04	**+0.08**	−0.01	**+0.06**	**+0.05**	**+0.07**
N-0.4	10	-1.31	**+0.10**	**+0.15**	−0.03	**+0.09**	0.0	**+0.07**	**+0.08**	**+0.08**
M15										
E-0.4	9[c]	-2.14	**−0.16**	0.0	+0.03	**−0.38**	−0.01	**−0.13**	**−0.14**	**−0.13**
N-0.2	9[c]	-2.14	+0.03	0.0	−0.01	+0.01	+0.02	+0.02	+0.02	+0.02
N-0.4	9[c]	-2.14	**+0.13**	+0.03	−0.03	**−0.06**	**+0.08**	−0.03	**+0.11**	+0.04
E-0.4	10	-2.62	**−0.19**	+0.01	+0.03	**−0.06**	−0.04	**−0.11**	**−0.18**	**−0.14**
N-0.2	8	-2.14	+0.01	0.0	0.0	+0.02	+0.01	+0.01	0.0	+0.01
N-0.4	10	-2.62	**+0.10**	+0.02	−0.03	**−0.09**	**+0.05**	0.0	+0.07	+0.04

Notes: Abundance differences are calculated relative to the best-fitting HRD abundances in Table 4.12, which were determined with Extended, $\eta = 0.2$ isochrones. Tests are organized by cluster, then by AGB prescription, with the original isochrone age and [Fe/H] listed first, followed by the new, best-fitting HRD.

[a] The AGB prescription indicates which BaSTI isochrones were utilized. "E-0.4" denotes Extended, $\eta = 0.4$ isochrones, "N-0.2" denotes Normal, $\eta = 0.2$ isochrones, and "N-0.4" denotes Normal, $\eta = 0.4$ isochrones.

[b] Ages are in Gyr.

[c] These tests utilized the original, best-fitting isochrone parameters from Chapter 5.2.1.

HRD-based abundances, particularly for 47 Tuc. For example, the large offsets in [Fe I/H], [Ti I/Fe I], [Ba II/Fe II], and [Eu II/Fe II] from assuming the original age and [Fe/H] are generally (though not always) reduced when new best-fitting HRDs are adopted. However, in some cases the offsets are still quite large (e.g. with M3's "Normal" AGBs), illustrating that the treatment of the AGB could be problematic for high-resolution, optical IL spectral studies of unresolved GCs.

Note that there is also some evidence to suggest that extreme second generation HB stars in GCs (the ones with high Na and low O) might not proceed to the AGB after core He exhaustion (from spectroscopic observations in NGC 6752; Campbell et al. 2013). In this case, the actual number of AGB stars would be lower than the predicted value from an IMF. Although the number of AGB stars in a GC is not high compared to the number of RGB stars, this discrepancy could lead to additional abundance offsets. Future tests on multiple populations will examine these effects.

5.2.5 Blue Stragglers

Isochrones do not contain models for blue stragglers (the stars that appear to lie on the main sequence, blueward of the turnoff; see Chapter 1.2). Though there are few of these stars, they are brighter and hotter than main sequence stars, and thus may have a non-negligible effect on the IL spectral lines. To test these effects the resolved BS boxes were included with the best-fitting isochrones. The results are shown in Table 5.12, and are generally quite small, except for a few cases where [Fe I/H], [Fe II/H], [Ba II/Fe II], and [Eu II/Fe II] are affected by up to 0.07 dex. This suggests that the inclusion of BS stars is not essential for the majority of elements, though the singly ionized elements are mildly sensitive to them. Furthermore, the BSs have only a slight effect on the Fe I trends with wavelength, REW, and EP, and therefore do not have a significant effect on the isochrone age.

5.2.6 Lower Mass Cutoff

In their IL analysis of 47 Tuc, MB08 found that a lower mass cutoff was necessary to reproduce the observed luminosity function (ostensibly because the IL spectrum only covers the cluster core, and mass segregation must be taken into account). This section investigates the effects of applying a lower mass cutoff such that all stars fainter than $M_V = +4.7$ are removed from the synthetic HRD—note that this was the cutoff adopted by MB08 to match 47 Tuc's observed luminosity function. (Note

Table 5.12: The effects of blue stragglers.

	Δ[X/H]		Δ[X/Fe]					
	Fe I	Fe II	Ca I	Ti I	Ti II	Ni I	Ba II	Eu II
47 Tuc	+0.02	0.0	0.0	0.0	+0.02	−0.01	+0.01	+0.01
M3	+0.02	**+0.07**	0.0	0.0	−0.03	+0.01	−0.03	**−0.06**
M13	+0.03	+0.04	−0.02	−0.02	−0.02	−0.02	−0.03	−0.03
NGC 7006	+0.02	+0.01	+0.01	−0.01	+0.02	−0.01	+0.02	0.0
M15	**+0.07**	+0.02	−0.02	−0.04	−0.04	−0.03	**+0.05**	+0.01

Notes: Abundance differences are calculated relative to the best-fitting HRD abundances in Table 4.12.

Table 5.13: The effects of a lower mass cutoff.

	Age	[Z/H]	Δ[X/H]	Δ[X/Fe]						
			Fe I	Fe II	Ca I	Ti I	Ti II	Ni I	Ba II	Eu II
47 Tuc	10	-0.35	**−0.05**	0.0	−0.04	**−0.07**	**−0.07**	−0.03	**−0.09**	**−0.12**
M3	9	-1.27	**+0.10**	−0.03	+0.02	**+0.24**	+0.03	+0.04	**+0.11**	**+0.10**
M13	11	-1.27	**+0.10**	−0.02	−0.01	**+0.16**	+0.02	+0.01	**+0.07**	**+0.08**
NGC 7006	5	-0.96	**+0.09**	**+0.12**	0.0	**+0.10**	0.0	**+0.05**	**+0.08**	**+0.09**
M15	9	-1.79	**−0.13**	**−0.05**	+0.04	−0.01	−0.04	−0.01	**−0.11**	**−0.05**

Notes: Abundance differences are calculated relative to the best-fitting HRD abundances in Table 4.12.

that this test is essentially the opposite of the Incompleteness test in Chapter 5.1.4, except that now new isochrones are identified.) This cutoff was applied to all the GCs, even though some of the IL spectra cover out to further radii where there may still be fainter stars. New best-fitting isochrones were then identified.

The new isochrone parameters and the abundance offsets from the original best-fitting HRDs are shown in Table 5.13. With the lower mass cutoff, the same isochrones are identified for 47 Tuc, M3, and M15; for M13 a slightly younger isochrone is preferred, while for NGC 7006 a more metal-rich, younger isochrone is preferred. Note that the slopes are never sufficiently flat for M15, as with the original best-fitting HRD (Chapter 5.2.1). The [Fe I/H], [Ti I/Fe I], [Ba II/Fe II], and [Eu II/Fe II] ratios are particularly affected (up to $\sim 0.1 - 0.2$ dex) by the absence of the lowest mass stars. However, this may be because more high mass stars are needed to maintain the same total cluster magnitude.

5.3 Uncertainties in all IL Analyses

Regardless of how the stellar population is modelled, some simplifying assumptions must be made in a high resolution IL analysis. These include:

1. The methods used to generate the stellar parameters (Chapters 5.3.1 and 5.3.2)
2. The models of stellar subpopulations (Chapters 5.3.3 and 5.3.4)
3. The influence of foreground stars (Chapter 5.3.5) and chemical variations in the model atmospheres (Chapter 5.3.6).

Again, the validity of these assumptions can differ between GCs in a given study.

5.3.1 CMD/HRD Boxes

In both CMD and HRD-based methods the stars are binned together to reduce computation time. The effects from the coarseness and definition of the boxes are investigated here. First, an abundance analysis is performed on 47 Tuc with *no* CMD boxes (i.e. EWs are computed for each star). The abundance differences (tabulated in Table 5.14) are completely negligible, suggesting that boxing the CMD is an appropriate choice to speed up computations. This is essential, since using the default number of 27 boxes speeds up computations by a factor of 200 compared to the no box case.

Box definition was then investigated with 47 Tuc and M13, to compare the effects of metallicity and HB morphology. Finer and coarser boxes are shown in Figure 5.3 with the old 47 Tuc and M13 boxes (in black). The finer boxes were reshaped to provide finer coverage of the upper red giant branch (RGB), horizontal branch (HB), and asymptotic giant branch (AGB), and to include more stars in the main sequence boxes. The coarser boxes still maintain finer resolution of the brightest stars. These abundance differences are also shown in Table 5.14. As expected, the differences are negligible for the cases with finer boxes. For the coarser boxes, the differences are significant for 47 Tuc when $5 - 17$ boxes are considered, while M13 is sensitive to the coarse 5 box case. A moderate number of boxes ($\sim 25 - 40$) therefore provides a compromise between faster computing time and precision. Using the default number of boxes (~ 30) only slows computations down by a factor of 2 over the coarsest box cases.

These tests were then performed on the synthetic HRDs. The original HRD-based abundances in Table 4.12 were produced using isochrones that were binned into boxes

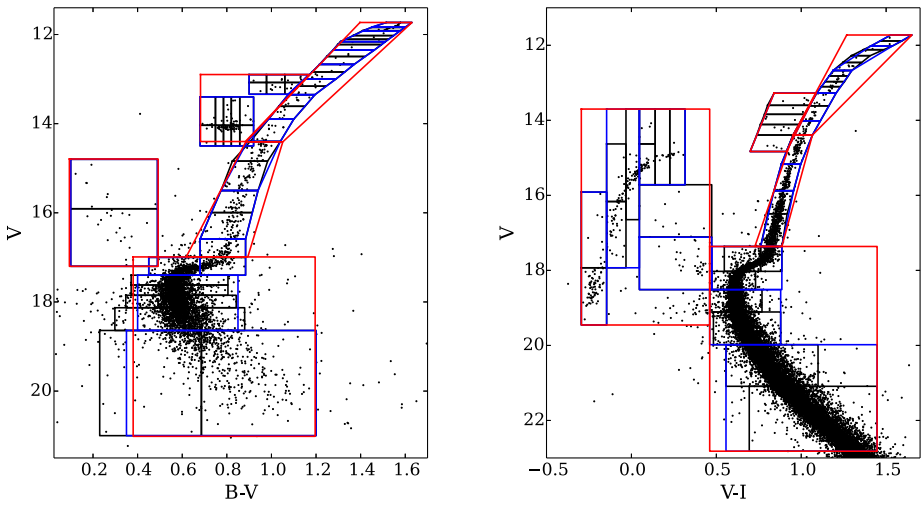

(a) 47 Tuc boxes

(b) M13 boxes

Figure 5.3: Comparisons of box definitions for 47 Tuc (left) and M13 (right). Finer boxes (in black) have increased resolution on the RGB, HB, and AGB. Coarser boxes are shown in blue and red.

Table 5.14: Differences in 47 Tuc abundance ratios as a result of different boxing methods.

	Δ[X/H]		Δ[X/Fe]					
	Fe I	Fe II	Ca I	Ti I	Ti II	Ni I	Ba II	Eu II
47 Tuc: CMD								
No boxes	0.0	+0.0	+0.01	+0.01	+0.01	+0.01	+0.01	+0.02
Finer boxes (49)	−0.01	0.0	+0.01	+0.01	0.0	+0.01	0.0	+0.04
Coarse boxes (17)	−0.01	+0.01	+0.01	+0.01	0.0	0.0	0.0	**+0.05**
Coarser boxes (5)	−0.02	0.0	+0.02	+0.03	−0.01	+0.01	0.0	**+0.07**
M3: CMD								
Finer boxes (40)	−0.03	+0.01	0.0	0.0	−0.01	0.0	−0.03	0.0
Coarse boxes (16)	−0.01	+0.02	+0.01	+0.01	0.0	0.0	−0.01	+0.01
Coarser boxes (5)	**+0.09**	**+0.08**	+0.02	+0.04	+0.04	0.0	**+0.05**	+0.03
47 Tuc: HRD								
1%	**−0.07**	+0.04	**−0.06**	**−0.14**	**−0.10**	−0.04	**−0.17**	**−0.12**
2%	−0.01	+0.01	−0.02	−0.03	−0.01	−0.01	−0.04	−0.03
5%	+0.01	−0.01	0.0	+0.02	+0.01	0.0	+0.01	+0.02
10%	−0.01	0.0	0.0	0.0	−0.01	0.0	+0.02	0.0
20%	−0.01	−0.02	+0.01	+0.03	0.0	+0.01	+0.01	+0.03
M13: HRD								
1%	**+0.11**	+0.01	−0.01	**+0.16**	+0.03	+0.03	**+0.09**	**+0.06**
2%	**+0.05**	0.0	0.0	**−0.06**	−0.03	−0.01	**−0.05**	−0.04
5%	**−0.09**	−0.02	+0.02	−0.04	−0.04	−0.01	**−0.07**	**−0.05**
10%	−0.03	−0.03	0.0	0.0	−0.03	0.0	−0.03	0.0
20%	+0.04	0.0	−0.01	+0.04	−0.01	+0.02	+0.02	+0.02

Notes: CMD-based abundance differences are calculated relative to the baseline abundances in Tables 4.5, 4.7, and 4.10, which use 27 boxes for 47 Tuc and 33 boxes for M13. HRD-based abundance differences are calculated relative to the best-fitting HRD-based values in Table 4.12, which use box sizes of 3.5%.

that each contained 3.5% of the total luminosity. Table 5.14 also shows the effects if these HRD boxes are redefined. For 47 Tuc, boxes of 2-20% lead to insignificant differences. Surprisingly, the 1% boxes have large offsets—this seems to be a result of rounding errors when individual boxes are assigned fractions of stars instead of round numbers (as discussed in Chapter 5.2.2). M13 is much more sensitive to HRD box definitions, though the 2% case seems to still be due to rounding errors. Thus, these results indicate that the HRD-based abundances are also largely insensitive (with offsets $\lesssim 0.05$ dex) to the precise box definitions.

Table 5.15: Differences in abundance ratios as a result of different microturbulence relations.

	Δ[X/H]		Δ[X/Fe]					
	Fe I	Fe II	Ca I	Ti I	Ti II	Ni I	Ba II	Eu II
47 Tuc								
MB08 + dispersion	<**0.08**	<**0.05**	<0.02	<0.02	<**0.06**	<0.01	<**0.09**	<0.03
Kirby et al. (2009)	−**0.07**	−0.04	−0.01	+0.01	−**0.05**	0.0	0.0	+0.04
Gratton et al. (1996)	−**0.13**	−**0.08**	−0.02	−0.03	−**0.10**	+0.01	**0.16**	+**0.06**
M3								
Kirby et al. (2009)	−0.04	−0.01	−0.01	+0.01	−0.04	0.0	−0.01	0.0
Gratton et al. (1996)	−**0.12**	−**0.05**	−0.03	+0.04	−**0.11**	0.0	**0.27**	+0.01
M15								
Kirby et al. (2009)	−**0.05**	0.0	+0.01	+0.04	−0.03	+0.03	−0.02	−0.03
Gratton et al. (1996)	−**0.21**	−0.01	+**0.05**	+**0.18**	−**0.10**	+**0.11**	−**0.30**	+**0.06**

Notes: Abundance differences are calculated relative to the baseline abundances in Tables 4.5, 4.7, and 4.10.

5.3.2 The Microturbulence Relation

Each box's microturbulent velocity is determined through an empirical relation with the surface gravity; this relationship is based on a fit to Arcturus and the Sun (see MB08 for details). `ILABUNDS` was rerun with alternate empirical microturbulence relations from Kirby et al. (2009, K09, calibrated to GC and dwarf galaxy stars) and Gratton et al. (1996, G96). Note that the MB08 and K09 relations are only dependent on $\log g$, though the G96 relation is dependent on $\log g$ and $T_{\rm eff}$. The differences in these relations will lead to slight variations in the subpopulations. Note that there are other microturbulence relations in the literature, but they are often only calibrated to dwarfs or giants, not both.

The abundance offsets are shown in Table 5.15 for 47 Tuc, M3, and M15 (to investigate [Fe/H] effects). With the exception of Ba II, the largest abundance differences are all $\lesssim 0.1$ dex. The differences between abundances with the MB08 and K09 relations are mostly insignificant, supporting that the small offset is negligible. The G96 relation has a significant effect on all abundances, depending on the cluster, where the offsets are largest for M15. It is not clear if it is valid to extend this relationship to the hottest stars in the blue HB clusters.

The "real" microturbulent velocities are dispersed about these relations. Furthermore, each box contains stars with a dispersion of microturbulent velocities. To test these effects, each star in a given box was assigned the same microturbulence value,

which was randomly selected from a Gaussian distribution with a standard deviation of 0.2 dex, centered on the MB08 relation. These microturbulence values were reselected one hundred times. The maximal abundance offsets (also shown in Table 5.15) are $\lesssim 0.1$ dex, with [Ba II/Fe II] having the greatest difference.

5.3.3 Anomalous Stars

Some cluster stars are distinctly different from the other cluster stars. This section investigates the effects of two different types of oddball stars: long period variables (Chapter 5.3.3) and carbon-enhanced stars (Chapter 5.3.3).

Long Period Variables

As discussed in MB08 and Chapter 5.1.3, the core region of 47 Tuc contains two bright, cool M giants. These stars are long period variables (LPVs), stars which exhibit large brightness variations over fairly long periods (days to years). These LPVs are only likely to exist in clusters at 47 Tuc's metallicity and above. MB08 showed that these M giants are troublesome in the B, V photometry because line blanketing reduces the B and V magnitudes such that the stars appear to lie further down the RGB; including those stars in boxes with incorrect atmospheric parameters leads to large abundance offsets. This problem does not occur in the V, I photometry (see Chapter 5.1.3)—however, since the M giants are LPVs, their atmospheric parameters change over time, such that the properties of the M giants in the photometry/isochrone may not match the conditions that were present when the IL spectra was obtained.

The original V, I abundances were calculated with the two bright M giants at the tip of the RGB. To test the worst case effects of long period variability, these two stars were moved to RGB boxes that were 1 mag fainter. The abundance offsets (with respect to the V, I based abundances in Chapter 5.1.3) are shown in Table 5.16. The [Fe I/H], [Ti I/Fe I], [Ti II/Fe II], and [Ba II/Fe II] ratios are all significantly affected, though the differences are < 0.1 dex. The other ratios are largely unaffected by the changes in the LPVs.

Carbon Enhanced CH Stars

Certain clusters (e.g. M15; Shetrone et al. 1999) have been observed to have anomalous bright stars with strong CH bands (which have been referred to as CH stars). To test the effects of these stars, the brightest star in M15 was made a CH star. Note

Table 5.16: Differences in abundance ratios as a result of various assumptions about the underlying stellar population.

	Δ[X/H]		Δ[X/Fe]					
	Fe I	Fe II	Ca I	Ti I	Ti II	Ni I	Ba II	Eu II
LPVs[a]								
47 Tuc	+0.01	**+0.07**	0.0	+0.03	+0.01	+0.03	0.0	0.0
CH stars[a]								
M15	0.0	0.0	+0.01	0.0	0.0	+0.01	0.0	+0.01
Hot Stars								
M13: Abundances	**+0.06**	+0.04	−0.01	0.0	−0.01	−0.03	+0.04	−0.04
M13: Rotation[a]	+0.02	+0.02	+0.01	−0.01	**+0.07**	+0.01	0.0	−0.02
Field stars[a]								
47 Tuc	**<0.09**	**<0.08**	**<0.09**	<0.04	**<0.07**	**<0.06**	**<0.10**	**<0.05**
NGC 7006	<0.04	<0.01	<0.0	<0.03	<0.02	<0.01	<0.03	<0.04
M15	**<0.10**	**<0.09**	<0.04	−[b]	<0.02	<0.03	**<0.07**	<0.04
ODFNEW Atms								
47 Tuc	**−0.05**	**−0.12**	+0.03	+0.02	+0.02	−0.01	−0.01	+0.02
M3	0.0	**−0.07**	+0.01	+0.01	+0.02	−0.02	−0.02	−0.01
M13	0.0	**−0.07**	+0.01	+0.01	+0.03	−0.02	−0.02	−0.01
NGC 7006	0.0	**−0.07**	0.0	+0.02	+0.02	−0.01	−0.03	−0.03
M15	+0.02	−0.02	0.0	+0.01	+0.01	+0.01	0.0	−0.03
CN-cycled Atms								
47 Tuc	**−0.05**	**−0.07**	0.0	−0.01	0.0	−0.01	−0.02	+0.01

Notes: Abundance differences are calculated relative to the baseline abundances in Tables 4.5, 4.7, and 4.10, unless otherwise noted.

[a] Baseline abundances were calculated separately (see text).

[b] Lines are too weak to measure in the synthesized spectra.

that this is not the real CH star in M15; instead, this provides an indication of a worst case scenario. During the EW analysis, the brightest star was assigned the [C/Fe], [N/Fe], and [O/Fe] abundances from Shetrone et al. (1999) and the standard cluster abundances for the lines of interest. These C, N, and O abundances are then included in the calculations for the continuous fluxes. Note that the effects of molecular lines would have to be investigated via spectrum syntheses.

The abundance offsets are shown in Table 5.16, and are insignificant for all elements.

5.3.4 Hot Stars

The hottest stars in a cluster ($T_{\rm eff} \gtrsim 8000 - 11500$ K) can have different properties from the other stars in the cluster. The effects of radiative levitation can drastically increase the surface abundances of hot stars, possibly increasing the metal-poor surface abundances of some elements (primarily the heavier elements) to Solar composition (e.g. Grundahl et al. 1999; Behr et al. 2000; Behr 2003; Michaud et al. 2011; Lovisi et al. 2012). The hottest stars can also have high rotation (e.g. Peterson 1985), with rotational velocities up to ~ 60 km/s (Behr, 2003); increased rotation broadens the line profiles and could affect the shape of an IL spectral line. In old GCs, the hottest stars are often blue HB stars, which do not contribute much to the IL. This section investigates the effects on the EWs of the Fe, Ca, Ti, Na, Ba, and Eu lines. Only M13 is considered for these tests, since 47 Tuc, M3, and NGC 7006 do not have hot stars.

Surface Composition

For this test, all stars hotter than 8000 K were given Solar composition, while all stars cooler than 8000 K were assigned the standard cluster chemistry. Note that this $T_{\rm eff}$ limit from Lovisi et al. (2012) is lower than the values quoted in Grundahl et al. (1999), Behr et al. (2000); Behr (2003), and Michaud et al. (2011); however, this test is meant to illustrate the worst case scenario. EWs were calculated for each box and were combined as in the standard method—however, the initial abundances were preserved, and *no* iterations were done to match the observed EWs. `ILABUNDS` was then rerun on the new EWs. The differences from the original abundances (listed in Table 5.16) provide indications of the effects of the hottest HB stars. With the exception of [Fe I/H], all abundance ratios are stable to within 0.04 dex.

Rotation

For stellar rotation, the same approach was employed as in Chapter 5.3.4, except that stars hotter than 8000 K were assigned rotational velocities of 60 km s^{-1} *and* Solar abundances.[6] Since rotation affects the shape of the line profiles, lines were synthesized (in 10 Å regions around the line of interest). Again, the boxes were combined and a new synthetic IL spectra was produced. To automate this process, EWs of the lines in the new synthetic IL spectra were measured in `DAOSPEC`, and the new EWs were fed to `ILABUNDS`. Because the success of IL spectrum synthesis is highly dependent on the input line list, the same procedure was applied *without the rotation enhancement in the hot stars*—these abundances were used as the original abundances in the calculation of the abundance differences, which are shown in Table 5.16. Table 5.16 shows that, with the exception of [Ti II/Fe II], all abundances are stable to within 0.02 dex.

5.3.5 Field Stars

There is always the possibility that an interloping field star could contaminate the IL spectra from the cluster. For Galactic clusters these field stars would be in the Milky Way—for extragalactic GCs these interloping field stars could also be in the host galaxy. Of course, any field stars that are significantly brighter than the clusters will be apparent in an image of the cluster. To test the possible effects of field stars, the worst case scenario is considered, i.e. that one of the brightest cluster stars is actually an undetected field star. Three factors are varied:

1. *Colour:* The field star is taken to be either the brightest star on the RGB, or the brightest blue star (which may not be included in any of the CMD boxes).

2. *Composition:* The field star is considered to be either Solar metallicity or a metal-poor star (with [Fe/H] = −2.5). In the latter case the field star is assumed to be α-enhanced.

3. *Luminosity Class:* The field star is taken to be either a dwarf or a giant. Physical parameters are then assigned to the field star based on isochrone fits with the DSED isochrones.

[6]Note that only considering rotation without enhanced abundances leads to very small differences in spectral features.

To test metallicity effects, 47 Tuc, NGC 7006, and M15 were all considered for these tests. Besançon models of the Galaxy[7] (Robin et al., 2003) were used to find the average radial velocity of a star at the same Galactic latitude and longitude as the target GC—the artificial field stars were then assigned these radial velocities. For each spectral line, synthetic spectra were generated for each CMD box (with the field star in its own box), EWs were remeasured in the combined synthetic spectrum, and `ILABUNDS` was rerun on the new EWs (this procedure is similar to that in Chapter 5.3.4). Because the input line lists are uncalibrated, the same procedure was performed on the original CMD boxes; those abundances serve as the baseline values for the comparisons.

The offsets are listed in Table 5.16, and are generally $\lesssim 0.1$ dex. For these resolved GCs, the abundance differences are likely to be upper limits, since the worst case scenarios were considered. For unresolved GCs a brighter field star of a vastly different colour could be included. Targets should therefore be inspected carefully for stellar contamination. Extragalactic GCs will have smaller Galactic field star contamination, but may also suffer from contamination from its host galaxy.

5.3.6 Model Atmosphere Chemistry

α-enhancement

Spectroscopic analyses typically adopt α-enhanced model atmospheres for metal-poor stars, since the [α/Fe] ratios in Milky Way stars and clusters are enhanced (e.g. see Chapter 1.3.5). To reflect this α-enhancement, the AODFNEW model atmospheres from the Kurucz database have all α-elements (Ne, Mg, Si, S, Ar, Ca, and Ti) enhanced by 0.4 dex over the scaled-solar abundances.[8] These α-enhanced model atmospheres have therefore been used for the baseline abundances of the target Galactic GCs, which are known to be α-enhanced. The α-enhanced atmospheres have also been used for extragalactic targets whose α-abundances indicate enhancement (e.g. Colucci et al. 2009).

However, the IL abundance analyses have shown that some α-elements are *not* enhanced in IL, such as Mg (e.g. Chapter 4, Colucci et al. 2009), because of the multiple populations in GCs. The abundances of, e.g., O and Mg, are expected to be lower in the second generation stars, as has been observed (e.g. Carretta et al. 2009a);

[7] `http://model.obs-besancon.fr/`

[8] Note that their high Solar O abundance means that O is actually enhanced by +0.54.

this has the effect of lowering the integrated abundances if the second generation stars dominate the IL spectrum. Since some of those elements are included in the model atmosphere α-enhancement, it may not be proper to use AODFNEW atmospheres for all stars. This effect is tested by using Solar-scaled ODFNEW atmospheres instead of AODFNEW ones. The abundance differences are tabulated in Table 5.16. For the vast majority of elements the differences are insignificant. Only for Fe II does the α-enhancement make a difference, with offsets up to ~ 0.1 dex. This is likely because for the brightest RGB stars, Fe II is the dominant ionization stage, and will be more affected by the presence or absence of free electrons.

Heavily CN-cycled atmospheres

Stellar abundances (in particular, the C and N abundances) can change as a star evolves up the RGB and proceeds through the HB and AGB phases (though the sum C+N+O remains constant). Furthermore, some clusters (e.g. 47 Tuc) shown CN bimodalities throughout the cluster (Briley et al., 2004). To test the worse case effects of C and N variations on the atmospheric opacities, the heavily CN-cycled MARCS atmospheres (Gustafsson et al., 2008) were adopted for all boxes with $\log g < 3.5$ dex (i.e. for all boxes that contained giants). The results are shown in Table 5.16, and are only significant for [Fe I/H] and [Fe II/H], though both are $\lesssim 0.07$ dex.

5.4 Partially Resolved GCs

The tests on HRD abundances (Chapter 5.2) show that the uncertainties in HB, AGB, RGB, and lower MS stars can be prohibitively large even without considering the errors from Chapter 5.3, with uncertainties as high as 0.4 dex in [Fe I/H] and [Ti I/Fe I], 0.3 dex in [Ba II/Fe II], 0.2 dex in [Fe II/H], and 0.1 dex in [Ca I/Fe I], [Ti II/Fe II], and [Ni I/Fe I] (depending on the cluster). Thankfully, observations of nearby clusters outside of the Milky Way and its dwarf satellite systems can provide photometry of the brightest stars in a cluster; the HB morphology, AGB prescription, etc. can then be characterized, eliminating or reducing many of these uncertainties. However, even with partial photometry, stars fainter than the HB still contribute a significant amount of light to the IL spectra. Furthermore, stars in cluster *cores* may not be resolvable. Given the large errors associated with sampling uncertainties, it may be preferable to model the stellar populations with stellar isochrones that can be refined based on the resolved photometry. This section investigates the effects of combining observations of the upper CMD with models of the lower HRD.

The [Fe/H] of a partially resolved cluster can be estimated through comparisons with Galactic GC fiducials (e.g. Mackey et al. 2013b). The [Fe/H] of the input isochrone can then be refined based on the output from `ILABUNDS`, as for completely unresolved clusters. Furthermore, a partially resolved GC's age can be very roughly constrained from the upper CMD (i.e. extended RGBs imply that the cluster must be older than $\sim 2-3$ Gyr). Here the spectroscopically-determined HRDs are found for all target GCs, adopting the criterion that the isochrone must fit the "observed portion" of the CMD (taken to be the portion down to the bottom of the HB). Initially, the best-fitting [Fe/H] values from the BaSTI isochrones (see Chapter 4.7) were chosen, since they fit the upper RGBs well (see Figure 5.4). Synthetic HBs were selected to best match the observed HB. The isochrones were populated and the default HBs were replaced with the synthetic ones. `ILABUNDS` was then rerun on the new stellar populations.

The parameters of the best spectroscopically-determined BaSTI isochrones are shown in Table 5.17. The [Z/H] values are in reasonable agreement with literature values, given the large spacings in the BaSTI grid. However, some of the cluster ages are not in agreement with Dotter et al. (2010, 2011) or VandenBerg et al. (2013) and Leaman et al. (2013); however, these tests have shown that the spectral lines in the $5300 - 7300\mathring{A}$ region are not very sensitive to age, and suggest that for old GCs the

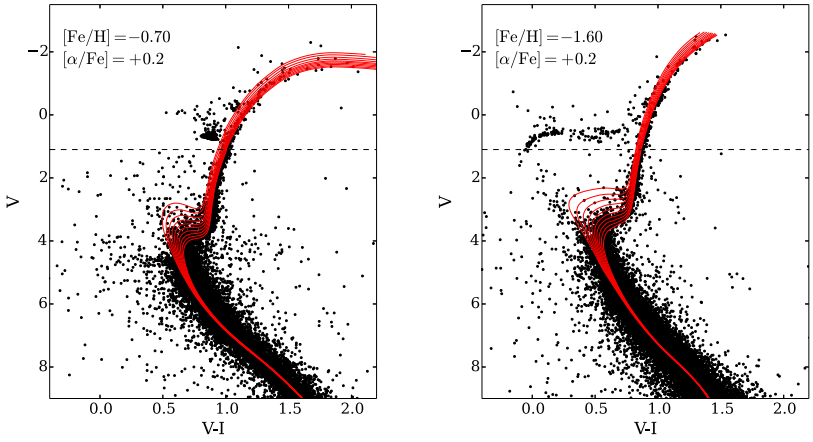

(a) 47 Tuc (b) M3

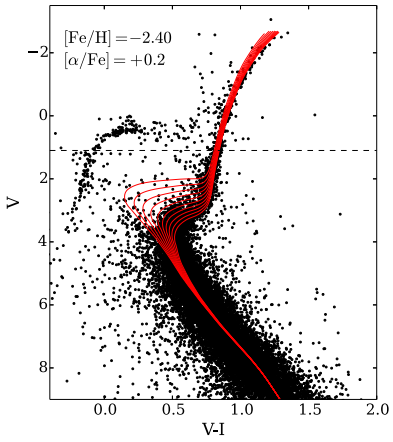

(c) M15

Figure 5.4: Examples of isochrones that might be used in an analysis of a partially resolved cluster. Here it is assumed that the GCs can only be observed to just below the HB, i.e. to the dashed line. The isochrones are from the DSED (Dotter et al., 2008) and have ages of 5, 6, 7, 8, 9, 10, 11, 12, 13, and 14 Gyr.

Table 5.17: Abundance differences for partially resolved clusters.

	Age (Gyr)	[Z/H]	Δ[X/H] Fe I	Fe II	Δ[X/Fe] Ca I	Ti I	Ti II	Ni I	Ba II	Eu II
47 Tuc	11	-0.35	**+0.09**	**+0.17**	**−0.06**	**−0.12**	0.0	+0.03	−0.04	**−0.08**
M3	13	-1.27	−0.04	**−0.15**	+0.04	−0.03	+0.02	**−0.06**	−0.03	−0.01
M13	13	-1.27	**−0.05**	**−0.12**	**+0.06**	−0.04	−0.03	**−0.05**	**−0.07**	−0.04
NGC7006	10	-1.27	+0.04	**+0.08**	+0.03	**−0.11**	**+0.09**	**−0.08**	+0.04	**−0.07**
M15	10	-1.79	0.0	**+0.06**	+0.01	−0.03	+0.01	−0.03	+0.02	−0.01

Notes: Abundance differences are calculated relative to the baseline abundances in Tables 4.5, 4.7, and 4.10.

ages cannot be constrained to less than $\sim 2-3$ Gyr in the partially resolved case. Considering these errors, the derived ages do agree with literature values.

The differences from the CMD-based abundances are shown in Table 5.17. All GCs converge on isochrone ages that agree slightly better with results from resolved photometry. For M3, M13, NGC 7006, and M15 (whose HB's were not modelled accurately with the default isochrones), the addition of synthesized HBs has brought many of the abundances into better agreement with the CMD-based ones. For 47 Tuc, however, the synthetic HBs introduce larger discrepancies with the CMD-based values, suggesting that for red HB GCs the default BaSTI HBs are likely to be sufficient. NGC 7006's [Ti I/Fe I] ratio remains discrepant, suggesting that the population is still not perfectly modelled.

Note that for nearby extragalactic clusters the *faint* detection limit will be just below the HB, and the photometric uncertainties will be much larger than in Figure 5.4. This means it will not be as easy to constrain the best-fitting metallicities from the CMDs. However, even if incorrect isochrone metallicities are chosen for these GCs, the abundances converge back on reasonable metallicities for the Galactic GCs.

5.5 Discussion

IL spectral analyses provide chemical abundances for individual GCs; *high resolution* IL spectroscopy is particularly well-suited for *chemical tagging* (see Chapter 1.3.6). In the MW, detailed abundances and kinematic info can link together individual stars and GCs that were accreted from the same dwarf galaxy. Due to the nature of IL analyses, it may not be possible to link GCs to specific streams—however, it should be possible to separate dwarf-associated GCs from those that formed in a massive galaxy. Chemically distinct GCs can only be identified if the abundance ratios are sufficiently robust to systematic uncertainties, ideally within 0.1 dex.[9] This section summarizes the accuracy of each abundance ratio and discusses implications for future extragalactic studies.

5.5.1 Summary of Results: Abundance Accuracy

Table 5.18 provides a summary of the largest effects on the chemical abundance ratios, based on the tests described in Chapters 5.1 through 5.3. Many of the uncertainties vary between clusters as a result of, e.g., metallicity or HB effects. The accuracy of the individual abundance ratios are discussed in detail below. The results presented here are dependent upon the observed lines, and may vary if different wavelength regions are observed.

[Fe/H]

In CMD-based analyses, the largest systematic uncertainties in [Fe I/H] and [Fe II/H] are ~ 0.1 and ~ 0.2 dex, respectively,[10] for all GCs. The potential HRD-based offsets are much larger, up to $\sim 0.1 - 0.4$ dex (depending on the GC) for [Fe I/H] and $\sim 0.2 - 0.3$ dex for [Fe II/H]. The HRD-based offsets are lowest for 47 Tuc, suggesting that red HB, metal-rich GCs may have smaller systematic offsets in HRD-based [Fe/H] ratios.

The [Fe I/H] ratio is particularly sensitive to:

1. Sampling of input photometry

[9] For instance, Milky Way halo stars at [Fe/H] $\lesssim -1$ have [α/Fe] $= +0.3$, while dwarf galaxy stars at similar metallicity have [α/Fe] ~ 0 (see Chapters 1.3.6 and 3). For a 3σ confirmation that a GC is chemically more like a dwarf galaxy, useful ratios should have systematic errors $\lesssim 0.1$ dex.

[10] The clear offset in the V, I Alonso et al. 1996, 1999 colour-temperature relations has been neglected.

Table 5.18: Summary of results.

	Δ[X/H]		Δ[X/Fe]						
	Fe I	Fe II	Ca I	Ti I	Ti II	Ni I	Ba II	Eu II	Δ[Ba/Eu]
CMD-based analyses									
Minimum errors[a]	**≤0.12**	**≤0.20**	**≤0.06**	**≤0.09**	**≤0.14**	≤0.04	**≤0.22**	**≤0.11**	**≤0.17**
CTRs[a,b]	**≤0.07**	≤0.01	≤0.02	≤0.03	≤0.03	≤0.04	**≤0.06**	≤0.04	≤0.04
Input photometry	≤0.04	**≤0.07**	≤0.02	≤0.04	≤0.04	≤0.01	**≤0.07**	≤0.02	**≤0.06**
Incompleteness	**≤0.07**	**≤0.07**	**≤0.05**	**≤0.06**	**≤0.07**	**≤0.04**	**≤0.07**	≤0.03	≤0.04
Sampling[c,d]	**≤0.22**	**≤0.10**	**≤0.09**	–	**≤0.10**	≤0.03	**≤0.21**	**≤0.09**	**≤0.14**
HRD-based analyses									
HRD vs. CMD[a]	**≤0.11**	**≤0.19**	**≤0.05**	**≤0.20**	**≤0.10**	≤0.04	**≤0.12**	**≤0.08**	**≤0.10**
Age/[Fe/H] Errors[a]	**≤0.16**	**≤0.16**	**≤0.07**	**≤0.12**	**≤0.10**	≤0.04	**≤0.19**	**≤0.08**	**≤0.10**
Diff. Isochrones	≤0.02	≤0.04	≤0.02	≤0.02	≤0.01	0.0	≤0.03	≤0.01	≤ 0.02
IMF	≤0.04	≤0.01	≤0.02	**≤0.06**	**≤0.05**	≤0.02	**≤0.07**	**≤0.05**	≤0.02
Cluster M_V^e	**≤0.36**	**≤0.10**	**≤0.10**	**≤0.41**	**≤0.14**	**≤0.10**	**≤0.33**	**≤0.23**	**≤0.10**
HB morphology[a]	**≤0.13**	**≤0.28**	≤0.04	**≤0.17**	**≤0.08**	**≤0.07**	**≤0.14**	**≤0.11**	**≤0.12**
AGB prescription	**≤0.19**	**≤0.15**	**≤0.05**	**≤0.23**	**≤0.09**	**≤0.13**	**≤0.19**	**≤0.14**	**≤0.07**
Blue stragglers	**≤0.07**	**≤0.07**	≤0.02	≤0.04	≤0.04	≤0.03	**≤0.05**	**≤0.06**	≤0.02
Low mass cutoff[a]	**≤0.13**	**≤0.12**	≤0.04	**≤0.24**	**≤0.07**	**≤0.05**	**≤0.11**	**≤0.12**	**≤0.05**
All analyses									
CMD/HRD Boxes	≤0.02	≤0.01	≤0.02	≤0.03	≤0.04	≤0.03	≤0.01	**≤0.07**	≤0.04
Microturbulence	**≤0.11**	**≤0.05**	≤0.03	≤0.02	**≤0.08**	**≤0.10**	**≤0.16**	≤0.04	**≤0.16**
LPVs	≤0.01	**≤0.07**	0.0	≤0.03	≤0.01	≤0.03	0.0	0.0	0.0
CH stars[a,d]	0.0	0.0	≤0.01	0.0	0.0	≤0.01	0.0	≤0.01	≤0.01
Hot stars	**≤0.06**	≤0.04	≤0.01	≤0.01	**≤0.07**	≤0.03	≤0.04	≤0.04	**≤0.08**
Field stars[d]	**≤0.10**	**≤0.09**	**≤0.09**	≤0.04	**≤0.07**	**≤0.06**	**≤0.10**	**≤0.05**	**≤0.09**
ODFNEW Atms	**≤0.05**	**≤0.12**	≤0.03	≤0.02	≤0.03	≤0.02	≤0.03	≤0.03	≤0.03
CN-cycled Atms	**≤0.05**	**≤0.12**	≤0.03	≤0.02	≤0.03	≤0.02	≤0.03	≤0.03	≤0.03

Notes: These upper limits are the largest uncertainties that occurred in all tests, and will likely not apply to all target GCs in the same way.

[a] Metallicity/cluster dependent result.

[b] The V, I errors with the Alonso et al. (1996, 1999) relations are not considered here; see the text.

[c] These error estimates are specific to M15's wedge shaped pointing pattern, and are likely to be much higher than would be expected for any extragalactic targets.

[d] Recall that these error estimates consider the worst case scenario.

[e] These large uncertainties arise in faint clusters due to stochastic sampling of the brightest stars, and should be mitigated by using fractional numbers of stars.

2. The usage of isochrones instead of resolved photometry

3. Uncertainties in isochrone parameters

4. Models of the AGB

5. Microturbulence variations in the brightest stars

6. The inclusion of bright field stars.

With well-sampled IL spectra and photometry that extends at least to the HB, the uncertainties in the parameters of the brightest stars are reduced, and the individual systematic offsets should be ~ 0.1 dex.

The [Fe II/H] ratio is strongly affected by bright RGB stars, AGB and HB stars, hot stars, and model atmosphere chemistries. The offsets tend to be larger for [Fe II/H] than [Fe I/H], and the systematic errors in [Fe II/H] remain ~ 0.2 dex, even with partially resolved photometry. This further confirms the suggestion by Colucci et al. (2009) that forcing the [Fe I/H] and [Fe II/H] solutions to be equal will not lead to more accurate isochrone solutions.

[Ca/Fe] and [Ti/Fe]

The *largest* [Ca I/Fe I] offsets are ~ 0.1 dex, and are due to

1. Sampling of the brightest stars

2. Uncertainties in isochrone parameters

3. Treatment of the AGB

4. The inclusion of bright field stars.

These results indicate that [Ca I/Fe I] is most affected by the numbers and properties of the bright RGB stars. For the wavelength regions examined here the [Ca I/Fe I] ratio is largely insensitive to the properties of hot stars. With partially resolved GCs and well-sampled IL spectra, the systematic errors in [Ca I/Fe I] should be reduced to $\lesssim 0.1$ dex, depending on GC metallicity.

The [Ti I/Fe I] and [Ti II/Fe II] ratios, on the other hand, are very sensitive to uncertainties in the underlying stellar population, with offsets of as much as ~ 0.2 dex. Like calcium, [Ti I/Fe I] is sensitive to the numbers and properties of the

brightest RGB stars. Ti I is particularly affected in HRD-based analyses: in the initial comparisons with CMD-based abundances, [Ti I/Fe I] is persistently lower than individual stellar values by $\sim 0.1 - 0.2$ dex (see Chapter 5.2.1). When uncertainties in HB morphology and AGB prescription are considered, [Ti I/Fe I] could therefore be uncertain by as much as $0.2 - 0.4$ dex when isochrones are used. In most tests, the [Ti II/Fe II] uncertainties are typically constrained only to within 0.15 dex.

[Ni/Fe]

Since Ni is an iron-peak element with an atomic structure similar to Fe, it is not surprising that the [Ni I/Fe I] is relatively stable to uncertainties in atmospheric parameters—for all tests and GCs, the *highest* systematic uncertainties in [Ni I/Fe I] are only ~ 0.1 dex. Nickel appears to be sensitive to both high and low mass stars, given that it is most affected by:

1. Sampling when the total cluster magnitude is adjusted
2. AGB prescription
3. The HRD low mass cutoff
4. The presence of field stars.

Despite these sensitivities, however, in general [Ni I/Fe I] is quite robust in both CMD- and HRD-based analyses. With a well-modelled stellar population, the systematic errors in [Ni I/Fe I] approach ~ 0.05 dex.

[Ba/Fe] and [Eu/Fe]

Both [Ba II/Fe II] and [Eu II/Fe II] are particularly sensitive to uncertainties in the underlying population, often in similar ways. In CMD-based analyses, [Ba II/Fe II] and [Eu II/Fe II] can be constrained to ~ 0.2 and ~ 0.1 dex, respectively, for all GCs. The offsets are higher in HRD-based analyses (up to ~ 0.3 and ~ 0.2, respectively).

Both Ba II and Eu II are sensitive to uncertainties in the brightest RGB stars and red/intermediate HB stars. The strongest effects are caused by:

1. Temperature and microturbulence uncertainties, including various microturbulence relations

2. Sampling of the brightest stars, whether from uncertain input photometry or from rounding errors in faint clusters

3. Isochrone age

4. AGB prescription.

In all clusters, the Ba II and Eu II abundances are insensitive to completeness of the lower main sequence, isochrone offsets, atmospheric [α/Fe], and properties of the blue HB stars.

When Ba and Eu are affected in similar ways, the uncertainties in [Ba/Eu] can be smaller than the individual uncertainties in Ba and Eu. This is true for, e.g., uncertainties in the AGB prescription, the total cluster magnitude, and the lower mass cutoff. Thus, in an HRD analysis [Ba/Eu] may have lower systematic errors than the individual [Ba II/Fe II] and [Eu II/Fe II] ratios.

5.5.2 High Resolution vs. Lower Resolution Analyses

High resolution ($R \gtrsim 20,000$) IL spectral analyses provide two major advantages over lower resolution studies.

1. More lines can be detected and resolved in a high resolution spectrum. With more independent measurements, the random errors in individual elemental abundances can be reduced.

2. Weaker features can be detected in high resolution IL spectra, enabling abundances to be obtained for more elements.

Despite these advantages, it requires more observing time to obtain high resolution IL spectra of a sufficient S/N, and a smaller wavelength region may have to be analyzed. This paper has shown that despite the increased precision offered by high resolution IL spectroscopy, the low accuracy in integrated abundances may render such sharp resolution unnecessary, depending on the science goals.

The cluster metallicity, [Fe/H], is an excellent example for when high resolution may be unnecessary. Although high resolution IL spectroscopy can reduce random errors in [Fe I/H] to $\sim$ 0.02 dex (depending on the S/N), the systematic errors can be as large as $\sim 0.1 - 0.4$ dex depending on the analysis type, cluster metallicity, etc. Thus, for studies that focus only on [Fe/H] (such as studies of population averages,

bimodalities, or gradients, e.g. Caldwell et al. 2011) the increased precision of high resolution offers no benefit. Similarly, for studies of large samples of GCs where the abundances are averaged together, high resolution provides no clear advantage (for example average values in certain galaxy types or abundance correlations with GC properties, e.g. Puzia et al. 2008; Schiavon et al. 2013).

Furthermore, access to wider wavelength coverage (e.g. into the blue) would provide additional diagnostics to constrain age and HB morphology. Given that the V, I CMDs are primarily sensitive to age only at the MS turnoff, it is not surprising that Fe I spectral lines in the optical are not very sensitive to cluster age. Even in the partially resolved case, the derived ages do not exactly agree with high precision analyses of resolved CMDs. This suggests that age cannot be well constrained with high resolution IL spectral analyses in this wavelength region, at least for old GCs. However, many of the derived abundances are not strongly affected by the isochrone age, and this uncertainty does not have a significant effect on the elements studied here. The intermediate and red HBs have potentially strong effects on the optical spectral lines, though it is still difficult to disentangle these effects from age differences. Access to the Balmer lines (e.g. Schiavon et al. 2004) or singly ionized features like the Ca II Ha and K lines (Percival & Salaris, 2011) would help constrain the HB morphology of unresolved systems. Thus, age and HB morphology determinations would likely best be completed over a wider wavelength range, even if it means sacrificing resolution.

The strength of high resolution IL spectroscopy is its ability to provide accurate abundances for individual clusters. High resolution is therefore essential for examining the detailed chemical abundances of GCs, e.g. for chemical tagging studies.

5.5.3 Optimal Abundance Ratios for Chemical Tagging

Based on the offsets presented in Table 5.18 and the discussion in Section 5.5.1, certain element ratios are more useful for chemical tagging purposes.

[Fe/H]: Most chemical comparisons require knowledge of the GC metallicity, [Fe/H]. Though the [Fe I/H] ratio can occasionally have large systematic errors, [Fe II/H] consistently also has large offsets, as well as larger statistical errors (because there are fewer Fe II lines). Therefore, in most cases, [Fe I/H] will be the preferable choice to represent the cluster metallicity.

[Ca/Fe]: The [α/Fe] ratio is particularly useful for chemical tagging of dwarf galaxy stars and GCs (see, e.g., Venn et al. 2004; Pritzl et al. 2005), where Ca and Ti have both been used as α-indicators in individual stellar analyses. (Though note that the behaviour of Ca and Ti is very different from other α-elements like O and Mg.) Given that [Ca I/Fe I] is very stable to uncertainties in the underlying stellar population for all GCs considered here, [Ca I/Fe I] is preferable to [Ti I/Fe I] or [Ti II/Fe II] for probing the [α/Fe] ratios of extra-galactic systems.

[Ni/Fe]: The [Ni/Fe] ratio may be useful for identifying chemically peculiar GCs. In particular, Pal 12 and Ter 7, the two metal-rich GCs that were accreted from the Sagittarius dwarf galaxy, are underabundant in [Ni/Fe] like the Sgr field stars (Cohen, 2004; Sbordone et al., 2005b, 2007). The integrated [Ni I/Fe I] ratios are generally quite stable to abundance uncertainties, and may therefore prove to be useful for integrated chemical tagging.

[Ba/Fe], [Eu/Fe], [Ba/Eu]: Ba and Eu both form through neutron captures onto iron-peak atoms. In the Sun, 97% of Eu forms from rapid neutron captures (the r-process) while 85% of Ba forms from the s-process (Burris et al., 2000). The nucleosynthetic sites for the two elements (and Fe) therefore differ, and the [Ba/Fe], [Eu/Fe], and [Ba/Eu] ratios differ between stars in the Milky Way and those in dwarf galaxies (see Chapter 5.5.3). Though the systematic uncertainties in [Ba II/Fe II], [Eu II/Fe II], and [Ba II/Eu II] are quite large for all GCs, taken together the three ratios could still prove useful for chemical tagging since all three ratios are unlikely to have simultaneously large offsets.

5.5.4 CMD- vs. HRD-based Analyses

Chapter 5.2.1 indicates that systematic offsets may occur between CMD-based and HRD-based analyses, since the best-fitting HRD-based abundances are not always in agreement with those from a CMD-based analysis (see Table 4.12), with differences up to 0.2 dex. These differences can be larger than the uncertainties from identifying the best isochrone (i.e. the offsets in Table 4.12 are sometimes larger than the uncertainties in Table 5.5). These offsets are likely due to discrepancies between the input isochrone and the true stellar populations—for example, changing the HB morphology can bring [Ti I/Fe I] back into agreement with the CMD-based ratio. However, the necessary alterations to the input isochrones may not be identifiable for unresolved GCs, particularly if the IL spectra are noisy.[11]

Table 5.18 indicates that if sampling problems are reduced or eliminated then CMD-based chemical abundances are more accurate than HRD-based abundances. This result is driven by the uncertainties in modelling the most evolved stars, notably the tip of the RGB, HB, and AGB stars. However, this approach is not currently feasible for extragalactic targets, for which IL methods are necessary.

Chapter 5.4 demonstrates that some of the HRD-based offsets disappear when CMDs of the brightest stars are combined with isochrones. This is important for IL analyses of nearby extragalactic GC systems, e.g. GCs in M31 (Mackey et al., 2007, 2013b), particularly if those GCs have blue or intermediate HBs. Thus, if accurate and uncontaminated CMDs can be obtained for the brightest stars in a GC, the systematic errors in integrated abundances can be reduced.

5.5.5 A Case Study: Partially Resolved Clusters in M31

To illustrate how the results of this paper can be applied to IL studies, Table 5.19 summarizes the systematic errors for the target clusters *if spectra of this quality were obtained from GCs in M31* and if those GCs had partially resolved *HST* photometry. The partially resolved CMDs would constrain the [Fe/H], HB morphology, AGB prescription, total observed magnitude, and the presence of severely different interloping field stars. The ideal science case would be to perform a chemical tagging analysis on these clusters. Table 5.19 therefore only shows the systematic uncertainties in the optimal abundance ratios for chemical tagging: [Fe I/H], [Ca I/Fe I], [Ni I/Fe I],

[11]Noisy IL spectra will lead to a larger dispersion in line-to-line Fe I abundances. A larger dispersion will then complicate the process of minimizing trends with wavelength, REW, and EP.

[Ba II/Fe II], [Eu II/Fe II], and [Ba II/Eu II]. It is not clear how to combine these errors in a meaningful way—however, if the errors are assumed to be independent then they can be conservatively added together in quadrature (though this may overestimate the errors). These total systematic errors are also shown in Table 5.19.

As an additional illustration of these errors, the cluster [Ca/Fe] and [Ba/Eu] abundances from Chapter 4 are compared to MW and dwarf galaxy abundances in Figure 5.5, *using the partially resolved systematic errors from Table 5.19*. The error bars show the total random *and* systematic errors, combined in quadrature. Note that though 47 Tuc has a high [Ba/Eu], it is still consistent with the MW field stars. M15's low [Ba/Eu] ratio is likely due to the star-to-star variations within the massive cluster (see Chapter 4.5.3). With the systematic errors included these Galactic targets would appear consistent with the Galactic field stars, even if they were located at M31's distance. Similarly, GCs associated with dwarf galaxies could be distinguished, even with systematic errors considered, if they are α-deficient and/or [Ba/Eu]-enhanced.

Table 5.19: Summary of errors for partially resolved clusters at the distance of M31.

		Δ[X/H]	Δ[X/Fe]				Δ[Ba/Eu]
		Fe I	Ca I	Ni I	Ba II	Eu II	
47 Tuc	Partially Resolved Errors	0.09	0.06	0.03	0.04	0.08	0.04
	Different Isochrones	0.03	0.01	0.01	0.03	0.02	0.02
	IMF	0.04	0.02	0.02	0.07	0.05	0.02
	Blue Stragglers	0.02	0.0	0.01	0.01	0.01	0.0
	Low Mass Cutoff	0.05	0.04	0.05	0.09	0.12	0.03
	Microturbulence Relations	0.07	0.01	0.0	0.0	0.04	0.04
	LPVs	0.01	0.0	0.03	0.0	0.0	0.0
	Field Stars	0.09	0.09	0.06	0.10	0.05	0.05
	α-enhanced atmospheres	0.05	0.03	0.01	0.01	0.02	0.01
	Total[a]	0.17	0.12	0.09	0.16	0.17	0.09
M3	Partially Resolved Errors	0.04	0.04	0.06	0.03	0.01	0.02
	Different Isochrones	0.05	0.02	0.03	0.06	0.03	0.03
	IMF	0.02	0.0	0.01	0.02	0.02	0.0
	Blue Stragglers	0.02	0.0	0.01	0.03	0.06	0.03
	Low Mass Cutoff	0.10	0.02	0.04	0.11	0.10	0.01
	Microturbulence Relations	0.04	0.01	0.0	0.01	0.0	0.01
	Field Stars	0.04	0.0	0.01	0.03	0.04	0.01
	α-enhanced atmospheres	0.0	0.01	0.02	0.02	0.01	0.01
	Total[a]	0.13	0.05	0.08	0.14	0.13	0.05
M13	Partially Resolved Errors	0.05	0.06	0.05	0.07	0.02	0.05
	Different Isochrones	0.05	0.02	0.03	0.06	0.03	0.03
	IMF	0.02	0.0	0.01	0.02	0.02	0.0
	Blue Stragglers	0.03	0.02	0.02	0.03	0.03	0.0
	Low Mass Cutoff	0.10	0.01	0.01	0.07	0.08	0.01
	Microturbulence Relations	0.04	0.01	0.0	0.01	0.0	0.01
	Hot Stars	0.06	0.01	0.03	0.04	0.04	0.08
	Field Stars	0.04	0.0	0.01	0.03	0.04	0.01
	α-enhanced atmospheres	0.0	0.01	0.02	0.02	0.01	0.01
	Total[a]	0.15	0.07	0.07	0.13	0.11	0.06
NGC7006	Partially Resolved Errors	0.04	0.03	0.08	0.04	0.07	0.11
	Different Isochrones	0.05	0.02	0.03	0.06	0.03	0.03
	IMF	0.02	0.0	0.01	0.02	0.02	0.0
	Blue Stragglers	0.02	0.01	0.01	0.02	0.0	0.02
	Low Mass Cutoff	0.09	0.0	0.05	0.08	0.09	0.01
	Microturbulence Relations	0.04	0.01	0.0	0.01	0.0	0.01
	Field Stars	0.04	0.0	0.01	0.03	0.04	0.01
	α-enhanced atmospheres	0.0	0.0	0.01	0.03	0.03	0.0
	Total[a]	0.13	0.04	0.10	0.12	0.13	0.12
M15	Partially Resolved Errors	0.0	0.01	0.03	0.02	0.01	0.03
	Different Isochrones	0.05	0.02	0.02	0.05	0.04	0.02
	IMF	0.03	0.01	0.02	0.02	0.02	0.02
	Blue Stragglers	0.07	0.02	0.03	0.05	0.01	0.04
	Low Mass Cutoff	0.13	0.04	0.01	0.11	0.05	0.06
	Microturbulence Relations	0.05	0.01	0.03	0.02	0.03	0.0
	Hot Stars	0.06	0.01	0.03	0.04	0.04	0.08
	Field Stars	0.10	0.04	0.03	0.07	0.04	0.03
	α-enhanced atmospheres	0.02	0.0	0.01	0.0	0.03	0.03
	Total[a]	0.20	0.07	0.07	0.16	0.10	0.12

[a] Total errors are conservatively estimated by adding the other errors in quadrature.

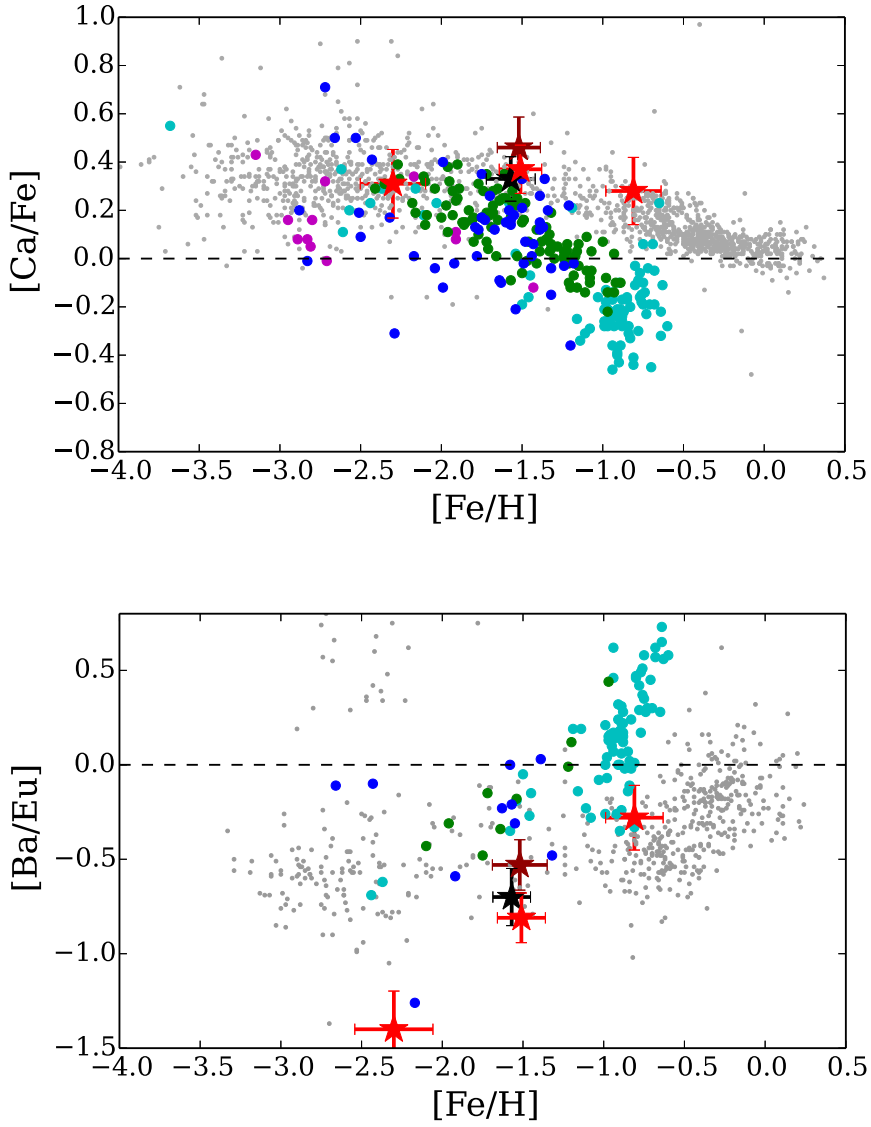

Figure 5.5: Chemical comparisons between Galactic and dwarf galaxy stars. The integrated abundances from the target GCs are shown with red stars for 47 Tuc, M3, and M15, with a black star for M13, and with a maroon star for NGC 7006. The error bars are the systematic *and* random errors (added in quadrature), assuming the GCs were partially resolved at the distance of M31 (see Table 5.19). The grey points are Milky Way stars. The cyan, green, blue, and magenta points are Fornax, Sculptor, Carina, and Sextans stars, respectively. All points are from the compilation assembled by Venn et al. (2012). This comparison shows that, even including the systematic errors, individual GCs can be chemically tagged based on their integrated abundances, provided that their abundances are distinct from the Milky Way stars.

5.6 Conclusions

This chapter presents a detailed investigation of the systematic uncertainties in high-resolution integrated abundance analyses that occur when GC stellar populations are modelled. High resolution IL spectra (covering $\sim 5320 - 7340$ Å) of the Galactic GCs 47 Tuc, M3, M13, NGC 7006, and M15 were combined with *HST* photometry and theoretical isochrones to investigate abundance accuracies over a wide range in metallicity and HB morphology. The stability of Fe, Ca, Ti, Ni, Ba, and Eu abundances is determined through IL analyses and various alterations to the underlying stellar population.

The tests in this paper show that:

1. The accuracy in integrated abundances can approach that of individual stellar analyses *if the stellar population is well-modelled.* The minimum systematic errors in the abundance ratios are $\lesssim 0.05$ dex in [Ca I/Fe I] and [Ni I/Fe I]; $\lesssim 0.1$ dex in [Fe II/H], [Ti I/Fe I], [Ti II/Fe II], and [Eu II/Fe II]; and $\lesssim 0.2$ dex in [Fe I/H] and [Ba II/Fe II].

2. CMD-based analyses are most sensitive to inaccuracies in the input photometry, both due to sampling of the brightest stars and incompleteness in the low mass stars. In the worst case scenario, the accuracy in integrated CMD-based abundances is $\lesssim 0.1$ dex in [Fe II/H], [Ca I/Fe I], [Ti I/Fe I], [Ti II/Fe II], [Ni I/Fe I], and [Eu II/Fe II], and $\lesssim 0.2$ dex in [Fe I/H] and [Ba II/Fe II]. It is therefore important to obtain symmetric, well-sampled IL spectra of the target GCs.

3. HRD-based analyses are highly sensitive to sampling of the highest and lowest mass stars, AGB prescription, and HB morphology. The uncertainties can be as high as $\lesssim 0.1$ dex in [Ca I/Fe I], [Ti II/Fe II], and [Ni I/Fe I]; $\lesssim 0.2$ dex in [Eu II/Fe II]; $\lesssim 0.3$ dex in [Fe II/H] and [Ba II/Fe II]; and $\lesssim 0.4$ dex in [Fe I/H] and [Ti I/Fe I].

These results have several important implications for IL analyses of extragalactic GCs in distant systems, for both analysis methods.

1. Certain abundance ratios are less sensitive to systematic uncertainties and are therefore more useful for chemical tagging studies.

- The [Fe I/H] ratio should serve as the best [Fe/H] indicator.
- The [Ca I/Fe I] ratio is an excellent [α/Fe] indicator.
- The [Ni I/Fe I] ratios are very stable to uncertainties
- Individually, [Ba II/Fe II], [Eu II/Fe II], and [Ba II/Eu II] have large systematic uncertainties. Together, however, the three ratios may prove useful for chemical tagging.

2. HRD-based abundances may be systematically offset from CMD-based abundances, making comparisons between studies/clusters difficult.

3. CMDs of only the brightest stars in a GC can be used to constrain properties of evolved stars, providing more accurate chemical abundance ratios in GCs with blue or intermediate HBs.

4. In an HRD-based analysis, high resolution does not provide an advantage for certain abundance ratios, such as [Fe/H]. Lower resolution ($R \lesssim 6500$) IL spectroscopy appears to be sufficient for [Fe/H] determinations, investigations of [Fe/H] distributions, and studies with large sample sizes. Lower resolution spectroscopy may also be crucial for providing constraints on age and HB morphology.

Chapter 6

Integrated Chemical Abundances of Outer Halo M31 Clusters from the Pan-Andromeda Archaeological Survey

Chapters 4 and 5 established the validity of high resolution spectroscopic techniques and identified the chemical abundance ratios that are least sensitive to uncertainties in the underlying stellar populations. These techniques can now be safely applied to extragalactic systems, particularly if the systems can be partially resolved. The extragalactic targets examined in this thesis are GCs that were discovered in PAndAS, as described in Chapter 2.1.3.

6.1 M31's Outer Halo

Previous studies of M31's outer halo have provided a substantial amount of information about its current stellar populations and assembly history. These studies have focused on photometric and low resolution spectroscopic observations of the field stars, the dwarf galaxies, the globular clusters, and the gas located at projected distances from the centre of M31 $\gtrsim$ 30 kpc. As discussed in Chapter 2.1.3, the coherent substructure in its outer halo implies that M31 has experienced a significant amount of accretion from satellite galaxies. This section summarizes the evidence for those conclusions and for the possible nature of the dwarf progenitors.

The PAndAS stellar density maps (e.g. Figure 2.2) provide a wealth of information about the structure of the outer halo and the stellar populations that reside there. Metallicities can be estimated for the individual field stars based on their positions in a CMD—by assuming that all the stars lie at the same distance and have the same foreground reddening, a star's metallicity can be approximated based on its proximity to an isochrone of a given metallicity. Ibata et al. (2014) provide maps for various metallicity cuts. They show that there are a multitude of streams, plumes, and clouds of metal-poor stars, along with a significant metal-rich population that is mostly located in the Giant Stellar Stream (GSS) south of M31. They further estimate that $\sim 42\%$ of the most metal-poor stars ([Fe/H] < -1.7) lie in coherent streams or clumps—the percentage of stars in streams rises with metallicity, increasing to $\sim 86\%$ for [Fe/H] > -0.6. The rest of the outer halo stars are distributed in "smooth" components.

Both streams and a smooth halo are expected signs of accretion. The morphology of any debris and/or dwarf satellite remnants will depend on when the galaxies were accreted. Through simulations of MW-sized halos, Johnston et al. (2008) show that well mixed, smooth components result from early accretions of satellites on nearly circular orbits, while streams, clouds, plumes, and shells result from more recent accretion or accretion of dwarfs on more eccentric orbits. Peñarrubia (2013) also demonstrate that accretion induces changes in the galactic potential that speed up dissipation of any stellar streams. Thus, the smooth components are consistent with ancient accretion, though the presence of streams indicates that a significant amount of recent accretion has taken place in M31's outer halo.

Accretion of M31's *current* dwarf galaxy population would not lead to a large metal-rich population, as most of the dwarf satellites are too metal-poor (because they are low mass; see Richardson et al. 2011, Collins et al. 2013, Ibata et al. 2014, Vargas et al. 2014). The presence of a significant amount of metal-rich stars in coherent streams therefore implies that M31 has accreted at least one fairly massive galaxy, creating the GSS (Fardal et al., 2013). This assertion is also supported by the detection of H I gas near the GSS, which suggests that M31 merged with a fairly massive, gas-rich galaxy (Lewis et al., 2013). The southwest cloud (associated with GCs PA7 and PA8; Mackey et al. 2013b) also has gas (Lewis et al., 2013) and metal-rich stars ([Fe/H] ~ -1.3), and may be the remnants of another fairly massive dwarf (Bate et al., 2014). The other metal-poor streams are gas free, and are likely to be from lower mass dwarf spheroidals.

Of the ~ 60 GCs discovered in PAndAS, many appear to lie along stellar streams. Mackey et al. (2010) demonstrated that the positions of these GCs are correlated with the positions of the streams, with a $< 1\%$ chance that these GCs are located along the streams by chance. PA7 and PA8 appear to be kinematically associated with each other (Mackey et al., 2010) and with the SW Cloud (Bate et al., 2014). Veljanoski et al. (2013, 2014) have shown that many of the clustered GCs which appear to be spatially associated with streams appear to be kinematically associated with each other. Even the GCs that are not obviously associated with any streams seem to have unusual properties. Huxor et al. (2014) showed that M31 has an excess of both luminous and faint outer halo GCs, compared to the MW; they conclude that some of these unusual clusters are likely to have been accreted. Veljanoski et al. (2014) also showed that the entire GC system shows clear signs of rotation (which are seen in both the GCs associated with streams and those that are unassociated with streams). This rotation suggests either that 1) M31 experienced a merger with a galaxy large enough (e.g. LMC-sized) to bring in a significant number of GCs, or 2) that the dwarfs were accreted along a preferred direction. The latter option is certainly possible if the dwarfs were aligned along a dark matter filament and is supported by the observed "plane" of dwarf satellites (Ibata et al., 2013). The first possibility calls into question how other stellar streams remained undisturbed during the merger (although the accreted satellites could have been tidal dwarfs; see the discussion in Veljanoski et al. 2014).

Ultimately, the observations indicate that M31 has experienced a merger with at least one massive dwarf and multiple lower mass dwarfs. The observations of M31's outer halo GCs indicate that this accretion of dwarf satellites is also bringing new GCs into M31's outer halo. These hypotheses can be further tested with the detailed abundances of the outer halo GCs. Like Pal 1 (Chapter 3), the outer halo GCs should have different abundance patterns from MW field stars if they originated in lower mass dwarf galaxies.

As described in Chapter 2, the GCs in this thesis were selected based on 1) observability and 2) large projected distances from M31. Figure 6.1 shows how the target GCs compare to the entire M31 GC system, and to the outer halo GC system, as selected from the Revised Bologna Catalog (RBC; Galleti et al. 2004).[1] Only confirmed, old GCs were selected from the catalog, while the outer halo clusters are from Huxor et al. (2014). The magnitudes of the target Galactic GCs are also

[1] `http://www.bo.astro.it/M31/`

indicated. The M31 targets in this thesis are among the brightest objects in the outer halo; however, they are very similar to the Galactic GCs analyzed in Chapters 4 and 5. Note that no confirmed Pal 1 objects have been observed in M31.

6.2 HRDs

As in Chapter 4.1, the first step in an IL analysis is to determine the atmospheric parameters of the underlying populations. The PAndAS clusters are far enough away that the central regions of the GCs cannot be resolved, preventing high quality CMDs from being obtained for the regions scanned in the IL spectra. However, the stars in the outer regions can be resolved with *HST*, enabling constraints to be placed on [Fe/H] and HB morphology, as discussed in Chapter 5.4. Six of the seven M31 clusters in this thesis have *HST* CMDs of the outer regions; the other, PA17, only has integrated photometry to help constrain the properties of the cluster. The abundances of the Fe I lines (from the EWs in Appendix C) are then used to constrain the isochrone's single age and metallicity.

6.2.1 Partially Resolved CMDs

The CMDs for H10 and H23 were first presented in Mackey et al. (2007), while those for PA06, PA53, PA54, and PA56 will be presented in Mackey et al. (in prep.) Images and CMDs of the clusters are shown in Figures 6.2 through 6.7, along with synthetic HBs. Note that synthetic HBs were not used for the metal-rich, red HB GCs H10 and H23, given the results for 47 Tuc (see Chapter 5.4). The CMDs indicate that all GCs are more metal-poor than [Fe/H ~ -1, though most are more metal-poor than [Fe/H ~ -1.5 (as indicated by the slope of the RGB). For clusters with detectable RGB bumps (e.g. H10), the magnitude difference between the bump and the HB also indicate that the GCs are fairly metal-poor ([Fe/H $\lesssim -1.5$; see Alves & Sarajedini 1999).

The spectroscopically-determined isochrones are also shown in Figures 6.2 through 6.7. These isochrones were found by minimizing trends between Fe I abundances and line wavelength, REW, and EP, as in Chapter 4.7. These isochrones were *not* fit to the CMDs (other than the synthetic HBs)—detailed photometric analyses will be presented by Mackey et al. (in prep.). The parameters of the spectroscopically-determined, best-fitting isochrones are shown in Table 6.1. The trends in Fe I abun-

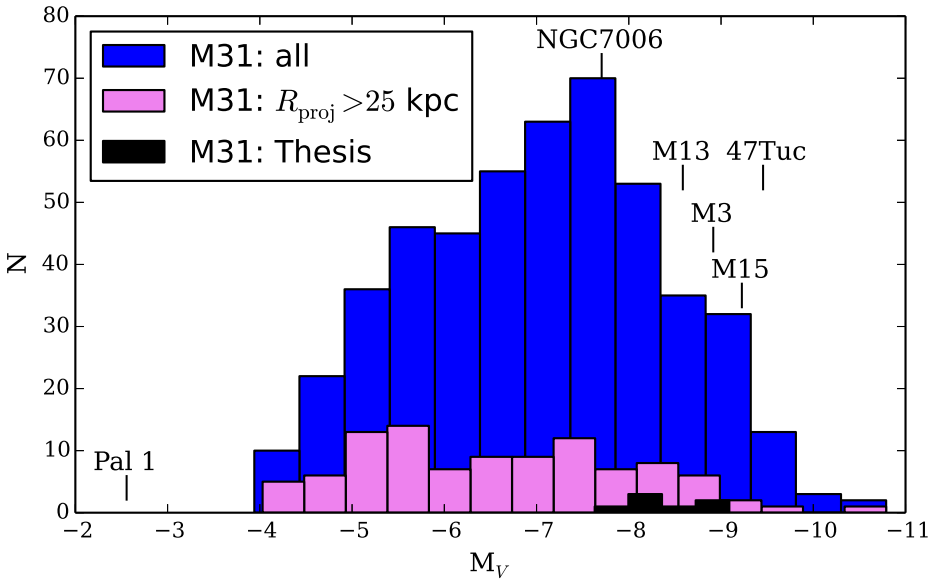

Figure 6.1: Numbers of M31 GCs at a given magnitude. The blue histogram shows all the confirmed, old GCs in the RBC. The magenta histogram shows the outer halo, confirmed GCs from Huxor et al. (2014). The thesis clusters are shown in black. The locations of the Galactic thesis targets are indicated. The M31 thesis sample consists of some of the brightest GCs in the outer halo, but the distribution agrees with the sample of Galactic GCs. Note that no confirmed Pal 1 objects have been observed in M31.

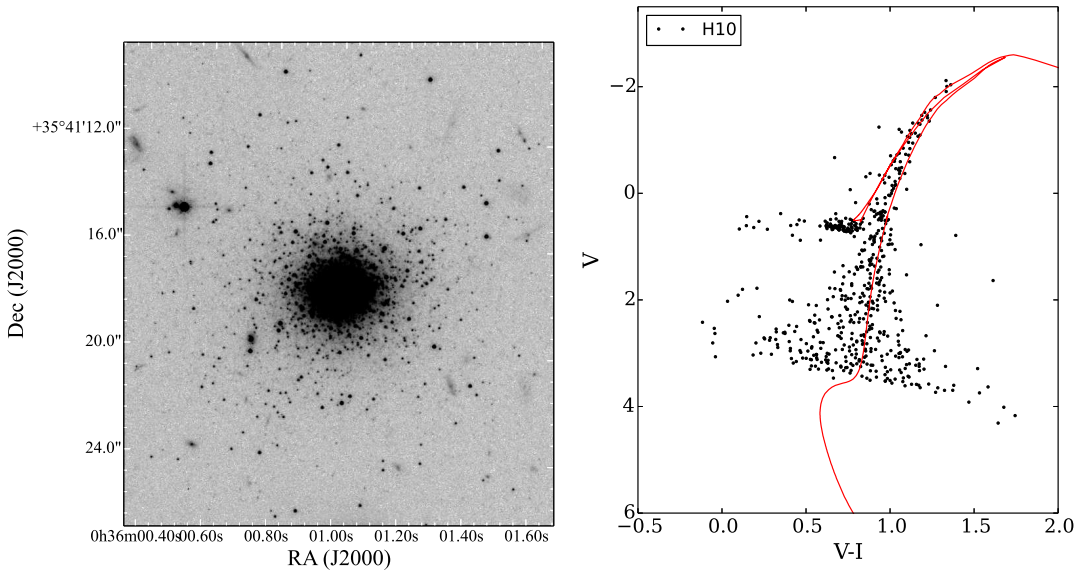

Figure 6.2: Image and CMD of H10. The spectroscopically-determined isochrone is shown (in red) to illustrate how the synthetic HRD is populated. Note that the isochrone appears to be slightly more metal-rich than the CMD indicates—this is likely because of the wide [Fe/H] spacings in the BaSTI grid.

dances with wavelength, REW, and EP are shown in Figures 6.8 through 6.13, and the slopes are tabulated in Table 6.2. Comparisons with the integrated colours are shown in Table 6.3. The differences are all $\lesssim 0.05$ magnitudes, which indicates that the populations are at least reasonably well modelled. Any colour inconsistencies may be due to incorrect ages or slight discrepancies in the RGBs, HBs, or AGBs.

These CMDs are only from the outer regions of the clusters, which are likely to contain more primordial, first generation stars than the inner regions. If there are significant chemical variations between the two populations (especially in Mg or Si; VandenBerg et al. 2012) then there could be slight differences in RGB slope between the inner and outer regions. Regardless, the general agreement between the spectroscopically-determined isochrones and the CMDs of the outer regions is encouraging.

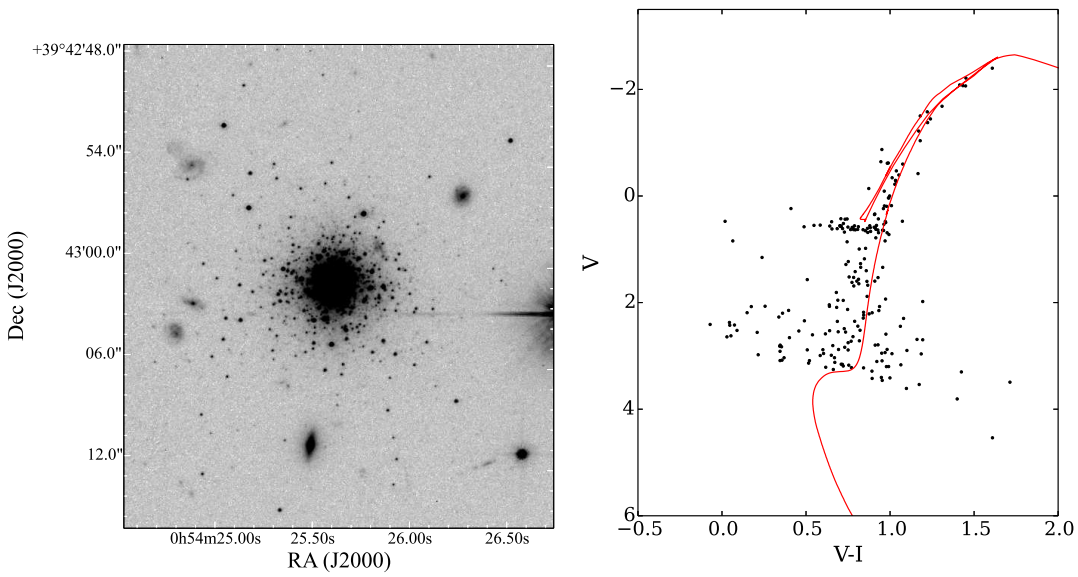

Figure 6.3: Image and CMD of H23. The spectroscopically-determined isochrone is shown (in red) on the CMD.

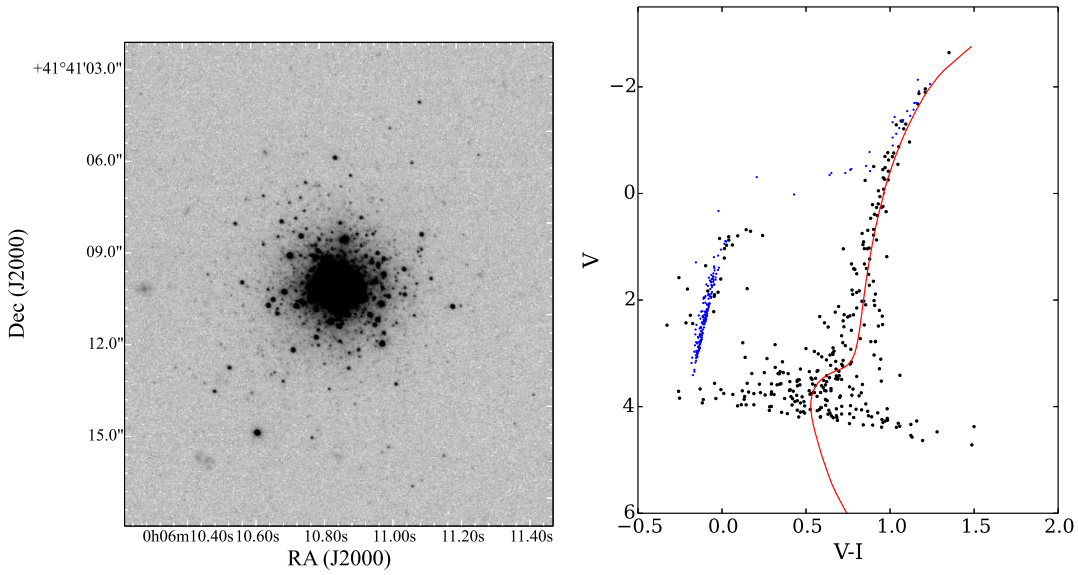

Figure 6.4: Image and CMD of PA06. The spectroscopically-determined isochrone is shown (in red) on the CMD. Synthetic HB stars are shown in blue.

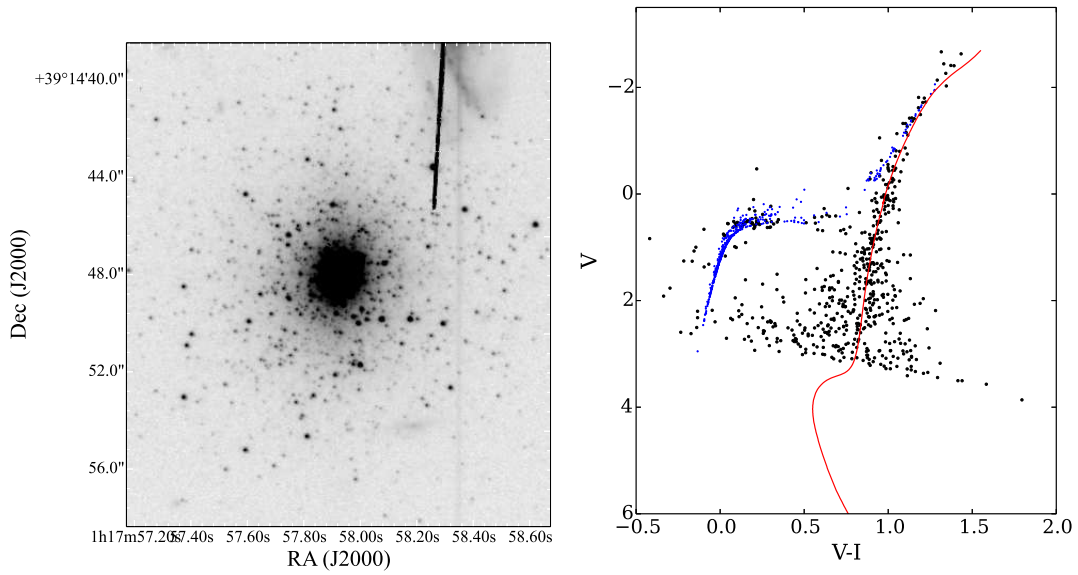

Figure 6.5: Image and CMD of PA53. The spectroscopically-determined isochrone is shown (in red) on the CMD. Synthetic HB stars are shown in blue.

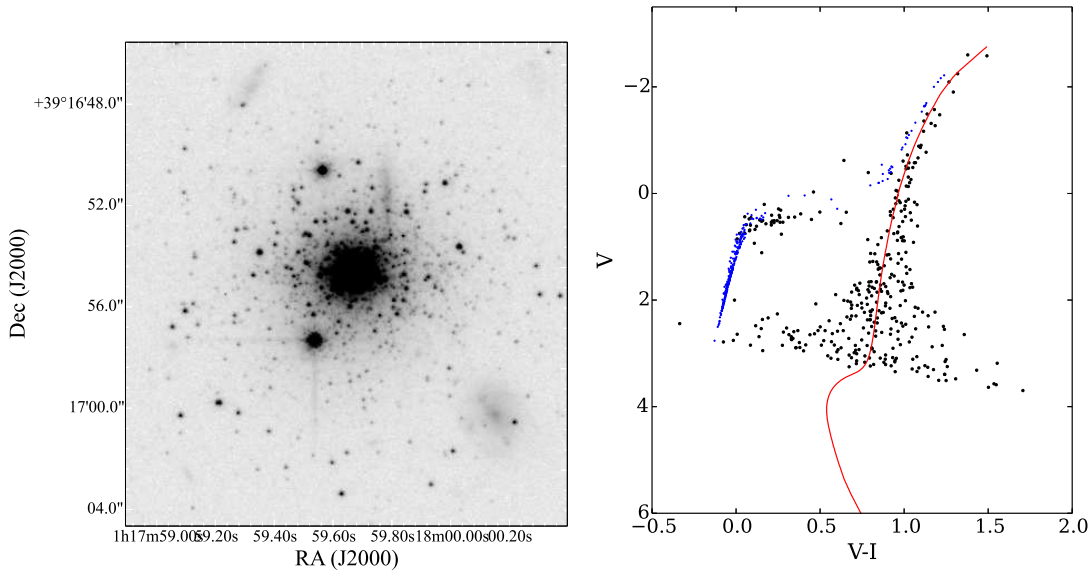

Figure 6.6: Image and CMD of PA54. The spectroscopically-determined isochrone is shown (in red) on the CMD. Synthetic HB stars are shown in blue.

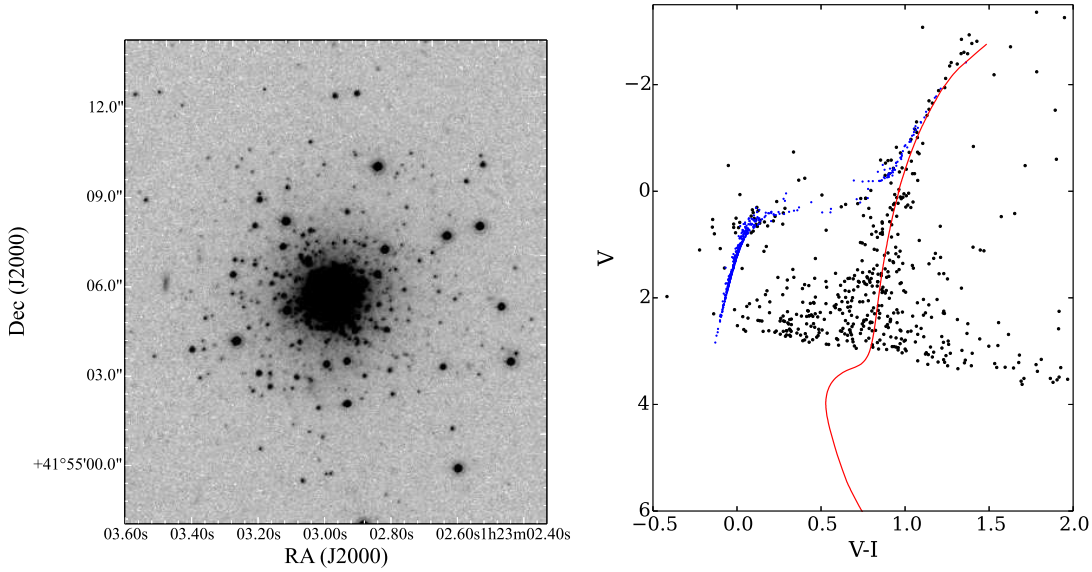

Figure 6.7: Image and CMD of PA56. The spectroscopically-determined isochrone is shown (in red) on the CMD. Synthetic HB stars are shown in blue.

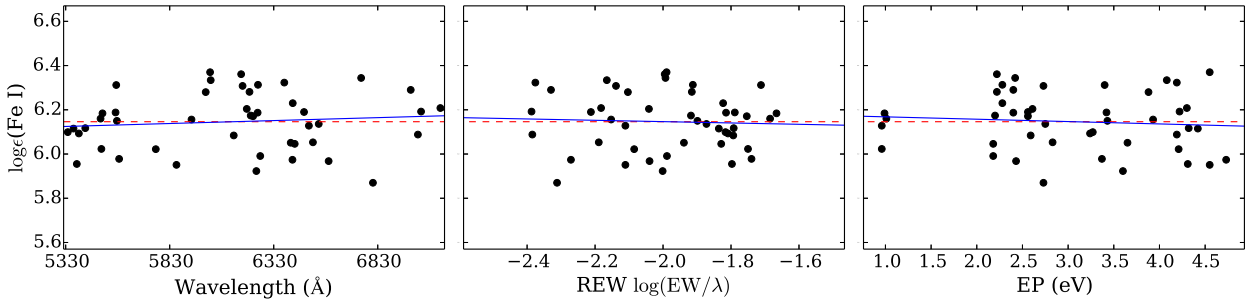

Figure 6.8: Trends in Fe I line abundances in H10. Each black point represents a separate Fe I spectral line. The dashed red line shows the average Fe I abundance. The solid blue line shows the linear least squares fit to the points. Slopes are shown in Table 6.2.

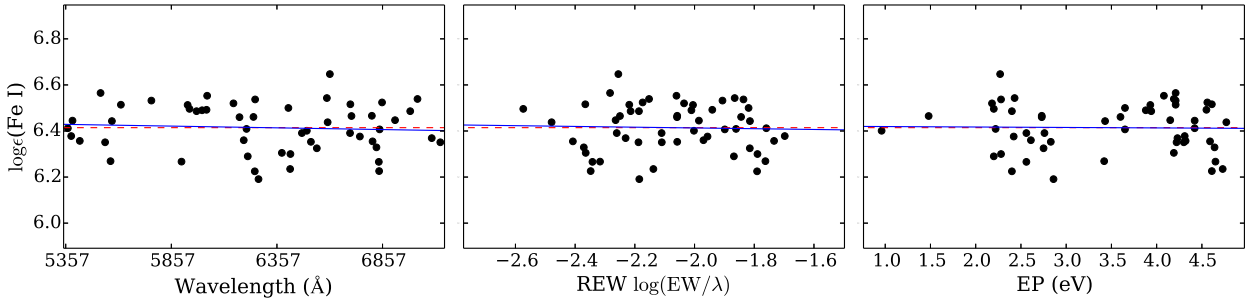

Figure 6.9: Trends in Fe I line abundances in H23. Points are as in Figure 6.8. Slopes are shown in Table 6.2.

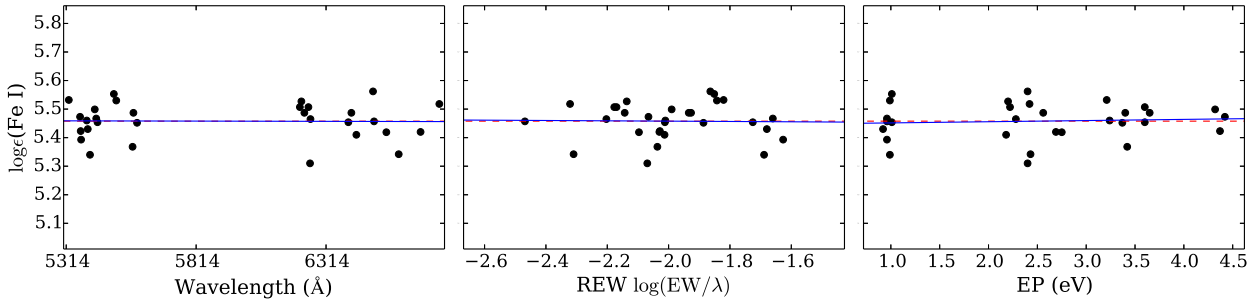

Figure 6.10: Trends in Fe I line abundances in PA06=. Points are as in Figure 6.8. Slopes are shown in Table 6.2.

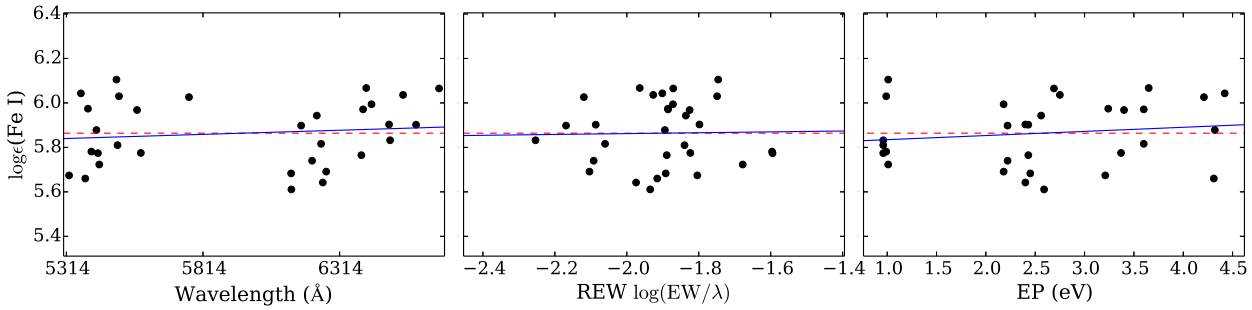

Figure 6.11: Trends in Fe I line abundances in PA53. Points are as in Figure 6.8. Slopes are shown in Table 6.2.

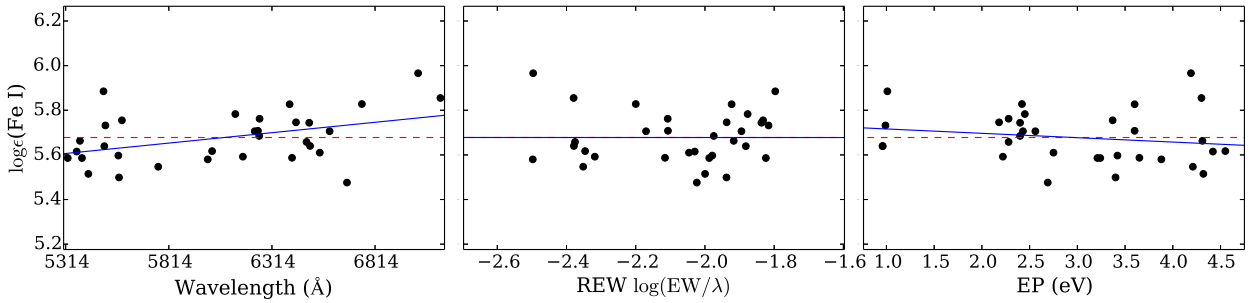

Figure 6.12: Trends in Fe I line abundances in PA54. Points are as in Figure 6.8. Slopes are shown in Table 6.2.

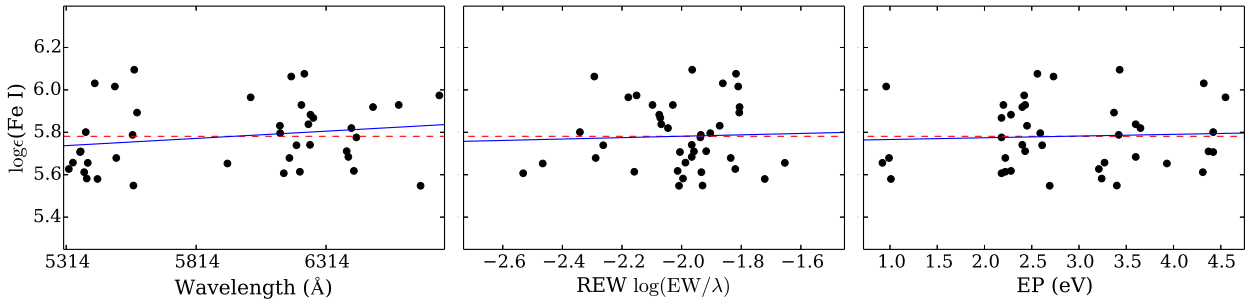

Figure 6.13: Trends in Fe I line abundances in PA56. Points are as in Figure 6.8. Slopes are shown in Table 6.2.

Table 6.1: Best fitting HRD parameters for the PAndAS Cluster

Cluster	Isochrone [Z/H]	Isochrone Age (Gyr)
H10	-0.96	12
H23	-0.96	9
PA06	-1.49	12
PA17[a]	-0.66	12
PA53	-1.27	12
PA54	-1.49	13
PA56	-1.49	12

[a] PA17 does not yet have a high-quality *HST* CMD; therefore, there are few *a priori* constraints on the underlying stellar population.

Table 6.2: Trends in Fe I abundance for the PAndAS Clusters

Cluster	Wavelength Slope	REW Slope	EP Slope
H10	$2.7 \times 10^{-5} \pm 4.0 \times 10^{-5}$	-0.030 ± 0.097	-0.011 ± 0.019
H23	$-1.5 \times 10^{-5} \pm 2.9 \times 10^{-5}$	-0.016 ± 0.067	-0.0020 ± 0.015
PA06	$-1.8 \times 10^{-6} \pm 2.3 \times 10^{-5}$	-0.0057 ± 0.058	0.0041 ± 0.011
PA17[a]	$3.3 \times 10^{-5} \pm 7.5 \times 10^{-5}$	0.035 ± 0.19	0.015 ± 0.029
PA53	$3.7 \times 10^{-5} \pm 5.7 \times 10^{-5}$	0.019 ± 0.18	0.019 ± 0.025
PA54	$9.3 \times 10^{-5} \pm 3.7 \times 10^{-5}$	-0.00018 ± 0.099	-0.020 ± 0.020
PA56	$6.8 \times 10^{-5} \pm 5.6 \times 10^{-5}$	0.033 ± 0.13	0.0081 ± 0.026

[a] PA17 does not yet have a high-quality *HST* CMD; therefore, there are few *a priori* constraints on the underlying stellar population.

Table 6.3: Integrated Colours of the PAndAS Cluster

Cluster	Observed $(V-I)_0$	Synthetic $(V-I)_0$	$\Delta(V-I)_0$
H10	0.95	0.94	−0.01
H23	1.01	0.98	−0.03
PA06[a]	0.87	0.91	+0.04
PA17[b]	1.14	1.05	−0.09
PA53[a]	0.85	0.89	+0.04
PA54[a]	0.84	0.89	+0.05
PA56[a]	0.89	0.88	−0.01

References: Observed colours are from Huxor et al. (2014).
[a] Synthetic HBs were used instead of the default HBs.
[b] PA17 does not yet have a high-quality *HST* CMD; therefore, there are few *a priori* constraints on the underlying stellar population.

6.2.2 PA17

Since PA17 does not yet have a high quality CMD there is no *a priori* information available to constrain its [Fe/H], HB morphology, or rough age. The default HBs were used, and `ILABUNDS` was run on a range of isochrones. The solution converges on a relatively metal-rich isochrone, with [Fe/H] ~ -1, and an age of 12 Gyr. The trends are shown in Figure 6.14 and Table 6.2 and are sufficiently flat. Given PA17's [Fe/H] and integrated colour ($(V-I)_0 = 1.14$, which is redder than H10 and H23; Huxor et al. 2014), the default BaSTI HB (which is red) is likely to be sufficient (see Table 6.3), although this cannot yet be verified. With the default HBs, the Fe I abundances imply a best-fitting age and [Z/H] of 12 Gyr and -0.66.

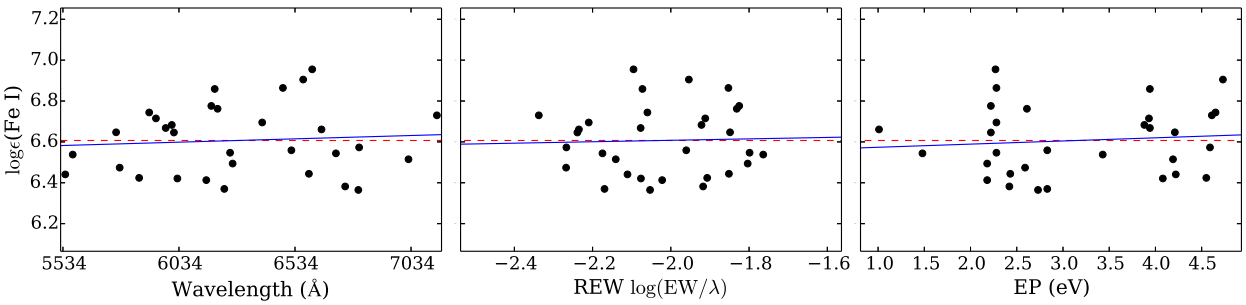

Figure 6.14: Trends in Fe I line abundances in PA17. Points are as in Figure 6.8. Slopes are shown in Table 6.2.

6.3 Line Measurements

EWs were measured with DAOSPEC, as described in Appendix C. All lines stronger than $\sim$ 110 mÅ were discarded unless absolutely necessary. This very conservative choice was made to reduce uncertainties in modelling strong lines—note that some boxes have EWs >200 mÅ even when the IL EW is $\sim$ 100 mÅ. The Fe lines were only measured with EWs. Ca, Ti, and Ni were measured with EWs and verified with spectrum syntheses. All other elements were measured with spectrum syntheses.

The abundances determinations are performed exactly as in Chapter 4. HFS and isotopic components (see 4.2.3) are included for Ba II and Eu II lines. Damping is included for all significant lines (see Chapter 4.2.3). Molecular lines (Chapter 4.2.3) are included in syntheses when features are noted in the Arcturus Atlas. No NLTE corrections are performed, though lines are selected to avoid necessary corrections (Chapter 4.5.2). All [Fe/H] and [X/Fe] ratios are calculated differentially, line by line, with respect to the Solar abundances derived from the EWs in Appendix C and the syntheses in Chapters 4.5.1 through 4.5.3.

6.4 Abundances

6.4.1 Iron

The Fe I and Fe II abundances are shown in Table 6.4. Three clusters, H10, H23, and PA17, are more metal-rich than [Fe/H] = -1.5, while the other four are metal-poor. The metal-poor clusters all have few detectable lines ($\sim$ 30 Fe I lines and 1-2 Fe II lines). The more metal-rich GCs have many more detectable lines, although some of them are stronger than the 110 mÅ limit or, in the case of PA17, were obscured by noise, cosmic rays, etc.

For the clusters with *HST* photometry the spectroscopic metallicities lead to isochrones that roughly fit the upper RGBs, as shown in Figures 6.2 through 6.7. H10 and H23 have literature [Fe/H] determinations from comparisons between the CMDs of the upper RGBs and Galactic GC fiducials. Based on these fits Mackey et al. (2007) find [Fe/H] values that are lower than the integrated [Fe I/H] ratios *and* the metallicities of the derived isochrones. The fiducial fits in Mackey et al. are performed with an optimization routine that finds the best combination of fiducial [Fe/H], distance modulus, and reddening necessary to fit the RGB. However, if the distance

Table 6.4: PAndAS Cluster Fe Abundances

	[Fe I/H]	N	[Fe II/H]	N
H10	-1.36 ± 0.02	46	-1.30 ± 0.04	5
H23	-1.12 ± 0.02	65	-1.21 ± 0.08	5
PA06	-2.06 ± 0.02	30	-2.09 ± 0.10	1
PA17	-0.93 ± 0.03	31	-0.96 ± 0.15	4
PA53	-1.64 ± 0.03	29	-1.68 ± 0.10	1
PA54	-1.84 ± 0.02	32	-1.75 ± 0.08	2
PA56	-1.73 ± 0.03	40	-1.71 ± 0.10	1

modulus and reddening are altered, the derived [Fe/H] an change. For example, Figure 6.15 shows H10's *HST* CMD plotted on top of the CMD from the ACS Survey of Galactic Globular Clusters (Sarajedini et al., 2007; Anderson et al., 2008). The distance modulus quoted in Mackey et al. (2007) leads to good agreement between the HB levels, while lowering the reddening brings the RGBs into agreement. The slope of the RGB is primarily sensitive to metallicity—this agreement therefore supports the higher spectroscopic [Fe/H] ~ -1.4, which is closer to M3's [Fe/H] ~ -1.5.

It is clear from Tables 2.3 and 6.4 that the metal-rich GCs have smaller projected distances from the centre of M31 than the metal-poor GCs. Based on their low resolution survey of inner halo, bulge, and disk M31 GCs, Caldwell et al. (2011) find evidence for an abundance gradient in the inner regions of M31—however, this gradient seems to flatten in the outer regions. (In the MW the gradient flattens at $R_{GC} \sim 2$ kpc; Harris 2000). H23 and PA17 are therefore more metal-rich than expected given their large distance from the centre of M31; however, these GCs are consistent with the metal-rich field stars identified in the outer halo of M31 (see, e.g., Ibata et al. 2014). The other GCs are consistent with a flat, metal-poor [Fe/H] distribution in the outer halo.

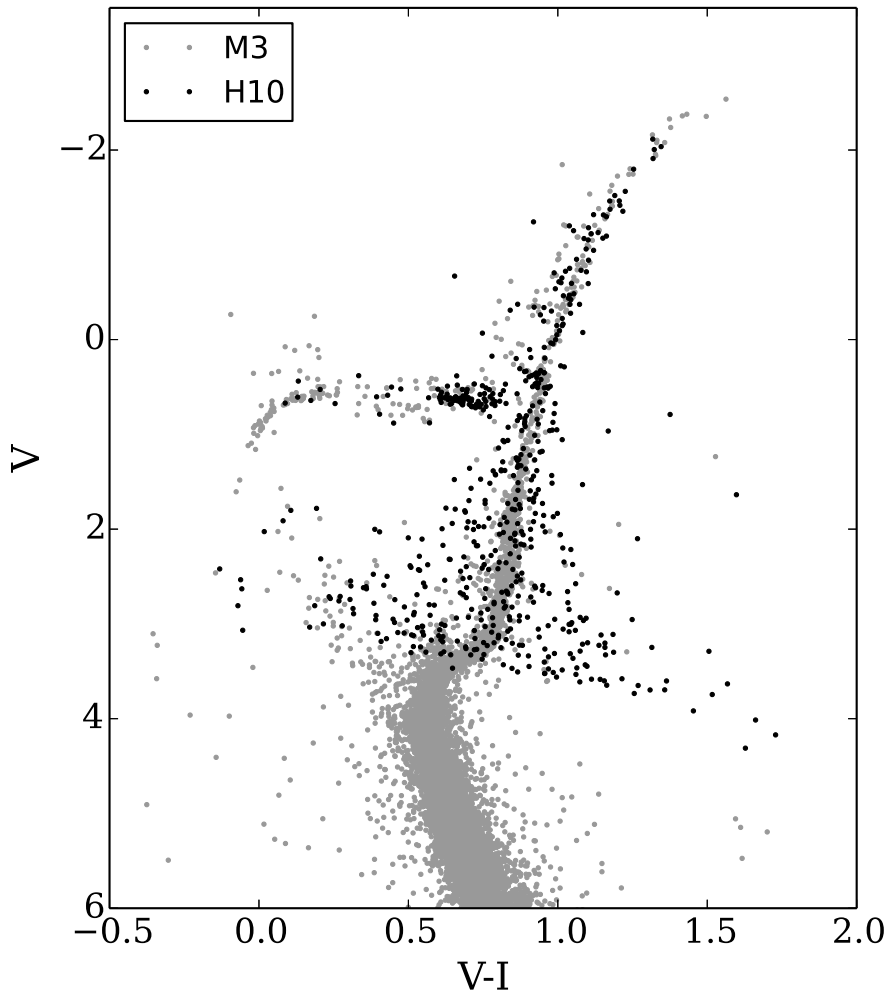

Figure 6.15: H10's *HST* CMD, overplotted on an *HST* CMD of M3. The general agreement between the HB and RGB suggest that H10 likely has a metallicity close to M3's. The distance modulus from Mackey et al. (2007) has been adopted, though the reddening has been lowered to $E(B-V) = 0.01$.

6.4.2 α-elements

The [Ca/Fe] and [Ti/Fe] abundances are given in Table 6.5; these [Ca I/Fe I] abundances are determined based on EWs of $\lesssim$ 10 spectral lines. It is therefore worth considering if the Ca I abundances are artificially low because of poorly measured EWs. All Ca I line EWs were verified by hand, and any uncertain lines were removed from the analysis. The Ti abundances generally agree with Ca, although these ratios are more sensitive to systematic uncertainties (see Chapter 5).

The [Ca/Fe] ratios are compared to MW and dwarf galaxy field stars in Figure 6.16. These ratios indicate that the most metal-poor GCs are Ca-enhanced. PA06, the most metal-poor GC, has a high [Ca/Fe]$\sim$ 0.5 dex that places it in agreement with M15 and dwarf galaxy and MW field stars. The other metal-poor GCs, PA53, PA54, and PA56, are lower than most of the MW field stars and M3, M13, and NGC 7006, while they agree well with the Sculptor and Carina stars. H23 seems to agree best with the Galactic field stars; in particular, H23's [Ca/Fe] is similar to 47 Tuc. Finally, H23 and PA17 is on the low end of the Galactic field stars and the upper end of the Sculptor and Fornax field stars. Figure 6.17 shows comparisons of the PAndAS GCs with MW field stars, inner halo M31 GCs (from Colucci et al. 2009), and dwarf galaxy GCs (coloured points). Sgr clusters are also shown in orange, notably stars from Ter 7 and Pal 12 (two clusters that are currently being accreted from Sgr). Pal 1 is also included even though it is not a classical GC, since its chemistry indicates that it likely originated in a dwarf galaxy (or formed during an accretion; see Chapter 3). The PAndAS clusters look very similar to the LMC and Sgr GCs, especially H10, PA17, PA53, PA54, and PA56. However, most of the Fornax clusters are more metal-poor than the PAndAS GCs. PA17 looks very similar to Pal 1, Ter 7, and Pal 12, suggesting that it comes from a massive dwarf galaxy.

6.4.3 Light Elements: Na and Mg

Table 6.6 shows the [Na/Fe] and [Mg/Fe] abundances for the PAndAS GCs. Recall that both ratios can be affected by star-to-star variations within the clusters, as was demonstrated by the Galactic GCs (Chapter 4.5.1 and 4.5.2). Several of the [Na/Fe] ratios do appear to be affected by star-to-star variations; for instance, PA06, PA17,

Table 6.5: PAndAS Cluster Ca and Ti Abundances

	[Ca I/Fe I]	N	[Ti I/Fe I]	N	[Ti II/Fe II]	N
H10	0.25 ± 0.04	10	0.39 ± 0.10	1	0.40 ± 0.03	2
H23	0.41 ± 0.04	6	0.56 ± 0.05	3	0.39 ± 0.10	1
PA06	0.46 ± 0.07	9	–	0	0.31 ± 0.10	2
PA17	0.04 ± 0.07	4	0.0 ± 0.10	1	0.17 ± 0.10	1
PA53	0.19 ± 0.03	10	0.16 ± 0.10	1	0.17 ± 0.06	2
PA54	0.28 ± 0.04	9	–	0	0.49 ± 0.10	1
PA56	0.24 ± 0.05	8	0.47 ± 0.10	1	–	0

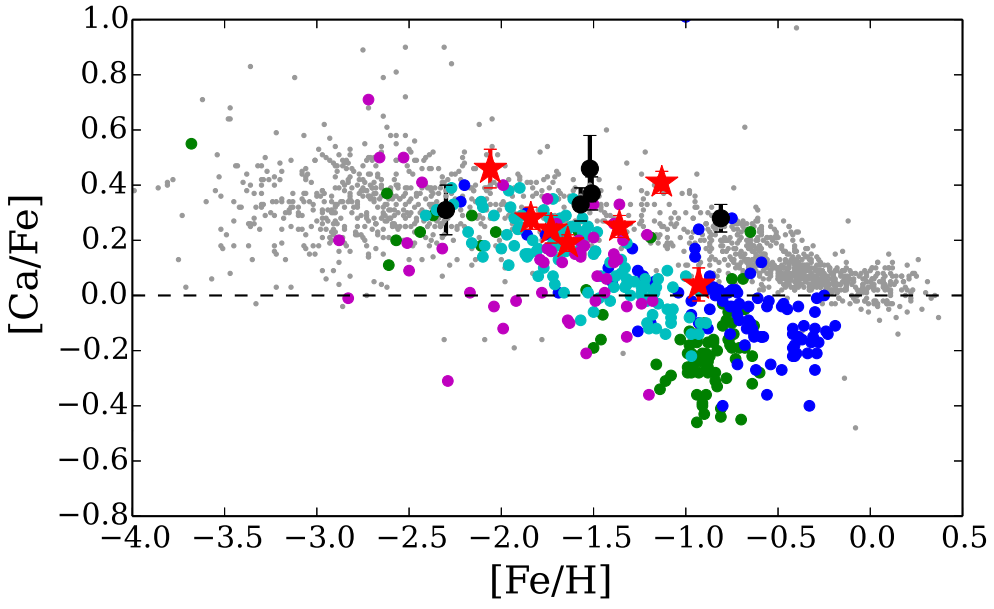

Figure 6.16: Comparisons of M31 clusters (red stars) to MW field stars (grey), dwarf galaxy field stars (LMC in blue, Fornax in green, Sculptor in cyan, and Carina in magenta), and the IL abundances of the MW clusters in Chapter 4 (black circles). References are given in Figure 1.7. The error bars show the random errors, and do not include the systematic errors from Chapter 5.

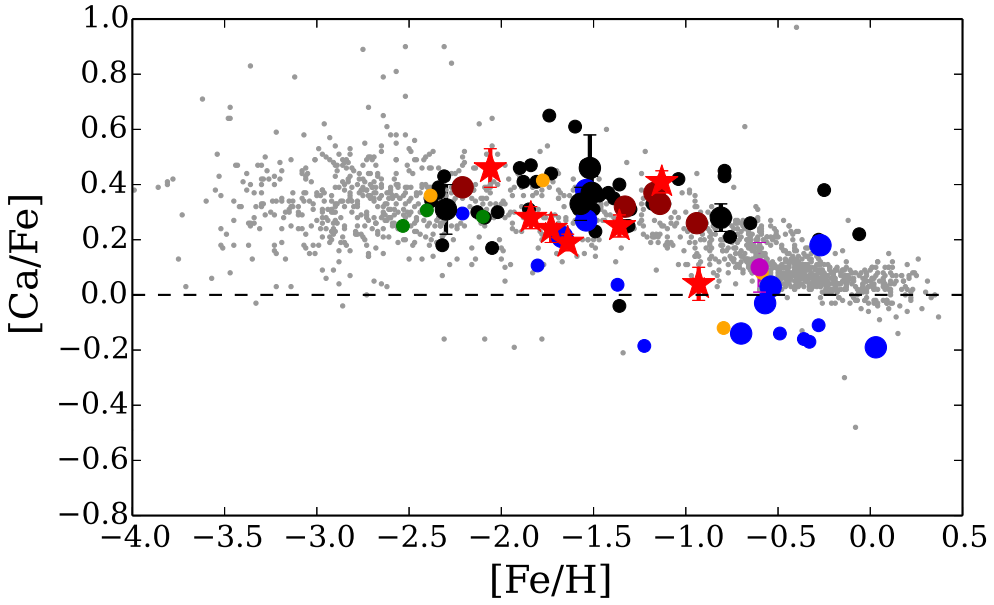

Figure 6.17: [Ca/Fe] ratios in the M31 clusters (red stars) compared to MW field stars (grey), MW clusters (black circles; larger circles are IL values from Chapter 4, while the smaller circles are cluster averages from Pritzl et al. 2005), the average Pal 1 abundances from Chapter 3 (magenta star), IL values of inner halo GCs (maroon circles, from Colucci et al. 2009), and dwarf galaxy GCs. LMC clusters are in blue; large circles show the IL abundances from Colucci et al. (2012), while the small circles show the individual stellar abundances from Johnson et al. (2006) and Mucciarelli et al. (2008). Sgr clusters are in orange and are from Cohen (2004), Sbordone et al. (2005b), and Mottini et al. (2008). Fornax clusters (green) are from Letarte et al. (2006). Larger symbols show IL [Ca/Fe] values, while smaller symbols show cluster averages from individual stars. The error bars show the random errors, and do not include the systematic errors from Chapter 5.

Table 6.6: PAndAS Cluster Na and Mg Abundances

	[Na I/Fe I]	N	[Mg I/Fe I]	N
H10	0.35 ± 0.25	1	0.50 ± 0.13	2
H23	-0.01 ± 0.23	2	0.30 ± 0.20	2
PA06	0.71 ± 0.25	2	0.14 ± 0.20	1
PA17	0.60 ± 0.15	2	0.64 ± 0.13	2
PA53	0.41 ± 0.30	1	0.20 ± 0.20	1
PA54	0.78 ± 0.30	2	0.32 ± 0.18	2
PA56	0.43 ± 0.20	2	0.54 ± 0.15	2

and PA54 all have high [Na/Fe] ratios, while the PA53 and PA56 ratios are mildly high. High [Na/Fe] ratios are a natural result of the Na/O anticorrelation that is observed in all Galactic GCs (Carretta et al., 2009a). Despite the presence of the anticorrelation, H10 and H23 have [Na/Fe] ratios that agree with Galactic stars.

For some of the GCs the integrated [Mg/Fe] ratios roughly agree with the [Ca/Fe] ratios, suggesting that [Mg/Fe] is unaffected by star-to-star abundance variations in those clusters. Several GCs (notably H10 and PA17) have rather high [Mg/Fe] ratios, compared to [Ca/Fe]. It is possible that the Mg abundances are systematically high because of the underlying populations. Since Mg was not included in the systematic errors analysis in Chapter 5, it is difficult to identify the source of these errors.

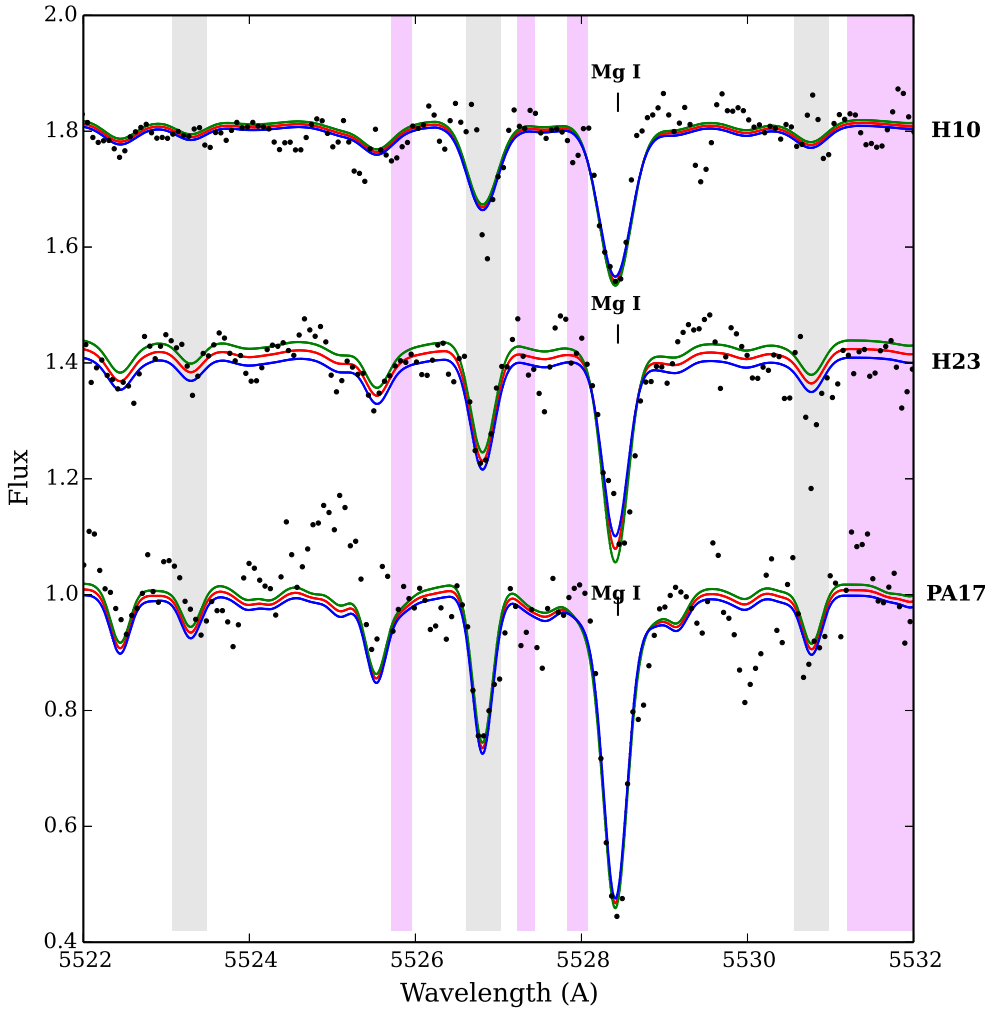

Figure 6.18: Syntheses of the 5528 Å Mg I line in the metal-rich clusters H10, H23, and PA17. The best continuum regions are selected based on the Galactic GC syntheses in Chapter 4. Black points show the observed data. Red lines show the best-fitting syntheses, while the green lines show the $+1\sigma$ errors and the blue lines show the -1σ errors.

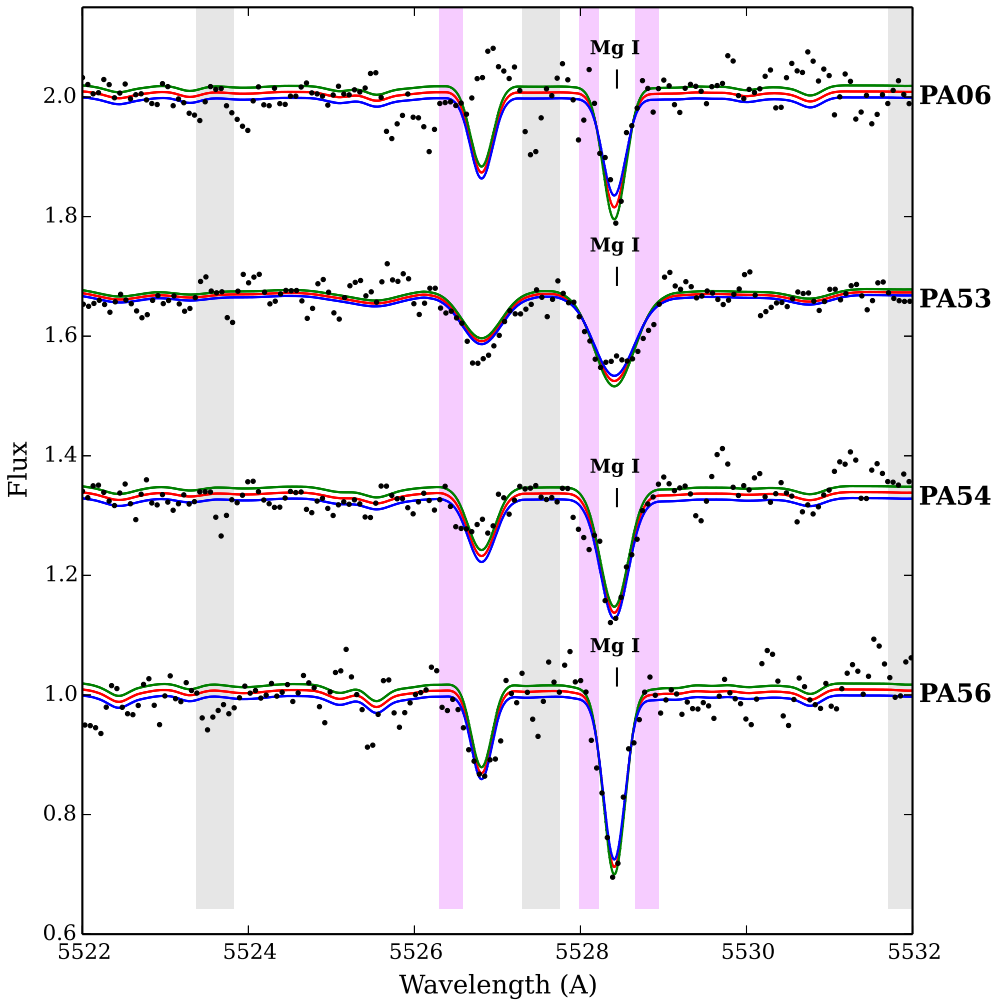

Figure 6.19: Syntheses of the 5528 Å Mg I line in the metal-poor clusters PA06, PA53, PA54, and PA56. Black points show the observed data. Red lines show the best-fitting syntheses, while the green lines show the $+1\sigma$ errors and the blue lines show the -1σ errors.

Table 6.7: PAndAS Cluster Ni Abundances

	[Ni I/Fe I]	N
H10	0.01 ± 0.04	7
H23	-0.07 ± 0.04	5
PA06	-0.02 ± 0.06	2
PA17	-0.08 ± 0.09	3
PA53	-0.11 ± 0.18	2
PA54	-0.05 ± 0.06	3
PA56	-0.10 ± 0.16	2

6.4.4 Nickel

The [Ni I/Fe I] abundance ratios are shown in Table 6.7. Note that these ratios were determined with EWs, even though there are few Ni I lines for most of the clusters—this leads to fairly large random abundance errors. However, these lines were carefully checked to ensure that they were clean (i.e. uncontaminated by cosmic rays, sky lines, or noise) and were measured properly. A comparison with MW field stars, GC, and dwarf galaxy field stars is shown in Figure 6.20, while a comparison with MW field stars, Pal 1, and dwarf galaxy GCs is shown in Figure 6.21. The PAndAS clusters all have [Ni/Fe] ratios that are consistent with MW and dwarf galaxy stars—however, H23 and PA17 both have slightly low Ni abundances that agree best with dwarf galaxy stars. In particular, PA17's [Ni I/Fe I] ratios agree well with the Pal 12 and Ter 7 ratios.

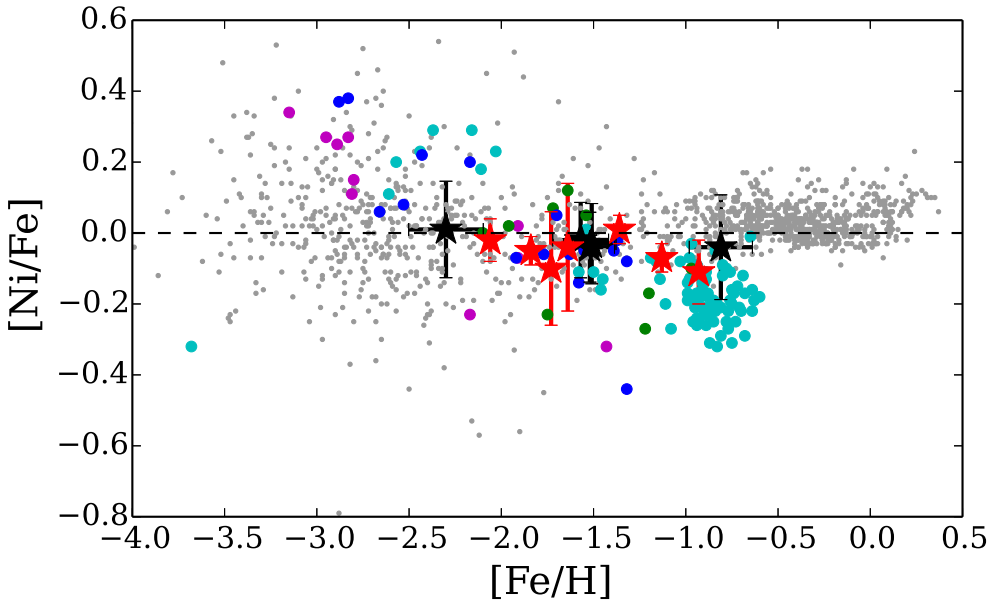

Figure 6.20: Comparisons of Ni abundances in M31 clusters (red stars) to those in MW field stars (grey), dwarf galaxy field stars (coloured points), and the IL abundances of the MW clusters in Chapter 4 (black circles). Points and references are as in Figure 6.16.

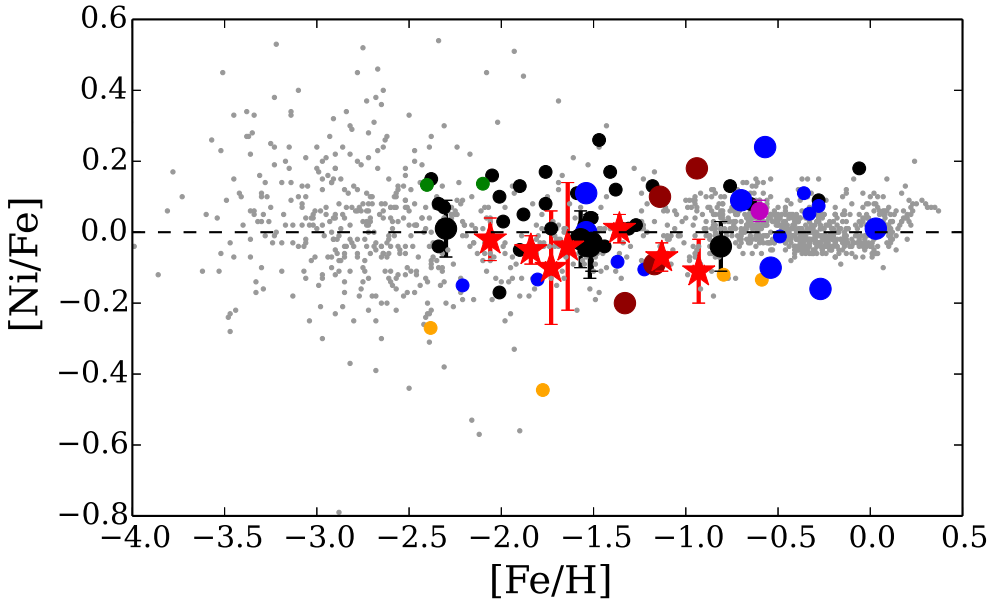

Figure 6.21: Comparisons of [Ni/Fe] ratios in M31 clusters to MW field stars and clusters, Pal 1, M31 GCs, and dwarf galaxy GCs. Points and references are as in Figure 6.17.

6.4.5 Neutron Capture Elements: Ba and Eu

The neutron capture abundance ratios are given in Table 6.8. Note that unlike the Galactic GC Ba II abundances in Chapter 4, these Ba II abundances are determined *with spectrum syntheses.* This is because of the importance of the Ba II ratio in chemical tagging (which requires high precision) and because it is more difficult to measure the strengths of the Ba II lines in the lower S/N targets. Only two Ba II lines were considered for these syntheses: the 5853 and 6141 Å lines. The 6496 Å line was removed because of possible NLTE effects, as discussed in Chapter 3.3.4. No molecular lines were included in these syntheses, since none were identified in the Arcturus Atlas. The syntheses of the Ba II 5853 Å line are shown in Figures 6.22 and 6.23. As in Chapter 4, the Eu II abundances are determined through syntheses of the 6645 Å line; these syntheses are shown in Figures 6.24 and 6.25.

Comparisons of [Ba/Eu] ratios between the PAndAS clusters, the MW clusters, and MW and dwarf galaxy field stars are shown in Figure 6.26, while comparisons with M31 and dwarf galaxy clusters are shown in Figure 6.27. PA06, PA17, and PA54 only have upper limits on [Eu II/Fe II], which leads to a lower limit in [Ba/Eu]. The estimated ratio resulting from only the r-process is shown with the red dashed line. H10, H23, and PA53, PA54, and PA56 all agree with MW field stars, the Galactic GCs, the Sgr clusters, and the LMC field stars and clusters. PA17's [Ba/Eu] ratio has only an upper limit; however, it is possible that it is higher than the MW field stars. In particular, PA17's best-fitting [Ba/Eu] ratio agrees quite well with the Pal 12 stars (and possible the LMC GC stars as well, although there are fewer Eu abundances for those clusters).

It is also clear from Figures 6.26 and 6.27 that PA56 has an extremely low [Ba/Eu] ratio. Both Ba and Eu have been known to vary within the most massive GCs (see, e.g., Sneden et al. 1997, Roederer 2011, and the discussion in Chapter 4.6.4); the IL abundances may be affected by the presence of multiple populations in these PAndAS GCs. The presence of multiple populations explain, for example, M15's high Eu abundance (and therefore low [Ba/Eu] ratio). Table 6.8 shows that PA56 has a moderate Ba abundance and a high Eu abundance, which leads to a [Ba/Eu] that is below the r-process only limit. Thus, PA56 may have star-to-star variations in heavy elements.

Figures 6.28 and 6.29 show the [Eu/Ca] ratios (which can serve as an [Eu/α] indicator) in different environments. PA56's large Eu abundance places it on the

Table 6.8: PAndAS Cluster Ba and Eu Abundances

	[Ba II/Fe II]	N	[Eu II/Fe II]	[Ba II/Eu II]	[Eu II/Ca I]
H10	-0.05 ± 0.11	2	0.75 ± 0.20	-0.80 ± 0.23	0.50 ± 0.20
H23	-0.03 ± 0.11	2	0.53 ± 0.25	-0.56 ± 0.27	0.23 ± 0.25
PA06	-0.17 ± 0.20	1	< 1.04	> -1.21	< 0.58
PA17	0.21 ± 0.25	2	0.51 ± 0.40	-0.30 ± 0.47	0.47 ± 0.30
PA53	0.03 ± 0.22	2	0.68 ± 0.25	-0.65 ± 0.33	0.49 ± 0.25
PA54	-0.10 ± 0.20	1	< 0.50	> -0.6	< 0.22
PA56	-0.39 ± 0.15	1	0.96 ± 0.15	-1.35 ± 0.21	0.72 ± 0.26

upper end of the MW stars. H23 and PA53 are in agreement with MW and dwarf galaxy field stars and clusters while H10 is higher than the Galactic stars and GCs. Again, PA17's upper limit makes it difficult to determine anything from the [Eu/Ca] ratio; however, it may be higher than the MW field stars, in agreement with the Pal 12 and LMC GC abundances.

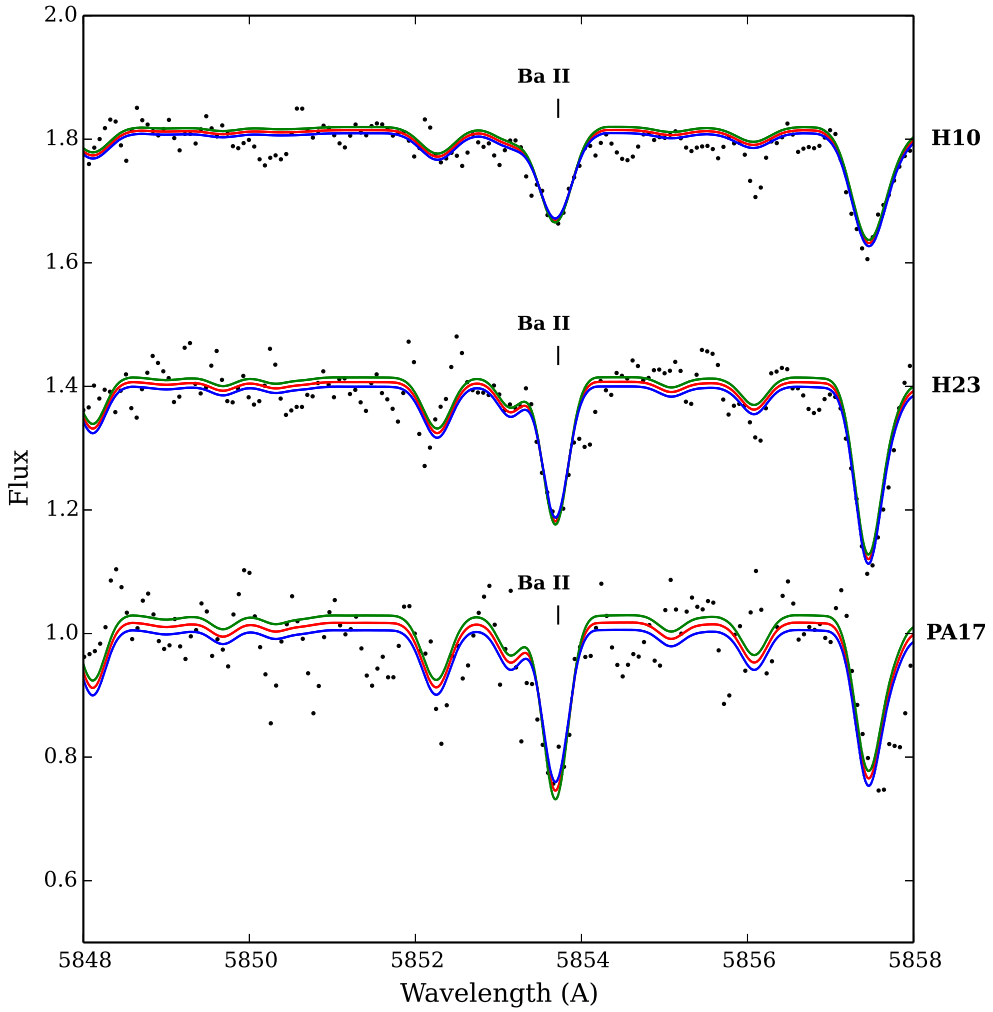

Figure 6.22: Syntheses of the 5853 Å Ba II line in the metal-rich clusters H10, H23, and PA17. Black points show the observed data. Red lines show the best-fitting syntheses, while the green lines show the $+1\sigma$ errors and the blue lines show the -1σ errors.

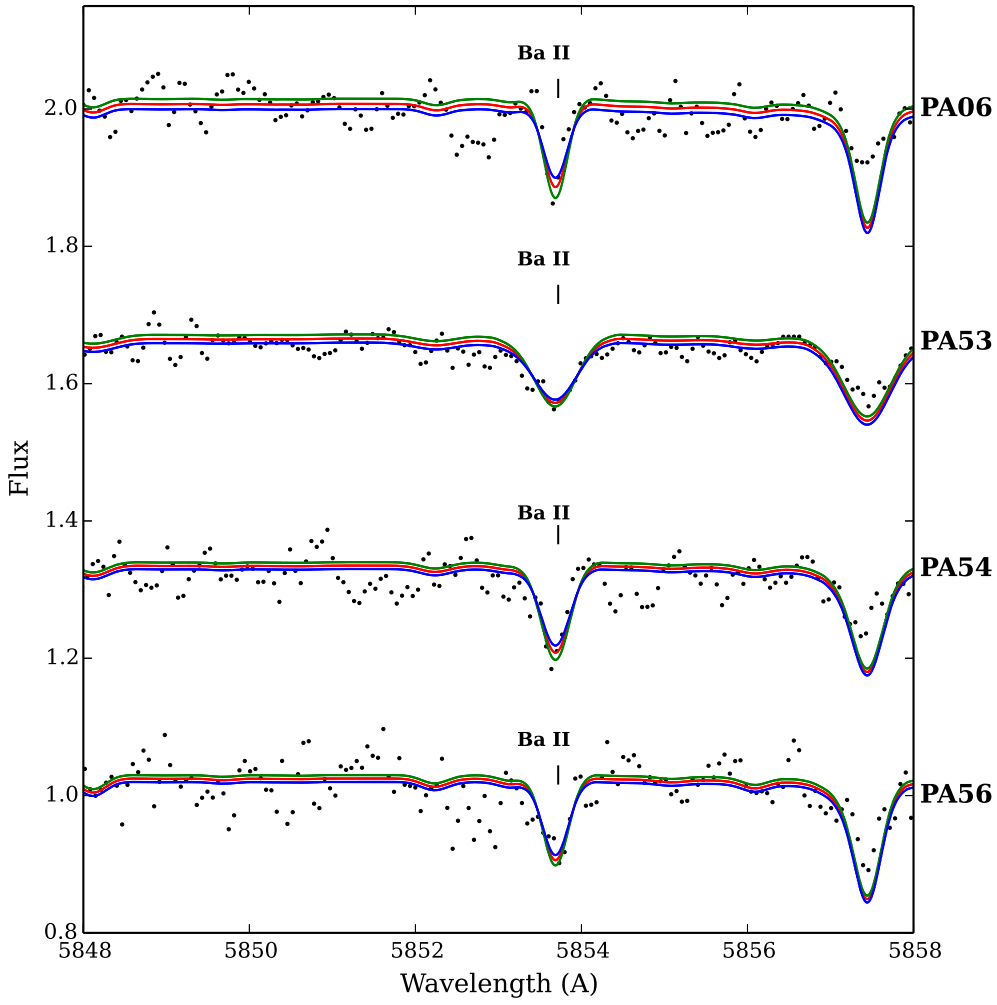

Figure 6.23: Syntheses of the 5853 Å Ba II line in the metal-poor clusters PA06, PA53, PA54, PA56. Points are as in Figure 6.22.

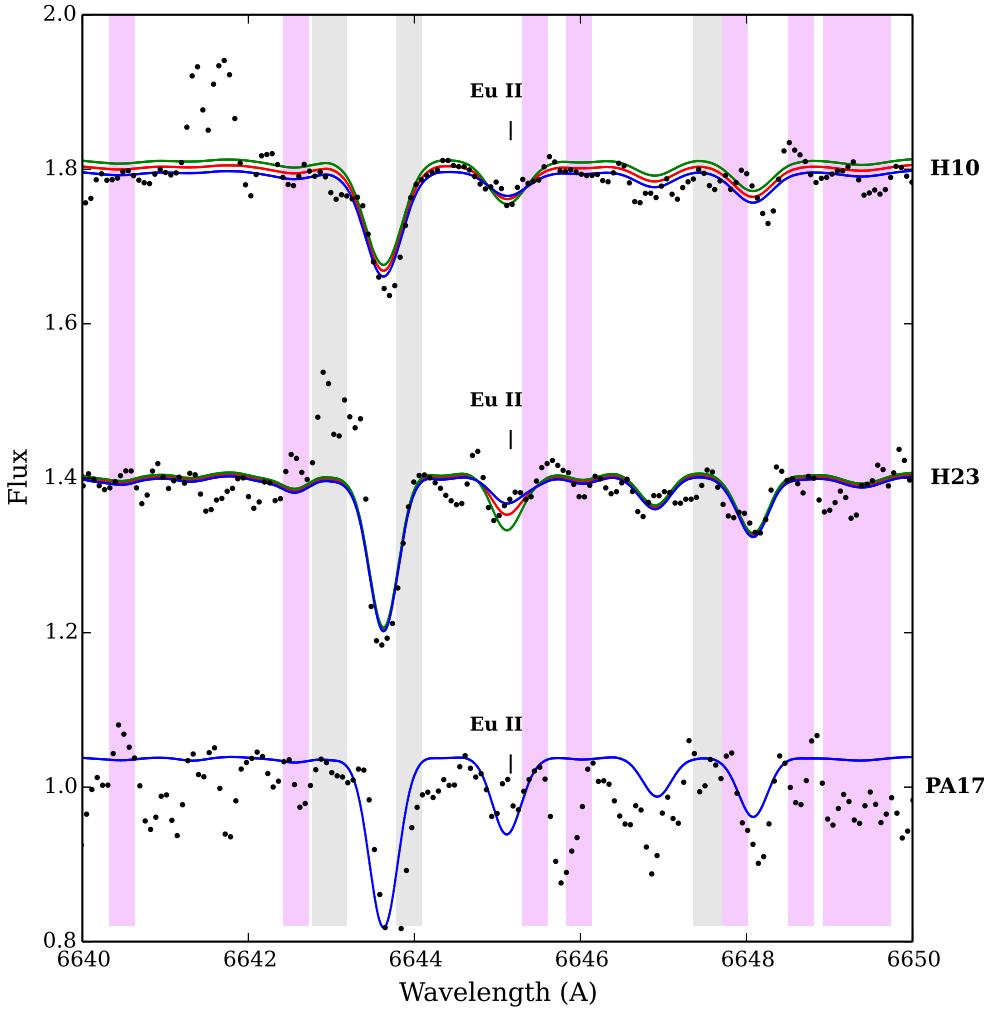

Figure 6.24: Syntheses the 6645 Å Eu II line in the metal-rich clusters H10, H23, and PA17. Points are as in Figure 6.22. Grey regions show areas with uncertain HFS, while purple regions indicate uncertain molecular features.

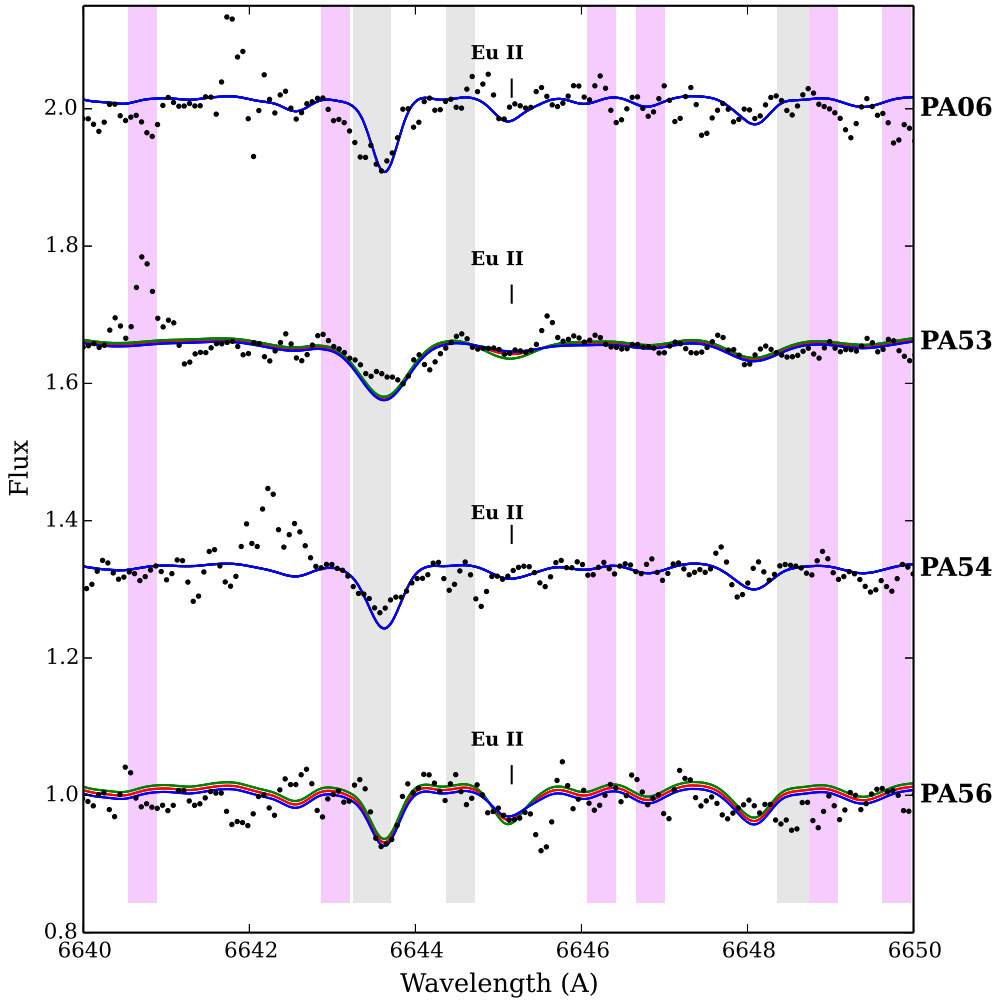

Figure 6.25: Syntheses the 6645 Å Eu II line in the metal-poor clusters PA06, PA53, PA54, PA56. Points are as in Figure 6.22. Grey regions show areas with uncertain HFS, while purple regions indicate uncertain molecular features.

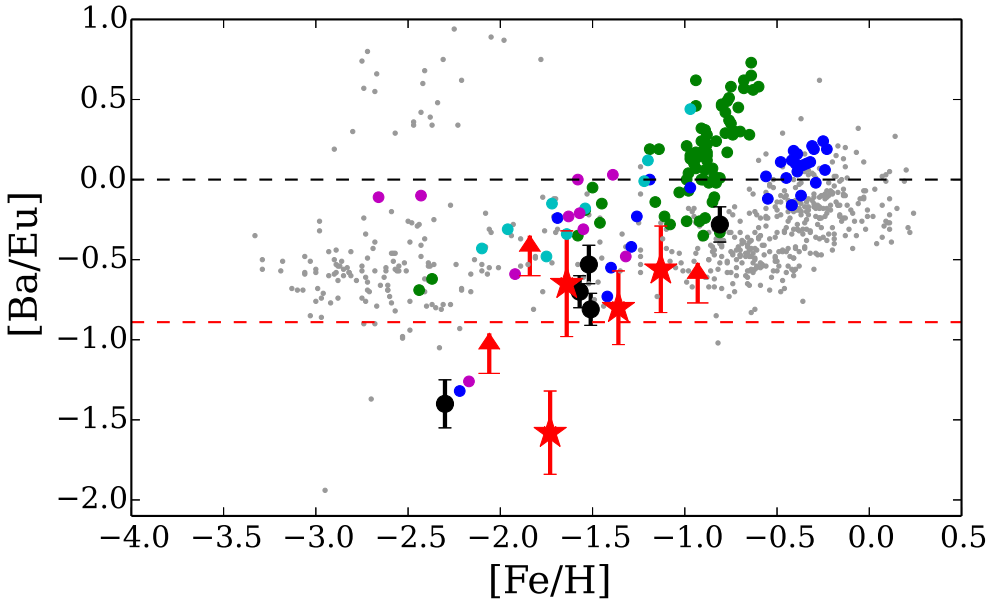

Figure 6.26: Comparisons of [Ba/Eu] ratios in M31 clusters to MW field stars and clusters and dwarf galaxy field stars. Points are as in Figure 6.16.

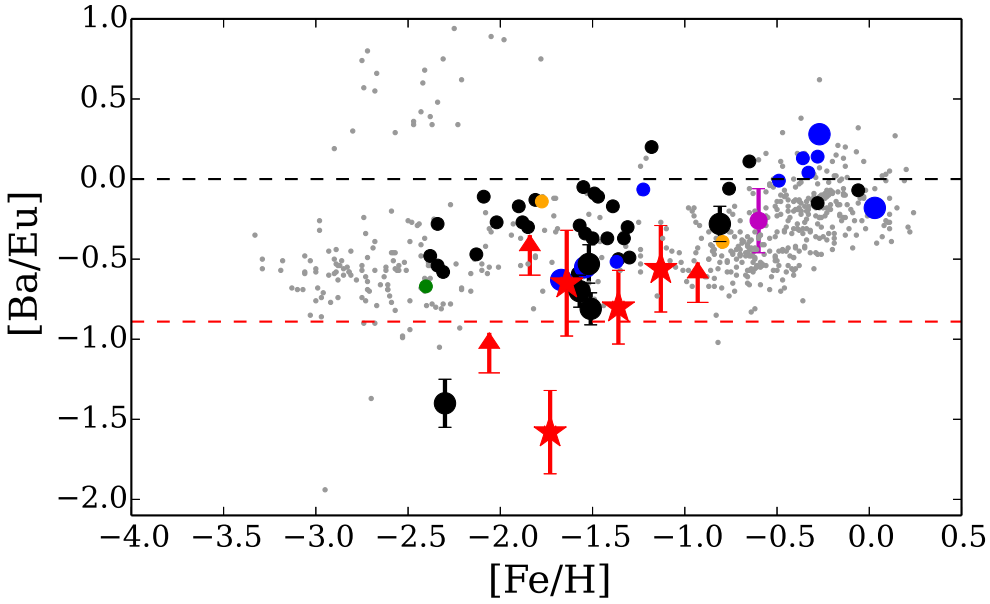

Figure 6.27: Comparisons of [Ba/Eu] ratios in M31 clusters to MW field stars and clusters, Pal 1, M31 GCs, and dwarf galaxy GCs. Points are as in Figure 6.17.

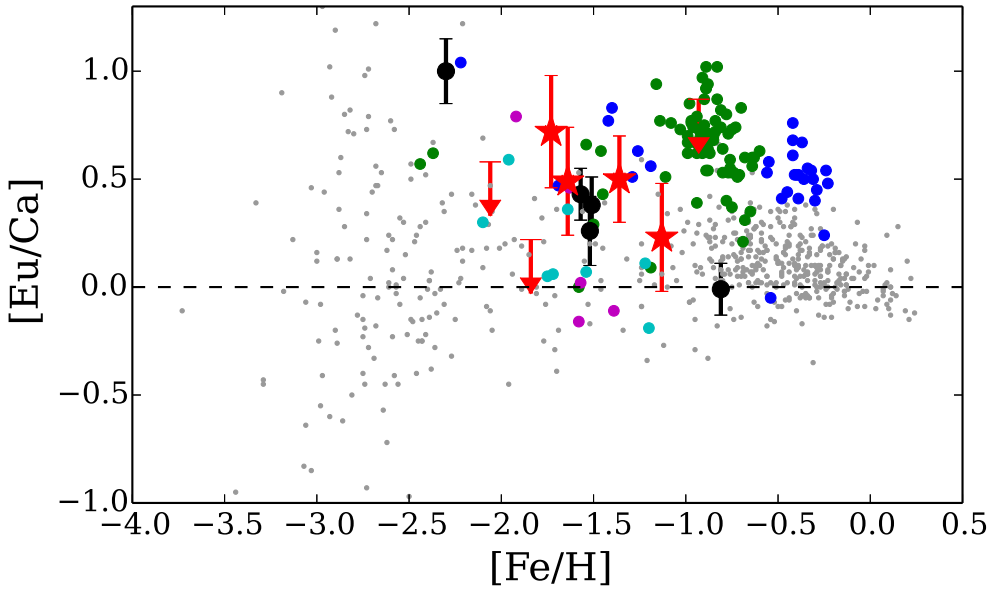

Figure 6.28: [Eu/Ca] ratios of M31 clusters vs. those of MW field stars and clusters and dwarf galaxy field stars. Points are as in Figure 6.16.

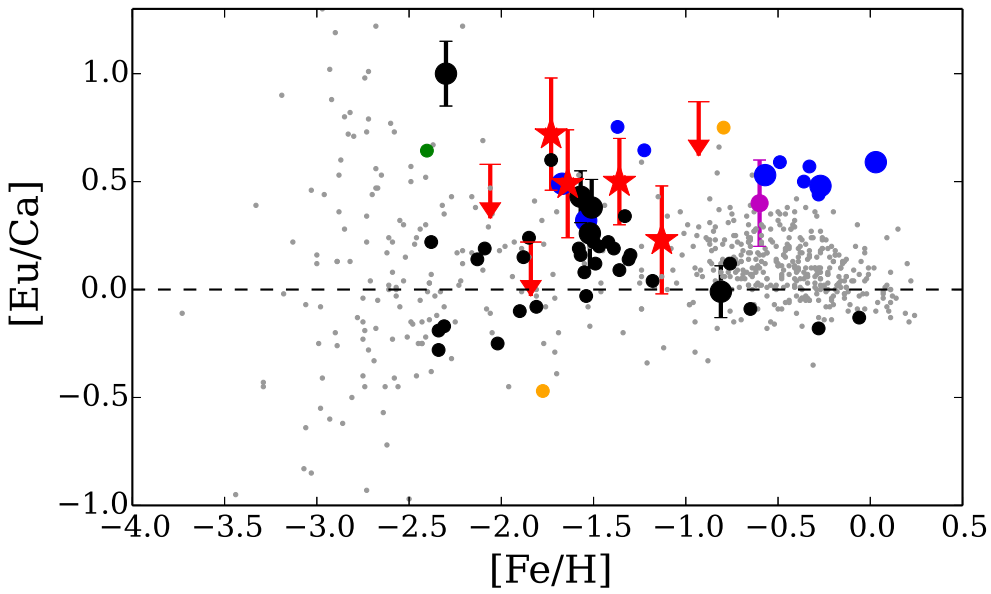

Figure 6.29: [Eu/Ca] ratios of M31 clusters vs. those of MW field stars and clusters, Pal 1, M31 GCs, and dwarf galaxy GCs. Points are as in Figure 6.16.

6.5 Discussion

The detailed abundances in this chapter can be used to infer the formation history of M31's outer halo and to determine the nature of the dwarf galaxies that are currently being accreted.

6.5.1 Individual Clusters: A Summary

Each of the PAndAS clusters presented in this thesis has its own unique chemical abundance signature that indicates something about its origins.

PA17: PA17 is the most metal-rich of the target clusters, at [Fe/H] ~ -0.9. Most GC systems in dwarf galaxies tend to be metal-poor, with more massive dwarf galaxies possessing more metal-rich GCs (recall the discussion of colour bimodalities and mass-metallicity relationships in Chapter 1.5). Thus, PA17's metallicity alone indicates that it formed in a fairly massive galaxy—its unusual location far away in the outer halo suggests that this host galaxy was a massive, LMC- or Sgr-mass dwarf.

PA17's high [Na/Fe] ratio suggests that it is a "classical" GC (under the Carretta et al. 2009a definition) with signs of a Na/O anticorrelation. Its [Mg/Fe] is high and does not follow [Ca/Fe]; this may indicate that systematic offsets are affecting the Mg abundance.

Based on its low [α/Fe] and potentially high [Ba/Eu] ratios, it is clear that PA17 formed in an environment in which intermediate mass stars had sufficient time to evolve (since Type Ia SNe would lower the [α/Fe] ratio and AGB stars would produce additional Ba, compared to the r-process). This suggests that PA17 did not form in the earliest rounds of star formation in its host galaxy. The [α/Fe] ratio is approximately Solar at [Fe/H]~ -0.9; this moderately low ratio (compared to MW field stars) indicates that PA17 formed in an environment with a moderately high star formation rate (in the Tinsley 1979 framework, as discussed in Chapter 5.5.3) or formed in an environment that was only slightly deficient in the highest mass stars (in the McWilliam et al. 2013 model; see the discussion in Chapter 5.5.3). Thus, PA17's detailed chemical abundance ratios also indicate that it formed in a galaxy that had sufficient mass to have a fairly high star formation rate or to populate the high mass end of the IMF.

From a chemical tagging point of view, PA17's slightly low [α/Fe] and [Ni/Fe] and possibly high [Ba/Eu] ratios put it in excellent agreement with Pal 1, the intermediate age LMC clusters, and the accreted Sgr clusters Pal 12 and Ter 7. Based on its metallicity and [α/Fe] ratio, PA17 is unlike the field stars in the lowest mass dwarf galaxies, and is unlike the (metal-poor) GCs in, e.g., Fornax. Again, the evidence suggests that PA17 formed in a massive dwarf galaxy.

H10 and H23: H10 and H23 are the third and second most metal-rich GCs in the sample, respectively. Based on the same arguments as for PA17, this indicates that the clusters likely originated in fairly massive dwarf galaxies. However, unlike PA17 the abundance ratios are not distinct from MW field stars: in all cases, the H23 abundance ratios agree with the MW field stars and the slightly more metal-poor Galactic GCs M3, M13, and NGC 7006. H10's [Eu/Ca] ratio is distinctly higher than the Galactic GCs at the same [Fe/H]. Though its slightly low [Ca/Fe] hints at a dwarf galaxy origin, it is still in agreement with the Galactic GCs. The normal [Ca/Fe] ratios do not mean that H10 and H23 did not originate in a dwarf galaxy—chemical evolution models (see Chapter 1.3.5) suggest that initially all stars should be α-enhanced (at [α/Fe]$\sim$ +0.4) and should have low [Ba/Eu] at the r-process limit. Over time these abundance ratios will change; the "knee" where the chemistries start to change will differ between galaxies of different mass (see Chapter 5.5.3). Thus, it is possible that H10 and H23 could have formed in a dwarf galaxy with a knee at [Fe/H] ~ -1.5 to -1.2. Their agreement with the LMC clusters supports this possibility.

PA53 and PA56: These clusters are fairly close to each other on the sky, and have very similar radial velocities and metallicities. Thus, it is possible that these clusters are (or were) actually physically associated with one another. Both are metal-poor ([Fe/H] ~ -1.7) and have [α/Fe] ratios slightly lower than the MW field stars. The [Ba II/Fe II] and [Eu II/Fe II] are quite different (and hence the [Ba/Eu] and [Eu/Ca] ratios are different); however, this could be a signature of multiple populations within the GCs (especially given PA56's low [Ba/Eu]), and the discrepant ratios do not preclude the possibility that they are related. Both GCs are slightly enhanced in Na (with [Na/Fe]$\sim$ 0.4), which may be a signature of the Na/O anticorrelation.

The abundance ratios in PA53 and PA56 agree best with the intermediate-mass dwarf galaxies Fornax and Sculptor. However, they are more metal-rich than

the GCs in Fornax, suggesting that their progenitor galaxy/galaxies formed a different GC population.

PA54: Although PA54 is extremely close to PA53 on the sky, their discrepant radial velocities imply that these clusters are not likely to be associated, nor is PA54 likely to be associated with PA56. However, PA54 has very similar abundance ratios as PA53 and PA56, even with only upper limits on [Eu/Fe]. This indicates that PA54 may have formed in a medium-mass dwarf galaxy as well. PA54's very high [Na/Fe] ratio also indicates that it is a classical GC, with a significant Na/O anticorrelation.

PA06: PA06 is the most metal-poor GC of the PAndAS sample, though it is still more metal-rich than the Galactic GC M15. It is Ca-enhanced, like most metal-poor clusters. The weakness of its lines means that only an upper limit can be obtained for Eu II. Again, PA06's high [Na/Fe] indicates the presence of a Na/O anticorrelation—additionally, its low [Mg/Fe] hints at a Mg/Al anticorrelation. Ultimately, PA06 is similar to the metal-poor GCs in the MW (particularly M15) and in the dwarf galaxies: it is α-enhanced, with low [Ba/Eu] and [Eu/α] ratios.

6.5.2 Comparisons with M31 Outer Halo Stars

The presence of streams in the metal-poor density map of M31's outer halo (see Figure 2.2) implies that some metal-poor (i.e. low mass) dwarf galaxies are currently being accreted. PA06, PA53, PA54, and PA56 are all consistent with having been accreted from at least one metal-poor dwarf galaxy (but more likely 3-4). None of these GCs have been associated with streams based on their positions. However, Ibata et al. (2014) estimate that $\sim 58\%$ of the metal-poor halo resides in a "smooth" component. If these GCs are part of this smooth component, then they may have been accreted long ago.

The presence of the metal-rich GSS, the associated H I gas, the outer halo stellar mass, and the number of metal-rich GCs in the outer halo indicate that M31 likely experienced a merger with a Sgr or LMC-mass galaxy. The high metallicities and abundance ratios of PA17, H10, and H23 indicate that they originated in higher mass, metal-rich dwarf galaxies like Sgr or the LMC. H23 has been tentatively linked to a stream near the GSS (Stream D; see Veljanoski et al. 2014) based on its position,

though its kinematics suggest that it is not associated with Stream D. H10 and PA17 are not linked to any streams. However, the regions around other bright outer-halo GCs have a large number of metal-rich stars (Richardson et al., 2009), suggesting that they could be located on low surface brightness streams that were undetectable in PAndAS. Ibata et al. (2014) estimate that 86% of the most metal-rich stars in the outer halo are associated with substructure from an accreted companion. It is therefore likely that these GCs were associated with a high mass dwarf satellite. It is also possible that H10, H23, and PA17 were once associated with the same galaxy. In this case, the [α/Fe] ratios clearly imply a knee at [Fe/H] ~ -1.3, indicating an LMC-mass galaxy. If an accretion of an LMC-mass galaxy did occur, it is also likely that several of the other outer halo clusters may be associated with that galaxy as well. Finally, H10's metallicity ([Fe/H] $= -1.36$), radial velocity, and position place it in agreement with the SW Cloud and its GCs PA7 and PA8 (Bate et al., 2014; Mackey et al., 2013a). It is therefore possible that H10 originated in the SW Cloud's progenitor galaxy.

6.6 Conclusions

The abundances presented here confirm that accretion has likely played some role in the formation of M31's outer halo. In particular, the PAndAS cluster abundances provide information about the dwarf progenitors that have been accreted by M31.

- PA17, H23, and H10's high metallicities in M31's outer halo suggest an accretion origin, while their chemical abundances indicate that their progenitor galaxy must have been a fairly massive dwarf, i.e. the size of the LMC or Sgr. The accretion of at least one massive dwarf galaxy is supported by the presence of the GSS and SW Cloud in M31's outer halo. Given its abundances, radial velocity, and location, H10 may be associated with the SW Cloud and its GCs PA7 and PA8.

- PA53, PA54, and PA56 have abundances and metallicities that are more typical of intermediate mass dwarf galaxies like Fornax or Sculptor. This suggests that they are currently being accreted from metal-poor dwarf galaxies and could be associated with the coherent, metal-poor streams observed in PAndAS. Based on their radial velocities PA53 and PA56 could be associated with the same

dwarf galaxy; despite its proximity on the sky, it is unlikely that PA54 is associated with either PA53 or PA56.

- PA06's metallicity makes it a difficult target for chemical tagging analyses because the chemistries between dwarf and massive galaxies have likely not had sufficient time to diverge at [Fe/H] ~ -2. PA06 could therefore have been associated with an intermediate mass dwarf galaxy like Fornax or could have formed *in situ* in a massive galaxy.

- Most of the GCs exhibit signs of the Na/O anticorrelation, which suggests that they are classical GCs.

These detailed IL chemical analyses of PAndAS clusters have identified GCs in an extragalactic system that may have been accreted from dwarf galaxies. This is the first time that such an analysis has been possible *outside of the MW*, as detailed investigations of the chemical abundance ratios of individual targets are only possible with *high resolution* IL spectroscopy.

Chapter 7

Concluding Remarks

This thesis has presented abundance analyses of individual stars and integrated GCs based on high resolution spectra. The methods were tested on well-studied Galactic standards (the stars M67-141 and Arcturus and the GCs 47 Tuc, M3, M13, NGC 7006, and M15) and were then applied to new targets (RGB stars in Pal 1 and outer halo M31 GCs).

The analyses of the standard stars and GCs produced several important findings.

- Abundances of individual stars can be robustly determined given appropriate line measurements and model atmospheres. Accuracy can be improved by employing *differential* analyses (where the Solar abundances are determined with the same lines).

- Integrated abundances from Fe, Ca, Ti, and Ni match the abundances from individual stars. The Na, Mg, Ba, and Eu abundances match the average literature abundances *only when the abundances do not vary between stars in a cluster*. When there are star-to-star variations the integrated abundances fall within the observed range.

- Precisions of ~ 0.1 dex can be obtained from syntheses of single IL spectral lines provided that the input line lists are well-calibrated (to the Sun and Arcturus) and provided that they include molecular features where necessary.

- The integrated abundances can be particularly sensitive to systematic uncertainties in the underlying stellar populations, particularly if the GCs are completely unresolved (such that no *a priori* information is available to constrain the best-fitting isochrone). The [Ca I/Fe I] and [Ni I/Fe I] ratios are the most

stable to these uncertainties. The [Ba/Eu] ratio is generally (though not always) more stable than the individual [Ba II/Fe II] and [Eu II/Fe II] ratios. These stable ratios are the most useful for chemical tagging of extragalactic systems.

After the measurement and analysis methods were well tested, the high resolution IL techniques were applied to two new systems: individual stars in the unusual cluster Palomar 1, and the PAndAS GCs in the outer halo of M31. These studies discovered some valuable clues to the formation of the MW and M31.

The Milky Way: Pal 1's detailed chemical abundances indicate that it may have formed in a dwarf galaxy that was accreted by the MW. This is further supported by its similarity to the intermediate-age LMC clusters and to the Sgr clusters Pal 12 and Ter 7. Thus, the MW's current halo has at least partially been built up from the accretion of dwarfs. Pal 1's progenitor stream has not yet been identified; however, its abundances indicate that it likely came from a fairly massive satellite (with a mass close to that of Sgr). Pal 1 cannot be considered a "classical" GC because of its lack of a Na/O anticorrelation (which is likely due to its low mass). There are other clusters which are similar to Pal 1 that would be interesting targets for future observations.

M31: Accretion has also played a significant role in the formation of M31's outer halo. PAndAS identified coherent metal-poor streams surrounding M31—this analysis identified several metal-poor GCs that may be associated with these streams. These clusters are chemically most like the metal-poor, intermediate mass dwarf galaxies Fornax and Sculptor. The PAndAS survey also identified a significant metal-rich outer halo component, whose stars could have been recently accreted from a massive dwarf. This analysis identified three GCs whose abundance patterns and locations hint at an origin in a massive dwarf like the LMC or Sgr. Thus, it seems as though M31 has had a fairly active accretion history, compared to the MW.

The projects presented in this thesis have provided small clues about the formation of the outer halos of the two large spiral galaxies in the Local Group, though a substantial amount of work remains to characterize fully the properties of galaxy formation, both in and out of the Local Group.

Other MW clusters and streams. Table 3.11 provided a list of more unusual clusters whose abundance patterns might be useful. In addition, future surveys

such as GAIA/ESO, the Apache Point Observatory Galactic Evolution Experiment (APOGEE), or the GALactic Archaeology with HERMES (GALAH) survey will provide comprehensive, homogeneous data sets with kinematic *and* abundance information. These surveys could identify more streams from accreted galaxies, as well as more chemically unusual clusters. These surveys will also be able to more fully characterize the various components of the MW (e.g. the thin and thick disks).

M31's outer halo. There are more PAndAS clusters that can be observed in integrated light. Additional observations of PA17 to increase the S/N would enable better determinations of the Eu II abundances, which would help constrain the abundance patterns. There are also many other interesting elements that could be investigated in IL (e.g. other α-elements such as Si, first-peak neutron capture elements like Y, or ambiguous elements like Cu). Furthermore, medium resolution observations of individual stars in the stellar streams would provide kinematics, metallicities, and [α/Fe] ratios of the accreted dwarf galaxy field stars.

Extragalactic systems. Ultimately, IL spectroscopy is ideal for targets outside of the Local Group. It is currently possible to reach targets as far away as ~ 4 Mpc (e.g. Colucci et al. 2013). With high resolution spectrographs on thirty metre telescopes, it will be possible to reach even more distant targets. More low resolution studies (e.g. CaT and Lick index surveys) will enable large numbers of GCs to be studied. Finally, observations in new wavelength regions, such as the near-infrared, will enable abundance ratios of different elements from the optical (e.g. C, N, O, Al) and may have different sensitivities to the underlying stellar populations.

Bibliography

Abell, G.O. PASP, 67, 258

Allende Prieto, C., Lambert, D.L., & Asplund, M. 2001, ApJ, 556, L63

Alonso, A., Arribas, S., & Martínez-Roger, C. 1996, A&AS, 117, 227

Alonso, A., Arribas, S., & Martínez-Roger, C. 1999, A&AS, 140, 261

Alonso, A., Arribas, S., & Martínez-Roger, C. 1999, A&A, 376, 1039

Alpaslan, M. 2009, arXiv:0912.4755

Alves, D.R. & Sarajedini, A. 1999, ApJ, 511, 225

Alves-Brito, A., Barbuy, B., Ortolani, S. et al. 2005, A&A, 435, 657

Anderson, J., Sarajedini, A., Bedin, L.R., et al. 2008, 135, 2055

Andreuzzi, G., Bragaglia, A., Tosi, M., & Marconi, G. 2011, MNRAS, 412, 1265

Aoki, W., Honda, S., Beers, T.C., et al. 2007, ApJ, 660, 747

Aoki, W., Arimoto, N., Sadakane, K., et al. 2009, A&A, 502, 569

Arp, H.C., Baum, W.A., & Sandage, A.R. 1952, AJ, 57, 4

Ashman, K.M. & Zepf, S.E. 1992, ApJ, 384, 50

Asplund, M., Grevesse, N., Sauval, J.A., & Scott, P. 2009, ARA&A, 47, 481

Barklem, P. S., Piskunov, N., & O'Mara, B. J. 2000, A&AS, 142, 467

Barklem, P. S. & Aspelund-Johansson, J. 2005, A&A, 435, 373

Bash, F. 1999, in 16th IEEE Instrumentation and Measurement Technology Conference: Measurements for the new millenium, ed. E.A. Whitaker, 639

Bate, N.F., Conn, A.R., McMonigal, B., et al. 2014, MNRAS, 437, 3362

Baumüeller, D., Butler, K., & Gehren, T. 1998, A&A, 338, 637

Behr, B.B., Cohen, J.G., & McCarthy, J.K. 2000, ApJ, 531, L37

Behr, B.B. ApJS, 149, 67

Bell, E.F., Zucker, D.B., Belokurov, V. et al. 2008, ApJ, 680, 295

Bergemann, M. & Cescutti, G. 2010, A&A, 522, A9

Bergemann, M. & Gehren, T. 2007, A&A, 473, 291

Biehl, D. 1976, PhD Thesis: Univ. Kiel

Bisterzo, S., Gallino, R., Straniero, O., Cristallo, S., & Käppeler, F. 2010, MNRAS, 404, 1529

Böhm-Vitense, E. 1989, Introduction to Stellar Astrophysics, Volume 2: Stellar Atmospheres (Cambridge: Cambridge University Press)

Bond, H.E. & Neff, J.S. 1969, ApJ, 158, 1235

Booth, A.J., Shallis, M.J., & Wells, M. 1983, MNRAS, 205, 191

Briley, M.M. 1997, AJ, 114, 1051

Briley, M.M., Harbeck, D., Smith, G.H., & Grebel, E. 2004, AJ, 127, 1588

Brodie, J.P. & Strader, J. 2006, ARA&A, 44, 193

Brown, J.A. & Wallerstein, G. 1992, AJ, 104, 1818

Buonanno, R., Corsi, C.E., Pulone, L., Fusi Pecci, F., & Bellazzini, M. 1998, A&A, 333, 505

Burris, D.L., Pilachowski, C.A., Armandroff, T.E., et al. 2000, ApJ, 544, 302

Caldwell, N., Schiavon, R., Morrison, H., Rose, J.A., & Harding, P. 2011, AJ, 141, 18

Cameron, S. 2009, PhD Thesis: The development of a detailed abundance analysis method intended for the integrated light spectra of extragalactic globular clusters (Michigan: University of Michigan)

Campbell, S.W., D'Orazi, V., Yong, D., et al. 2013, *Nature*, 498, 198

Carollo, D., Beers, T.C., Lee, Y.S. 2007, *Nature*, 450, 1020

Carraro, G., Bresolin, F., Villanova, S., et al. 2004, AJ, 128, 1676

Carraro, G., Zinn, R., & Bidin, M. 2007, A&A, 466,181

Carraro, G., & Bensby, T. 2009, MNRAS, 397, L106

Carretta, E., Gratton, R.G., Bragaglia, A., Bonifacio, P., & Pasquini, L. 2004, A&A, 416, 925

Carretta, E., Bragaglia, A., Gratton, R., & Lucatello, S. 2009a, A&A, 505, 139

Carretta, E., Bragaglia, A., Gratton, R., D'Orazi, V., & Lucatello, S. 2009b, A&A, 508, 695

Carretta, E., Bragaglia, A., Gratton, R., Lucatello, S., Bellazzini, M., & D'Orazi, V. 2010a, ApJ, 712, L21

Carretta, E., Bragaglia, A., Gratton, R.G., et al. 2010b, A&A, 516, 55

Carroll, B.W. & Ostlie, D.A. 2006, Benjamin Cummings (2nd ed.; New York)

Casagrande, L., Ramírez, I., Meléndez, J., Bessell, M., & Asplund, M. 2010, A&A, 512, 54

Castelli, F. & Kurucz, R. L. 2004, in IAU Symp. 210, Modelling of Stellar Atmospheres, ed. N. Piskunov, W.W. Weiss, & D. F. Gray (San Francisco: ASP), A20

Cayrel, R. 1988, in IAU Symp. 132, The Impact of Very High S/N Spectroscopy on Stellar Physics, ed. G. Cayrel de Strobel & M. Spite (Dordrecht: Kluwer), 345

Cayrel, R. et al. 2004, A&A, 416, 1117

Cescutti, G., Matteucci, F., Lanfranchi, G.A., & McWilliam, A. 2008, A&A, 491, 401

Chaboyer, B., Demarque, P., & Sarajedini, A. 1996, ApJ, 459, 558

Chabrier, G. 2003, PASP, 115, 763

Chies-Santos, A.L., Larsen, S.S., Kuntschner, H. 2011, A&A, 525, A20

Chou, M.-Y., Cunha, K., Majewski, S.R., et al. 2010a, ApJ, 708, 1290

Chou, M.-Y., Majewski, S.T., Cunha, K., et al. 2010b, ApJ, 720, 10

Clementini, G. 2010, in Variable Stars, The Galactic Halo and Galaxy Formation, ed. Sterken, C., Samus, N. & Szabados, L., 111

Coc, A. 2009, *Nuclear Instruments and Methods in Physics Research Section A*, 611, 224

Coelho, P., Percival, S.M., & Salaris, M. 2011, ApJ, 734, 72

Cohen, J. 2004, AJ, 127, 1545

Cohen, J.G. & Melendez, J. 2005, AJ, 129, 303

Cohen, J., Christlieb, N., McWilliam, A., et al. 2008, ApJ, 672, 320

Cohen, J.G. 2011, ApJ, 740, L38

Cohen, J.G. & Kirby, E. N. 2012, ApJ, 760, 86

Collins, M.L.M., Chapman, S.C., Rich, R.M., et al. 2013, ApJ, 768, 172

Colucci, J.E., Bernstein, R.A., Cameron, S., McWilliam, A., & Cohen, J.G. 2009, ApJ, 704, 385

Colucci, J.E., Bernstein, R.A., Cameron, S.A., & McWilliam, A. 2011, ApJ, 735, 55

Colucci, J.E. & Bernstein, R.A. 2011, EAS Pub. Ser., 48, 275

Colucci, J.E., Bernstein, R.A., Cameron, S.A., & McWilliam, A. 2012, ApJ, 746, 29

Colucci, J.E., Duran, M.F., Bernstein, R.A., & McWilliam, A. 2013, ApJ, 773, 36

Conroy, C. & Spergel, D.N. 2011, ApJ, 726, 36

Cordero, M.J., Pilachowski, C.A., Johnson, C.I., McDonald, I., Zijlstra, A.A., & Simmerer, J. 2014, ApJ, 780, 94

Cordier, D., Pietrinferni, A., Cassisi, S., & Salaris, M. 2007, AJ, 133, 468

Côté, P., Pryor, C., McClure, R.D., Fletcher, J.M., & Hesser, J.E. 1996, AJ, 112, 574

Côté, P., Marzke, R.O., & West, M.J. 1998, ApJ, 501, 554

Côté, P., Marzke, R.O., West, M.J., & Minniti, D. 2000, ApJ, 533, 869

Crane, J., Majewski, S., Rocha-Pinto, H., et al. 2003, ApJ, 594, L119

Da Costa, G.S. & Armandroff, T.E. 1995, AJ, 109, 2533

Decressin, T., Meynet, G., Charbonnel, C., Prantzos, N., & Ekström, S. 2007, A&A, 464, 1029

De Marchi, F., De Angeli, F., Piotto, G., Carraro, G., & Davies, M.B. 2006, A&A, 459, 489

Denissenkov, P. & Hartwick F.D.A. 2013, MNRAS, 437, L21

Djorgovski, S.G., Gal, R.R., McCarthy, J.K., et al. 1997, ApJ, 474, L19

Dotter, A. 2008, ApJ, 687, L21

Dotter, A., Chaboyer, B., Jevremović, D., Kostov, V., Baron, E., & Ferguson, J.W. 2008, ApJS, 178, 89

Dotter, A., Sarajedini, A., Anderson, J., et al. 2010, ApJ, 708, 698

Dotter, A., Sarajedini, A., & Anderson, J. 2011, ApJ, 738, 74

Eggen, O.J., Lynden-Bell, D., & Sandage, A.R. 1962, ApJ, 136, 748

Faber, S.M., Friel, E.D., Burstein, D., & Gaskell, C.M. 1985, ApJS, 57, 711

Fagerholm, E. 1906, Inaugural dissertation, Uppsala

Fardal, M.A., Weinberg, M.D., Babul, A., et al. 2013, MNRAS, 434, 2779

Ferguson, J.W., Alexander, D.R., Allard, F. et al. 2005, ApJ, 623, 585

Forbes, D.A., Brodie, J.P., & Grillmair, C.J. 1997, AJ, 113, 1652

Forbes, D.A., & Bridges, T. 2010, MNRAS, 404, 1203

Forbes, D.A., Spitler, L.R., Strader, J. et al. 2011, MNRAS, 413, 2943

Forte, J.C., Vega, E.I., & Faifer, F. 2009, MNRAS, 397, 1003

Foster, C., Forbes, D.A., Proctor, R.N., et al. 2010, AJ, 139, 1566

Foster, C., Spitler, L.R., Romanowsky, A.J. et al. 2011, MNRAS, 415, 3393

Frebel, A., Kirby, E., & Simon, J. D. 2010, *Nature*, 464, 72

Freeman, K. & Bland-Hawthorn, J. 2002, ARA&A, 40, 487

Friel, E.D., Jacobson, H.R., & Pilachowski, C.A. 2010, AJ, 139, 1942

Frinchaboy, P.M., Muñoz, R.R., Phelps, R.L., Majewski, S.R., & Kunkel, W.E. 2006, AJ, 131, 922

Fulbright, J.P. 2000, AJ, 120, 1841

Fulbright, J.P. 2002, AJ, 123, 404

Fulbright, J.P., McWilliam, A., & Rich, R.M. 2006, ApJ, 636, 821

Fulbright, J.P., McWilliam, A., & Rich, R.M. 2007, ApJ, 661, 1152

Galleti, S., Federici, L., Bellazzini, M., Fusi Pecci, F., & Macrina, S. 2004, A&A, 416, 917

Gallino, R., Arlandini, C., Busso, M., et al. 1998, ApJ, 497, 388

Geisler, D., Smith, V. V., Wallerstein, G., Gonzalez, G., & Charbonnel, C. 2005, AJ, 129, 1428

Geisler, D., Wallerstein, G., Smith, V.V., & Casetti-Dinescu, D.I. 2007, PASP, 119, 939

Georgiev, I.Y., Puzia, T.H., Goudfrooij, P., & Hilker, M. 2010, MNRAS, 406, 1967

Gibson, B.K., Madgwick, D.S., Jones, L.A., Da Costa, G.S., & Norris, J.E. 1999, AJ, 118, 1268

Gilroy, K.K. & Brown, J.A. 1991, ApJ, 371, 578

Goldsbury, R., Richer, H.B., Anderson, J., Dotter, A., Sarajedini, A., & Woodley, K. 2010, AJ, 140, 1830

Goldsbury, R., Heyl, J., & Richer, H. 2013, ApJ, 778, 57

Gratton, R.G., Carretta, E., & Castelli, F. 1996, A&A, 314, 191

Gratton, R.G., Sneden, C., Carretta, E., & Bragaglia, A. 2000, A&A, 354, 169

Gratton, R.G., Carretta, E., & Bragaglia, A. 2012, ARA&A, 20, 50

Gratton, R.G., Lucatello, S., Sollima, A. et al. 2013, A&A, 549, 41

Graves, G.I. & Schiavon, R.P. 2008, ApJS, 177, 446

Grundahl, F., Catelan, M., Landsman, W.B., Stetson, P.B., & Andersen, M.I. 1999, ApJ, 524, 242

Guhathakurta, P., Yanny, B., Schneider, D.P., & Bahcall, J.N. 1992, AJ, 104, 1790

Gustafsson, B., Edvardsson, B., Eriksson, K., Jørgensen, U.G., Nordlund, A., Plez, B. 2008, A&A, 486, 951

Hammer, F., Puech, M., Flores, H., Yang, Y.B., Wang, J.L., & Fouquet, S. 2011, in "Assembling the Puzzle of the Milky Way," Le Grand-Bornand, France, ed. Reylé, C., Robin, A., & Schultheis, M.; EPJ Web of Conferences, 19

Harris, W.E. & van den Bergh, S. 1981, AJ, 86, 1627

Harris, W.E. 1996, AJ, 112, 1487 (2010 edition)

Harris, W.E. 2000, Globular Cluster Systems, Saas-Fee Lectures

Harris, W.E., Whitmore, B.C., Karakla, D., et al. 2006, ApJ, 636, 90

Harris, W.E. 2009a, ApJ, 699, 254

Harris, W.E. 2009b, ApJ, 703, 939

Hartwick, F. D. A. 1987, in *The Galaxy*, ed. Gilmore, G. & Carsswell, B., NATO ASI Series 207, Reidel, Dordrecht

Helmi, A. & White, S.D.M. 1999, MNRAS, 307, 495

Hertzprung, E. 1915, ApJ, 41, 10

Herwig, F. 2005, ARA&A, 43, 435

Herwig, F., VandenBerg, D.A., Navarro, J.F., Ferguson, J., & Paxton, B. 2012, ApJ, 757, 132

Hinkle, K., Wallace, L., Livingston, W., Ayres, T., Harmer, D., & Valenti, J. 2003, in *The Future of Cool-Star Astrophysics: 12th Cambridge Workshop on Cool Stars, Stellar Systems, and the Sun (2001 July 30 - August 3)*, eds. A. Brown, G.M. Harper, and T.R. Ayres, (University of Colorado), 851

Høg, E., Fabricius, C., Makarov, V.V., et al. 2000, A&A, 355L, L27

Howell, J.H., Guhathakurta, P., & Gilliland, R.L. 2000, PASP, 112, 1200

Huxor, A.P, Tanvir, N.R., Ferguson, A.M.N., et al. 2008, MNRAS, 385, 1989

Huxor, A.P., Mackey, A.D., Ferguson, A.M.N., et al. 2014, MNRAS, arXiv:1404.5807

Ibata, R.A., Lewis, G.F., Conn, A.R., et al. 2013, *Nature*, 493, 62

Ibata, R.A., Lewis, G.F., McConnachie, A.W., et al. 2014, ApJ, 780, 128

Iwamoto, K., Brachwitz, F., Nomoto, K., et al. 1999, ApJS, 125, 439

Janes, K.A. & Smith, G.H. 1984, AJ, 89, 487

Jasniewicz, G., de Laverny, P., Parthasarathy, M., Lèbre, A., & Thévenin, F. 2004, A&A, 423, 353

Johnson, J.A., Ivans, I.I., & Stetson, P.B. 2006, ApJ, 640, 801

Johnson, C.I. & Pilachowski, C.A. 2010, ApJ, 722, 1373

Johnson, C.I. & Pilachowski, C.A. 2012, ApJ, 754, L38

Johnston, K.V., Bullock, J.S., Sharma, S. et al. 2008, ApJ, 689, 936

Jones, L. A. & Worthey, G. 1995, ApJ, 446, L31

Kirby, E.N., Guhathakurta, P., & Sneden, C. 2008, ApJ, 682, 1217

Kirby, E.N., Guhathakurta, P., Bolte, M., Sneden, C., & Geha, M.C. 2009, ApJ, 705, 328

Koch, A., Grebel, E. K., Gilmore, G. F., et al. 2008, AJ, 135, 1580

Koch, A. & McWilliam, A. 2008, AJ, 135, 1551

Korn, A.J., Maraston, C., & Thomas, D. 2005, A&A, 438, 685

Korn, A.J., Grundahl, F., Richard, O. et al. 2007, ApJ, 671, 402

Kraft, R.P., Sneden, C., Smith, G.H., Shetrone, M.D., & Fulbright, J. 1998, AJ, 115, 1500

Kravtsov, V., Alcaino, G., Marconi, G., & Alvarado, F. 2014, A&A, 527, L9

Kroupa, P. 2002, *Science*, 295,82

Kupka, F., Ryabchikova, T.A., Piskunov, N.E., Stempels, H.C., & Weiss, W.W. 2000, *Baltic Astronomy*, 9, 590

Kurucz, R.L. 2005, Mem. Soc. Astron. Italiana, 8, 189

Lambert, D.L. & Ries, L.M. 1981, ApJ, 248, 228

Lata, S., Pandey, A.K., Sagar, R., & Mohan, V. 2002, A&A, 388, 158

Law, D.R., & Majewski, S.R. 2010, ApJ, 718, 1128

Lawler, J.E., Bonvallet, G., & Sneden, C. 2001a, ApJ, 556, 452

Lawler, J.E., Wickliffe, M.E., den Hartog, E.A., & Sneden, C. 2001b, ApJ, 563, 1075

Leaman, R., VandenBerg, D.A., & Mendel, J.T. 2013, MNRAS, 436, 122

Lee, H.-C., Yoon, S.-J., & Lee, Y.-W. 2000, AJ, 120, 998

Lee, H.-C. & Worthey, G. 2005, ApJS, 160, 176

Lee, H., Worthey, G., Dotter, A. et al. 2009, ApJ, 694, 902

Leigh, N., Knigge, C., Sills, A., Perets, H.B., Sarajedini, A., Glebbeek, E. 2013, MNRAS, 428, 897

Letarte, B., Hill, V., Jablonka, P., Tolstoy, E., François, P., & Meylan, G. 2006, aap, 453, 547

Letarte, B., Chapman, S.C., Collins, M. et al. 2009, MNRAS, 400, 1472

Letarte, B., Hill, V., Tolstoy, E., et al. 2010, A&A, 523, 17

Lewis, G.F., Braun, R., McConnachie, A.W., et al. 2013, ApJ, 763, 4

Lind, K., Asplund, M., Barklem, P.S., & Belyaev, A.K. 2011, A&A, 528, 103

Liu, C., Peng, E.W., Jordán, A., et al. 2011, ApJ, 728, 116

Lodders, K., Palme, H., & Gail, H.P. 2009, in the Landolt-Brnstein Database: 4.4 Abundances of the elements in the Solar System, e.d. Trmper, J.E. (Berlin:Springer-Verlag)

Lovisi, L., Mucciarelli, A., Lanzoni, B. et al. 2012, ApJ, 754, 91

Mackey, A.D. & van den Bergh, S. 2005, MNRAS, 360, 631

Mackey, A.D., Huxor, A., Ferguson, A.M.N., et al. 2007, ApJ, 655, L85

Mackey, A.D., Huxor, A.P., Ferguson, A.M.N. et al. 2010, ApJ, 717, 11

Mackey, A.D., Huxor, A.P., Ferguson, A.M.N., et al. 2013a, MNRAS, 429, 281

Mackey, A.D., Huxor, A.P., Martin, N.F., et al. 2013b, ApJ, 770, 17

Maraston, C. 2005, MNRAS, 362, 799

Martin, N.F., Ibata, R.A., Bellazzini, M., et al. 2004, MNRAS, 348, 12

Mashonkina, L.I., Shimanskiĭ, V.V., & Sakhibullin, N.A. 2000, *Astronomy Reports*, 44, 790

Massey, P., Valdes, F., & Barnes, J. 1992, A User's Guide to Reducing Slit Spectra with IRAF (`http://iraf.noao.edu/docs/spectra.html`)

Matteucci, F., Spitoni, E., Recchi, S., & Valiante, R. 2009, A&A, 501, 531

McCall, M.L. 2004, AJ, 128, 2144

McConnachie, A.W. et al. 2009, *Nature*, 461, 66

McConnachie, A.W. & Côté, P. 2010, ApJ, 722, L209

McWilliam, A., Preston, G.W., Sneden, C., & Shectman, S. 1995a, AJ, 109, 2736

McWilliam, A., Preston, G.W., Sneden, C., & Searle, L. 1995b, AJ, 109, 2757

McWilliam, A. 1998, AJ, 115, 1640

McWilliam, A. & Smecker-Hane, T.A. 2005, in ASP Conf. Ser. 336, Cosmic Abundances as Records of Stellar Evolution and Nucleosynthesis in honor of David L. Lambert, ed. T.G. Barnes III & F.N. Bash (San Francisco, CA: ASP), 221

McWilliam, A. & Bernstein, R. 2008, ApJ, 684, 326

McWilliam, A., Wallerstein, G., & Mottini, M. 2013, ApJ, 778, 149

Michaud, G., Richer, J., & Richard, O. 2011, aap, 529, A60

Milone, A.P., Bedin, L.R., Piotto, G., & Anderson, J. 2009, A&A, 497, 755

Milone, A.P., Piotto, G., Bedin, L.R., et al. 2012, ApJ, 744, 58

Monaco, L., Bellazzini, M., Bonifacio, P., et al. 2007, A&A, 464, 201

Monaco, L, Saviane, I., Correnti, M., Bonifacio, P, & Geisler, D. 2011, A&A, 525, 124

Mottini, M., Wallerstein, G., McWilliam, A. 2008, AJ, 136, 614

Mucciarelli, A., Carretta, E., Origlia, L., Ferraro, F.R. 2008, AJ, 136, 375

Niederste-Osholt, M., Belokurov, V., Evans, N.W., et al. 2010, MNRAS, 408, L66

Nissen, P.E. & Schuster, W.J. 2011, A&A, 530, A15

Noguchi, K., Aoki, W., Kawanomoto, S., et al. 2002, *PASJ*, 54, 855

Ocvirk, P. 2010, ApJ, 709, 88

Önehag, A., Korn, A., Gustafsson, B., Stempels, E., & VandenBerg, D.A. 2011, A&A, 528, 85

Pancino, E., Carrera, R., Rossetti, E., & Gallart, C. 2010, A&A, 511, A56

Peñarrubia, J. 2013, MNRAS, 433, 2576

Peng, E., Jordán, A., Côté, P. et al. 2006, ApJ, 639, 95

Percival, S.M. & Salaris, M. 2009, ApJ, 703, 1123

Percival, S. & Salaris, M. 2011, MNRAS, 412, 2445

Peterson, R.C. 1985, ApJ, 294, L35

Pietrinferni, A., Cassisi, S., Salaris, M. & Castelli, F. 2004, ApJ, 612, 168

Pietrinferni, A., Cassisi, S., Salaris, M. & Castelli, F. 2006, ApJ, 642, 797

Pilachowski, C., Sneden, C., Freeland, E., & Casperson, J. 2003, AJ, 125, 794

Plez, B. & Lambert, D.L. 2002, A&A, 386, 1009

Pompéia, L., Hill, V., Spite, M., et al. 2008, A&A, 480, 379

Preston, G.W., Sneden, C., Thompson, I.B., Shectman, S.A., & Burley, G.S. 2006, AJ, 132, 85

Pritzl, B.J., Venn, K.A., & Irwin, M. 2005, AJ, 130, 2140

Prochaska, J.X., Naumov, S.O., Carney, B.W., McWilliam, A., & Wolfe, A.M. 2000, AJ, 120, 2513

Puzia, T.H., Kissler-Patig, M., & Goudfrooij, P. 2006, ApJ, 648, 383

Puzia, T.H. & Sharina, M.E. 2008, ApJ, 674, 909

Ramirez, I., & Melendez, J. 2005, ApJ, 626, 465

Ramírez, I. & Allende Prieto, C. 2011, ApJ, 743, 135

Ramsey, L.W., Adams, M.T., Barnes, T.G., et al. 1998, Proc. SPIE, 3352, 34

Reddy, B.E., Tomkin, J., Lambert, D.L., Allende Prieto, C. 2003, MNRAS, 340, 304

Reddy, B.E., Lambert, D.L., & Prieto, C.A. 2006, MNRAS, 367, 1329

Rejkuba, M., Greggio, L., Harris, W.E., Harris, G.L.H., & Peng, E.W. 2005, ApJ, 631, 262

Richardson, J.C., Ferguson, A.M.N., Mackey, A.D., et al. 2009, MNRAS, 396, 1842

Richardson, J.C., Irwin, M.J., McConnachie, A.W., et al. 2011, ApJ, 732, 76

Robin, A.C., Reylé, C., Derrière, S., & Picaud, S. 2003, A&A, 409, 523

Roederer, I.U. 2011, ApJ, 732, L17

Rosenberg, A., Saviane, I., Piotto, G., Aparicio, A., & Zaggia, S.R. 1998a, AJ, 115, 648

Rosenberg, A., Piotto, G., Saviane, I., Aparicio, A., & Gratton, R. 1998b, AJ, 115, 658

Sakari, C.M., Venn, K.A., Irwin, M., Aoki, W., Arimoto, N., & Dotter, A. 2011, ApJ, 740, 106

Sakari, C.M., Shetrone, M., Venn, K., McWilliam, A., & Dotter, A. 2013, MNRAS, 434, 358

Salaris, M. & Weiss, A. 2002, A&A, 388, 492

Salpeter, E.E. 1955, ApJ, 121, 161

Sandage, A.R. 1953, AJ, 58, 61

Sandage, A. & Wallerstein, G. 1960, ApJ, 131, 598

Sandage, A. & Wildey, R. 1967, ApJ, 150, 469

Sanders, W.L. 1977, A&AS, 27, 89

Sarajedini, A.,Bedin, L.R., Chaboyer, B., et al. 2007, AJ, 133, 1658

Saviane, I., Monaco, L., Correnti, M., Bonifacio, P., Geisler, D. 2010, EAS Pub. Ser., 48, 251

Sbordone, L., Bonifacio, P., Marconi, G., Zaggia, S., & Buonanno, R. 2005a, A&A, 430, L13

Sbordone, L., Bonifacio, P., Marconi, G., Buonanno, R., & Zaggia, S. 2005b, A&A, 437, 905

Sbordone, L., Bonifacio, P., Buonanno, R., et al. 2007, A&A, 465, 815

Schiavon, R.P., Faber, S.M., Castilho, B.V., & Rose, J.A. 2002, ApJ, 580, 850

Schiavon, R.P., Rose, J.A., Courteau, S., & MacArthur, L.A. 2004, ApJ, 608, L33

Schiavon, R.P., Caldwell, N., Conroy, C., et al. 2013, ApJ, 776, L7

Schlegel, D.J., Finkbeiner, D.P., & Davis, M. 1998, ApJ, 500, 525

Schroeder, D.J. 1987, Astronomical Optics (1st ed.; Toronto: Academic Press, Inc.)

Schuberth, Y., Richtler, T., Hilker, M., et al. 2010, A&A, 513, A52

Searle, L. & Zinn, R. 1978, ApJ, 225, 357

Shetrone, M.D., Smith, G.H., Briley, M.M., Sandquist, E., & Kraft, R.P. 1999, PASP, 111, 1115

Shetrone, M.D., Côté, P., & Sargent, W.L.W. 2001, ApJ, 548, 592

Shetrone, M., Venn, K., Tolstory, E., et al. 2003, AJ, 125, 684

Shetrone, M.D., Cornell, M.E., Fowler, J.R., et al. 2007, PASP, 119, 556

Shetrone, M.D., Siegel, M.H., Cook, D.O., & Bosler, T. 2009, AJ, 137, 62

Short, C.I., & Hauschildt, P.H. 2006, ApJ, 641, 494

Simmerer, J., Sneden, C., Cowan, J.J., et al. 2004, ApJ, 617, 1091

Sirianni, M., Jee, M.J., Benítez, N., et al. 2005, PASP, 117, 1049

Sneden, C. 1973, ApJ, 184, 839

Sneden, C., Kraft, R.P., Shetrone, M.D., Smith, G.H., Langer, G.E., & Prosser, C.F. 1997, AJ, 114, 1964

Sneden, C., Kraft, R.P, Guhathakurta, P., Peterson, R.C., & Fulbright, J. 2004, AJ, 127, 2162

Sobeck, J.S., Lawler, J.E., & Sneden, C. 2007, ApJ, 667, 1267

Sobeck, J.S., Kraft, R.P., Sneden, C. et al. 2011, AJ, 141, 175

Springel, V., White, S.D.M., Jenkins, A., et al. 2005, *Nature*, 435, 629

Stetson, P.B. & Pancino, E. 2008, PASP, 120, 1332

Suda, T., Katsuta, Y., Yamada, S. et al. 2008, PASJ, 60, 1159

Tafelmeyer, M., Jablonka, P., Hill, V., et al. 2010, A&A, 524, A58

Tanvir, N.R., Mackey, A.D., Ferguson, A.M.N., et al. 2012, MNRAS, 422, 162

Tautvaišienė, G., Edvardsson, B., Tuominen, L., Ilyin, I. 2000, A&A, 360, 499

Tinsley, B.M. 1979, ApJ, 229, 1046

Tollerud, E.J., Beaton, R.J., Geha, M.C., et al. 2012, ApJ, 752, 45

Tolstoy, E., Hill, V., & Tosi, M. 2009, ARA&A, 47, 371

Tonry, J. & Davis, M. 1979, AJ, 84, 1511

Travaglio, C., Gallino, R., Arnone, E., et al. 2004, ApJ, 601, 864

Tripicco, M.J. & Bell, R.A. 1995, AJ, 110, 3035

Tull, R.G., 1998, Proc. SPIE, 3355, 387

VandenBerg, D.A., Swenson, F.J., Rogers, F.J., Iglesias, C.A., & Alexander, D.R. 2000, ApJ, 532, 430

VandenBerg, D. & Stetson, P. 2004, PASP, 116, 997

VandenBerg, D.A., Bergbusch, P.A., & Dowler, P.D. 2006, ApJS, 162, 375

VandenBerg, D.A., Bergbusch, P.A., Dotter, A., et al. 2012, ApJ, 755, 15

VandenBerg, D.A., Brogaard, K., Leaman, R., & Casagrande, L. 2013, ApJ, 775, 134

Vargas, L.C., Geha, M.C., & Tollerud, E.J. 2014, ApJ, arXiv:1406.0510

Vazdekis, A., Salaris, M., Arimoto, N., & Rose, J. 2001, ApJ, 549, 274

Veljanoski, J., Ferguson, A.M.N., Mackey, A.D., et al. 2013, ApJ, 768, 33

Veljanoski, J., Mackey, A.D., Ferguson, A.M.N., et al. 2014, MNRAS, arXiv:1406.0186

Venn, K.A., Irwin, M., Shetrone, M.D., et al. 2004, AJ, 128, 1177

Venn, K.A., Shetrone, M.D., Irwin, M.J. et al. 2012, ApJ, 751, 102

Ventura, P. & D'Antona, F. 2009, A&A, 499, 835

Ventura, P. & D'Antona, F. 2011, MNRAS, 410, 2760

Vesperini, E., McMillan, S.L.W., D'Antona, F., & D'Ercole, A. 2013, MNRAS, 429, 1913

Walker, M.G., Mateo, M., Olszewski, E.W., et al. 2006, AJ, 131, 2114

Wanajo, S., Janka, H.-T., Müller, B. 2013, ApJ, 767, L26

Woodley, K.A., Harris, W.E., Puzia, T.H. et al. 2010, ApJ, 708, 1335

Woosley, S.E. & Weaver, T.A. 1995, ApJS, 101, 181

Worley, C.C., Cottrell, P.L., Freeman, K.C., & Wylie-de-Boer, E.C. 2009, MNRAS, 400, 1039

Worley, C.C., Hill, V., Sobeck, J., & Carretta, E. 2013, A&A, 553, A47

Worthey, G., Faber, S.M., González, J.J., & Burstein, D. 1994, ApJS, 94, 687

Worthey, G. 1994, ApJS, 95, 107

Worthey, G., Tang, B., & Serven, J. 2014, ApJ, 783, 20

Wylie, E.C., Cottrell, P.L., Sneden, C.A., & Lattanzio, J.C. 2006, ApJ, 649, 248

Yong, D., Grundahl, F., Lambert, D.L., Nissen, P.E., & Shetrone, M.D. 2003, A&A, 402, 985

Yong, D., Carney, B.W., & Teixera de Almeida, M.L. 2005, AJ, 130, 597

Yong, D., Aoki, W., & Lambert, D.L. 2006, ApJ, 638, 1018

Yong, D., Karakas, A.I., Lambert, D.L., Chieffi, A., & Limongi, M. 2008, ApJ, 689, 1031

Yong, D., Meléndez, J., Grundahl, F., et al. 2013, MNRAS, 434, 3542

Yoon, S.-J., Yi, S.K., & Lee, Y.-W. 2006, Science, 311, 1129

Zhang, L., Ishigaki, M., Aoki, W., Zhao, G., & Chiba, M. 2009, ApJ, 706, 1095

Zhao, B. & Bailyn, C.D. 2005, AJ, 129, 1934

Zolotov, A., Willman, B., Brooks, A.M. et al. 2009, ApJ, 702, 1058

Zolotov, A., Willman, B., Brooks, A.M., et al. 2010, ApJ, 721, 738

Appendix A

Acronyms Used in this Thesis

Below is a list of the acronyms used in this paper. Object designations (e.g. 47 Tuc, M3, etc.) and reference abbreviations (e.g. MB08) are not included here.

AGB = Asymptotic Giant Branch
AMR = Age Metallicity Relation
BS = Blue Straggler
CDM = Cold Dark Matter
CMD = Colour-Magnitude Diagram
CTR = Colour-Temperature Relation
EW = Equivalent Width
FWHM = Full Width at Half Maximum
GC = Globular Cluster
GSS = Giant Stellar Stream (in M31)
HB = Horizontal Branch
HDS = High Dispersion Spectrograph, on the Subaru Telescope
HET = Hobby-Eberly Telescope
HFS = Hyperfine Structure
HRS = High Resolution Spectrograph, on the HET
HST = *Hubble Space Telescope*
IL = Integrated Light
IMF = Initial Mass Function
LF = Luminosity Function
LPV = Long Period Variable
LTE = Local Thermodynamic Equilibrium

MMR = Mass Metallicity Relation
MS = Main Sequence
MW = Milky Way
NLTE = Non-LTE
PAndAS = Pan-Andromeda Archaeological Survey
RGB = Red Giant Branch
SED = Spectral Energy Distribution
S/N = Signal to Noise SN = Supernova (plural, SNe = supernovae)
SS = Spectrum Synthesis
UFD = Ultra-faint dwarf

Appendix B

PAndAS Clusters not Observed in this Thesis

Table B.1 shows the properties of the other PAndAS clusters that were not observed in this thesis. They are grouped based on the reasons they were not observed. The first group shows the PAndAS GCs that were rejected only because they are closer to the centre of M31; however, given the nature of PA17 (see Chapter 6) they may be interesting targets in the future. The second group shows clusters that are slightly too faint for the HET, and require more than 8 hours of observation time to achieve S/N= 70; however, these clusters can still be observed as IL targets. Some of these targets are so faint that they may suffer from large uncertainties due to sampling problems, as described in Chapter 5. The third group shows clusters that are too sparse to be IL targets; most of the PAndAS clusters fall into this category. Finally, three clusters have uncertain parameters because of their locations on the edge of the CCD during the original survey.

Table B.1: Other PAndAS Clusters.

Cluster	M_V	$(V-I)_0$	$R_{\rm proj}$ (kpc)
Future Candidates:[a]			
Closer In			
PA16	-8.44	0.97	50.81
PA27	-7.69	0.93	56.58
PA36	-7.30	0.94	30.14
PA37	-7.35	1.13	48.06
PA44	-7.72	0.82	39.35
PA46	-8.67	0.85	44.31
Future Candidates:[b]			
Require More Time			
PA01	-7.48	0.83	118.92
PA02	-6.82	0.90	114.74
PA04	-7.09	0.89	124.62
PA09	-6.75	0.83	90.82
PA11	-6.74	0.87	83.23
PA13	-6.49	0.85	67.98
PA14	-7.01	0.90	86.20
PA21	-7.06	0.87	37.68
PA34	-6.64	0.98	20.85
PA42	-6.59	1.05	42.18
PA52	-7.58	0.96	78.05
Not Candidates:[c]			
Too Sparse			
PA03	-4.17	0.86	100.00
PA05	-5.05	0.97	100.60
PA07	-5.00	0.89	85.95
PA08	-5.40	1.03	88.26
PA10	-5.43	0.93	90.00
PA12	-5.33	0.94	69.21

Table B.1: Other PAndAS Clusters.

Cluster	M_V	$(V-I)_0$	$R_{\rm proj}$ (kpc)
PA15	-5.04	0.93	51.90
PA18	-5.35	0.94	41.55
PA19	-4.73	0.91	37.87
PA20	-5.43	1.00	30.59
PA22	-6.18	1.06	28.73
PA23	-5.02	1.17	33.74
PA24	-4.68	0.91	42.81
PA25	-5.21	1.04	34.79
PA26	-5.10	1.09	43.92
PA28	-5.65	0.85	18.60
PA29	-4.35	0.91	23.04
PA30	-5.42	0.96	46.35
PA31	-4.41	0.99	25.38
PA32	-5.58	1.11	17.94
PA33	-5.39	0.88	36.28
PA35	-5.24	1.21	9.07
PA38	-4.50	0.83	92.33
PA39	-6.19	1.04	26.40
PA40	-5.13	0.95	26.51
PA43	-5.27	0.97	38.92
PA45	-4.06	0.96	41.66
PA47	-5.66	1.14	44.26
PA48	-4.73	0.81	141.34
PA49	-4.81	1.07	48.21
PA50	-6.38	1.10	106.68
PA57	-5.70	0.91	116.41
PA58	-6.17	1.04	119.42
PA59	-4.93	0.76	18.28
PA Cand1	-4.03	0.70	13.70
PA Cand2	-5.26	0.86	114.60

Table B.1: Other PAndAS Clusters.

Cluster	M_V	$(V-I)_0$	$R_{\rm proj}$ (kpc)
Uncertain:[d]			
PA41	-	-	33.09
PA51	-	-	53.42
PA55	-	-	111.50

References: Magnitudes, colours, and projected radii are from the PAndAS Catalog (Huxor et al., 2014).

[a] These clusters were rejected from this analysis because they have smaller projected distances from M31.

[b] These clusters were rejected from this analysis because they required longer observation times.

[c] These clusters have total magnitudes $M_V > -7.3$ and are too faint for a robust IL analysis.

[d] These clusters have uncertain parameters due to cluster positions on the CCD; see Huxor et al. (2014).

Appendix C

Measuring Equivalent Widths with DAOSPEC

As discussed in Chapter 3.2, one way to quantify the strength of a spectral line is to measure its equivalent width (EW). This Appendix describes the techniques used to measure the EWs of all targets.

C.1 Line Selection

The measured spectral lines are from the line list by Shetrone et al. (2003), with supplemental lines from Cayrel et al. (2004), Aoki et al. (2007), Cohen et al. (2008), Letarte et al. (2009), Tafelmeyer et al. (2010), Frebel et al. (2010), and Venn et al. (2012). For IL targets the line lists of MB08 and Colucci et al. (2009) were preferred, with occasional supplements from the above sources.

C.2 EWs with *splot*

A basic technique for measuring EWs is to fit the lines with Gaussian profiles via the *splot* task in IRAF. The basic procedure for this process is:

1. *Identify the line of interest.* A line list provides the wavelength of a spectral line, though this wavelength may not match up with any obvious features, due to, e.g., small uncertainties in the wavelength, the weakness of the feature, possible blends, or low S/N. With noisy spectra visual comparisons with the higher S/N spectra can help to identify lines.

2. *Locate the continuum.* Depending on how well the spectra have been normalized, the continuum should be roughly at an intensity of 1. However, noise, broad features, or imperfect normalization can make the continuum appear higher or lower.

3. *Determine if the line is isolated, or is a blend with other features.* If a line is blended with other features, it is more difficult to measure the EW of a single line. If the blend is severe and there are many other lines available for a given element, the line may be discarded. Otherwise deblending techniques or spectrum syntheses should be used.

4. *Decide how to fit the line.* The Gaussian fitting routines in *splot* allow a line to be in different ways (e.g. to the centre of the line, to the left, to the right, etc.). Depending on noise, blends, or improperly removed cosmic rays or sky features, different fits may produce slightly different EWs.

For high S/N targets *splot* produces EWs that can be reproduced with other methods and that give reasonable abundances. Naturally, features in low S/N spectra are much more difficult. EW measurements from the low S/N ratio Pal 1-I spectrum can be compared to those from Monaco et al. (2011). Unfortunately there are very few lines in common for a comparison, due to differences in the spectral range and S/N. For the lines in common, Figure C.1 shows *splot*-measured EWs versus the Monaco et al. EWs from the higher S/N ratio spectrum. Also shown are the line of perfect agreement (solid red line), estimated 1σ EW errors (black dashed lines), and the average trend (dotted blue line). The *splot* EWs tend to be slightly higher than those from Monaco et al., with an average offset of 7 ± 6 mÅ. However, the majority of the points in Figure C.1 lie within the dashed lines, which implies that the *splot*-based EWs are robust.

C.3 EWs with DAOSPEC

EWs can also be measured with automated programs such as DAOSPEC,[1] which is intended for high resolution ($R > 15000$), high S/N (> 30) spectra (Stetson & Pancino, 2008). The program iteratively fits a continuum to the input spectrum,

[1]DAOSPEC has been written by P.B. Stetson for the Dominion Astrophysical Observatory of the Herzberg Institute of Astrophysics, National Research Council, Canada.

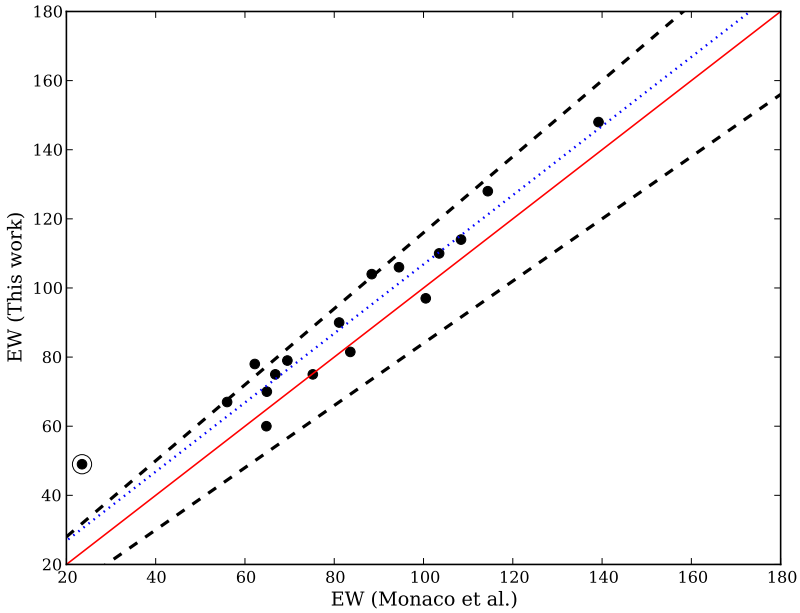

Figure C.1: A comparison between the *splot* EWs for Pal 1-I, and those measured by Monaco et al. (2011), for the lines in common between the analyses. EW errors were not given in Monaco et al. (2011). The circled point is a Cr I line that is unusually discrepant; for that reason it has been removed from the analysis. The dashed lines represent the EW errors. The blue dotted line shows the average offset between the two data sets. Note that though the *splot* EWs are slightly larger, the differences are typically less than the EW errors.

detects the spectral lines in a defined region, and fits Gaussian profiles to the lines, providing their EWs. Some advantages of DAOSPEC over IRAF's *splot* include a fixed full-width at half maximum (FWHM) for all lines, an effective continuum that takes weak features into account, and the ability to quickly measure large numbers of spectral lines with little user input. In individual stars, the FWHM is often dominated by the instrumental broadening of the spectrograph; in IL spectra, however, the velocity dispersion often dominates the line FWHM, blending together many of the spectral lines. To ensure that DAOSPEC can detect these features, the program was modified to detect lines that are separated by a least half of a FWHM (rather than the default separation of one FWHM).

C.3.1 Measurements with *splot* vs. DAOSPEC

Figure C.2 shows a comparison between *splot* EWs (from this work) and DAOSPEC EWs (from Pancino et al. 2010) for the star M67-141, which has the highest resolution and S/N in the Pal 1 study. The EW errors from DAOSPEC are also shown. The majority of the offsets between the *splot* and the DAOSPEC measurements are within the adopted EW measurement errors (shown as dashed lines; see Chapter 3.3.2 for a description of how these errors are calculated), and are therefore not significant. The few lines outside these errors are weak lines that are slightly stronger than DAOSPEC measures—this difference may be attributed to continuum placement (see Stetson & Pancino 2008 for a discussion of their effective continuum). For the weak lines (> 60 mÅ), the average discrepancy between the two analyses (shown as a dotted blue line) is 4 ± 6 mÅ.

With low S/N spectra it appears that DAOSPEC can have difficulty fitting the continuum. The poor quality of the Pal 1-I and -II spectra necessitate *splot* measurements. For consistency, IRAF *splot* measurements are therefore preferred for all targets in the Pal 1 study.

C.3.2 DAOSPEC measurements on IL spectra

The success of DAOSPEC is dependent on the choice of input parameters, particularly for IL spectra. DAOSPEC has the option to determine its own FWHM. However, because IL spectra contain so many weak and/or blended features, the FWHM was fixed; this input FWHM is the sum (in quadrature) of the broadening from the velocity dispersion, the spectrograph, and the intrinsic broadening of Arcturus, and

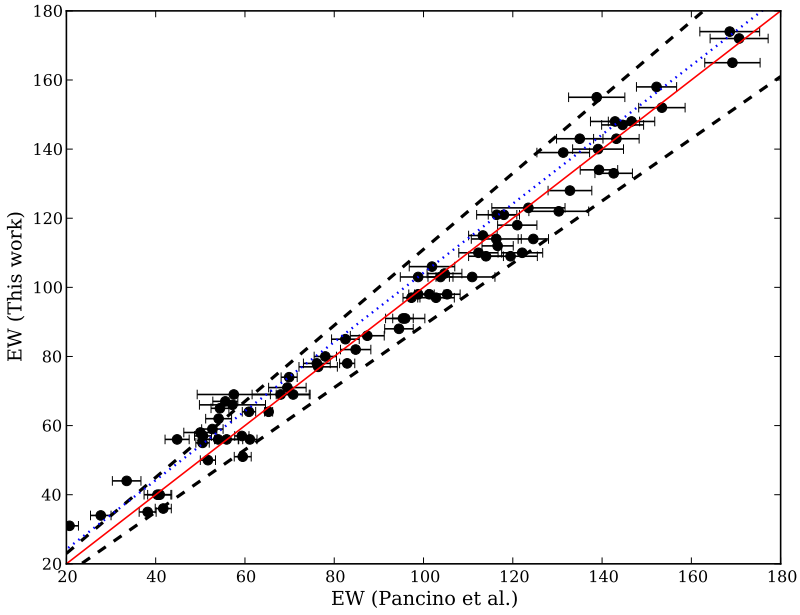

Figure C.2: A comparison of the EWs as measured with *splot* in IRAF to those measured by the program DAOSPEC (from Pancino et al. 2010) for the standard star M67-141. The red line shows equal EW measurements. The blue dotted line shows the average offset between the weak lines in the two data sets. The dashed lines show the EW errors (EW_{min} + 10% EW) as calculated using the Cayrel (1988) formula (see Chapter 3.3.2).

is given in pixels. This FWHM was then allowed to scale with wavelength. Another important input is the order of the polynomial-fit to the continuum. For individual stars, Stetson & Pancino (2008) found that higher-order continuum fits produced the best results. Again, however, IL spectra suffer from contributions from a variety of stars, severe blends, and line blanketing; high-order fits could therefore remove real features from the spectra, leading to underestimates of the line strengths. As described in Chapter 2.3.2, the HET spectra presented here have been carefully and conservatively normalized—thus the continuum level was fixed as well. Occasionally valuable lines were mis-measured by DAOSPEC; these lines were remeasured with Gaussian fits in IRAF's *splot* task.

DAOSPEC is capable of reproducing *splot* EWs of lines in 47 Tuc's IL spectrum. Figure C.3a shows that for Fe lines the agreement between DAOSPEC and *splot* EWs is excellent, with an average offset of only 1.76 mÅ, though the scatter about the average is significant (±9.93 mÅ). This scatter is likely caused by blends in the IL spectrum, which can be difficult to detect by eye. DAOSPEC also reproduces the EWs of MB08, which were measured with the program GETJOB (McWilliam et al., 1995a). The offset between the data sets remains insignificant (0.37 mÅ, with the DAOSPEC EWs slightly higher), and the scatter is smaller (±6.69 mÅ). Note that MB08 did not combine their apertures; the spectral lines in the overlapping regions were measured twice, and both measurements were included in their analysis. For this EW comparison the two EWs were averaged together for all lines in the overlapping regions. In individual stars, DAOSPEC often underestimates the EWs of the strongest lines (e.g. Sakari et al. 2011)—thus, the EWs of these lines have been verified or corrected in *splot*.

DAOSPEC is therefore capable of accurately reproducing the EWs of the lines in the 47 Tuc IL spectrum. Since 47 Tuc has a higher velocity dispersion than most of the targets in this work (except for M15 and PA53; see Tables 2.5 and 2.6), DAOSPEC should also be able to accurately measure the EWs for all the target GCs. However, care must be taken with the strongest lines to ensure they are properly measured, and attention must be paid to lines in regions with uncertain continuum normalization.

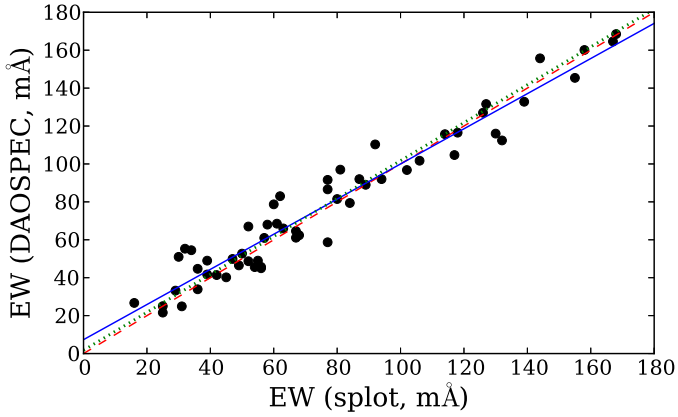

(a) DAOSPEC vs. *splot*

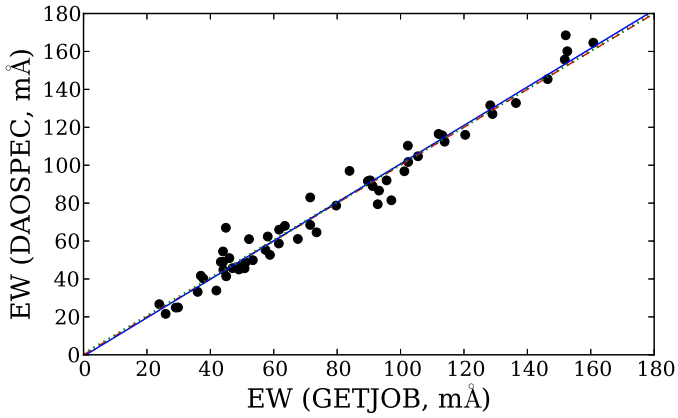

(b) DAOSPEC vs. GETJOB

Figure C.3: Comparisons of EW measurements on the IL spectrum of 47 Tuc for the Fe lines in common between the studies. Figure C.3a compares the DAOSPEC measurements to those from *splot*, while Figure C.3b compares measurements from DAOSPEC and GETJOB (from MB08). Each black point is a separate spectral line. The dashed red lines show perfect agreement, while the dotted green lines show the average offset. The solid blue lines are linear least squares fits to the points. The agreement is excellent in both cases.

C.4 Final EWs

Solar and Arcturus EWs

The final Solar EWs (in mÅ) are shown in Table C.1, along with the wavelengths (in Å), excitation potentials (in eV), and $\log gf$ values. These EWs were measured in DAOSPEC but were carefully checked and refined in *splot*. Lines stronger than 150 mÅ were removed from the abundance analysis (see the discussions in McWilliam et al. 1995b) These EWs were used to determine the Solar abundances, which are also listed in Table C.1. The average Solar abundances were used for the Pal 1 [Fe/H] and [X/Fe] ratios, while the IL ratios were calculated *line by line*.

Table C.1: The Solar & Arcturus Line Lists.

Wavelength (Å)	Element	E.P. (eV)	log gf	Equivalent width (mÅ) Sun	Arcturus
4443.19	Fe I	2.86	-1.043	134.0	-
4484.22	Fe I	3.60	-0.864	100.0	-
4489.75	Fe I	0.12	-3.899	91.0	-
4592.66	Fe I	1.56	-2.462	99.0	-
4710.28	Fe I	3.02	-1.612	80.0	-
4733.59	Fe I	1.48	-2.988	82.0	-
4741.53	Fe I	2.83	-1.764	83.0	-
4939.69	Fe I	0.86	-3.252	94.0	-
4966.10	Fe I	3.33	-0.871	122.0	-
4994.13	Fe I	0.92	-2.969	111.0	-
5041.07	Fe I	0.96	-3.086	114.0	-
5068.77	Fe I	2.94	-1.041	133.0	-
5079.75	Fe I	0.99	-3.245	94.0	-
5083.35	Fe I	0.96	-2.842	115.0	-
5123.72	Fe I	1.01	-3.058	107.0	-
5127.36	Fe I	0.92	-3.249	99.0	-
5150.85	Fe I	0.99	-3.037	110.0	-
5151.92	Fe I	1.01	-3.321	93.0	-
5159.05	Fe I	4.28	-0.810	67.0	-
5162.29	Fe I	4.18	0.020	160.0	-

5166.28	Fe I	0.00	-4.123	110.0	-
5196.08	Fe I	4.26	-0.450	89.0	-
5215.19	Fe I	3.27	-0.930	134.0	-
5217.39	Fe I	3.21	-1.160	100.0	-
5225.53	Fe I	0.11	-4.755	73.0	-
5250.21	Fe I	0.12	-4.898	68.0	-
5253.02	Fe I	2.28	-3.810	17.0	-
5254.95	Fe I	0.11	-4.764	70.0	-
5281.79	Fe I	3.04	-0.833	152.0	-
5283.62	Fe I	3.24	-0.524	180.0	-
5302.30	Fe I	3.28	-0.880	135.0	-
5307.37	Fe I	1.61	-2.912	83.0	-
5339.937	Fe I	3.266	-0.72	145.0	-
5364.86	Fe I	4.45	0.228	156.0	-
5367.476	Fe I	4.415	0.443	-	142.3
5369.974	Fe I	4.371	0.536	-	144.0
5386.34	Fe I	4.16	-1.740	31.0	-
5389.486	Fe I	4.415	-0.41	86.8	96.7
5393.176	Fe I	3.241	-0.715	139.0	-
5395.22	Fe I	4.45	-1.730	19.0	-
5400.51	Fe I	4.37	-0.150	139.0	-
5417.04	Fe I	4.42	-1.420	32.0	-
5436.30	Fe I	4.39	-1.350	39.0	-
5464.28	Fe I	4.14	-1.402	37.0	-
5470.09	Fe I	4.45	-1.600	24.0	-
5501.477	Fe I	0.958	-3.046	115.8	-
5522.446	Fe I	4.209	-1.45	48.0	66.0
5539.29	Fe I	3.64	-2.590	17.0	-
5543.936	Fe I	4.218	-1.04	67.5	83.0
5560.212	Fe I	4.435	-1.09	51.0	67.0
5576.099	Fe I	3.43	-0.9	113.4	136.4
5618.632	Fe I	4.209	-1.275	56.1	69.8
5633.946	Fe I	4.991	-0.23	67.0	77.8
5652.318	Fe I	4.26	-1.85	26.0	45.3
5662.52	Fe I	4.18	-0.573	94.0	-

5701.54	Fe I	2.56	-2.143	82.0	-
5741.848	Fe I	4.256	-1.672	31.0	54.5
5752.032	Fe I	4.549	-0.864	59.4	66.7
5763.002	Fe I	4.209	-0.45	103.7	119.5
5775.081	Fe I	4.22	-1.297	56.0	83.6
5778.453	Fe I	2.588	-3.44	23.0	73.2
5862.357	Fe I	4.549	-0.051	89.5	97.6
5905.671	Fe I	4.652	-0.69	66.0	74.3
5934.655	Fe I	3.929	-1.07	80.8	106.4
5956.69	Fe I	0.86	-4.498	55.0	-
5976.777	Fe I	3.943	-1.503	63.0	-
6003.011	Fe I	3.882	-1.12	87.5	106.8
6012.21	Fe I	2.223	-4.038	23.0	81.7
6024.058	Fe I	4.549	-0.12	109.0	113.9
6027.051	Fe I	4.076	-1.089	68.0	88.3
6056.01	Fe I	4.73	-0.450	69.0	-
6065.48	Fe I	2.61	-1.410	119.0	-
6078.491	Fe I	4.796	-0.481	80.3	82.4
6079.008	Fe I	4.652	-1.02	45.0	58.3
6082.72	Fe I	2.22	-3.548	35.0	-
6096.664	Fe I	3.984	-1.83	37.0	61.4
6120.26	Fe I	0.91	-5.940	6.0	-
6136.624	Fe I	2.453	-1.41	147.0	-
6136.99	Fe I	2.20	-2.932	67.0	-
6137.702	Fe I	2.588	-1.346	137.0	-
6151.617	Fe I	2.176	-3.3	49.0	114.5
6157.75	Fe I	4.07	-1.260	62.0	-
6159.38	Fe I	4.61	-1.970	12.0	-
6165.36	Fe I	4.14	-1.473	45.0	-
6173.341	Fe I	2.22	-2.863	67.0	133.5
6180.209	Fe I	2.73	-2.628	55.0	109.0
6187.995	Fe I	3.94	-1.673	52.5	74.6
6200.313	Fe I	2.609	-2.386	79.0	129.3
6213.437	Fe I	2.22	-2.49	88.0	-
6219.287	Fe I	2.2	-2.428	91.0	-

6226.74	Fe I	3.88	-2.200	28.0	-
6229.232	Fe I	2.83	-2.821	42.5	85.7
6230.736	Fe I	2.559	-1.276	173.0	-
6240.65	Fe I	2.22	-3.173	49.0	-
6246.327	Fe I	3.6	-0.796	113.8	141.0
6252.565	Fe I	2.404	-1.767	120.1	-
6254.253	Fe I	2.28	-2.435	91.0	-
6265.141	Fe I	2.18	-2.532	86.0	-
6270.231	Fe I	2.86	-2.543	52.0	-
6271.28	Fe I	3.32	-2.960	21.0	-
6297.799	Fe I	2.22	-2.681	74.0	-
6301.508	Fe I	3.65	-0.701	114.8	138.3
6302.49	Fe I	3.69	-1.150	80.0	-
6307.85	Fe I	3.64	-3.270	5.5	-
6311.51	Fe I	2.83	-3.220	28.0	-
6322.694	Fe I	2.59	-2.438	75.0	139.7
6335.337	Fe I	2.2	-2.175	101.6	-
6336.83	Fe I	3.69	-0.840	106.2	126.9
6344.15	Fe I	2.43	-2.877	62.0	-
6353.849	Fe I	0.91	-6.36	2.5	35.6
6355.035	Fe I	2.84	-2.328	65.0	126.8
6380.75	Fe I	4.19	-1.366	52.0	75.6
6392.538	Fe I	2.28	-3.957	18.0	70.4
6411.658	Fe I	3.65	-0.646	-	141.9
6419.956	Fe I	4.73	-0.183	97.0	93.2
6421.36	Fe I	2.28	-1.979	117.0	-
6430.856	Fe I	2.18	-1.954	122.0	-
6475.632	Fe I	2.56	-2.929	55.0	119.0
6481.878	Fe I	2.28	-2.985	64.0	128.7
6498.945	Fe I	0.96	-4.675	44.0	145.0
6518.366	Fe I	2.832	-2.397	63.7	112.0
6546.252	Fe I	2.75	-1.536	111.0	-
6569.224	Fe I	4.73	-0.38	72.0	89.4
6574.23	Fe I	0.99	-5.022	27.0	-
6581.22	Fe I	1.48	-4.680	21.0	-

6593.874	Fe I	2.43	-2.377	85.0	-
6597.571	Fe I	4.77	-0.97	44.0	53.9
6608.044	Fe I	2.27	-3.939	18.0	74.3
6609.11	Fe I	2.56	-2.661	65.0	-
6627.56	Fe I	4.53	-1.559	31.6	36.5
6633.75	Fe I	4.56	-0.799	64.0	-
6646.966	Fe I	2.6	-3.917	9.0	50.9
6648.121	Fe I	1.01	-5.73	7.8	73.4
6653.85	Fe I	4.15	-2.520	10.0	-
6677.997	Fe I	2.69	-1.395	146.0	-
6703.576	Fe I	2.76	-3.059	37.0	89.1
6705.105	Fe I	4.61	-1.06	45.0	64.6
6710.323	Fe I	1.48	-4.807	15.0	87.8
6715.386	Fe I	4.59	-1.54	30.1	47.2
6726.666	Fe I	4.607	-1.087	51.4	60.3
6739.524	Fe I	1.56	-4.801	13.9	75.3
6750.164	Fe I	2.42	-2.592	76.0	136.7
6752.716	Fe I	4.64	-1.263	39.4	-
6806.856	Fe I	2.73	-2.633	39.4	93.1
6810.267	Fe I	4.59	-0.992	54.6	66.8
6820.371	Fe I	4.638	-1.214	44.8	61.8
6828.596	Fe I	4.64	-0.843	60.8	68.4
6839.835	Fe I	2.56	-3.378	30.0	87.8
6841.341	Fe I	4.61	-0.733	70.5	81.9
6842.689	Fe I	4.64	-1.224	44.l	56.5
6843.655	Fe I	3.65	-0.863	-	76.5
6851.652	Fe I	1.6	-5.247	5.5	46.6
6855.161	Fe I	4.559	-0.741	77.6	89.4
6855.723	Fe I	4.39	-1.747	23.0	38.2
6858.155	Fe I	4.59	-0.939	56.6	66.0
6911.512	Fe I	2.424	-3.967	17.1	61.5
6916.686	Fe I	4.15	-1.359	57.0	86.6
6988.524	Fe I	2.404	-3.519	34.0	95.3
7022.957	Fe I	4.19	-1.148	66.0	87.6
7038.22	Fe I	4.22	-1.214	59.0	87.2

7068.423	Fe I	4.07	-1.319	66.1	92.1
7072.8	Fe I	4.07	-2.767	7.9	17.7
7090.39	Fe I	4.23	-1.109	66.0	94.7
7130.925	Fe I	4.3	-0.708	105.0	120.1
7132.985	Fe I	4.06	-1.635	48.8	67.8
7145.312	Fe I	4.61	-1.24	43.1	74.7
7151.464	Fe I	2.48	-3.657	29.3	-
7180.004	Fe I	1.48	-4.707	23.8	-
7219.682	Fe I	4.076	-1.617	47.0	-
4416.83	Fe II	2.78	-2.610	85.0	-
4491.40	Fe II	2.86	-2.690	79.0	-
4508.29	Fe II	2.86	-2.220	102.0	-
4515.34	Fe II	2.84	-2.480	89.0	-
4520.22	Fe II	2.81	-2.610	82.0	-
4541.52	Fe II	2.86	-3.050	61.0	-
4555.89	Fe II	2.83	-2.280	92.0	-
4576.34	Fe II	2.84	-3.040	66.0	-
4582.84	Fe II	2.84	-3.090	61.0	-
4583.83	Fe II	2.81	-2.020	114.0	-
4629.34	Fe II	2.81	-2.380	94.0	-
4993.35	Fe II	2.81	-3.620	40.0	-
5197.57	Fe II	3.23	-2.100	94.0	-
5234.63	Fe II	3.22	-2.118	88.0	-
5264.81	Fe II	3.23	-3.210	45.0	-
5284.10	Fe II	2.89	-3.190	58.0	-
5414.08	Fe II	3.22	-3.610	26.0	-
5425.25	Fe II	3.20	-3.360	40.0	-
5534.848	Fe II	3.245	-2.79	62.0	54.5
5991.38	Fe II	3.15	-3.740	30.0	-
6149.25	Fe II	3.89	-2.720	35.0	-
6238.39	Fe II	3.889	-2.69	46.7	30.6
6247.557	Fe II	3.892	-2.38	-	37.7
6416.928	Fe II	3.89	-2.74	39.0	35.5
6432.683	Fe II	2.89	-3.63	45.5	39.7
6456.391	Fe II	3.903	-2.075	-	45.2

6516.08	Fe II	2.891	-3.44	54.0	51.3
6154.23	Na I	2.10	-1.560	35.0	-
6160.75	Na I	2.10	-1.260	54.0	-
5711.09	Mg I	4.35	-1.728	115.0	-
6318.72	Mg I	5.11	-1.970	44.0	-
6319.24	Mg I	5.11	-2.210	29.0	-
6696.03	Al I	3.14	-1.570	36.0	-
6698.67	Al I	3.14	-1.890	21.0	-
5645.66	Si I	4.91	-2.140	35.0	-
5665.60	Si I	4.90	-2.040	39.0	-
5684.52	Si I	4.93	-1.650	59.0	-
6125.03	Si I	5.62	-1.570	31.0	-
6142.48	Si I	5.62	-1.510	34.0	-
6145.02	Si I	5.61	-1.370	39.0	-
6155.14	Si I	5.62	-0.800	86.0	-
6237.33	Si I	5.61	-1.020	74.0	-
6243.82	Si I	5.61	-1.270	48.0	-
6244.48	Si I	5.61	-1.270	46.0	-
4425.44	Ca I	1.88	-0.360	186.0	-
4435.68	Ca I	1.89	-0.520	144.0	-
5581.979	Ca I	2.523	-0.555	97.0	-
5598.49	Ca I	2.52	-0.087	143.0	-
5867.572	Ca I	2.930	-1.640	25.0	-
6102.73	Ca I	1.88	-0.790	132.0	-
6156.03	Ca I	2.52	-2.390	10.0	-
6161.295	Ca I	2.520	-1.266	60.0	-
6166.440	Ca I	2.520	-1.142	71.0	-
6169.04	Ca I	2.52	-0.800	88.0	-
6169.56	Ca I	2.52	-0.480	113.0	-
6449.81	Ca I	2.52	-0.502	105.0	-
6455.605	Ca I	2.520	-1.290	62.3	-
6471.662	Ca I	2.526	-0.686	97.0	-
6572.795	Ca I	0.000	-4.310	32.0	-
6717.68	Ca I	2.71	-0.610	91.0	-
7326.160	Ca I	2.930	-0.230	110.0	-

4400.39	Sc II	0.61	-0.540	91.0	-
4670.41	Sc II	1.36	-0.580	59.0	-
5031.02	Sc II	1.36	-0.400	70.0	-
5526.79	Sc II	1.77	0.030	74.0	-
5641.00	Sc II	1.50	-1.130	38.0	-
5667.16	Sc II	1.50	-1.310	30.0	-
5669.06	Sc II	1.50	-1.200	33.0	-
5684.21	Sc II	1.51	-1.070	36.0	-
6245.62	Sc II	1.51	-0.970	35.0	-
6309.90	Sc II	1.50	-1.520	22.0	-
6604.58	Sc II	1.36	-1.310	36.0	-
4512.73	Ti I	0.84	-0.424	64.0	-
4533.25	Ti I	0.85	0.480	97.0	-
4534.78	Ti I	0.84	0.280	90.0	-
4548.76	Ti I	0.83	-0.298	69.0	-
4681.91	Ti I	0.05	-1.015	72.0	-
4840.87	Ti I	0.90	-0.450	66.0	-
4913.62	Ti I	1.87	0.216	48.0	-
4981.73	Ti I	0.84	0.500	106.0	-
4991.06	Ti I	0.84	0.380	103.0	-
4997.10	Ti I	0.00	-2.060	30.0	-
4999.50	Ti I	0.83	0.250	97.0	-
5009.65	Ti I	0.02	-2.203	25.0	-
5016.16	Ti I	0.85	-0.510	65.0	-
5024.84	Ti I	0.82	-0.546	67.0	-
5036.46	Ti I	1.44	0.186	67.0	-
5038.40	Ti I	1.43	0.069	63.0	-
5039.96	Ti I	0.02	-1.130	74.0	-
5064.65	Ti I	0.05	-0.930	82.0	-
5113.44	Ti I	1.44	-0.727	25.0	-
5145.47	Ti I	1.46	-0.518	35.0	-
5192.97	Ti I	0.02	-1.010	81.0	-
5210.39	Ti I	0.05	-0.580	88.0	-
5490.16	Ti I	1.46	-0.933	22.0	-
5503.90	Ti I	2.58	-0.190	13.0	-

5648.570	Ti I	2.495	-0.260	12.4	-
5866.451	Ti I	1.067	-0.840	47.0	-
5978.54	Ti I	1.87	-0.440	24.0	-
6126.22	Ti I	1.07	-1.425	22.0	-
6220.50	Ti I	2.68	-0.140	9.0	-
6258.10	Ti I	1.44	-0.355	52.0	-
6303.77	Ti I	1.44	-1.570	7.5	-
6312.24	Ti I	1.46	-1.550	7.0	-
6336.10	Ti I	1.44	-1.740	6.0	-
6554.238	Ti I	1.440	-1.218	18.0	-
6556.077	Ti I	1.460	-1.074	18.0	-
6599.13	Ti I	0.90	-2.090	10.0	-
6743.127	Ti I	0.900	-1.630	19.0	-
7209.468	Ti I	1.460	-0.500	43.0	-
7216.190	Ti I	1.440	-1.150	21.0	-
7251.717	Ti I	1.430	-0.770	34.0	-
4417.72	Ti II	1.16	-1.430	94.0	-
4441.73	Ti II	1.18	-2.410	56.0	-
4443.79	Ti II	1.08	-0.710	143.0	-
4444.56	Ti II	1.12	-2.030	57.0	-
4450.48	Ti II	1.08	-1.450	82.0	-
4464.45	Ti II	1.16	-2.080	67.0	-
4468.51	Ti II	1.13	-0.620	171.0	-
4470.86	Ti II	1.16	-2.280	61.0	-
4488.33	Ti II	3.12	-0.820	49.0	-
4493.51	Ti II	1.08	-2.740	30.0	-
4501.27	Ti II	1.12	-0.750	127.0	-
4518.33	Ti II	1.08	-2.560	49.0	-
4533.97	Ti II	1.24	-0.770	135.0	-
4544.03	Ti II	1.24	-2.410	44.0	-
4563.76	Ti II	1.22	-0.960	115.0	-
4568.31	Ti II	1.22	-2.650	31.0	-
4571.97	Ti II	1.57	-0.520	121.0	-
4589.96	Ti II	1.24	-1.780	79.0	-
4708.67	Ti II	1.24	-2.210	49.0	-

4779.99	Ti II	2.05	-1.370	62.0	-
4798.53	Ti II	1.08	-2.670	42.0	-
4865.61	Ti II	1.12	-2.590	50.0	-
4911.18	Ti II	3.12	-0.340	53.0	-
5005.15	Ti II	1.57	-2.730	23.0	-
5129.16	Ti II	1.89	-1.390	73.0	-
5154.07	Ti II	1.57	-1.520	69.0	-
5185.91	Ti II	1.89	-1.350	69.0	-
5188.68	Ti II	1.58	-1.220	96.0	-
5226.55	Ti II	1.57	-1.000	89.0	-
5336.780	Ti II	1.582	-1.700	68.0	-
5381.010	Ti II	1.566	-2.080	56.0	-
5418.77	Ti II	1.58	-2.110	48.0	-
6559.59	Ti II	2.05	-2.019	39.0	-
6606.95	Ti II	2.06	-2.790	8.0	-
6680.13	Ti II	3.09	-1.860	7.0	-
6090.21	V I	1.08	-0.060	33.0	-
6119.53	V I	1.06	-0.320	22.0	-
6135.37	V I	1.05	-0.750	10.0	-
6199.19	V I	0.29	-1.290	13.0	-
6216.36	V I	0.28	-1.290	34.0	-
6224.51	V I	0.29	-2.010	5.0	-
6233.20	V I	0.28	-2.070	5.0	-
6243.11	V I	0.30	-0.980	29.0	-
6251.82	V I	0.29	-1.300	14.0	-
6274.66	V I	0.27	-1.670	10.0	-
6285.16	V I	0.28	-1.560	9.0	-
6292.82	V I	0.29	-1.520	12.0	-
4496.84	Cr I	0.94	-1.150	95.0	-
4600.75	Cr I	1.00	-1.260	84.0	-
4616.14	Cr I	0.98	-1.190	90.0	-
4626.19	Cr I	0.97	-1.320	84.0	-
4651.28	Cr I	0.98	-1.460	76.0	-
4652.16	Cr I	1.00	-1.030	94.0	-
5247.56	Cr I	0.96	-1.640	79.0	-

5345.80	Cr I	1.00	-0.980	108.0	-
5409.80	Cr I	1.03	-0.720	121.0	-
6330.09	Cr I	0.94	-2.920	27.0	-
4558.65	Cr II	4.07	-0.660	73.0	-
4848.24	Cr II	3.86	-1.130	58.0	-
4754.04	Mn I	2.28	-0.090	132.0	-
4762.37	Mn I	2.89	0.430	118.0	-
4783.43	Mn I	2.30	0.042	141.0	-
4823.52	Mn I	2.32	0.140	147.0	-
6013.51	Mn I	3.07	-0.252	86.0	-
6021.82	Mn I	3.08	0.035	94.0	-
5483.34	Co I	1.71	-1.488	50.0	-
5647.23	Co I	2.28	-1.560	14.0	-
4648.66	Ni I	3.42	-0.160	94.0	-
4855.41	Ni I	3.54	0.000	100.0	-
5017.59	Ni I	3.54	-0.080	101.0	-
5080.52	Ni I	3.65	0.130	113.0	-
5084.08	Ni I	3.68	0.030	96.0	-
5137.07	Ni I	1.68	-1.990	88.0	-
5578.73	Ni I	1.68	-2.670	56.0	-
5587.87	Ni I	1.93	-2.370	58.0	-
5589.37	Ni I	3.90	-1.150	28.0	-
5593.75	Ni I	3.90	-0.790	44.0	-
6128.97	Ni I	1.68	-3.390	26.0	-
6130.14	Ni I	4.27	-0.980	21.0	-
6176.82	Ni I	4.09	-0.430	61.0	-
6177.25	Ni I	1.83	-3.500	15.0	-
6186.72	Ni I	4.11	-0.900	32.0	-
6204.61	Ni I	4.09	-1.150	22.0	-
6223.99	Ni I	4.10	-0.970	28.0	-
6230.10	Ni I	4.11	-1.200	20.0	-
6322.17	Ni I	4.15	-1.210	17.0	-
6327.604	Ni I	1.680	-3.150	38.0	-
6378.26	Ni I	4.15	-0.820	31.0	-
6384.67	Ni I	4.15	-1.000	24.0	-

6482.809	Ni I	1.930	-2.630	46.3	-
6586.319	Ni I	1.951	-2.810	42.0	-
6598.61	Ni I	4.24	-0.930	25.0	-
6635.14	Ni I	4.42	-0.750	24.0	-
6643.638	Ni I	1.676	-2.300	86.0	-
6767.784	Ni I	1.826	-2.170	79.0	-
6772.321	Ni I	3.660	-0.980	49.0	-
7110.905	Ni I	1.930	-2.980	36.0	-
7122.206	Ni I	3.542	0.040	128.0	-
5105.50	Cu I	1.39	-1.505	100.0	-
5700.24	Cu I	1.64	-2.330	38.0	-
5782.13	Cu I	1.64	-1.720	87.0	-
4722.15	Zn I	4.03	-0.338	71.0	-
4810.54	Zn I	4.08	-0.170	74.0	-
6362.35	Zn I	5.80	0.140	26.0	-
4883.69	Y II	1.08	0.070	53.0	-
4900.11	Y II	1.03	-0.090	54.0	-
5087.43	Y II	1.08	-0.170	46.0	-
5200.42	Y II	0.99	-0.570	38.0	-
5402.78	Y II	1.84	-0.510	12.0	-
4554.03	Ba II	0.00	0.170	162.0	-
5853.688	Ba II	0.604	-1.010	61.0	-
6141.727	Ba II	0.704	-0.076	111.0	-
6496.908	Ba II	0.604	-0.377	99.0	-
5301.97	La II	0.40	-1.140	7.0	-
5303.52	La II	0.32	-1.350	3.2	-
6320.43	La II	0.17	-1.562	4.5	-
6774.27	La II	0.13	-1.708	2.0	-
5249.59	Nd II	0.98	0.200	15.0	-
5319.82	Nd II	0.55	-0.140	12.0	-

Pal 1 EWs

The Pal 1 EWs were measured by hand with *splot*, though DAOSPEC measurements are very similar in the two high S/N spectra, Pal 1-III and Pal 1-C. The final EWs are listed in Table C.2. For all stars, lines stronger than 200 mÅ were rejected. For Fe, the Pal 1 lines with EWs stronger than 150 mÅ were also thrown out, in order to best constrain the atmospheric parameters.

Table C.2: The Pal 1 Line List.

λ	Element	E.P.	log gf	Equivalent width (mÅ)				
(Å)		(eV)		M67-141	Pal 1-I	Pal 1-II	Pal 1-III	Pal 1-C
4443.19	Fe I	2.86	-1.043	171.0	-	-	-	-
4476.02	Fe I	2.85	-0.819	-	-	-	157.0	-
4484.22	Fe I	3.60	-0.864	122.0	-	-	76.0	117.0
4489.75	Fe I	0.12	-3.899	-	-	120.0	-	-
4592.66	Fe I	1.56	-2.462	185.0	-	-	-	-
4710.28	Fe I	3.02	-1.612	148.0	-	-	-	-
4733.59	Fe I	1.48	-2.988	158.0	-	-	99.0	-
4736.77	Fe I	3.21	-0.752	-	-	-	123.0	-
4741.53	Fe I	2.83	-1.764	148.0	-	-	75.0	101.0
4939.69	Fe I	0.86	-3.252	182.0	-	-	105.0	-
4966.10	Fe I	3.33	-0.871	169.0	-	-	106.0	-
4994.13	Fe I	0.92	-2.969	-	-	-	124.0	-
5041.07	Fe I	0.96	-3.086	-	-	-	115.0	-
5068.77	Fe I	2.94	-1.041	167.0	-	-	-	-
5079.75	Fe I	0.99	-3.245	179.0	-	-	107.0	-
5083.35	Fe I	0.96	-2.842	-	-	-	137.0	-
5123.72	Fe I	1.01	-3.058	195.0	-	-	108.0	-
5127.36	Fe I	0.92	-3.249	185.0	-	-	121.0	-
5150.85	Fe I	0.99	-3.037	-	-	-	122.0	-
5151.92	Fe I	1.01	-3.321	179.0	141.0	-	107.0	-
5159.05	Fe I	4.28	-0.810	97.0	-	-	-	66.0
5162.29	Fe I	4.18	0.020	172.0	132.0	-	103.0	-
5165.41	Fe I	4.22	-0.040	145.0	-	-	-	-
5166.28	Fe I	0.00	-4.123	-	-	-	119.0	-
5196.08	Fe I	4.26	-0.450	119.0	-	-	-	91.0
5215.19	Fe I	3.27	-0.930	160.0	131.0	-	102.0	-
5217.39	Fe I	3.21	-1.160	147.0	112.0	-	104.0	114.0
5225.53	Fe I	0.11	-4.755	-	125.0	-	92.0	-
5250.21	Fe I	0.12	-4.898	-	-	-	87.0	116.0
5253.02	Fe I	2.28	-3.810	69.0	-	-	-	41.0
5254.95	Fe I	0.11	-4.764	-	-	-	93.0	-

5281.79	Fe I	3.04	-0.833	-	-	-	114.0	-
5283.62	Fe I	3.24	-0.524	199.0	-	-	-	-
5302.30	Fe I	3.28	-0.880	170.0	-	-	104.0	-
5307.37	Fe I	1.61	-2.912	167.0	-	-	107.0	130.0
5339.93	Fe I	3.27	-0.720	180.0	-	-	112.0	-
5364.86	Fe I	4.45	0.228	148.0	123.0	-	99.0	120.0
5367.48	Fe I	4.42	0.443	175.0	145.0	-	109.0	-
5369.96	Fe I	4.37	0.536	-	147.0	-	121.0	-
5383.37	Fe I	4.31	0.645	-	-	-	138.0	-
5386.34	Fe I	4.16	-1.740	66.0	-	-	33.0	35.0
5389.48	Fe I	4.42	-0.400	110.0	-	-	79.0	85.0
5393.17	Fe I	3.24	-0.920	172.0	134.0	-	99.0	-
5395.22	Fe I	4.45	-1.730	49.0	-	-	-	30.0
5400.51	Fe I	4.37	-0.150	-	-	-	97.0	119.0
5415.20	Fe I	4.39	0.643	-	150.0	-	-	-
5417.04	Fe I	4.42	-1.420	68.0	35.0	-	27.0	38.0
5424.07	Fe I	4.32	0.520	-	142.0	-	-	-
5436.30	Fe I	4.39	-1.350	71.0	-	-	33.0	39.0
5464.28	Fe I	4.14	-1.402	78.0	-	-	-	57.0
5470.09	Fe I	4.45	-1.600	56.0	-	-	20.0	30.0
5497.52	Fe I	1.01	-2.825	-	-	-	146.0	-
5539.29	Fe I	3.64	-2.590	57.0	-	-	-	-
5569.62	Fe I	3.42	-0.540	186.0	153.0	-	113.0	-
5572.84	Fe I	3.40	-0.310	-	151.0	-	128.0	-
5576.09	Fe I	3.43	-1.000	153.0	120.0	113.0	91.0	120.0
5586.76	Fe I	3.37	-0.144	-	180.0	-	-	-
5662.52	Fe I	4.18	-0.573	128.0	89.0	107.0	88.0	99.0
5701.54	Fe I	2.56	-2.143	148.0	-	-	85.0	111.0
5956.69	Fe I	0.86	-4.498	130.0	102.0	115.0	69.0	98.0
6003.03	Fe I	3.88	-1.110	118.0	-	93.0	-	88.0
6024.05	Fe I	4.55	-0.110	134.0	-	122.0	87.0	102.0
6027.05	Fe I	4.07	-1.089	103.0	83.0	96.0	65.0	77.0
6056.01	Fe I	4.73	-0.450	-	-	-	-	74.0
6065.48	Fe I	2.61	-1.410	195.0	-	-	114.0	-
6078.50	Fe I	4.79	-0.370	104.0	75.0	64.0	63.0	79.0
6079.01	Fe I	4.65	-0.950	78.0	-	45.0	33.0	48.0
6082.72	Fe I	2.22	-3.548	97.0	-	-	41.0	61.0
6120.26	Fe I	0.91	-5.940	56.0	-	-	14.0	-
6136.99	Fe I	2.20	-2.932	136.0	95.0	-	77.0	104.0
6151.62	Fe I	2.18	-3.371	109.0	-	90.0	-	87.0
6157.75	Fe I	4.07	-1.260	112.0	-	-	51.0	72.0
6159.38	Fe I	4.61	-1.970	36.0	-	-	-	-
6165.36	Fe I	4.14	-1.473	82.0	-	60.0	46.0	51.0

6173.34	Fe I	2.22	-2.850	133.0	101.0	-	76.0	100.0
6180.20	Fe I	2.73	-2.649	114.0	-	-	53.0	80.0
6187.99	Fe I	3.94	-1.580	91.0	-	-	39.0	-
6200.31	Fe I	2.61	-2.373	139.0	-	-	77.0	95.0
6213.43	Fe I	2.22	-2.481	147.0	126.0	-	-	-
6219.28	Fe I	2.20	-2.448	165.0	-	120.0	98.0	119.0
6226.74	Fe I	3.88	-2.200	64.0	-	-	22.0	41.0
6229.23	Fe I	2.84	-2.900	97.0	-	-	42.0	64.0
6230.74	Fe I	2.56	-1.276	-	-	-	137.0	-
6240.65	Fe I	2.22	-3.173	114.0	-	-	62.0	92.0
6252.56	Fe I	2.40	-1.767	189.0	150.0	152.0	-	-
6265.13	Fe I	2.18	-2.540	168.0	-	127.0	96.0	-
6271.28	Fe I	3.32	-2.960	69.0	-	-	24.0	43.0
6290.97	Fe I	4.73	-0.760	102.0	-	72.0	49.0	68.0
6297.79	Fe I	2.22	-2.640	155.0	-	-	73.0	99.0
6301.50	Fe I	3.65	-0.720	166.0	-	-	-	-
6302.49	Fe I	3.69	-1.150	121.0	-	-	-	94.0
6307.85	Fe I	3.64	-3.270	23.0	-	-	-	-
6311.51	Fe I	2.83	-3.220	84.0	-	-	21.0	48.0
6322.68	Fe I	2.59	-2.469	143.0	-	-	-	-
6330.85	Fe I	4.73	-1.220	66.0	-	36.0	-	-
6335.33	Fe I	2.20	-2.177	172.0	141.0	-	101.0	-
6336.82	Fe I	3.69	-1.050	152.0	115.0	118.0	-	109.0
6344.15	Fe I	2.43	-2.877	120.0	90.0	90.0	63.0	-
6355.03	Fe I	2.84	-2.291	-	-	-	-	103.0
6380.74	Fe I	4.19	-1.375	-	-	-	-	62.0
6392.54	Fe I	2.28	-3.950	-	-	-	31.0	52.0
6419.96	Fe I	4.73	-0.240	-	83.0	-	78.0	76.0
6421.35	Fe I	2.28	-2.014	-	-	-	107.0	-
6430.85	Fe I	2.18	-1.946	-	-	-	116.0	-
6481.87	Fe I	2.27	-3.010	129.0	-	-	-	98.0
6498.94	Fe I	0.96	-4.689	124.0	-	-	-	-
6518.37	Fe I	2.83	-2.297	-	-	116.0	65.0	86.0
6533.93	Fe I	4.55	-1.460	54.0	-	-	-	-
6556.81	Fe I	4.79	-1.720	35.0	-	-	-	-
6569.22	Fe I	4.73	-0.420	110.0	-	-	58.0	-
6574.23	Fe I	0.99	-5.022	123.0	-	103.0	-	84.0
6581.22	Fe I	1.48	-4.680	98.0	-	68.0	43.0	61.0
6593.87	Fe I	2.43	-2.366	161.0	114.0	-	89.0	-
6597.56	Fe I	4.79	-1.070	69.0	-	-	-	43.0
6608.03	Fe I	2.28	-3.940	81.0	-	-	21.0	44.0
6609.11	Fe I	2.56	-2.661	136.0	100.0	107.0	-	102.0
6627.54	Fe I	4.54	-1.680	67.0	-	-	15.0	34.0

6633.75	Fe I	4.56	-0.799	103.0	-	-	52.0	60.0
6646.93	Fe I	2.60	-3.990	57.0	-	-	-	35.0
6653.85	Fe I	4.15	-2.520	35.0	-	-	-	-
4416.83	Fe II	2.78	-2.610	119.0	-	-	-	-
4491.40	Fe II	2.86	-2.690	106.0	-	-	74.0	89.0
4508.29	Fe II	2.86	-2.220	108.0	-	108.0	83.0	-
4515.34	Fe II	2.84	-2.480	128.0	-	-	80.0	-
4520.22	Fe II	2.81	-2.610	103.0	-	-	65.0	79.0
4541.52	Fe II	2.86	-3.050	97.0	-	-	59.0	62.0
4555.89	Fe II	2.83	-2.280	113.0	-	-	-	-
4576.34	Fe II	2.84	-3.040	91.0	-	-	-	54.0
4582.84	Fe II	2.84	-3.090	78.0	-	-	62.0	55.0
4583.83	Fe II	2.81	-2.020	-	-	-	113.0	-
4629.34	Fe II	2.81	-2.380	-	-	-	73.0	101.0
4731.45	Fe II	2.89	-3.370	-	-	-	-	47.0
4923.92	Fe II	2.89	-1.320	180.0	-	-	131.0	-
4993.35	Fe II	2.81	-3.620	64.0	-	-	-	55.0
5196.08	Fe II	4.26	-0.450	-	-	-	98.0	-
5197.57	Fe II	3.23	-2.100	101.0	-	-	81.0	85.0
5234.63	Fe II	3.22	-2.118	105.0	-	-	71.0	89.0
5264.81	Fe II	3.23	-3.210	57.0	-	-	31.0	41.0
5284.10	Fe II	2.89	-3.190	87.0	-	-	47.0	61.0
5414.08	Fe II	3.22	-3.610	41.0	-	-	23.0	24.0
5425.25	Fe II	3.20	-3.360	57.0	-	-	42.0	49.0
5534.85	Fe II	3.24	-2.920	69.0	-	-	58.0	44.0
5991.38	Fe II	3.15	-3.740	59.0	-	-	-	34.0
6149.25	Fe II	3.89	-2.720	50.0	39.0	35.0	33.0	36.0
6238.38	Fe II	3.89	-2.670	67.0	-	-	25.0	38.0
6247.56	Fe II	3.89	-2.360	60.0	-	-	-	45.0
6416.93	Fe II	3.89	-2.790	-	-	-	35.0	42.0
6432.68	Fe II	2.89	-3.710	-	-	-	28.0	45.0
6456.39	Fe II	3.90	-2.080	74.0	-	-	55.0	55.0
6516.08	Fe II	2.89	-3.450	83.0	-	-	48.0	52.0
6300.31	O I	0.00	-9.750	SS	SS	SS	SS	SS
6363.79	O I	0.02	-10.250	15.0	-	-	-	8.0
5682.65	Na I	2.10	-0.700	-	110.0	-	99.0	99.0
5688.21	Na I	2.10	-0.370	-	114.0	120.0	99.0	112.0
6154.23	Na I	2.10	-1.560	98.0	-	-	33.0	50.0
6160.75	Na I	2.10	-1.260	109.0	-	79.0	42.0	62.0
4703.00	Mg I	4.34	-0.670	-	-	-	151.0	165.0
5528.41	Mg I	4.34	-0.480	-	180.0	SS	177.0	190.0
5711.09	Mg I	4.35	-1.728	-	-	-	86.0	107.0
6318.72	Mg I	5.11	-1.970	75.0	-	-	-	48.0

6319.24	Mg I	5.11	-2.210	62.0	-	-	21.0	21.0
6319.49	Mg I	5.11	-2.430	42.0	-	-	11.0	16.0
6696.03	Al I	3.14	-1.570	91.0	-	-	24.0	42.0
6698.67	Al I	3.14	-1.890	51.0	-	-	14.0	21.0
5645.66	Si I	4.91	-2.140	69.0	-	-	-	38.0
5665.60	Si I	4.90	-2.040	74.0	-	-	24.0	40.0
5684.52	Si I	4.93	-1.650	78.0	-	-	43.0	56.0
6125.03	Si I	5.62	-1.570	52.0	-	-	13.0	31.0
6142.48	Si I	5.62	-1.510	42.0	-	-	22.0	-
6145.02	Si I	5.61	-1.370	52.0	-	-	28.0	37.0
6155.14	Si I	5.62	-0.800	103.0	SS	63.0	53.0	68.0
6237.33	Si I	5.61	-1.020	80.0	-	-	-	-
6243.82	Si I	5.61	-1.270	61.0	-	-	46.0	32.0
6244.48	Si I	5.61	-1.270	67.0	-	-	32.0	44.0
4425.44	Ca I	1.88	-0.360	-	-	-	116.0	-
4435.68	Ca I	1.89	-0.520	-	-	-	-	133.0
4455.89	Ca I	1.90	-0.530	-	-	-	127.0	147.0
5581.97	Ca I	2.52	-0.555	140.0	104.0	109.0	95.0	108.0
5588.75	Ca I	2.52	0.210	-	169.0	-	119.0	156.0
5598.49	Ca I	2.52	-0.087	-	-	-	126.0	-
5857.45	Ca I	2.93	0.230	174.0	139.0	128.0	104.0	127.0
6102.73	Ca I	1.88	-0.790	184.0	146.0	-	128.0	149.0
6122.23	Ca I	1.89	-0.320	-	184.0	-	163.0	165.0
6156.03	Ca I	2.52	-2.390	40.0	-	-	-	18.0
6161.30	Ca I	2.52	-1.270	120.0	-	-	70.0	85.0
6162.17	Ca I	1.90	-0.090	-	-	-	160.0	197.0
6166.44	Ca I	2.52	-1.140	115.0	-	-	69.0	86.0
6169.04	Ca I	2.52	-0.800	143.0	-	-	89.0	96.0
6169.56	Ca I	2.52	-0.480	158.0	-	108.0	84.0	116.0
6439.08	Ca I	2.52	0.390	-	-	-	-	171.0
6449.81	Ca I	2.52	-0.502	155.0	-	-	89.0	134.0
6455.60	Ca I	2.52	-1.290	108.0	-	-	60.0	83.0
6471.67	Ca I	2.52	-0.760	148.0	-	-	84.0	99.0
6493.79	Ca I	2.52	-0.320	170.0	-	144.0	119.0	135.0
6499.65	Ca I	2.52	-0.820	140.0	-	-	-	-
6717.68	Ca I	2.71	-0.610	-	97.0	-	-	-
4400.39	Sc II	0.61	-0.540	153.0	-	-	-	118.0
4415.56	Sc II	0.60	-0.640	152.0	-	-	-	135.0
4670.41	Sc II	1.36	-0.580	-	-	-	77.0	97.0
5031.02	Sc II	1.36	-0.400	132.0	-	-	90.0	-
5318.37	Sc II	1.36	-2.010	44.0	-	-	-	30.0
5526.79	Sc II	1.77	0.030	118.0	-	SS	88.0	96.0
5641.00	Sc II	1.50	-1.130	90.0	-	-	50.0	76.0

5667.16	Sc II	1.50	-1.310	85.0	67.0	-	54.0	58.0
5669.06	Sc II	1.50	-1.200	86.0	60.0	-	53.0	73.0
5684.21	Sc II	1.51	-1.070	80.0	-	-	-	79.0
6245.62	Sc II	1.51	-0.970	86.0	-	-	56.0	65.0
6309.90	Sc II	1.50	-1.520	55.0	-	-	-	48.0
6604.58	Sc II	1.36	-1.310	86.0	79.0	-	54.0	76.0
4512.73	Ti I	0.84	-0.424	131.0	-	-	63.0	89.0
4533.25	Ti I	0.85	0.480	176.0	-	-	102.0	-
4534.78	Ti I	0.84	0.280	177.0	-	-	-	126.0
4548.76	Ti I	0.83	-0.298	134.0	-	-	-	-
4681.91	Ti I	0.05	-1.015	153.0	-	-	93.0	-
4840.87	Ti I	0.90	-0.450	128.0	104.0	-	69.0	98.0
4913.62	Ti I	1.87	0.216	95.0	-	-	58.0	65.0
4981.73	Ti I	0.84	0.500	173.0	-	-	109.0	153.0
4991.06	Ti I	0.84	0.380	188.0	-	-	101.0	135.0
4997.10	Ti I	0.00	-2.060	107.0	-	-	56.0	86.0
4999.50	Ti I	0.83	0.250	198.0	-	-	104.0	-
5009.65	Ti I	0.02	-2.203	108.0	-	-	56.0	77.0
5016.16	Ti I	0.85	-0.510	130.0	-	-	-	102.0
5024.84	Ti I	0.82	-0.546	138.0	102.0	112.0	70.0	-
5036.46	Ti I	1.44	0.186	141.0	-	-	85.0	-
5038.40	Ti I	1.43	0.069	123.0	-	92.0	-	-
5039.96	Ti I	0.02	-1.130	152.0	-	-	88.0	110.0
5064.65	Ti I	0.05	-0.930	178.0	-	-	101.0	118.0
5113.44	Ti I	1.44	-0.727	93.0	-	-	30.0	-
5145.47	Ti I	1.46	-0.518	104.0	-	-	42.0	73.0
5173.74	Ti I	0.00	-1.120	178.0	-	-	102.0	111.0
5192.97	Ti I	0.02	-1.010	179.0	-	151.0	98.0	129.0
5210.39	Ti I	0.05	-0.580	191.0	-	-	-	134.0
5490.16	Ti I	1.46	-0.933	-	-	-	26.0	58.0
5503.90	Ti I	2.58	-0.190	52.0	-	-	-	14.0
5978.54	Ti I	1.87	-0.440	87.0	-	-	-	49.0
6126.22	Ti I	1.07	-1.425	97.0	-	-	32.0	60.0
6220.50	Ti I	2.68	-0.140	50.0	-	-	-	-
6258.10	Ti I	1.44	-0.355	122.0	75.0	73.0	54.0	82.0
6303.77	Ti I	1.44	-1.570	62.0	-	-	15.0	-
6312.24	Ti I	1.46	-1.550	58.0	-	-	-	-
6336.10	Ti I	1.44	-1.740	58.0	-	-	-	15.0
6554.24	Ti I	1.44	-1.218	88.0	-	-	-	51.0
6556.08	Ti I	1.46	-1.074	91.0	-	-	34.0	57.0
6599.13	Ti I	0.90	-2.090	77.0	-	-	-	-
6743.13	Ti I	0.90	-1.630	101.0	-	-	24.0	66.0
4395.85	Ti II	1.24	-2.170	101.0	-	-	-	-

4399.77	Ti II	1.24	-1.290	144.0	-	-	95.0	-
4417.72	Ti II	1.16	-1.430	156.0	-	-	-	116.0
4441.73	Ti II	1.18	-2.410	-	-	-	52.0	-
4443.79	Ti II	1.08	-0.710	198.0	-	-	118.0	-
4444.56	Ti II	1.12	-2.030	116.0	-	-	69.0	-
4450.48	Ti II	1.08	-1.450	137.0	-	-	93.0	112.0
4464.45	Ti II	1.16	-2.080	115.0	-	-	69.0	85.0
4468.51	Ti II	1.13	-0.620	196.0	-	-	120.0	-
4469.14	Ti II	1.08	-2.870	95.0	-	-	31.0	-
4470.86	Ti II	1.16	-2.280	113.0	-	-	56.0	76.0
4488.33	Ti II	3.12	-0.820	77.0	-	-	44.0	46.0
4493.51	Ti II	1.08	-2.740	82.0	-	-	-	-
4501.27	Ti II	1.12	-0.750	-	-	-	134.0	185.0
4518.33	Ti II	1.08	-2.560	93.0	-	-	44.0	-
4533.97	Ti II	1.24	-0.770	186.0	-	-	113.0	138.0
4544.03	Ti II	1.24	-2.410	95.0	-	-	-	-
4545.14	Ti II	1.13	-1.810	122.0	-	-	81.0	-
4563.76	Ti II	1.22	-0.960	-	-	-	115.0	144.0
4568.31	Ti II	1.22	-2.650	87.0	-	-	42.0	71.0
4571.97	Ti II	1.57	-0.520	-	-	-	123.0	158.0
4589.96	Ti II	1.24	-1.780	123.0	-	-	70.0	106.0
4708.67	Ti II	1.24	-2.210	-	-	-	66.0	78.0
4779.99	Ti II	2.05	-1.370	98.0	-	-	47.0	79.0
4798.53	Ti II	1.08	-2.670	93.0	-	-	44.0	78.0
4805.09	Ti II	2.06	-1.120	-	-	-	64.0	-
4865.61	Ti II	1.12	-2.590	91.0	-	-	43.0	82.0
4911.18	Ti II	3.12	-0.340	90.0	-	-	45.0	65.0
5005.15	Ti II	1.57	-2.730	63.0	-	-	31.0	48.0
5129.16	Ti II	1.89	-1.390	114.0	-	-	55.0	90.0
5154.07	Ti II	1.57	-1.520	122.0	-	-	75.0	-
5185.91	Ti II	1.89	-1.350	106.0	-	-	56.0	85.0
5188.68	Ti II	1.58	-1.220	135.0	135.0	-	-	-
5226.55	Ti II	1.57	-1.000	159.0	-	98.0	86.0	132.0
5336.77	Ti II	1.58	-1.700	112.0	-	-	72.0	87.0
5381.01	Ti II	1.57	-1.780	124.0	101.0	-	67.0	82.0
5418.77	Ti II	1.58	-2.110	88.0	84.0	-	60.0	77.0
6559.59	Ti II	2.05	-2.019	-	-	72.0	-	-
6606.95	Ti II	2.06	-2.790	41.0	-	-	-	-
6680.13	Ti II	3.09	-1.860	23.0	-	-	-	-
6090.21	V I	1.08	-0.060	112.0	-	79.0	48.0	-
6119.53	V I	1.06	-0.320	105.0	-	-	-	64.0
6128.33	V I	1.05	-2.300	14.0	-	-	-	-
6135.37	V I	1.05	-0.750	82.0	-	-	24.0	44.0

6150.15	V I	0.30	-1.790	101.0	-	45.0	19.0	45.0
6199.19	V I	0.29	-1.290	123.0	-	79.0	-	68.0
6216.36	V I	0.28	-1.290	129.0	SS	-	48.0	85.0
6224.51	V I	0.29	-2.010	77.0	-	46.0	10.0	33.0
6233.20	V I	0.28	-2.070	72.0	-	-	-	39.0
6243.11	V I	0.30	-0.980	143.0	-	-	49.0	92.0
6251.82	V I	0.29	-1.300	114.0	-	-	-	79.0
6274.66	V I	0.27	-1.670	87.0	-	-	-	48.0
6285.16	V I	0.28	-1.560	95.0	-	-	-	68.0
6292.82	V I	0.29	-1.520	101.0	-	-	-	52.0
6357.29	V I	1.85	-0.910	26.0	-	-	-	-
6452.32	V I	1.19	-1.210	52.0	-	-	-	25.0
6504.19	V I	1.18	-1.230	65.0	-	-	-	17.0
4496.84	Cr I	0.94	-1.150	-	-	-	103.0	136.0
4600.75	Cr I	1.00	-1.260	146.0	-	-	83.0	-
4616.14	Cr I	0.98	-1.190	151.0	-	-	98.0	107.0
4626.19	Cr I	0.97	-1.320	137.0	-	-	95.0	104.0
4651.28	Cr I	0.98	-1.460	143.0	-	-	91.0	105.0
4652.16	Cr I	1.00	-1.030	171.0	-	-	93.0	117.0
5206.04	Cr I	0.94	0.019	-	-	-	194.0	-
5247.56	Cr I	0.96	-1.640	154.0	-	-	75.0	110.0
5345.80	Cr I	1.00	-0.980	198.0	-	-	123.0	149.0
5409.80	Cr I	1.03	-0.720	-	-	-	126.0	147.0
6330.09	Cr I	0.94	-2.920	103.0	49.0	-	35.0	57.0
4558.65	Cr II	4.07	-0.660	100.0	-	-	63.0	82.0
4848.24	Cr II	3.86	-1.130	87.0	-	-	60.0	65.0
4754.04	Mn I	2.28	-0.090	-	-	-	100.0	138.0
4762.37	Mn I	2.89	0.430	-	-	-	114.0	135.0
4783.43	Mn I	2.30	0.042	-	-	-	110.0	149.0
4823.52	Mn I	2.32	0.140	-	-	-	116.0	168.0
5432.55	Mn I	0.00	-3.795	168.0	-	-	-	120.0
5516.77	Mn I	2.18	-1.847	131.0	-	-	-	83.0
6013.51	Mn I	3.07	-0.252	156.0	-	-	-	107.0
6021.82	Mn I	3.08	0.035	159.0	-	116.0	-	106.0
5483.34	Co I	1.71	-1.488	129.0	-	-	63.0	104.0
5647.23	Co I	2.28	-1.560	76.0	-	-	20.0	52.0
4648.66	Ni I	3.42	-0.160	118.0	-	-	83.0	-
4714.42	Ni I	3.38	0.230	199.0	-	-	99.0	146.0
4855.41	Ni I	3.54	0.000	152.0	-	-	100.0	-
5017.59	Ni I	3.54	-0.080	121.0	-	-	96.0	-
5080.52	Ni I	3.65	0.130	150.0	-	-	82.0	96.0
5084.08	Ni I	3.68	0.030	114.0	-	-	77.0	90.0
5137.07	Ni I	1.68	-1.990	159.0	114.0	-	84.0	117.0

5578.73	Ni I	1.68	-2.670	124.0	-	-	-	-
5587.87	Ni I	1.93	-2.370	110.0	-	-	70.0	99.0
5589.37	Ni I	3.90	-1.150	53.0	-	-	30.0	43.0
5593.75	Ni I	3.90	-0.790	72.0	-	-	34.0	47.0
6128.97	Ni I	1.68	-3.390	88.0	-	69.0	38.0	56.0
6130.14	Ni I	4.27	-0.980	46.0	-	-	14.0	-
6176.82	Ni I	4.09	-0.430	98.0	-	-	57.0	68.0
6177.25	Ni I	1.83	-3.500	69.0	-	-	-	33.0
6186.72	Ni I	4.11	-0.900	64.0	-	-	-	32.0
6204.61	Ni I	4.09	-1.150	55.0	-	-	27.0	24.0
6223.99	Ni I	4.10	-0.970	56.0	-	-	-	26.0
6230.10	Ni I	4.11	-1.200	56.0	-	39.0	-	25.0
6322.17	Ni I	4.15	-1.210	47.0	-	-	-	-
6327.60	Ni I	1.68	-3.090	116.0	-	79.0	47.0	74.0
6378.26	Ni I	4.15	-0.820	-	-	-	-	47.0
6384.67	Ni I	4.15	-1.000	-	-	-	14.0	32.0
6482.80	Ni I	1.94	-2.850	107.0	70.0	79.0	51.0	80.0
6586.32	Ni I	1.95	-2.790	110.0	78.0	-	61.0	69.0
6598.61	Ni I	4.24	-0.930	57.0	-	-	28.0	-
6635.14	Ni I	4.42	-0.750	65.0	-	-	-	37.0
6767.78	Ni I	1.83	-2.170	147.0	-	114.0	87.0	105.0
5105.50	Cu I	1.39	-1.505	186.0	-	-	108.0	129.0
5700.24	Cu I	1.64	-2.330	143.0	-	-	61.0	-
5782.13	Cu I	1.64	-1.720	194.0	-	SS	-	-
4722.15	Zn I	4.03	-0.338	99.0	-	-	61.0	83.0
4810.54	Zn I	4.08	-0.170	88.0	-	-	61.0	72.0
6362.35	Zn I	5.80	0.140	35.0	-	-	18.0	20.0
4883.69	Y II	1.08	0.070	104.0	-	-	49.0	75.0
4900.11	Y II	1.03	-0.090	102.0	-	-	43.0	63.0
5087.43	Y II	1.08	-0.170	82.0	-	-	39.0	61.0
5200.42	Y II	0.99	-0.570	91.0	-	-	33.0	57.0
5402.78	Y II	1.84	-0.510	40.0	-	-	-	13.0
4554.03	Ba II	0.00	0.170	-	-	-	-	-
4934.16	Ba II	0.00	-0.150	-	-	-	175.0	-
5853.69	Ba II	0.60	-1.010	121.0	106.0	114.0	76.0	112.0
6141.73	Ba II	0.70	-0.077	SS	SS	SS	SS	SS
5301.97	La II	0.40	-1.140	40.0	-	-	-	-
5303.52	La II	0.32	-1.350	29.0	-	-	-	26.0
6320.43	La II	0.17	-1.562	32.0	-	-	17.0	31.0
6774.27	La II	0.13	-1.708	34.0	-	-	-	16.0
5249.59	Nd II	0.98	0.200	69.0	-	-	20.0	37.0
5319.82	Nd II	0.55	-0.140	64.0	53.0	-	36.0	55.0
5416.38	Nd II	0.86	-0.980	10.0	-	-	-	-

5431.54	Nd II	1.12	-0.470	19.0	-	-	-	-
5485.71	Nd II	1.26	-0.120	31.0	-	-	-	-
6645.13	Eu II	1.37	0.120	SS	SS	SS	SS	SS

Integrated Light EWs

All IL EWs were measured in DAOSPEC. Any deviant lines and all those stronger than 100 mÅ were checked and refined in *splot*. The Galactic GC EWs are listed in Table C.3, while the PAndAS EWs are given in Table C.4. For the Galactic GCs, all lines stronger than 150 mÅ were removed from the abundance analysis. For the PAndAS clusters, a stricter limit of $\sim$ 110 mÅ was adopted, unless otherwise noted.

Table C.3: The Galactic GC Line List.

Wavelength	Element	E.P.	log gf	Equivalent width (mÅ)				
(Å)		(eV)		47 Tuc	M3	M13	NGC 7006	M15
5324.191	Fe I	3.211	-0.103	-	112.0	97.2	103.0	38.6
5339.937	Fe I	3.266	-0.72	-	80.1	75.1	87.0	-
5367.476	Fe I	4.415	0.443	114.0	70.0	68.0	78.0	22.9
5369.974	Fe I	4.371	0.536	147.0	72.5	73.2	75.1	-
5371.501	Fe I	0.958	-1.644	-	183.0	167.6	186.0	108.6
5383.38	Fe I	4.312	0.645	135.3	82.7	77.9	87.2	-
5389.486	Fe I	4.415	-0.41	-	34.9	32.5	43.0	-
5393.176	Fe I	3.241	-0.715	133.6	82.5	72.6	95.9	32.2
5397.141	Fe I	0.915	-1.982	-	-	-	-	95.0
5405.785	Fe I	0.99	-1.852	-	-	-	-	89.9
5424.08	Fe I	4.32	0.52	124.0	90.5	80.7	82.8	48.1
5429.706	Fe I	0.958	-1.881	-	-	-	-	86.0
5434.534	Fe I	1.011	-2.126	-	144.0	138.9	132.2	86.0
5446.924	Fe I	0.99	-3.109	-	-	148.0	-	107.2
5455.624	Fe I	0.0	-2.091	-	-	-	-	105.1
5497.526	Fe I	1.011	-2.825	-	110.0	110.4	120.1	59.3
5501.477	Fe I	0.958	-3.046	-	102.2	101.4	102.9	50.1
5506.791	Fe I	0.99	-2.789	-	111.0	107.3	104.6	53.5
5522.446	Fe I	4.209	-1.45	-	14.3	-	19.5	-
5543.936	Fe I	4.218	-1.04	-	19.0	19.4	32.9	-
5560.212	Fe I	4.435	-1.09	40.2	12.4	-	12.7	-
5569.631	Fe I	3.417	-0.5	133.4	85.0	74.7	72.7	-
5572.851	Fe I	3.396	-0.275	137.0	108.0	93.0	89.4	51.7
5576.099	Fe I	3.43	-0.9	114.5	70.1	58.0	53.4	26.5
5586.771	Fe I	3.37	-0.12	-	110.9	103.6	127.1	52.8
5618.632	Fe I	4.209	-1.275	49.9	14.0	-	18.3	-
5633.946	Fe I	4.991	-0.23	45.7	14.9	10.5	-	-
5652.318	Fe I	4.26	-1.85	-	18.0	-	15.8	-
5741.848	Fe I	4.256	-1.672	24.9	-	-	-	-
5752.032	Fe I	4.549	-0.864	48.7	17.8	-	23.3	-

5763.002	Fe I	4.209	-0.45	98.6	39.2	52.0	45.7	-
5775.081	Fe I	4.22	-1.297	41.4	18.2	14.2	18.1	-
5778.453	Fe I	2.588	-3.44	-	14.4	-	13.0	-
5862.357	Fe I	4.549	-0.051	-	32.1	28.9	38.4	-
5905.671	Fe I	4.652	-0.69	61.0	14.4	-	23.2	-
5934.655	Fe I	3.929	-1.07	81.5	32.6	31.0	26.8	-
5976.777	Fe I	3.943	-1.503	55.3	28.2	26.1	37.6	-
6003.011	Fe I	3.882	-1.12	-	42.3	37.0	25.3	-
6012.21	Fe I	2.223	-4.038	-	10.0	-	16.4	-
6024.058	Fe I	4.549	-0.12	97.0	52.7	47.0	65.0	-
6027.051	Fe I	4.076	-1.089	66.0	29.9	22.3	32.7	-
6078.491	Fe I	4.796	-0.481	-	22.1	25.8	28.8	-
6079.008	Fe I	4.652	-1.02	-	11.0	10.6	-	-
6096.664	Fe I	3.984	-1.83	-	12.0	-	21.0	-
6136.624	Fe I	2.453	-1.41	-	109.0	-	107.0	56.4
6137.702	Fe I	2.588	-1.346	-	96.0	88.0	96.6	42.4
6151.617	Fe I	2.176	-3.3	68.0	39.6	30.3	30.9	-
6173.341	Fe I	2.22	-2.863	89.0	42.3	42.8	62.5	-
6180.209	Fe I	2.73	-2.628	83.0	30.5	26.9	28.1	-
6187.995	Fe I	3.94	-1.673	45.0	19.1	-	21.8	-
6200.313	Fe I	2.609	-2.386	-	53.1	45.7	57.1	19.0
6213.437	Fe I	2.22	-2.49	116.0	69.4	63.5	79.9	18.5
6219.287	Fe I	2.2	-2.428	120.0	72.2	67.4	76.5	22.5
6229.232	Fe I	2.83	-2.821	62.4	23.0	-	-	-
6230.736	Fe I	2.559	-1.276	-	116.6	102.0	109.5	54.9
6246.327	Fe I	3.6	-0.796	110.3	64.0	56.9	54.9	-
6252.565	Fe I	2.404	-1.767	135.3	91.4	81.6	83.5	41.5
6254.253	Fe I	2.28	-2.435	127.0	73.4	73.3	67.3	24.5
6265.141	Fe I	2.18	-2.532	116.5	64.2	60.7	84.9	28.4
6270.231	Fe I	2.86	-2.543	58.7	34.0	24.4	26.3	-
6297.799	Fe I	2.22	-2.681	104.7	-	-	-	-
6301.508	Fe I	3.65	-0.701	112.4	-	-	-	-
6322.694	Fe I	2.59	-2.438	92.0	-	-	-	-
6335.337	Fe I	2.2	-2.175	132.8	-	-	-	-
6336.83	Fe I	3.69	-0.840	101.7	-	-	-	-
6353.849	Fe I	0.91	-6.36	28.0	-	-	-	-
6355.035	Fe I	2.84	-2.328	102.5	43.0	35.0	-	-
6380.75	Fe I	4.19	-1.366	52.7	27.4	-	22.4-	
6392.538	Fe I	2.28	-3.957	-	17.0	15.0	- -	
6393.612	Fe I	2.43	-1.505	-	103.0	97.3	104.5	54.3
6400.009	Fe I	3.602	-0.29	-	96.3	-	101.0	42.3
6411.658	Fe I	3.65	-0.646	115.7	72.0	68.7	77.0	-
6419.956	Fe I	4.73	-0.183	78.5	33.9	28.0	39.8	-

6421.36	Fe I	2.28	-1.979	-	91.8	76.0	-	42.0
6430.856	Fe I	2.18	-1.954	-	96.7	90.5	95.7	40.0
6475.632	Fe I	2.56	-2.929	86.6	39.2	30.2	44.9	-
6481.878	Fe I	2.28	-2.985	96.8	50.6	35.8	-	-
6494.994	Fe I	2.4	-1.246	-	105.0	119.0	127.4	63.0
6498.945	Fe I	0.96	-4.675	106.1	35.0	47.0	39.1	-
6518.366	Fe I	2.832	-2.397	91.6	47.1	35.0	32.8	-
6546.252	Fe I	2.75	-1.536	131.6	83.8	71.2	91.5	27.0
6569.224	Fe I	4.73	-0.38	-	38.0	-	22.0	-
6593.874	Fe I	2.43	-2.377	103.0	62.6	61.4	58.8	-
6597.571	Fe I	4.77	-0.97	-	11.2	-	-	-
6608.044	Fe I	2.27	-3.939	46.5	15.5	16.9	-	-
6627.56	Fe I	4.53	-1.559	26.7	-	-	-	-
6646.966	Fe I	2.6	-3.917	21.6	-	-	-	-
6648.121	Fe I	1.01	-5.73	37.0	15.0	12.4	-	-
6677.997	Fe I	2.69	-1.395	145.4	97.0	98.5	94.1	48.4
6703.576	Fe I	2.76	-3.059	67.0	27.0	19.6	29.2	-
6705.105	Fe I	4.61	-1.06	41.0	12.5	-	-	-
6710.323	Fe I	1.48	-4.807	49.0	25.9	17.3	-	-
6715.386	Fe I	4.59	-1.54	-	-	-	11.4	-
6726.666	Fe I	4.607	-1.087	44.7	10.6	-	-	-
6739.524	Fe I	1.56	-4.801	-	15.0	-	-	-
6750.164	Fe I	2.42	-2.592	92.0	58.7	56.3	-	-
6752.716	Fe I	4.64	-1.263	-	10.0	-	-	-
6806.856	Fe I	2.73	-2.633	-	23.7	25.0	16.0	-
6810.267	Fe I	4.59	-0.992	42.0	23.0	-	-	-
6820.371	Fe I	4.638	-1.214	33.9	-	-	-	-
6828.596	Fe I	4.64	-0.843	-	20.0	17.1	-	-
6839.835	Fe I	2.56	-3.378	49.0	21.0	-	33.0	-
6841.341	Fe I	4.61	-0.733	64.6	22.9	-	-	-
6842.689	Fe I	4.64	-1.224	-			21.6	-
6843.655	Fe I	3.65	-0.863	-	18.3	-	-	19.2
6851.652	Fe I	1.6	-5.247	25.0	-	-	-	-
6855.161	Fe I	4.559	-0.741	68.5	25.2	-	33.6	-
6855.723	Fe I	4.39	-1.747	-	14.0	-	-	-
6858.155	Fe I	4.59	-0.939	51.0	15.0	13.6	-	-
6911.512	Fe I	2.424	-3.967	-	-	-	-	27.4
6916.686	Fe I	4.15	-1.359	-	23.0	31.4	-	-
6988.524	Fe I	2.404	-3.519	-	25.0	19.4	-	-
7022.957	Fe I	4.19	-1.148	-	21.5	20.0	22.1	-
7038.22	Fe I	4.22	-1.214	-	26.4	22.0	-	-
7068.423	Fe I	4.07	-1.319	79.4	25.0	27.0	50.9	-
7072.8	Fe I	4.07	-2.767	-	-	-	25.2	-

7090.39	Fe I	4.23	-1.109	78.7	23.9	19.5	-	36.7
7130.925	Fe I	4.3	-0.708	-	48.6	41.0	38.0	-
7132.985	Fe I	4.06	-1.635	57.4	16.3	-	-	-
7145.312	Fe I	4.61	-1.24	-	12.0	-	-	-
7151.464	Fe I	2.48	-3.657	-	24.8	-	-	-
7180.004	Fe I	1.48	-4.707	61.1	-	-	24.8	-
7219.682	Fe I	4.076	-1.617	45.6	-	-	12.2	-
5534.848	Fe II	3.245	-2.79	64.5	30.0	29.6	37.8	-
6238.39	Fe II	3.889	-2.69	-	-	-	17.8	6.0
6247.557	Fe II	3.892	-2.38	41.7	21.0	-	27.0	-
6416.928	Fe II	3.89	-2.74	33.2	12.9	-	12.8	-
6432.683	Fe II	2.89	-3.63	-	22.7	23.0	20.9	-
6456.391	Fe II	3.903	-2.075	47.8	48.2	36.2	34.4	-
6516.08	Fe II	2.891	-3.44	54.5	35.0	29.6	31.7	-
5581.979	Ca I	2.523	-0.555	113.0	50.3	-	63.3	-
5588.764	Ca I	2.526	0.358	-	103.7	97.2	124.0	47.0
5590.126	Ca I	2.521	-0.571	112.1	58.1	53.9	67.4	-
5601.286	Ca I	2.526	-0.690	113.9	56.0	51.7	57.0	-
5857.459	Ca I	2.933	0.240	131.0	86.5	74.0	95.0	-
5867.572	Ca I	2.930	-1.640	36.3	15.0	-	-	-
6122.226	Ca I	1.886	-0.320	-	127.5	122.1	124.9	71.8
6161.295	Ca I	2.520	-1.266	-	40.4	33.4	-	-
6162.180	Ca I	1.899	-0.090	-	135.5	136.0	145.0	70.3
6166.440	Ca I	2.520	-1.142	89.1	35.0	36.0	34.9	-
6439.083	Ca I	2.526	0.390	-	122.3	116.9	127.0	56.4
6455.605	Ca I	2.520	-1.290	-	38.5	26.3	26.6	-
6471.662	Ca I	2.526	-0.686	116.0	63.1	-	-	-
6493.781	Ca I	2.521	-0.109	-	91.0	83.4	96.3	39.2
6572.795	Ca I	0.000	-4.310	97.0	48.0	-	32.3	-
7148.150	Ca I	2.709	0.137	-	107.3	94.7	116.0	39.9
7326.160	Ca I	2.930	-0.230	124.0	66.5	62.0	138.0	-
5401.379	Ti I	0.818	-2.890	20.0	-	-	-	-
5648.570	Ti I	2.495	-0.260	28.7	-	-	14.0	10.3
5866.451	Ti I	1.067	-0.840	104.4	47.0	47.0	57.6	-
6554.238	Ti I	1.440	-1.218	78.3	21.9	17.4	29.7	-
6556.077	Ti I	1.460	-1.074	-	19.0	22.9	-	-
6743.127	Ti I	0.900	-1.630	-	31.0	29.6	27.8	-
7209.468	Ti I	1.460	-0.500	-	-	40.4	39.0	-
7216.190	Ti I	1.440	-1.150	74.8	26.0	-	33.0	-
7251.717	Ti I	1.430	-0.770	89.7	40.0	15.0	13.8	-
5336.780	Ti II	1.582	-1.700	103.3	63.1	62.0	-	31.9
5381.010	Ti II	1.566	-2.080	86.0	55.0	55.1	56.4	29.8
6327.604	Ni I	1.680	-3.150	60.0	-	-	-	-

6482.809	Ni I	1.930	-2.630	70.9	40.3	33.0	-	-
6586.319	Ni I	1.951	-2.810	57.5	35.0	25.0	28.0	-
6643.638	Ni I	1.676	-2.300	122.3	72.0	68.0	68.5	-
6767.784	Ni I	1.826	-2.170	101.2	63.6	60.7	70.2	27.0
6772.321	Ni I	3.660	-0.980	44.4	16.3	17.0	24.6	-
7110.905	Ni I	1.930	-2.980	60.7	28.0	19.5	31.2	-
7122.206	Ni I	3.542	0.040	-	62.0	63.0	66.0	-
5853.688	Ba II	0.604	-1.010	105.0	65.6	66.1	-	32.5
6141.727	Ba II	0.704	-0.076	-	110.2	112.8	117.2	65.8
6496.908	Ba II	0.604	-0.377	143.0	114.0	114.1	117.9	65.0

Table C.4: The PAndAS GC Line List.

λ (Å)	Element	E.P. (eV)	log gf	Equivalent width (mÅ) H10	H23	PA06	PA17	PA53	PA54	PA56
5324.191	Fe I	3.21	-0.103	-	-	80.0	-	83.1	79.4	80.0
5339.937	Fe I	3.27	-0.720	81.0	-	-	-	-	-	54.8
5367.476	Fe I	4.42	0.443	77.9	93.9	46.0	-	68.0	50.0	53.2
5369.974	Fe I	4.37	0.536	-	-	50.0	-	-	-	59.4
5371.501	Fe I	0.96	-1.644	-	-	126.0	-	-	-	-
5383.380	Fe I	4.31	0.645	85.4	109.0	-	-	65.0	65.4	62.3
5389.486	Fe I	4.42	-0.410	-	56.0	-	-	-	-	24.7
5393.176	Fe I	3.24	-0.715	83.0	-	52.2	-	70.7	55.0	54.0
5397.141	Fe I	0.92	-1.982	-	-	112.0	-	-	-	119.2
5405.785	Fe I	0.99	-1.852	-	-	110.0	-	-	-	-
5424.080	Fe I	4.32	0.520	87.0	101.0	55.2	-	69.0	54.0	75.0
5429.706	Fe I	0.96	-1.881	-	-	118.0	-	-	-	-
5434.534	Fe I	1.01	-2.126	-	-	101.5	-	113.2	-	102.4
5497.526	Fe I	1.01	-2.825	-	-	77.0	-	99.4	88.4	-
5501.477	Fe I	0.96	-3.046	97.0	-	-	-	79.0	71.6	85.7
5506.791	Fe I	0.99	-2.789	-	-	78.6	-	99.0	84.7	81.1
5522.446	Fe I	4.21	-1.450	-	29.0	-	-	-	-	-
5543.936	Fe I	4.22	-1.040	-	36.0	-	43.0	-	-	-
5569.631	Fe I	3.42	-0.500	90.4	97.0	51.0	-	-	58.0	65.1
5572.851	Fe I	3.40	-0.275	102.0	-	65.6	-	84.0	64.0	65.0
5576.099	Fe I	3.43	-0.900	70.0	86.0	-	97.0	-	-	61.0
5586.771	Fe I	3.37	-0.120	101.0	-	72.0	-	83.4	83.0	87.8
5618.632	Fe I	4.21	-1.275	-	34.3	-	-	-	-	-
5763.002	Fe I	4.21	-0.450	47.0	72.0	-	82.1	44.0	25.5	-
5778.453	Fe I	2.59	-3.440	-	-	-	31.0	-	-	-
5862.357	Fe I	4.55	-0.051	45.0	-	-	72.0	-	-	-
5905.671	Fe I	4.65	-0.690	-	28.7	-	51.7	-	-	-
5934.655	Fe I	3.93	-1.070	41.5	59.1	-	73.0	-	-	20.2
5943.578	Fe I	2.20	-4.456	-	16.0	-	-	-	-	-
5976.777	Fe I	3.94	-1.503	-	39.0	-	50.3	-	-	-
6003.011	Fe I	3.88	-1.120	47.5	59.0	-	72.6	-	19.0	-
6012.210	Fe I	2.22	-4.038	-	-	-	35.0	-	-	-
6024.058	Fe I	4.55	-0.120	59.0	69.4	-	-	-	27.0	40.0
6027.051	Fe I	4.08	-1.089	-	52.8	-	50.4	-	-	
6136.624	Fe I	2.45	-1.410	-	-	-	-	78.0	82.0	83.0
6137.702	Fe I	2.59	-1.346	98.2	-	-	-	70.9	-	77.0
6151.617	Fe I	2.18	-3.300	-	57.3	-	58.0	-	-	18.0
6173.341	Fe I	2.22	-2.863	60.0	-	-	93.0	42.0	29.5	32.0
6180.209	Fe I	2.73	-2.628	45.2	54.3	-	-	-	-	31.7

6187.995	Fe I	3.94	-1.673	-	-	-	52.6	-	-	-
6200.313	Fe I	2.61	-2.386	56.6	67.0	-	92.0	-	-	34.1
6213.437	Fe I	2.22	-2.490	76.0	86.4	41.0	-	50.0	-	43.0
6219.287	Fe I	2.20	-2.428	74.7	85.0	45.0	-	-	-	58.4
6229.232	Fe I	2.83	-2.821	-	-	-	42.0	-	-	-
6230.736	Fe I	2.56	-1.276	109.0	-	72.0	-	91.5	80.1	95.5
6246.327	Fe I	3.60	-0.796	62.0	90.0	42.0	-	54.0	49.0	53.6
6252.565	Fe I	2.40	-1.767	95.5	102.0	53.0	-	65.8	66.9	68.0
6254.253	Fe I	2.28	-2.435	73.0	92.0	39.0	100.0	-	49.2	53.0
6265.141	Fe I	2.18	-2.532	64.0	-	-	99.0	49.0	-	53.5
6270.231	Fe I	2.86	-2.543	-	41.0	-	-	-	-	-
6380.750	Fe I	4.19	-1.366	-	27.7	-	-	-	-	-
6392.538	Fe I	2.28	-3.957	-	-	-	39.7	-	-	-
6393.612	Fe I	2.43	-1.505	-	-	-	-	82.1	-	78.0
6400.009	Fe I	3.60	-0.290	-	-	62.0	-	84.0	76.9	69.8
6411.658	Fe I	3.65	-0.646	73.2	98.1	46.0	-	70.0	48.9	58.0
6419.956	Fe I	4.73	-0.183	34.1	47.0	-	-	-	-	-
6421.360	Fe I	2.28	-1.979	97.2	105.0	-	-	-	-	61.9
6430.856	Fe I	2.18	-1.954	94.7	-	62.0	-	86.9	74.8	75.0
6475.632	Fe I	2.56	-2.929	39.7	50.4	-	-	-	-	-
6481.878	Fe I	2.28	-2.985	-	-	-	91.7	-	27.2	-
6494.994	Fe I	2.40	-1.246	-	-	88.0	-	104.4	95.4	102.5
6498.945	Fe I	0.96	-4.675	50.0	65.0	22.0	-	36.0	27.0	-
6518.366	Fe I	2.83	-2.397	41.9	57.3	-	72.0	-	-	-
6546.252	Fe I	2.75	-1.536	87.0	101.0	52.0	-	78.0	58.5	-
6569.224	Fe I	4.73	-0.380	-	-	-	73.5	-	-	-
6593.874	Fe I	2.43	-2.377	59.9	90.6	32.0	92.0	54.4	45.0	53.0
6597.571	Fe I	4.77	-0.970	-	22.0	-	-	-	-	-
6608.044	Fe I	2.27	-3.939	-	37.0	-	53.2	-	-	-
6648.121	Fe I	1.01	-5.730	-	-	-	39.0	-	-	-
6677.997	Fe I	2.69	-1.395	-	-	62.0	-	90.7	63.0	65.0
6703.576	Fe I	2.76	-3.059	-	37.0	-	-	-	-	-
6705.105	Fe I	4.61	-1.060	-	29.0	-	-	-	-	-
6710.323	Fe I	1.48	-4.807	-	38.0	-	45.0	-	-	-
6750.164	Fe I	2.42	-2.592	61.0	75.0	32.0	81.0	-	43.0	48.0
6806.856	Fe I	2.73	-2.633	33.0	60.0	-	60.0	-	-	-
6810.267	Fe I	4.59	-0.992	-	26.8	-	37.0	-	-	-
6828.596	Fe I	4.64	-0.843	-	29.2	-	-	-	-	-
6839.835	Fe I	2.56	-3.378	-	31.3	-	-	-	-	-
6841.341	Fe I	4.61	-0.733	-	31.0	-	-	-	-	-
6843.655	Fe I	3.65	-0.863	-	87.1	-	-	-	-	-
6855.161	Fe I	4.56	-0.741	-	46.1	-	-	-	-	-
6916.686	Fe I	4.15	-1.359	-	38.0	-	-	-	-	-

6988.524	Fe I	2.40	-3.519	33.0	43.0	-	-	-	-	-
7022.957	Fe I	4.19	-1.148	28.8	49.6	-	51.0	-	22.5	-
7038.220	Fe I	4.22	-1.214	29.0	-	-	-	-	-	-
7090.390	Fe I	4.23	-1.109	-	42.0	-	-	-	-	-
7130.925	Fe I	4.30	-0.708	47.0	55.8	-	-	-	30.0	-
7145.312	Fe I	4.61	-1.240	-	-	-	33.0	-	-	-
5534.848	Fe II	3.25	-2.790	-	40.8	-	-	28.0	26.0	-
6238.390	Fe II	3.89	-2.690	21.6	30.8	-	21.0	-	-	-
6247.557	Fe II	3.89	-2.380	-	-	-	-	-	22.0	-
6416.928	Fe II	3.89	-2.740	21.0	-	-	16.4	-	-	-
6432.683	Fe II	2.89	-3.630	30.8	19.8	12.0	36.7	-	-	-
6456.391	Fe II	3.90	-2.075	45.0	40.8	-	68.0	-	-	-
6516.080	Fe II	2.89	-3.440	32.0	42.6	-	-	-	-	29.0
5581.979	Ca I	2.52	-0.555	59.1	91.0	-	-	-	36.0	-
5588.764	Ca I	2.53	0.358	104.0	-	84.3	-	84.7	78.3	76.0
5590.126	Ca I	2.52	-0.571	63.4	88.0	-	80.0	41.0	38.0	39.0
5601.286	Ca I	2.53	-0.690	54.1	82.0	-	82.7	-	32.9	-
5857.459	Ca I	2.93	0.240	79.0	-	46.0	-	57.0	48.1	49.0
6122.226	Ca I	1.89	-0.320	-	-	94.0	-	98.0	93.0	-
6161.295	Ca I	2.52	-1.266	-	63.0	15.7	-	-	-	-
6162.180	Ca I	1.90	-0.090	-	-	-	-	100.0	-	-
6166.440	Ca I	2.52	-1.142	52.0	-	-	-	-	-	26.4
6439.083	Ca I	2.53	0.390	-	-	-	-	98.0	84.6	102.0
6455.605	Ca I	2.52	-1.290	-	57.0	-	70.0	-	-	-
6471.662	Ca I	2.53	-0.686	-	-	-	-	50.0	-	42.0
6493.781	Ca I	2.52	-0.109	106.0	-	56.5	-	69.0	61.2	69.0
6572.795	Ca I	0.00	-4.310	49.0	70.0	-	-	31.0	-	-
7148.150	Ca I	2.71	0.137	109.0	-	74.0	-	73.1	-	-
7326.160	Ca I	2.93	-0.230	75.0	-	34.0	-	-	-	42.0
5866.451	Ti I	1.07	-0.840	56.0	-	-	-	32.3	-	-
6743.127	Ti I	0.90	-1.630	-	62.0	-	58.0	-	-	-
7209.468	Ti I	1.46	-0.500	-	82.0	-	-	-	-	35.9
5336.780	Ti II	1.58	-1.700	76.0	-	44.0	-	47.0	-	-
5381.010	Ti II	1.57	-2.080	69.0	67.0	34.0	71.0	41.0	51.0	-
6482.809	Ni I	1.93	-2.630	42.4	48.0	-	-	-	-	-
6586.319	Ni I	1.95	-2.810	38.2	-	-	-	-	-	-
6643.638	Ni I	1.68	-2.300	74.5	91.4	44.2	97.0	55.0	51.0	48.0
6767.784	Ni I	1.83	-2.170	74.7	85.0	44.0	-	-	45.0	-
6772.321	Ni I	3.66	-0.980	29.0	32.0	-	-	-	-	-
7110.905	Ni I	1.93	-2.980	28.9	-	-	54.0	-	-	-
7122.206	Ni I	3.54	0.040	68.4	81.0	-	99.0	63.0	50.0	54.0